# Drone-based sensing for identification of at-risk water and nitrogen stress areas for on-farm management

A thesis submitted in partial fulfilment of
the requirement for the degree of

**Doctor of Philosophy**

by

**Rahul Raj**

(IITB Roll: 164314003, Monash ID: 28845250)

Under the supervision of

**Prof. J. Adinarayana**
(Centre of Studies in Resources Engineering, IIT Bombay)

**Prof. Jeffrey Walker**
(Department of Civil Engineering, Monash University)

*The course of study for this award was jointly developed by Monash University, Australia and the Indian Institute of Technology Bombay, India, and administered by IITB-Monash Research Academy*

(June 2021)

# Copyright notice

# Declaration

I hereby declare that the work presented in this thesis entitled “Drone-based sensing for identification of at-risk water and nitrogen stress areas for on-farm management” submitted by me, to Department of Civil Engineering of Monash University, CSRE of IIT-Bombay, and IITB-Monash Research Academy is a record of the research work carried out by me under the supervision of Prof. Jeffery Walker (Professor, Department of Civil engineering, Monash University) and Prof. J. Adinarayana (Professor, Centre of Studies in Resources Engineering, IITB).

I further declare that this written submission represents my ideas in my own words and where other’s ideas or words have been included, I have adequately cited and referenced the original sources. I affirm that I have adhered to all principles of academic honesty and integrity and have not misrepresented or falsified any idea/data/fact/source to the best of my knowledge. I understand that any violation of the above will cause for disciplinary action by the Institute and can also evoke penal action from the sources which have not been cited properly.

Place: Patna, Bihar, India
Date: 19 Jan 2022

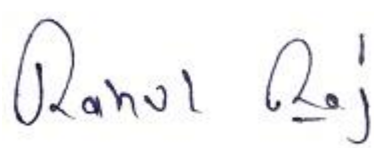

(Signature)
Rahul Raj
164314003 / 28845250

*This page has intentionally been left blank.*

*Dedicated to my parents,*

*Rekha Devi and Late Yogendra Kumar,*

*for their unwavering trust, support,*

*and endless sacrifices…*

*This page has intentionally been left blank.*

# Acknowledgements

Apart from my efforts, the success of this thesis depends largely on the encouragement, guidance, prayers, and trust of many others. I take this opportunity to express my gratitude to the people who have supported me not only in the preparation of this thesis but also in managing my personal and professional life.

First, I would like to remember my late father, who died fighting cancer in 2016. Throughout his life, he provided all the possible support to me so that I can study without any trouble. I am sad that he is physically not here to see me getting this degree, but I believe that my father will always be alive within me. After my father's death, my mother took all the responsibilities and encouraged me to complete this PhD degree to honour my father's sacrifices. Accordingly, most of the credit goes to my mother, who trusted me and sent me away to study in the worst stage of her life. I would also like to thank my sister, who supported me and took care of our mother. They are the ones who need to be recognized for the completion of this thesis.

Now, I would like to show my greatest appreciation to my project guides, Professor Jeffrey Walker and Professor J. Adinarayana. I can't say thank you enough for their tremendous support and help. Without their encouragement and guidance, this research would not have materialized. Prof. Adi gave me enormous opportunities and exposure to participate and contribute to international interdisciplinary projects. He always encouraged me to think high and achieve more significant objectives. Jeff's weekly meeting discussions added a lot to this research which I could not have done without his guidance. Despite having a very packed schedule, Jeff always took weekly progress meetings and gave very constructive feedback, which has not only improved the quality of this research but also motivated me to keep expanding my capabilities. I felt motivated and encouraged every time I attended his meetings. Thank you for all your constructive critical comments and in-depth discussions. I hope to receive similar guidance from Jeff even in my post PhD life. I would also like to thank Dr Vanessa Wong (my research progress committee member) and Mr Rohit Nandan (my lab-mate and a good friend) for their informative discussions on the topic. It was

Vanessa who suggested me to use the CHNS analyser instrument for leaf nitrogen content analysis. This suggestion has saved me a lot of analysis time. Rohit Nandan was always there for all the field data collection, and maybe without him this PhD journey would not have been this smooth. I want to give special thanks to Mr Rohit Pingale, who worked along with me on related aspects of this project for almost two years and helped me in data collection, data curation, and visualization of the results. Thank you, Mr Subramoni, Mr Shashibhusan, Mr Priyankar Chand and Mr Bhupendra Sharma, for helping me out in chemical analysis and preprocessing of the leaf samples. Special thanks to Mr Rishav Saphia for his initial help in demystifying the hyperspectral data. Thank you, Mr Prabhakar, for supporting me during the initial stage of my PhD. Thank you, Ramit, for being such a good friend academically and personally. Thank you to all the interns (Aravind, Chetan, Dishank, Devyani, Shravan, Vishal, Sana, Shreya, Shubham, and Sumant) to make this research journey more fruitful even during the COVID pandemic time. Thank you to my friends Lokesh, Abhishek, Alok, Gaurav, Apurv, Nataraj to give moral support throughout this journey. Thank you, NIRD and ARI, Hyderabad, for supporting me in the farm data collection. Thank you, Prof. Wei Guo, Prof. Ninomiya and Prof. Honda, for asking the correct questions so that I could find the right answer and providing me with soil moisture data. Thank you, Mr Naveen, for helping in soil sample collection and giving farm information when I was away. Thank you, Saurav sir, and Soumya ma'am, for being there with me during the sinusoidal journey of my PhD.

The guidance and support received from my IITB research progress committee members – Prof Alok Porwal and Prof Surya Durbha, were vital for the success of this PhD. I am grateful for their constant support and help. At last, I would like to thank IITB-Monash Research Academy, which funded my research for four years and three months. All the staff members of the academy always helped me in getting things done at an administrative level.

Rahul Raj

(Rahul Raj)

*This page has intentionally been left blank.*

# Abstract

Farming in small-scale, resource-poor farming systems is majorly dependent on the traditional knowledge of farmers, with non-judicial, time-consuming and labor-intensive agricultural practices commonly implemented, leading to low productivity and degradation of resources. This creates a strong need across small-scale farming systems to provide leap-frog techniques and technologies that would rapidly, inexpensively, and preferably asymptomatically detect crop stress and provide management decision in near-real-time to enhance productivity, input use efficiency, profitability and sustainability of small-scale farming systems. Precision agricultural (PA) practices offer great opportunities for improvement in the present context of sustainability and climate variability. Moreover, it offers the opportunity for a farmer to apply the right input, in the right amount, at the right time, at the right location, and in the right manner. However, to collect timely high-resolution data, unmanned aerial vehicle (UAV) based sensing and image interpretation are required. These high-resolution images can give detailed information about the soil and crop condition at plant-level, which can be used for farm management purposes.

The precise remote estimation of crop biophysical parameters like crop leaf area index (LAI), especially during the reproductive stage, is a challenge due to the canopy closure effect. Additionally, leaf water content (LWC) estimation for early growth stages, and distinguishing water and nitrogen stress in plants using remotely sensed optical data are unanswered research questions. This thesis has documented conceptual and data-driven models to solve these research gaps. Moreover, all the biophysical and simulation-based results have been incorporated into one model to predict crop stress better. To solve these research questions, a field experiment has been carried out on a maize crop in a semi-arid region of central India for two *Rabi* seasons being 2018-19 and 2019-20. The drone-based and ground-truth data of crop biophysical and biochemical contents were collected during different crop growth stages.

Two alternate methods have been developed and compared for estimating the LAI of a maize crop. Both methods used drone-based RGB images to estimate the canopy height and the green-canopy cover together with a 'vertical leaf area distribution factor' (*VLADF*) from allometric relations (using crop height from RBG images and days after sowing). The first method used an empirical approach to estimate the LAI from training a linear function of the above inputs to Licor canopy analyser values of LAI. The method was found to have validation results with an $R^2$ of 0.84 and RMSE of 0.36 for the 2018-19 *Rabi* season data, and $R^2$ of 0.77 and RMSE of 0.45 for the 2019-20 *Rabi* season data, when compared with Licor LAI values. While seemingly acceptable, the Licor canopy analyser gives a foliage area index and so the accuracy of this model was very low ($R^2$ of 0.56 and RMSE of 1.34) when evaluated with true LAI from manual measurements of the leaf area. Consequently, a refinement was introduced using only *VLADF*, green-canopy cover estimates from the RBG images, and a field measured top leaf angle. The output derived from this conceptual model had an $R^2$ of ~0.6 and RMSE of 0.73 when compared with the true LAI values. Importantly, the LAI from this conceptual model was unaffected by canopy closure during the reproductive stage of the crop. The percentage of tasselling in each plot during the first week of tasselling was estimated using a 701 nm centred band image obtained from drone-based hyperspectral images. The growth rate of the number of tassels from its first day of onset indicates the severity of crop stress, thus a good indicator to be captured remotely. The image processing methods used to detect and count the tassels, gave an accuracy of 96.4%.

The APSIM crop simulation model was used to obtain reference crop LAI and crop height under optimal and actual farm management conditions. The optimal condition results were used as a reference for healthy crop parameters. The estimated temporal crop LAI and crop height were compared against the respective simulated references. These comparisons, along with the tasselling percentage information, were used in a model to get the health status of the crop. The temporal healthiness maps were created, and the healthiness factor correlation with the crop yield was obtained. The maximum $R^2$ of 0.67, 0.61, and 0.45 was obtained during the dough stage, tasselling stage, and early vegetative stage of the crop, respectively. The healthiness maps were able to indicate the stress area, but it cannot give the reason behind that stress.

This research also developed a new model for estimating LWC based on newly identified, pure-pixel, water sensitive indices from high spatial resolution hyperspectral data. The spectroradiometer data were used to explore the wavelengths sensitive to vibrational overtone frequencies of O-H bonds of water molecules present in leaves. The identified wavelengths were used to create normalized indices. These indices' minimum and maximum values were used to create synthetic data for training a gradient boost machine (GBM) model. The model was used to make high spatial resolution maps of LWC using drone-based hyperspectral data. The early growth stage maps of LWC were able to distinguish between water-stressed and well-irrigated plots with an $R^2$ of 0.93 and RMSE of 1.6 % (g/g). The leaf nitrogen content (LNC) model was also developed by identifying new indices and understanding its sensitivity towards the EM spectra behaviour in the red-edge region. The LNC model gave a maximum $R^2$ of 0.64 for water-stressed areas but a maximum $R^2$ of 0.26 was obtained for higher LWC areas. The LNC and LWC model results were overlapped on the healthiness map created using biophysical properties to understand the crop water and nitrogen stress in the crop.

# Table of contents

# List of Figures

# List of Tables

# Abbreviations

| | |
|---|---|
| APSIM | Agricultural Production Systems sIMulator |
| BGI | Blue-Green ratio Index |
| BRDF | Bidirectional Reflectance Distribution Function |
| CI | Chlorophyll Index |
| COSBNDI | Combined Overtone of Stretching Bands – Normalized Difference Index |
| CR | Canopy Reflectance |
| CWA | Continuous Wavelet Analysis |
| CWSI | Crop Water Stress Index |
| DAS | Days After Sowing |
| DBH | Diameter at Breast Height |
| DCNI | Double peak Canopy Nitrogen Index |
| DEM | Digital Elevation Model |
| DSM | Digital Surface Model |
| EM | Electro-Magnetic |
| EVI | Enhanced Vegetation Index |
| EWT | Equivalent Water Thickness |
| FCC | False Colour Composition |
| FIR | Far InfraRed |
| FNR | False Negative Rate |
| FPR | False Positive Rate |

| | |
|---|---|
| FOSBNDI | Forth Overtone of Stretching Bands – Normalized Difference Index |
| FSOSBNDI | Fifth and Sixth Overtone of Stretching Bands - Normalized Difference Index |
| GA | Genetic Algorithm |
| GBM | Gradient Boost Machine |
| GCC | Green Canopy Cover |
| GCP | Ground Control Points |
| GDD | Growing Degree Days |
| GIS | Geographical Information System |
| GPS | Global Positioning System |
| HFN | High-Frequency Noise |
| LAD | Leaf Angle Distribution |
| LAI / gLAI | Leaf Area Index / green Leaf Area Index |
| LEAFMOD | Leaf Experimental Absorptivity Feasibility MODel |
| LIBERTY | Leaf Incorporating Biochemistry Exhibiting Reflectance and Transmittance Yields |
| LIDF | Leaf Inclination Distribution function |
| LNC | Leaf Nitrogen Content |
| LWC | Leaf Water Content |
| MDWI | Maximum Difference Water Index |
| MSI | Moisture Stress Index |
| MSM | Measured Soil Moisture |

| | |
|---|---|
| NDI | Normalized Difference Index |
| $NDI_{opt}$ | Normalized Difference Index at optimum |
| NDII | Normalized Difference Infrared Index |
| NDVI | Normalized Difference Vegetation Index |
| $NDVI_{g-b}$ | green-blue Normalized Difference Vegetation Index |
| NDWI | Normalized Difference Water Index |
| NGRDI | Normalized Green-Red Difference Index |
| NIR | Near Infrared |
| OSAVI | Optimised Soil Adjusted Vegetation Index |
| PA | Precision Agriculture |
| PLS | Partial Least Square |
| PRI | Photochemical Reflectance Index |
| PROSPECT | PROperties SPECTra |
| RDVI | Renormalized Difference Vegetation Index |
| RT | Radiative Transfer |
| SAIL | Scattering by Arbitrary Inclined Leaves |
| SAPSBNDI | Small Absorption Peak of Stretching Bands - Normalized Difference Index |
| SD | Standard Deviation |
| SKYL | fraction of incident radiation that is diffused |
| SOSBNDI | Second Overtone of Stretching Bands - Normalized Difference Index |

| | |
|---|---|
| SR | Simple Ratio |
| TCARI | Transformed Chlorophyll Absorption in Reflectance Index |
| UAS /UAV | Unmanned Aerial System / Vehicle |
| $VI_{opt}$ | optimal Vegetation Index |
| VIS | Visible Spectrum |
| VLADF | Vertical Leaf Area Distribution Factor |
| WASCOSBNDI | Water Absorption Shoulder due to Combined Overtone of Stretching Bands - Normalized Difference Index |
| WDRVI | Wide Dynamic Range Vegetation Index |

# Chapter 1
# Introduction

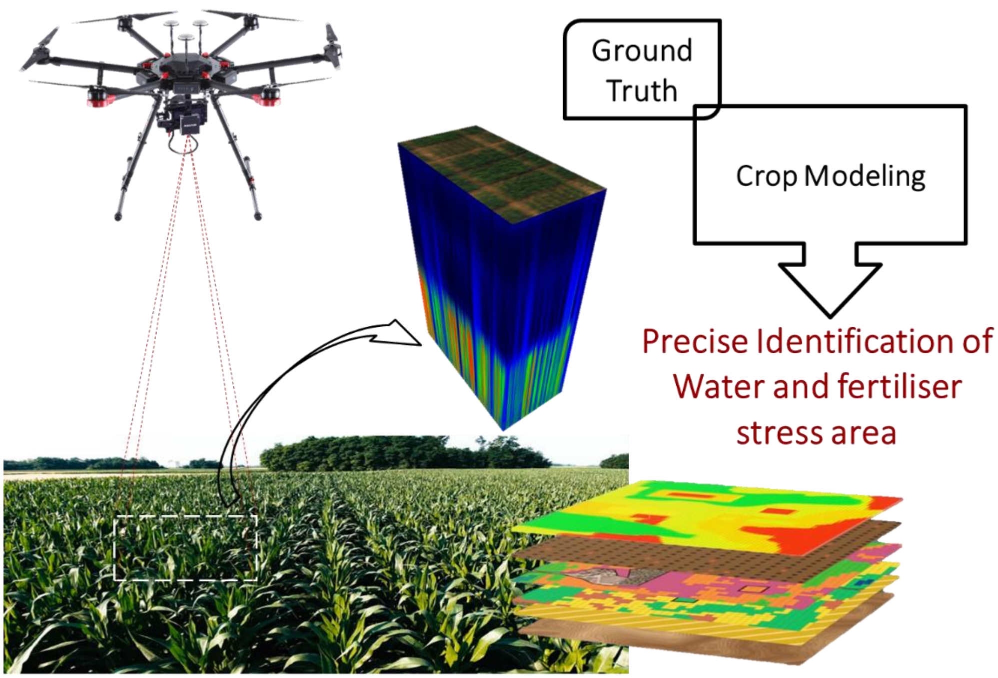


*Drone-based sensors provide data at very high spatial resolution which can be used to create plant level management decisions. This evolving technology is predicted to be an integral part of future farming.*

*"We have neglected the truth that a good farmer is a craftsman of the highest order, a kind of artist." - Wendell Berry.*

# 1. Introduction

In this research work, conceptual and data-driven models have been developed to estimate crop biophysical (Leaf area index, canopy height, tasseling percentage) and ultimately biochemical (leaf water and nitrogen content) properties of the crop, using only UAV based high-resolution RGB and hyperspectral (VIS and NIR) reflectance data. The study was focused on the analysis of growth-stage based behaviour of crop biophysical and biochemical properties in conjunction with the input resources supplied on the farm. Collection and analysis of hand-held spectroradiometer and drone-mounted hyperspectral imager based leaf-level hyperspectral reflectance spectra along with CHNS analysis of destructive leaf samples make this research data novel. New indices for leaf-water and leaf-nitrogen content were developed and tested for pure pixel hyperspectral images. The developed models were implemented to obtain the spatial and temporal distribution of water and nitrogen stress in the farm. This research work suggested that the stress areas can be identified using estimated crop biophysical properties and further identified as water or nitrogen stress areas using biochemical estimation models.

## 1.1 Background and problem statement

Water and nitrogen are the two most important input parameters for any grain crop production (Olson et al., 1964; Terman et al., 1969; Spratt and Gasser, 1970), as these factors control plant growth (Welch, 1979; Sinclair et al., 1986; Gonzalez-Dugo et al., 2010). Optimised water and nitrogen use as farm input can minimise the yield gap (Welch, 1979; Sinclair et al., 1986; Mueller et al., 2012). Water also helps nutrients to travel to various parts of the plant. It has been observed that even when the soil's supply of nutrients to a plant is adequate, the plant can still show nutrition deficiency if there is water scarcity (Keller, 2005). Moreover, being an energetic macronutrient, nitrogen needs to be maintained above a certain level in plants (Blumenthal et al., 2008; Lemaire and Gastal, 2018; Gupta, 2020) because it is required to produce chlorophyll, proteins, nucleic acids, and amino acids in plants (Muñoz-Huerta et al., 2013). Thus, nitrogen is essential for a crop to maintain healthy growth, and its critical value represents the minimum concentration in the plant for maximising growth. However, excess amount of nitrogen in the farm leads to water pollution (Broadbent and Rauschkolb, 1977) as the irrigated water gets wasted through runoff and leaching (Elrashidi et al., 2005; Knox et al., 2012). Thus, for optimal management of a farm, it is crucial to estimate the spatial distribution of crop water and nitrogen content in the context of the crop growth stage (Samoy et al., 2008).

Various vegetation indices are available for estimating crop biophysical and biochemical properties, but they usually show a saturation effect, especially NDVI (Huete et al., 2002; Freitas et al., 2005; Wu et al., 2008). Moreover, most of the indices are derived from satellite data in which the percentage of mixed pixels remain very high. Accordingly, there is a need to explore new/modified vegetation indices, which may work better on drone-based data where most of the pixels are pure (as the spatial resolution is around 1 cm), and atmospheric effect on the data is least. There is also a need to improve the sensitivity of these indices' by incorporating prior information and combining various indices. Generally, the bands sensitive to leaf nitrogen is affected by water molecules around plant protein (nitrogen is present in the plants in the form of proteins). The three-dimensional structure of plant proteins is supported by water molecules, also known as protein hydration (Franks , 1988; Chaplin, 2006), meaning that crop water and/or nitrogen stress cannot be distinguished easily. This opens an opportunity to identify the indices which are more sensitive to leaf-nitrogen than leaf-water content.

Apart from indices, another method to extract crop biophysical and biochemical properties from reflectance spectra is through the inversion of canopy models like PROSAIL (Jacquemoud, 2009). PROSAIL is a powerful simulation model to understand the reflectance properties of vegetation with change in leaf-level and canopy-level properties. However, for accurate estimation of critical properties like leaf water content, the PROSAIL inversion model requires transmittance data along with reflectance data (Jacquemoud et al., 1996; Baret and Fourty, 1997), otherwise it results in a poor estimation (Colombo et al., 2008). Unfortunately, transmittance data cannot be acquired using airborne/satellite sensors. Moreover, the models do not allow the extraction of leaf nitrogen content. Researchers are therefore trying to use a combined N-PROSPECT and SAILH model to obtain leaf nitrogen, but so far have not been able to achieve a coefficient of determination better than 0.48 (Li et al., 2018). The radiative transfer model also assumes that the leaf surface roughness parameter, the refractive index of leaf material, and the specific absorption coefficient of leaf absorbers remains the same for all leaf species. However, even for one species, these values change with change in the crop's growth stage. Moreover, the spectrum data that PROSAIL needs to simulate the canopy model for extracting leaf constituents is from 400-2500nm (Duan et al., 2014). The spectrum range selection is critical as the model assumes that the specific absorption coefficient of each leaf constituent is wavelength-dependent (Jacquemoud et al., 2008). This assumption allows the model to make changes in spectra at only those wavelengths at which the absorption coefficient of a particular leaf constituent changes. For example, a change in leaf water content will not affect the simulated leaf spectra in the range of 400-900 nm. However, due to the change in leaf water content, other leaf properties also change, making a significant change in leaf spectra even between the 400-900 nm wavelength region (Peñuelas et al., 1994). These changes can be used to generate proxy indices to estimate those leaf constituents in which absorption happens after the 1000 nm wavelength. Photochemical reflectance index (PRI) is a classic example of such index, used as a proxy for detecting water stress in the crop (Thenot et al., 2002). Despite these limitations, PROSAIL is one of the best vegetation spectra simulation models to date for understanding vegetation's reflectance and transmittance properties. However, due to its limitations and the type of available data, the use of the PROSAIL model is out of scope of this research.

Other popular crop simulation models like DSSAT, APSIM, WOFOST, and

MLCan use local weather, environmental, soil, and crop properties to simulate crop photosynthesis and respiration, and connects them to plant growth. These models need to be calibrated for local conditions. Moreover, these models are point-based and do not provide spatial variability of crop properties in the farm. These crop simulation models don't use hyperspectral information, and thus a critical analysis of these are outside the scope of this research. However, the APSIM model is used in this research to simulate reference crop biophysical properties (LAI and height) based on local weather conditions to compare the simulated values against measured/estimated values.

Most of the existing Leaf water content (LWC) estimation models available in hyperspectral sensing are based on mixed-pixel (vegetation and visible background in the same pixel) data taken either from satellite or high-altitude airborne platforms. These platforms can map huge areas but suffer from coarser spatial resolution (mixed-pixel) data that cannot capture the changes happening in the weak water-sensitive bands (Kokaly and Clark, 1999), especially when the crop is at the early growth stage with little canopy coverage (Cheng et al., 2006), due to the higher overtones of the water's O-H molecule stretching frequencies losing sensitivity for broadband and mixed pixel data (Thorpe et al., 2006; Thenkabail et al., 2002; Fan et al., 2009; Jones and Sirault, 2014). Moreover, optical observations from high altitude platforms are highly affected by atmospheric interference (aerosol, water vapour content, and various gases present in the atmosphere), which is incredibly challenging to correct due to limitations of 'atmospheric correction' algorithms (Gao et al., 2009; Zheng and Zeng, 2004). Accordingly, the small changes in these bands are unable to provide useful information on critical vegetation parameters from these sensors (Hadjimitsis et al., 2004).

Interestingly, Kim et al. (2010) used active hyperspectral sensing (whereby a consistent light source is used to illuminate the target to eliminate atmospheric effects) to identify the plant water stress on young apple trees and found narrowband 750 nm wavelength observations useful for LWC estimation.

Zygielbaum et al. (2009) used 400-750 nm spectroradiometer data and found that 520 nm wavelength useful in the retrieval of relative water content from maize. In another study, Corti et al. (2017) used the partial least square algorithm to estimate water stress in spinach plants using line-scanner camera-based 400-1000 nm hyperspectral data. However, Corti et al. (2017) could not point out specific bands related to water stress but gave ranges of wavelength based on the partial least square algorithm. Feilhauer et al. (2015) has used the PROSPECT model data along with leaf-level spectroradiometer data (400-2500 nm) of various crops to select spectral bands for LWC (gram/$cm^2$) estimation. Using an ensemble approach, bands near 750 nm were identified from the 400-1000 nm range for LWC estimation. From the 1000-2500 nm range, 1412 nm, 1978 nm, 2004 nm, and 2401 nm have been identified for LWC estimation. Casas et al. (2014) has used satellite, airborne, and field-based hyperspectral data based indices to estimate temporal variation in canopy water content. They identified that longer SWIR region-based indices gave an improved correlation with canopy water content. Ge et al. (2019) has used UAV based hyperspectral imagery to estimate soil moisture using machine learning techniques and identified 420, 440, 460, 700, and 750 nm bands as relatively strong absorption bands. The usefulness and reasoning of some of these bands with respect to the vibrational absorption frequencies of water molecules are discussed in this thesis.

In this research, the need for a crop-growth stage based decision support system was identified, driven not only by the basic science of the crop but also considering on-ground real-time easily collectable data, noting that crop biophysical and biochemical properties change as the crop makes the transition from one growth-stage to another. The model assimilates information from crop growth parameters like canopy height, LAI, simulated soil moisture, and other critical indices to spatially classify the crop in different nitrogen and water stress categories. The basic outline of the approach used in this research is shown in Figure 1.1. The assimilation of such data gives a better estimation of crop stress conditions, which can be further used to decide the spatial distribution of

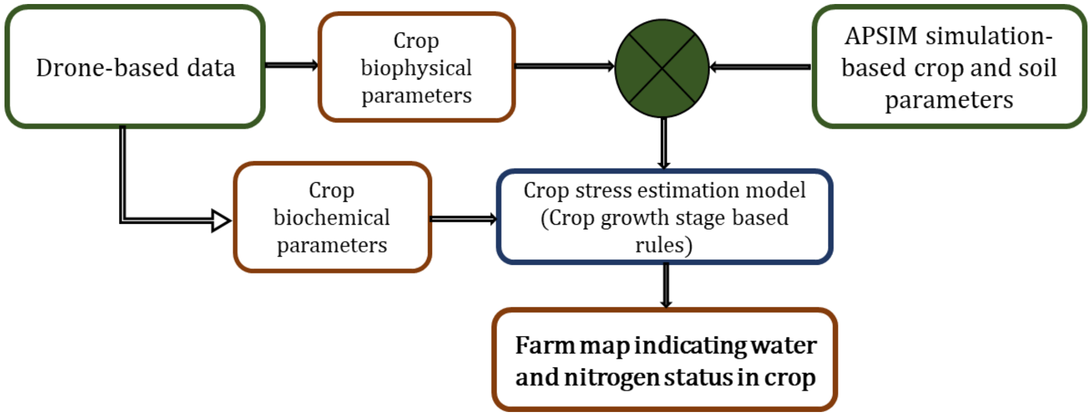


Figure 1.1: Outline of the approach.

irrigation and fertilization treatment that needs to be given on the farm (Note that suggesting irrigation and fertiliser amount is not part of the PhD thesis).

Some of the long term benefits of crop water and nitrogen estimation include:

- Reduction in groundwater pollution by minimising the nitrate-nitrogen losses from agricultural land (Meisinger and Randall, 1991; Viets, 1971).
- Increase in crop yield due to judicious application of input resources (Moore and Tyndale-Biscoe, 1999; Osborne et al., 2002).
- Reduction in soil pollution, especially soil heavy metal concentration by application of the optimal amount of fertilisers (Atafar et al., 2010; Rahman and Zhang, 2018; Savci, 2012).
- Economic benefits to the stakeholders of the farm produce by saving input resources and achieving optimal yield (Bell et al., 2008; Bullock and Bullock, 2000; Henry et al., 1995; Kingwell and Fuchsbichler, 2011).
- Food safety through reduced risk of health issues to the consumers and farmers as a result of optimal use of chemicals in the farm leading to less percentage of harmful chemical contents in the food grain (Sharma and Singhvi, 2017; Weisenburger, 1993).

- Food security through optimal use of fertilisers helps in achieving optimal yield without damaging soil fertility in the long run (Arvin and Syers, 2013; Hossain and Singh, 2000; Jones et al., 2013).

## 1.2 Objective, Assumptions, and Scope

The main objective of this research was to develop models to detect crop stress and distinguish the water and nitrogen stress present in the crop, using crop biophysical and biochemical properties, estimated using drone-based 400-1000 nm spectral range data. This required collection and investigation of ground-truth and remotely sensed data of a research farm for a complete crop cycle. The research gaps are explained in section 2.8. The sub-objectives include:

- Develop and validate a model to estimate near-to-actual crop height, tasseling percentage and LAI.
- Develop a model to estimate the leaf water content and nitrogen content of maize crop using 400-1000 nm hyperspectral data.
- Fusion of crop biophysical and biochemical model results to distinguish between crop water and nitrogen stress.

The hypothesis behind these questions are as follows:

- Crop height, LAI, and properties like the number of tassels are sensitive to water and nitrogen present in the farm, and due to the stress, these values change significantly;
- Narrowband high spatial (pure pixel) and temporal resolution hyperspectral data will have the least effect of canopy background, solar angle, and atmospheric effect resulting in better information (less noise due to pure pixel) about the crop properties than satellite data;
- Change in reflectance values due to change in water and nitrogen content of a leaf will be driven by the wavelengths where the absorption coefficient of water and nitrogen are high and will be affected by the other changes happening in the leaf due to change in water and nitrogen content.

The methodology followed in this research is shown in Figure 1.2. Drone-based RGB images were used for the estimation of crop height and Leaf Area Index. Drone-based hyperspectral data was used for leaf water and nitrogen content estimation, and one hyperspectral band was also used for tassel counting of the maize crop. The crop biophysical and biochemical properties and APSIM simulated results were then compared and analysed to early-stage and long-term stress area identification.

These objectives have been achieved progressively throughout the PhD candidature and have resulted in the following peer-reviewed publications:

1. Raj, R., Walker, J.P., Pingale, R., Banoth, B.N. and Jagarlapudi, A., 2021. Leaf nitrogen content estimation using top-of-canopy airborne hyperspectral data. International Journal of Applied Earth Observation and Geoinformation, 104, p.102584. https://doi.org/10.1016/j.jag.2021.102584
2. Raj R., Walker J., Vinod V., Pingale R., Naik B., Jagarlapudi A., 2021. Leaf water content estimation using top-of-canopy airborne hyperspectral images. International Journal of Applied Earth Observation and Geoinformation. https://doi.org/10.1016/j.jag.2021.102393.
3. Raj, R., Walker, J.P., Pingale, R., Nandan, R., Naik, B. and Jagarlapudi, A., 2021. Leaf area index estimation using top-of-canopy airborne RGB images. International Journal of Applied Earth Observation and Geoinformation, 96, p.102282. https://doi.org/10.1016/j.jag.2020.102282.
4. Raj R., Kar S., Nandan R., Jagarlapudi A. (2020) Precision Agriculture and Unmanned Aerial Vehicles (UAVs). In: Avtar R., Watanabe T. (eds) Unmanned Aerial Vehicle: Applications in Agriculture and Environment. Springer, Cham. https://doi.org/10.1007/978-3-030-27157-2_2
5. Raj R., Suradhaniwar S., Nandan R., Jagarlapudi A., Walker J. (2020) Drone-Based Sensing for Leaf Area Index Estimation of Citrus Canopy. In: Jain K., Khoshelham K., Zhu X., Tiwari A. (eds) Proceedings of UASG 2019. UASG 2019. Lecture Notes in Civil Engineering, vol 51. Springer, Cham. https://doi.org/10.1007/978-3-030-37393-1_9

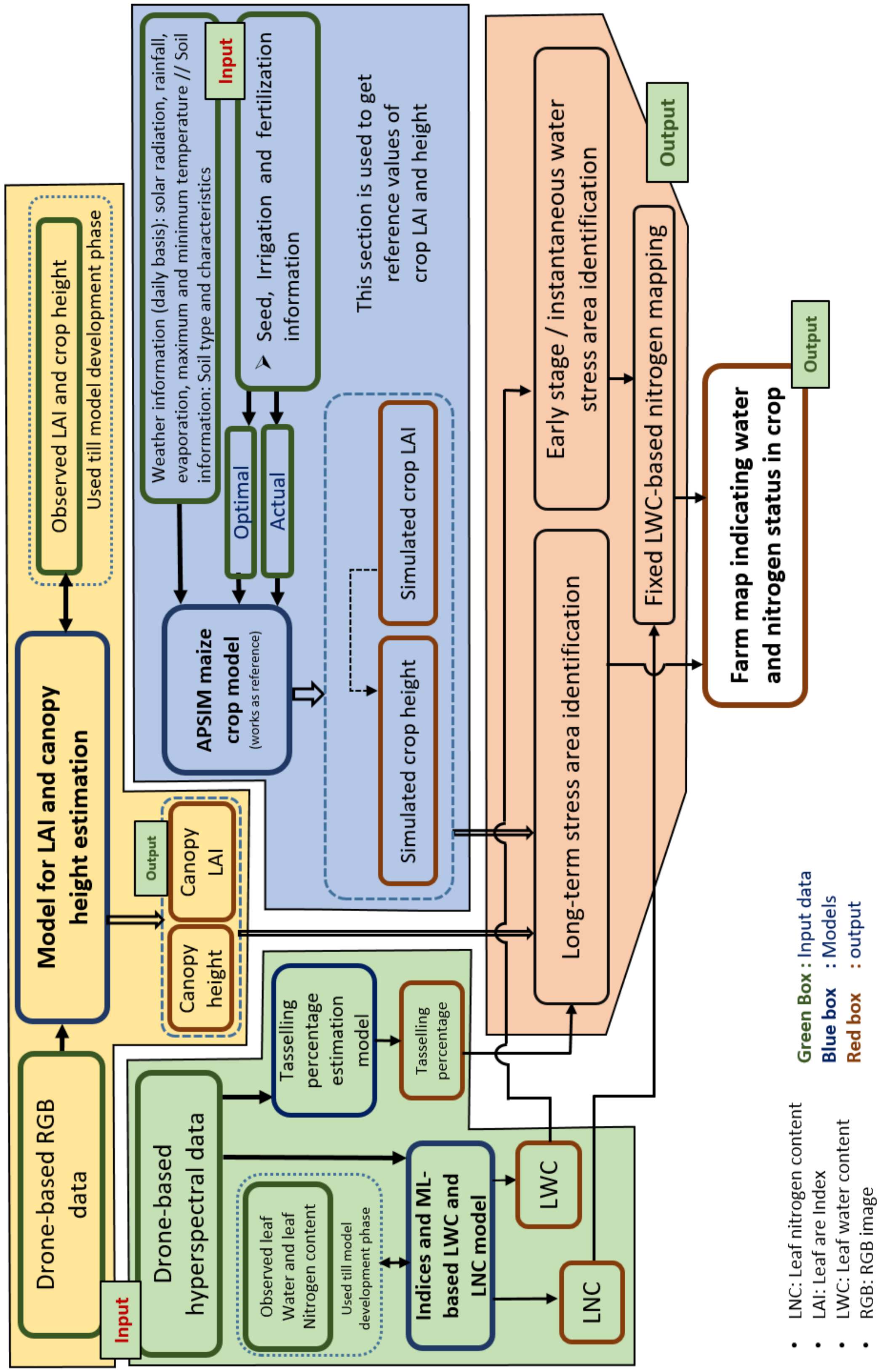


Figure 1.2: Flowchart of overall methodology followed in this thesis.

## 1.3 Organisation of thesis

The research embodied in this thesis is divided into seven chapters. Chapter two gives a detailed literature review on the estimation of various biophysical and biochemical properties of the crop using remote sensing data, followed by a section on the identified research gaps.

The third chapter comprises a detailed explanation of the experiment design, instruments and data collection methods. Various details of this chapter are also linked to the appendix section.

The fourth chapter is dedicated to the biophysical properties estimation (Leaf area Index, canopy height, and tasseling percentage) of maize crop using drone-based images. These biophysical properties are good indicators of long term water and other stress present in the farm.

The fifth chapter explains the crop stress estimation process using crop biophysical parameters derived in chapter four and APSIM crop simulation model. The APSIM simulated optimal condition results were taken and processed against the estimated crop biophysical parameters of the crop.

The sixth chapter talks about the crop biochemical properties (leaf water and nitrogen content) estimation using drone-based hyperspectral images. LWC is a good indicator of instantaneous water stress, which may lead to long-term water stress if not handled using correct irrigation practices. The crop stress map generated in chapter five is further classified in water and nitrogen stress areas using the models developed in this chapter.

The seventh chapter presents the conclusion and future work of this research. The limitations of this research and potential ways to address those limitations are also discussed in this chapter.

*This page has intentionally been left blank.*

# Chapter 2
# Literature review

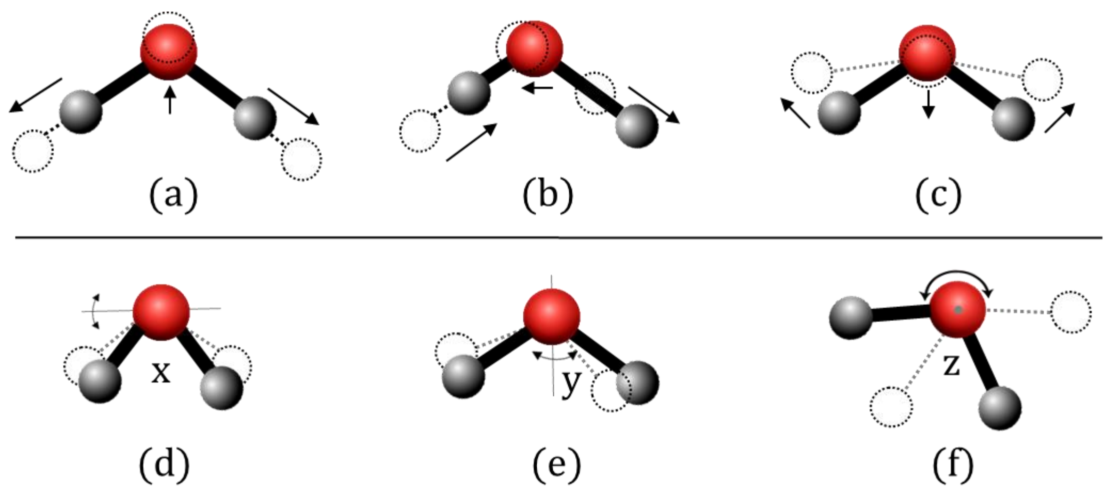


*(a), (b), and (c) shows the symmetric, asymmetric, and bending stretch in water molecules. The red colour atom represents the oxygen (O) atom, and the grey colour atoms represent hydrogen (H) atoms. The arrows show the direction of motion of the atoms. (d), (e), and (f) show the three libration modes of water molecules with respect to x, y, and z axes. When a band frequency of electromagnetic spectrum matches with the vibrational frequency of these O-H bonds, then that particular wavelength energy gets absorbed by the water molecule (adapted from Chaplin, 2008 and redrawn by Rahul Raj).*

# 2. Literature review

The Industrial Revolution has pushed agriculture practices towards greater energy inputs through big machinery, chemicals and fertilisers. However, these practices may lead to low soil fertility, soil erosion, soil salinisation, compaction of sub-soils and soil-water pollution, which have negative societal and environmental implications (Liaghat and Balasundram, 2010). In order to optimise the use of input resources for sustainable farming, plant-level management decisions are needed. Implementation of scientific farm management requires information about the crop, soil, and its environment/climate properties. These crops, soil, and environment properties can be estimated/simulated/predicted using various empirical, conceptual, and mathematical methods, including the use of radiative transfer or process-based models. However, considering the focus of this PhD research on high-spatial-resolution (plant-level) analysis, the literature review has been narrowed to corresponding methods for estimating crop biophysical and biochemical properties. It must be noted that process-based and radiative-transfer crop models are beneficial but are out of the scope for this study.

The high spatial resolution data provided by the drone-based sensors can help estimate important crop biophysical and biochemical variables, which can be used to make plant-level management decisions. This chapter review both of these critical crop variables. This chapter is divided into nine sections — sections 2.1 to 2.3 talk about drone-based platforms and sensors/instruments for precision agriculture. Section 2.4 discusses the available vegetation indices. Section 2.5 constitutes the methods for estimating crop biophysical properties; section 2.6 discusses crop biochemical properties and their retrieval using remote sensing data; section 2.7 talks about the basis of radiative transfer models; section 2.8 enlists the research gaps; section 2.9 presents a summary for this chapter.

Note: Parts of this chapter have been published as:

- Raj, R., Walker, J.P., Pingale, R., Banoth, B.N. and Jagarlapudi, A., 2021. Leaf nitrogen content estimation using top-of-canopy airborne hyperspectral data.

International Journal of Applied Earth Observation and Geoinformation, 104, p.102584. https://doi.org/10.1016/j.jag.2021.102584

- Raj R., Walker J., Vinod V., Pingale R., Naik B., Jagarlapudi A., 2021. Leaf water content estimation using top-of-canopy airborne hyperspectral images. International Journal of Applied Earth Observation and Geoinformation. https://doi.org/10.1016/j.jag.2021.102393.
- Raj, R., Walker, J.P., Pingale, R., Nandan, R., Naik, B. and Jagarlapudi, A., 2021. Leaf area index estimation using top-of-canopy airborne RGB images. International Journal of Applied Earth Observation and Geoinformation, 96, p.102282. https://doi.org/10.1016/j.jag.2020.102282.
- Raj R., Kar S., Nandan R., Jagarlapudi A. (2020) Precision Agriculture and Unmanned Aerial Vehicles (UAVs). In: Avtar R., Watanabe T. (eds) Unmanned Aerial Vehicle: Applications in Agriculture and Environment. Springer, Cham. https://doi.org/10.1007/978-3-030-27157-2_2
- Raj R., Suradhaniwar S., Nandan R., Jagarlapudi A., Walker J. (2020) Drone-Based Sensing for Leaf Area Index Estimation of Citrus Canopy. In: Jain K., Khoshelham K., Zhu X., Tiwari A. (eds) Proceedings of UASG 2019. UASG 2019. Lecture Notes in Civil Engineering, vol 51. Springer, Cham. https://doi.org/10.1007/978-3-030-37393-1_9

## 2.1 Precision agriculture

Precision agriculture (PA) is an innovative and integrated farming approach that enables farmers to use evidence-based decision making at the farm level to ensure optimal use of resources to minimise such societal and environmental implications (Tokekar et al., 2013). PA can use traditional knowledge together with spatial information and management-intensive technologies. Scientific decision making helps in making the system sustainable, productive, and profitable. In 2019, the International Society of Precision Agriculture had defined precision agriculture as: "Precision Agriculture is a management strategy that gathers, processes and analyses temporal, spatial and individual data and combines it with other information to support management decisions according to estimated variability for improved resource use efficiency, productivity, quality, profitability and sustainability of agricultural production." The technologies frequently used in PA include a Geographic Information System, Global Positioning System, remote sensing, computer modelling, variable rate technology and advanced information processing for timely crop management (Liaghat and Balasundram, 2010). The PA cycle has three components

i. Data collection: Measurement, monitoring and mapping of within-field variability in soil and crop parameters and local weather conditions.
ii. Data interpretation: Data interpretation using various crop models or image interpretation, data assimilation, or machine learning techniques to identify spatially variable parameters.
iii. Application: Data processing of results enables farmers to use the right input, in the right amount, at the right time, at the right location, and in the right manner.

Data collection and database generation is an integral part of PA, requiring a wise selection of sensors and their deployment in the farm to ensure accuracy and precision of on-farm decisions using a decision support system. Sensors can be on-ground or airborne to find information such as the crop's health, its growth stage, physical and chemical properties of the soil/plant, temporal meteorological data, etc. Remote sensing and geospatial techniques are an integral part of the data collection and analysis process and can detect in-field variation of crop/soil properties. High-resolution satellite imagery is beneficial for studying variations in crop and soil conditions. However, problems associated with the availability and cost of such imagery at an appropriate spatial and temporal resolution suggest that an alternative, such as small unmanned aerial systems (UAS)', is needed for operational PA (Zhang and Kovacs, 2012).

## 2.2 Satellite vs drone-based sensing

Satellite-based remote sensing is one of the traditional methods to acquire remotely sensed data. Still, the freely available images can only provide data at a resolution of 30 m or lower spatial resolution, which is too coarse for many applications. However, some commercial satellites provide sub-meter resolution satellite imagery (spatial resolution < 1 m for panchromatic and >1 m for multispectral) for a given time and place at a given price, but are typically infrequent in time (Liaghat and Balasundram, 2010). While satellite images may offer a better option for huge areas, their coarse resolution and infrequent repeat significantly limit its application, particularly when considering the cloud's impact. Consequently, images taken by low altitude remote sensing platforms such as small unmanned aerial vehicles (UAVs) or small crewed aircraft provide an alternative. The operation cost is low for UAVs, and they can map areas with very high spatial resolution and at the desired temporal repeat (Zhang and Kovacs, 2012). Moreover, UAVs can fly below the cloud, maximising data availability. However, other problems affect drone operation, including windy conditions in which the drone can't be flown, higher risk of a crash in case of operator error, sudden weather change or loss of power and low battery life, limiting spatial coverage. Conversely, commercial satellites generally take seven days to provide processed images. Moreover, it is challenging for a small or medium-scale farmer to get commercial satellite images as the cost is high and the minimum area that can be ordered is in the range of 25 $km^2$ (Anon, 2018). Importantly, drones can be flown at any time as per the requirement with minimal operational cost. Another advantage of drone data is that canopy images can be taken at various view angles to analyse the canopy's architectural structure. The limitations associated with satellite data over drone-based high-resolution images are summarised in Table 2.1. The type of drones which can be used for agricultural applications may depend on the size of the farm and type of cameras/sensors which need to be used. Battery capacity is also an important parameter which decides flight time of a drone. Table 2.2 shows the types of drones and their capability to carry various sensors.

Drones can be helpful in on-farm decision-making even before sowing starts. When the farm soil bed is being prepared for sowing, a UAV-mounted LiDAR sensor can be flown to check the farm's flatness. If it is found that the soil bed is not flat enough, then based on elevation difference, the farm can be uniformly flattened. A uniformly flat field is one of the critical requirements to stop unwanted water movement on the farm. After sowing, temporal monitoring of the farms can be done using a drone-mounted RGB camera. Images taken from these cameras can be used to monitor crop growth (biomass, LAI, height, etc.). The RGB images can detect weed location on the farm and can also identify pest-affected areas. In some crops like maize, where tasseling happens, these images can be used to count the number of tassels which helps in the early estimation of yield. During the crop vegetative stage, multispectral and hyperspectral cameras can also be used to estimate biophysical and biochemical properties (leaf nutrient, water content, etc.) of the crop. Once the location of water-stressed areas, weeds, pests, and nutrient distribution is identified, drones can be used to take corrective measures. They can spray pesticides, fertilisers, and water at the precise location on the farm. Figure 2.1 shows the UAV-based precision agriculture cycle.

Despite the multiple benefits of the drone platform, some aspects need more research. For example, the optical images get impacted if solar radiation varies due to change in cloud cover during the drone flight. This effect is more important when solar radiance is taken as the reference (e.g. multi or hyperspectral data). Accordingly, this kind of data acquisition may need a recording of real-time solar radiation during data collection. Moreover, data acquisition at a different time of the day may change radiance values for the same geographical location. In such cases, BRDF correction of data has to be undertaken (Schläpfer et al., 2020; Cristóbal et al., 2021), similar to its use in satellite data. The BRDF effect becomes critical for hyperspectral signatures, where sun angle, surface slope, and camera angle values are accounted for in deriving the collected hyperspectral signatures. One big disadvantage of a drone platform is the low

Table 2.1: Limitations of satellite data vs drone-based sensing (Raj et al., 2020).

| **Sub-meter resolution commercial satellite image** | **Drone-based high-resolution image** |
|---|---|
| Cloud cover and atmospheric dust particles create a bottleneck on image acquisition | Low flight height makes a limited effect of cloud cover |
| Real-time image acquisition and processing are not possible and usually takes some days delay | Images can be obtained and processed in a few hours, depending on the size of the farm |
| Images captured at some fixed time of day depending on the frequency of revolution of the satellite. | Images can be captured at the desired time of day |
| Maximum available Panchromatic geometrical resolution is 30 cm, while Multispectral resolution would be 1.2 m | Sub-cm spatial resolution can be achieved as per requirement |
| Minimum area map which can be ordered is 25 $km^2$ or more. If only natural color map required, then 10 $km^2$. | The map can be generated for a small and medium area which would be much cheaper than satellite imaging |
| Optical images are generally taken from zenith | Images at a different angle can be taken, which will help in getting architectural information of canopies |

flight time. Most commercial drones are not capable of having a flight time of more than 45 minutes. However, with evolving power technologies, few drones have shown multi-hour flight time capabilities (Cetinsoy, 2015). Gas-electric drones are a good example of high flight time drones, which allow the user to scan a large area in a single flight.

With the increase in IoT technologies and improvement in sensor properties, drones are destined for routine agricultural application in the future. This will certainly raise issues of air traffic, which needs to be addressed at a policy level. Many countries, including India, have introduced air traffic guidelines for the operation of UAVs. These guidelines need to be followed for a sustainable UAV

Table 2.2: Types of drones and their capability to carry a sensor (Raj et al., 2020).

| Type | Weight in kg (including payload) | Types of sensors which can be mounted on the drone | Area coverage capacity of the drone |
|---|---|---|---|
| Nano | Less than 0.25 | This has not been used in agriculture till now as sensors are usually of more weight and cannot be lifted by nano drones | NA |
| Micro | 0.25 < weight < 2 | Small RGB, lighter multispectral camera, and small LiDAR sensor can be mounted on this drone | Can cover up to 4-5 acre of ground area depending on the height of flight. Flight height is generally kept lower than 100 meters |
| Small | 2 < weight < 25 | High-resolution RGB camera, multispectral camera, LiDAR sensor, a lightweight hyperspectral imager, microwave sensor, and small thermal imager can be mounted on the drone | Can cover up to 10-20 acre of ground area depending on the height of flight |
| Medium | 25 < weight < 150 | Bigger high-resolution RGB camera, multispectral camera, LiDAR sensor, medium weight hyperspectral imager, microwave sensor, and the thermal camera can be mounted on the drone. It can also be used for spraying of pesticides | Can cover up to 100 acres of ground area depending on the height of flight. Flight height is generally higher than 50 meters |
| Large | Greater than 150 | Bigger and heavyweight cameras and sensors can be mounted on the drone. It can be used for spraying of pesticides | Can cover more than 100 acres of ground area. Flight height is generally higher than 100 meters |

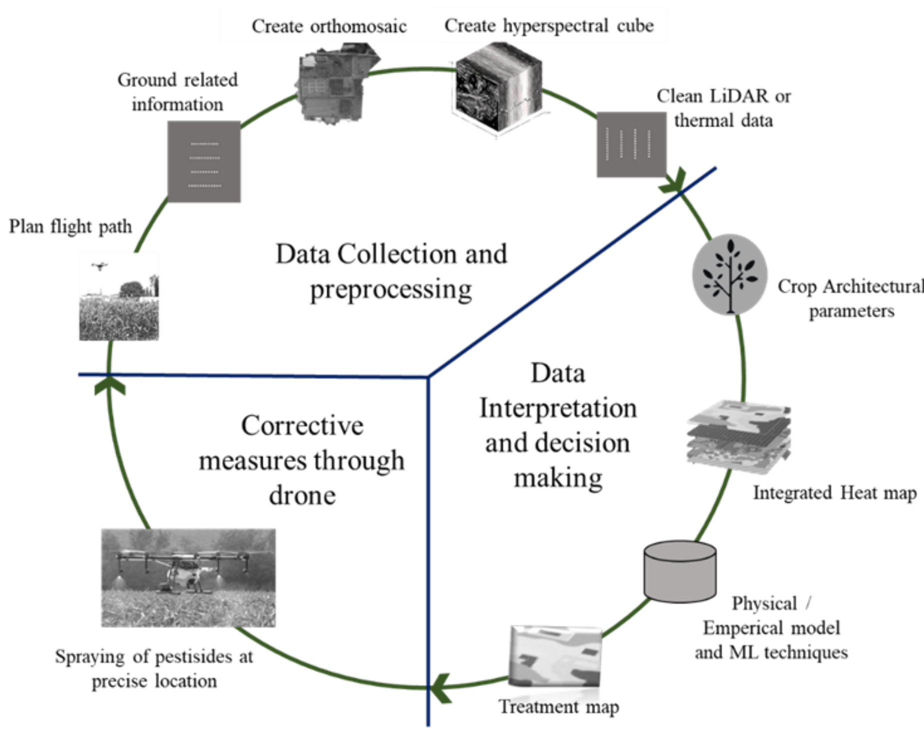


Figure 2.1: The UAV based precision agriculture cycle (Raj et al., 2020 ).

ecosystem, but governments must be willing to make ongoing amendments to these laws as the technology evolves. Another major concern with existing UAV operations is the lack of system safety and robustness. There are cases where anti-social elements hacked drones and used them for destructive purposes. Thus, research is also required to make UAV platforms robust and hack-proof.

For a country like India, where the majority of farmers have small land-holdings, the current cost of a drone-based system will make this technology unaffordable for most. However, if such technology can be implemented at the 'gram panchayat' (village council) level, the operational cost can be divided using a pooling method, and the cost per farmer minimised. Moreover, the Indian gram panchayat system is a powerful constitutional body, and considering projects like the "Svamitva scheme" where the Indian government is mapping all Indian villages using a drone-based imaging system, the opportunity of using drones in Indian farms for precision agriculture looks hopeful.

## 2.3 Drone-based sensing for precision agriculture

Applied agricultural research is generally related to productivity improvement, yield quality enhancement, cost-effective technologies, better crop genotypes, and weather-resistant crops. There is much literature available in this sector (Raj et al., 2020). However, more than 50 % (~3000) of the papers available on the use of drone in agriculture has been published after 2016, with almost 90 % of the papers published after 2013 (Web of Science, April 2021). This is due to the improved efficiency of UAVs and scanning imagers over the last five years, together with dissatisfaction with satellite images for making on-farm decisions in near-real-time (Matese et al., 2015). Moreover, current satellite data is not able to meet the spatial and temporal resolution requirements for making decisions at a small farm level. Different vegetation indices and soil properties can be calculated using various airborne sensors from remote sensing techniques. For example, leaf area index and NDVI are two popular indices used to indicate crop health/state, and thermal cameras can estimate crop water stress (Berni et al., 2009). Canopy reflectance can be used to identify the canopy's various biophysical and biochemical properties through either a physical or data-driven model, such as a machine learning model evolving quickly, which has shown better results in many cases (Tsouros et al., 2019). It is essential to collect reliable farm data representing the farm at sufficient spatial and temporal resolution to create and validate a trustworthy crop model. Since the spatial resolution of satellite sensors is coarse for a small farm, ground-based sensors cannot cover a big area on the field; thus, drone-based data collection provides an alternative approach to collect data at such temporal and spatial resolution.

UAVs can carry various sensors, which are useful for studying crop-related parameters. Literature shows that drones can be integrated with optical sensors like RGB, multispectral, hyperspectral, and thermal cameras, which help identify water and other types of stress in the crop (Calderón et al., 2013). LiDAR sensors are used on drones to estimate the canopy's height and structure, which ultimately helps in biomass estimation of the crop. Apart from digital data collection, drones have also been applied to aero-biological sampling above agricultural fields for early identification of pest attacks on the crop (Schmale et al., 2008). Drones can also be used to take corrective measures in farms, like spraying pesticides in stressed areas. Table 2.3 shows the different sensors which can be installed on a drone to study various characteristics of crops.

The drone-based data collection process is limited by the availability and weight of the sensors which can be put on the drone, e.g. little work has been done on drone-based microwave sensing as the sensors' weight is quite heavy, limiting its use for data collection. This section discusses various sensors used on the drone for precision agriculture applications. These sensors are useful for some precision agriculture applications, but RGB and line-scanner hyperspectral imagers were used in this research.

### 2.3.1 Optical sensors (400–2500 nm)

Imagers in the visible and IR spectrum are popularly used from a drone

Table 2.3: Drone-based sensors and their use (Raj et al., 2020).

| **Drone-based sensing of precision agriculture**<br>(Following cameras/sensors/Instruments can be installed on a drone, and data can be collected which can further used for estimation of various crop parameters) |
|---|
| 1. Optical sensors (400 – 2500 nm)<br>a. RGB camera (broadband centred at 450, 550, and 660 nm)<br>b. Multispectral camera / Red-edge camera (450, 550, 660, 725, and 850 nm)<br>c. Hyperspectral imager (narrow bands between 400 – 2500 nm)<br>i. Snapshot imager<br>ii. Line-scanner imager |
| 2. Thermal camera (3000 – 12000 nm) |
| 3. LiDAR sensor |
| 4. L-band passive microwave sensor |
| 5. Aero-Biological sampling |
| 6. Spraying of pesticides through drone |
| 7. Improving pollination process |

platform for vegetation mapping. These optical sensors can be used to estimate biomass, LAI, identification of various growth stages, and healthiness of a crop. Pest identification, farm survey, mapping, etc., are also done using these sensors (Tsouros et al., 2019). Below is the list of optical sensors available for drone-based sensing.

RGB camera: A digital RGB camera can be mounted on a UAV, and top-of-the-canopy or stereo images of the farm can be captured. These images are in 'visible bands' (400–700 nm), collecting reflectance in three broad ranges of wavebands: red, green, and blue. The spatial resolution of the image depends on camera specifications and the height from which the drone was flown. These cameras can collect very high spatial resolution images with good flight planning and give pixel resolution up to 1 mm. However, the spatial resolution is decided as per the objective of the work. Collecting extremely high spatial resolution data might not be a good idea as it will require more space to store and greater time to process. These images can be used to make an orthomosaic of the farm, studying the architectural properties of plants/trees (RAMI, 2018), detecting the weed location or pest-affected areas in the farm, and estimating the LAI of the crop. Height estimation of the crop is also possible from drone-based RGB images, which help in biomass estimation. These cameras are cheaper than multispectral or hyperspectral imagers, easy to operate, lighter in weight, and very popular for vegetation studies (Rueda-Ayala et al., 2019; Sritarapipat et al., 2014).

Multispectral camera/Red-edge camera: Multispectral cameras consist of 5–12 bands of around 10–50 nm bandwidth in blue, green, red, red-edge, and NIR regions of the electromagnetic spectrum (Deng et al., 2018). These cameras are generally used to calculate various normalized difference vegetation indices (Navia et al., 2016) and can identify highly stressed areas in the farm. These cameras are lightweight and can be mounted on micro UAVs. Multispectral cameras are the most used cameras in precision agriculture as it is easy to operate and give decent information about crop health.

Hyperspectral imager (400–2500 nm):

**Snapshot imager:** These can acquire complete images in several narrow bands from the visible to infrared electromagnetic spectrum region (Ishida et al., 2018). Bandwidth is generally around 10 nm (broader than line scanner imagers). Compared to line scanners, these images are easy to handle, and data is relatively easy to process as the imager generates a raster file. However, snapshot imagers cannot give ultra-high spectral resolution data and have a low frame rate, limiting the areal platform's data collection speed. One of the major issues of snapshot imagers is their unreliable band-to-band co-registration due to sensor movement.

**Line scanner imager:** These imagers are comparatively complex to operate. The camera frame rate decides the speed of the drone. The camera captures a narrow row on the ground at a given time (width determined by IFOV and length determined by FOV of the imager), and thus flight should be synchronized accordingly. The bandwidth of collected data can be as narrow as two nm, and the collected data is complex to process as it involves multiple spectral, spatial and geometric corrections (Jia et al., 2020).

### 2.3.2 Thermal camera (3000–12000 nm)

Thermal cameras are very useful in determining water stress in the crop. It has been seen that the crops with water stress are at a relatively higher temperature than the crops that do not have water stress. However, this temperature difference is time-dependent (morning, afternoon, or evening) and is affected by varying solar radiation. The temperature difference captured by the thermal camera can easily distinguish the water-stressed crop during the afternoon when the sky is clear and solar radiation is available (Bellvert et al., 2014). This detection is possible because, due to excessive water loss from stomata, leaves close their stomata opening, resulting in increased canopy temperature. Calibrating thermal images under unknown surface emissivity conditions is one of the challenging processes.

### 2.3.3 LiDAR sensor

The Light Detection and Ranging (LiDAR) sensor is instrumental in measuring canopy height (Xu et al., 2020). The sensor can collect data from up to 250 m height (depending on the manufacturer) and the accuracy of a few millimetres. This LIDAR point cloud data can be processed in dedicated software for further analysis (Christiansen et al., 2017).

### 2.3.4 L-band passive microwave sensor

L-band passive microwave data has the capability to measure surface soil moisture (top 5 cm). The penetration of the L-band signal into the vegetation canopy depends on the vegetation water content. Thus, L-band microwave data is also useful in estimating the crop's water content (Konings et al., 2017). The heavyweight of the microwave sensor limits its use on a UAV platform. However, some research is available where L-band microwave sensors have been installed on a UAV, and the collected data is used for soil moisture estimation over various soil types (Luo et al., 2019; Acevo-Herrera et al., 2010; and Wu et al., 2019).

### 2.3.5 Aerobiological sampling

At the research level, drones have also been used to collect air samples from above agricultural farms. An air-sampler is fitted on a drone to collect and store air samples and fly above agricultural farms. The air samples are then analyzed for the presence of potential agricultural threat agents (pathogens, insects, etc.). The analysis of these aerobiological samples helps in the early identification of pest attacks on the crop (Schmale et al., 2008).

### 2.3.6 Spraying of pesticides

This is a corrective measure that can be implemented through the drone. Drones carry tankers filled with pesticides, and the spraying can be done precisely in those areas that are found to be stressed after processing the collected image dataset (Spoorthi et al., 2017; Seo and Umeda, 2021).

### 2.3.7 Improving pollination

Some researchers have used drones for helping plants in the pollination process by distributing the pollen to a broader area to increase the probability of pollination. Abutalipov et al. (2016) have demonstrated that nano-copters can collect and deliver pollen in automatic control mode, while Yang and Miyako (2020) have used drones to spray soap bubbles for enhanced pollination.

## 2.4 Vegetation indices for agricultural data

Use of vegetation indices for estimating various crop biophysical and biochemical characteristics are one of the popular methods. However, there is always a sensitivity issue associated with indices. E.g. LAI or NDVI tends to saturate with the increased amount of biomass (Goswami et al., 2015). Indices have shown promising results with satellite data with reasonable classification accuracy (Wall et al., 2008). However, satellite images are mixed pixel and indices based on mixed pixel data may perform differently on pure pixel drone-based data (Petrou, 1999). Table 2.4 tabulates all the important vegetation indices compiled through a detailed literature review.

Table 2.4: Popular vegetation indices (Raj et al., 2020).

| | | |
|---|---|---|
| NDVI (Normalised Difference Vegetation Index) | $NDVI = \frac{NIR - R}{NIR + R}$ | Rouse et al., 1973 |
| WDRVI (Wide Dynamic Range Vegetation Index) | $WDRVI = \frac{a*NIR-R}{a*NIR+R}$ $(0 < a < 1)$ | Gitelson et al., 2004 |
| RDVI (Renormalized Difference Vegetation Index) | $RDVI = \frac{R800 - R670}{(R800 + R670)^{0.5}}$ | Roujean et al., 1995 |
| OSAVI (Optimised Soil Adjusted Vegetation Index) | $OSAVI = \frac{(1 + 0.16)(R800 - R670)}{(R800 + R670 + 0.16)}$ | Rondeaux et al., 1996 |
| EVI (Enhanced Vegetation Index used for LAI estimation) | $EVI = 2.5 * \left(\frac{NIR - R}{NIR + (6 * R) - (7.5 * B) + 1}\right)$ | Justice et al., 1998 |
| EVI2 (Modified EVI) (Less soil sensitive than NDVI) | $EVI2 = 2.5 * \frac{NIR - R}{(NIR + (2.4 * R) + 1)}$ | Jiang et al., 2008 |
| NGRDI (Normalized Green-Red Difference Index) | $\text{NGRDI} = \frac{(Green\ DN - Red\ DN)}{(Green\ DN + Red\ DN)}$ | Hunt et al., 2005 |
| Red Edge Reflectance Index | $\frac{R750}{R710}$ | Zarco-Tejada et al., 2001 |
| DCNI (Double Peak Canopy Nitrogen Index) | $DCNI = \frac{\frac{R720 - R700}{R700 - R670}}{(R720 - R760 + 0.16)}$ | Chen et al., 2010 |
| TCARI (Transformed Chlorophyll absorption in reflectance index) | $TCARI = 3\left[\frac{(R700 - R670) - 0.2(R700 - R550)}{\frac{R700}{R670}}\right]$ | Haboudane et al., 2002 |
| Combined TCARI / OSAVI | $\frac{TCARI}{OSAVI}$ | Haboudane et al., 2002 |
| Carotenoid Index | $\frac{R515}{R570}$ | Hernández-Clemente et al., 2012 |

Table 2.4: Popular vegetation indices (continued).

| | | |
|---|---|---|
| PRI (Photochemical Reflectance Index) | $PRI = \frac{R570 - R539}{R570 + R539}$ | Gago et al., 2015 |
| Normalized PRI | $PRI\ norm = \frac{R515 - R531}{R515 + R531}$ | Gago et al., 2015 |
| Normalized PRI | $PRI\ norm = \frac{PRI}{RDVI\left(\frac{R700}{R670}\right)}$ | Ihuoma et al., 2019 |
| BGI1 | $BGI1 = \frac{R400}{R550}$ | Zarco-Tejada et al., 2005 |
| BGI2 | $BGI2 = \frac{R450}{R550}$ | Zarco-Tejada et al., 2005 |
| MSI (Moisture Stress Index) | $MSI = \frac{R1600}{R820}$ | Hunt et al., 1989 |
| NDWI (Normalized Difference Water Index) | $NDWI = \frac{R860 - R1240}{R860 + R1240}$ | Gao, 1996 |
| NDII (Normalized Difference Infrared Index) | $NDII = \frac{R820 - R1600}{R820 + R1600}$ | Hardisky et al., 1983 |
| MDWI (Maximum Difference Water Index) | $MDWI = \left[\frac{Rmax - Rmin}{Rmax + Rmin}\right]$ $from\ 1500 - 1700$ | Eitel et al., 2006 |
| CWSI | $\text{CWSI} = \frac{(Tc - Ta) - (Tc - Ta)LL}{(Tc - Ta)UL - (Tc - Ta)LL}$ | Idso et al., 1981; Bellvert et al., 2014 |

## 2.5 Crop biophysical parameters

The biophysical parameters of a crop are crucial indicators for crop growth. These parameters can be seen physically during the growth of the plant/canopy. Fractional cover of green vegetation (fCover), Leaf Area Index (LAI), crop height, number of flowers/tassels, fraction of Absorbed Photosynthetically Active Radiation (fAPAS), and fractional cover of non-photosynthetic brown vegetation (fNPV) are some biophysical parameters of the crop. However, change in these biophysical parameters is induced by the biochemical properties of the crop. Determination of crop biophysical parameters are relatively simpler than the determination of crop biochemical parameters. Thus, biophysical parameters are easy and useful indicators that can be used for precision agriculture.

### 2.5.1 Leaf area index (LAI)

Leaf Area Index (LAI) is a biophysical property that may reflect the health of the crop (Bryson et al., 1997). It largely depends on the crop growth stage, crop height, architecture of the leaves and density of the plants (Vose et al., 1994), but can also be affected by short-term water stress due to leaf rolling (Chen and Black, 1992). Importantly, an increase in the LAI represents an increase in the leaf stomatal area and thus gaseous exchanges between the crop and the vegetation (Patanè, 2011). LAI can be used as an input to simulate the energy balance equations to understand the physical processes that occur between plants and the atmosphere. Also, inversion of crop models can utilise LAI to calculate 'light use efficiency' (Bonan, 1993; Drewry et al., 2010; Qu et al., 2016; Running and Coughlan, 1988). LAI is also used in crop yield prediction and water balance modelling, defined as the total one-sided area of photosynthetic tissue per unit ground surface area (Jonckheere et al., 2004).

The most accurate method to find the LAI of any area is termed the 'direct method', involving the destructive sampling of leaves, which is very time consuming and labour-intensive (Behera et al., 2010; Dufrêne and Bréda, 2010). Conversely, indirect methods are approximations and so use terms like foliage area index, effective plant area index (Garrigues et al., 2008), vegetation area index (Fassnacht et al., 1994), effective leaf area index (Chen and Black, 1991) etc. However, the term 'LAI' is often used even in the case of indirect measurements, even though indirect methods are affected by non-leafy parts of the canopy. Fortuitously, it has been shown that the LAI obtained from instruments such as the Licor-2000 or Licor-2200C canopy analyzer is correlated with LAI measurements from the direct method (Liu and Pattey 2010; Stroppiana et al. 2006). However, Bendig et al. (2015) show that it is difficult to estimate the true LAI from indirect techniques at the reproductive stage because canopy closure results in signal saturation.

As explained above, the direct method can be based on destructive sampling or allometry, point contact and litterfall collection (Chen et al., 1997). In destructive sampling, leaves are plucked from the plant, and the physical area of leaves are found. For upscaling the process, homogeneity in the structure is assumed. The allometry method requires some destructive sampling and also involves a large sampling error (Behera et al., 2010). In this process, the relationship between leaf area and the dimension of canopy components need to be found. These canopy components may be Diameter at Breast Height (DBH) or sapwood (for tree canopies). The point contact method is used for short vegetation with larger leaves, thus not used for a forest. It is calculated by counting the number of contacts a needle makes when penetrated through a canopy. In the litter-fall collection method, fallen leaves need to be collected, and thus frequent collection is required so that leaf decay can be avoided. This method is useful for the deciduous forest but not for a conifer or evergreen forest. The problem with all these direct methods is that they are time-consuming and labour intensive (Behera et al., 2010; Dufrêne and Bréda, 2010).

Indirect methods use different optical equipment/sensors to measure radiation transmittance to calculate leaf property and LAI. There are some commercially available instruments, e.g. Li-Cor LAI-2000/2200C Plant Canopy Analyser, CID Digital Plant Canopy Imager, Decagon Sunfleck Ceptometer, Demon, TRAC etc. LAI can also be measured from spherical photos. The hemisphere photography system includes WinSCANOPY from Regen, Can-Eye, Hemiview. Apart from these, remote sensing (aircraft/satellite) images have been used to estimate LAI, e.g. MODIS LAI – Sea (uses spectral method) and LiDAR. There are two canopy attributes that affect radiation penetration and indirect LAI measurement. These attributes are leaf angle distribution and spatial leaf distribution. Leaf angular distribution affects radiation transmission through the canopy at different angles, and spatial leaf distribution is more critical because it affects the amount of radiation transmitting through the canopy. Further, spatial leaf distribution can be of three types - Random, Clumped, and Regular distribution. Random distribution is generally used to represent crop architectural property for grain crops, where 37 % of overlapping should be considered for each layer of leaves, and the value of the clumping index should be taken as 'one'. Clumped distribution is used in the case of natural canopies; more than 37 % of overlapping is taken for each layer of leaves, and the clumping index is considered less than one. Regular distribution is used for a few crops; the Clumping index is considered greater than one, and less than 37 % overlapping is considered for each layer of leaves (Jonckheere et al., 2004; Sea et al., 2011).

The modified Beer's law

$$P(\theta) = e^{-\frac{G(\theta)\Omega L}{cos(\theta)}}, \qquad (2.1)$$

can be used to calculate LAI. Here $P$ is the gap fraction, and it is defined as the "fraction of sky seen from underneath the canopy". It is a function of the view zenith angle. $\theta$ is the zenith angle, $\Omega$ is the clumping index and for random canopy taken as 1. $G(\theta)$ is the projection coefficient, and $L$ is the effective Leaf area index (LAI). It should be noted that the gap fraction is not gap size. There can be different gap size distributions for the same gap fraction (Sea et al., 2011).

The use of vegetation indices is one of the popular methods for estimating LAI. However, there is always a sensitivity issue associated with indices. E.g. the normalized difference vegetation index (NDVI) tends to saturate with increasing LAI (Gamon et al., 1995). When the LAI value is increased from approximately 3 to 4 (depending on the canopy), then NDVI loses its sensitivity towards change in LAI and starts saturating. This is because chlorophyll is a highly efficient absorber of red radiation. Thus, after some point, adding more chlorophyll to the canopy or increasing leafy material in the canopy will not change red reflectance much. Several solutions have been developed to overcome this situation. One of the simplest solutions is to use the wide dynamic range vegetation index (WDRVI). In this index, a weighting factor ranging from 0 to 1 is used with NIR reflectance (in the numerator as well as in denominator) in the formula of NDVI (Gitelson 2004),

$$NDVI = \frac{NIR-R}{NIR+R} \quad \& \quad WDRVI = \frac{a*NIR-R}{a*NIR+R} . \tag{2.2}$$

When the weighting factor approaches 0, the linearity of the WDRVI – LAI graph tends to increase, but for sparse canopies, the change in LAI shows less sensitivity towards change in index values. Another index that shows better sensitivity with LAI uses blue bands. This is called the Enhanced vegetation index (EVI) (Jiang et al., 2008)

$$EVI = 2.5 * \left(\frac{NIR - R}{NIR + (6*R) - (7.5*B) + 1}\right). \tag{2.3}$$

Later, EVI was modified and the blue band removed. The modified version of EVI is known as EVI2 (Jiang et al., 2008)

$$EVI2 = 2.5 * \frac{NIR - R}{(NIR + (2.4* R) + 1)} . \tag{2.4}$$

Apart from having a linear relationship with LAI, EVI2 has less soil sensitivity compared to NDVI.

LAI can be combined with other vegetation indices to achieve maximal sensitivity. For maize-soybean rotation crop, calculated green LAI (gLAI) for maize and soybean ranged from 0 - 6.5 and 0 - 5.5, respectively. For gLAI lower than 2, NDVI is most sensitive, while for gLAI greater than 2, Simple Ratio

$$Simple\ Ratio = \frac{NIR}{R}, \tag{2.5}$$

and Chlorophyll indices

$$Chlorophyll\ Index = \frac{NIR}{G-1} , \tag{2.6}$$

are more sensitive. However, this relationship is crop-specific and may change with other crops.

Nguy-Robertson et al. (2012) found that the best index combination for LAI estimation for maize and soybean has been found to be the combination of NDVI and SR. With this combination, the coefficient of variance for maize and soybean was less than 20 % and 23 %, respectively.

### 2.5.2 Canopy height

Canopy height is a critical crop biophysical parameter. Information about canopy height helps in estimating crop biomass and yield. The most accurate way to estimate canopy height is through manual measurements of plant heights from various parts of the farm. However, manual measurements are extremely time-consuming and labour intensive. Thus, it is crucial to estimate the canopy height through remote sensing methods.

One of the efficient ways to estimate the canopy height is by using Lidar data (St-Onge et al., 2003; Mielcarek et al., 2018). Lidar stands for 'Light Detection and Ranging'. It is an active sensing technique where the sensor sends a light signal and records the time in which the reflected light comes back to the sensor's detector. Lidar sensor data are capable of giving highly accurate height estimation as compared to other available remote sensing techniques (Yuan et al., 2018). Drone-based RGB or multispectral images can also be used to estimate the canopy height based on photogrammetric techniques. Various techniques like 'shape from x', 'region growth algorithm', 'surface from motion' etc., are being used for height or distance (from sensor) estimation using RGB and lidar images (Kim et al., 2021; Jin et al., 2018; Chaudhary et al. 2012). Once the digital elevation model or digital surface model is created, then various logical operations can be carried out to find the canopy height. One such logical process is

$$Canopy\ height\ =\ Digital\ surface\ model - Digital\ elevation\ model. \tag{2.7}$$

## 2.6 Crop biochemical parameters

Biochemical contents present in the crop are a basic reason for the change in crop behaviour. The crop biochemical contents are driven by inputs provided in the farm, crop verities, and weather parameters. Leaf water content, leaf nitrogen content, leaf chlorophyll content or any nutrient present in the crop constitutes a biochemical property. Moreover, water and nitrogen act as the two main contributors to optimise crop yield for grain crops.

### 2.6.1 Leaf water content

Water is one of the most important input parameters for any grain crop production, as irrigation management has a major control on plant growth (Gonzalez et al., 2010). Accordingly, crop water stress increases the difference between attainable and actual yield, minimising the 'yield gap' through optimized irrigation (Mueller et al., 2012). Water also helps nutrients from the soil to travel to various parts of the plant, and so even with adequate nutrients supplied to the soil, the crop may show nutrition deficiency if the crop is suffering from water stress (Wang and Xing, 2016). Thus, information about the spatio-temporal distribution of crop water content for optimal farm management plays a crucial role. One way to identify potentially water-stressed areas in the farm is through soil moisture mapping. However, remote sensing techniques are currently incapable of directly measuring soil moisture across grain crops' effective root zone (~30-50 cm). Interestingly, microwave sensors can estimate soil moisture in the top 5 cm of soil depth (Shen et al., 2020; Walker et al., 2004; Etminan et al., 2020; Finn et al., 2011; Xu et al., 2016).

There are two different perspectives to plant water stress – instantaneous water stress and long-term water stress (Aroca, 2012). The effect of instantaneous water stress can lower the LWC and affect the gaseous exchanges between plants and their atmosphere. However, long-term water stress significantly affects crop biophysical parameters like Leaf Area Index, canopy height, and yield (Ma et al., 2018; Reddy et al., 2003; Blum, 2011; Pinheiro et al., 2011). If instantaneous water stress in the crop is not adequately managed, it creates the basis for long-term water stress, leading to a significant crop yield reduction (Hsiao et al., 1976). Conversely, the instantaneous water stress gives an early indication of potential yield loss (Ma et al., 2018), which can be avoided with correct ongoing irrigation management. The LWC during the early crop growth stage needs to be maintained above a critical value. For example, if the LWC of maize leaves goes below 82.5%

(g/g) during the seedling/jointing stage, the photosynthetic rate may reduce by as much as a factor of 3.2 (Ma et al., 2018). Moreover, the reduction in LWC below a critical level increases the loss in turgor pressure, further minimising the cell division and enhancement, resulting in inhibited leaf expansion and stomatal closure, which delays the gaseous exchanges between the plant and the atmosphere (Hsiao, 1973; Schulze and Hall, 1982; Blum, 2011; Pinheiro et al., 2011). Thus, early detection of patches of water-stressed plants by estimating LWC can provide opportunities to ameliorate the stress through suitable agronomic management for improved crop yield.

Various sensors have been used for remote estimation of leaf (or vegetation) water content, including microwave (Huang et al., 2015; Merlin et al., 2010; Yilmaz et al., 2008; Hunt et al., 2011), thermal (Merlin et al., 2010; Yilmaz et al., 2008), and optical (Gao et al., 2015; Ceccato et al., 2001; Neinavaz et al., 2017; Clevers et al., 2010). However, microwave data is low spatial resolution (Migliaccio and Gambardella, 2005), thermal gets affected by the soil temperature, especially when the canopy coverage is low (Kim et al., 2016; Han et al., 2016), and short-wave infrared are affected by the atmosphere (Wang, 2007). The water absorption wavelengths above 1000 nm range in hyperspectral data (1940 nm, 1450 nm, and 1190 nm) have been the primary wavelengths for vegetation water sensing (Thenkabail and Lyon, 2016). The SWIR zone of EM spectra has stronger absorption than water absorption wavelengths of NIR zone EM spectra (400-1000 nm) (Thenkabail and Lyon, 2016; Carter, 1991). Sensors operating in this range are much more expensive and difficult to maintain, mainly due to the required cooling mechanism to increase the sensitivity of the InGaAs sensors to the low amounts of earth-leaving radiation at those wavelengths. Importantly a secondary water absorption band exists between 400-1000 nm at around 970 nm (Thenkabail and Lyon, 2016). Moreover, other narrowband wavelengths within the 400-1000 nm range also show sensitivity towards water molecules (Büning-Pfaue, 2003).

For the estimation of crop water content, accurate retrieval of leaf water is very important. Various techniques are available to retrieve leaf water content – spectral indices method, inversion of radiative transfer models, and methods based on machine learning techniques like wavelet analysis and genetic algorithm (Fang et al., 2017). Before exploring these techniques, the science of EM absorption by water molecules is first discussed.

The absorption of electromagnetic radiation by water molecules is determined by rotational transitions, intermolecular and intramolecular vibrational transitions, and electronic transitions of $H_2O$ molecules. Rotational transition and intermolecular vibrational transitions are responsible for absorption in the microwave and far-infrared EM spectrum region (Mohorič et al., 2020). The electronic transitions create absorption in the ultraviolet region (Underwood et al., 2005). Absorption in the visible (VIS), near-infrared (NIR), and mid-infrared (MIR) range is due to intramolecular vibrational transitions (Hunter et al., 2018). In the VIS and NIR regions, water absorption is majorly due to a stretching overtone frequency and combination of vibrational absorption of the O-H bands of $H_2O$ molecules (Chaplin, 2008).

Water molecules vibrate in the symmetric stretch, asymmetric stretch, bend stretch and three libration modes shown in Figure 2.2 (Chaplin, 2008). Even though the VIS and NIR regions show very low water absorption characteristics compared to after 1000 nm, the water's overtone bands have been found to create spectral niches for photosynthetic organisms (Stomp et al., 2007). Water absorption can be seen at 401 and 449 nm due to the fifth and sixth overtone of vibrational symmetric and asymmetric stretches of O-H bands (Pope et al., 1997; Stomp et al., 2007). It has also been found that the fifth overtone of the intramolecular stretches produces a very small absorption at 514 nm (Yakovenko et al., 2002; Sogandares and Fry 1997; Braun and Smirnov, 1993; Stomp et al., 2007). At 605 nm, a fourth overtone band of symmetric and asymmetric stretches have been documented (Yakovenko et al., 2002; Sogandares and Fry 1997; Braun and Smirnov, 1993; Stomp et al., 2007). At 660 nm, absorption occurs due to combined vibrational symmetric, asymmetric, and bending stretches of O-H overtone bonds (Tsubomura et al., 1980; Braun and Smirnov, 1993). At 698 nm,

the fourth overtone of the O-H bands' vibrational symmetric and asymmetric stretches has created water absorption in the EM spectrum (Braun and Smirnov, 1993). Spectroscopy has also shown a small absorption peak at 750 nm due to the third overtone of vibrational symmetric and asymmetric stretches of O-H bands (Tsubomura et al., 1980; Braun and Smirnov, 1993). A water absorption shoulder has been observed at around 836-850 nm due to the combined overtone of vibrational symmetric, asymmetric, and
bending stretches of O-H bands (Tsubomura et al., 1980; Braun and Smirnov, 1993). At 970 nm, a water absorption band is found due to the second overtone of vibrational symmetric and asymmetric stretches of O-H bands (Tsubomura et al., 1980; Büning-Pfaue, 2003; Stomp et al., 2007). Table 2.5 shows the list of water absorption bands found in the literature.

The use of spectral indices for estimating leaf-water content is the simplest

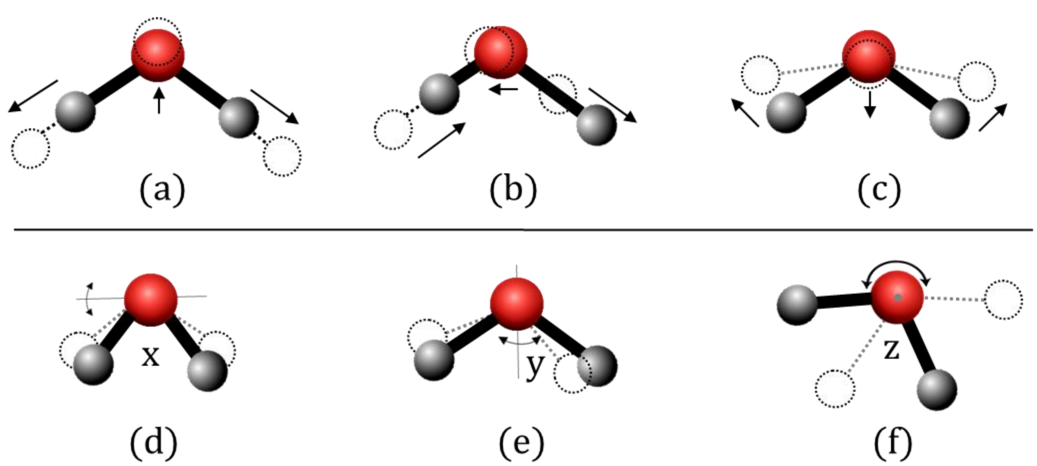


Figure 2.2: (a), (b), and (c) shows the symmetric, asymmetric, and bending stretch in water molecules. The red colour atom represents the Oxygen atom, and the grey colour atoms represent hydrogen atoms. The arrows show the direction of motion of the atoms. (d), (e), and (f) show the three libration modes of water molecules with respect to x, y, and z axes (adapted from Chaplin, 2008).

method. However, spectral indices are often species-dependent, and tend to saturate after some level of leaf-water content. This saturation may be because individual spectral indices consider only a few numbers of wavebands, and information in other wavebands are discarded, which can be used as proxy indicators. There are a few indices based on hyperspectral data which can give pre-visual indicators of water stress in the crop (Zarco et al., 2012). For example, the Photochemical Reflectance Index (PRI) is related to the epoxidation state of the xanthophyll cycle pigments and hence photosynthetic efficiency. An increase in the xanthophyll cycle means the presence of water stress, so PRI can serve as a proxy for water stress detection (Peguero et al., 2008). Steady-state chlorophyll fluorescence is sensitive to the stomatal conductance of the leaves. Further, stomatal conductance is inversely proportional to water stress (Moya et al., 2004), and thus these relations can be used to estimate water stress on the farm. Inversion of radiative transfer models such as PROSAIL can also be used to estimate leaf water thickness. Input to the inversion model is reflectance signatures between 400-2500 nm. However, any part of this wavelength range can be used to estimate EWT, but will lead to a decrease in the model's accuracy.

Various advanced machine learning techniques can also be used to extract spectral features of the leaf related to water. e.g. continuous wavelet analysis (CWA). Further, techniques like partial least squares (PLS) coupled genetic algorithm (GA) can be used to link retrieved spectral features with LWC. These techniques are very efficient, but at the same time, very complex and computationally intensive with large datasets.

Table 2.5: Water absorption bands in the visible, and NIR region of EM spectrum.

| EM region | Absorption Wavelength | Reason for absorption | Reference |
|---|---|---|---|
| VIS | 401 nm | Fifth and sixth overtone of vibrational symmetric, and asymmetric stretches of O-H bands | Pope et al., 1997 |
| | 449 nm | | Stomp et al., 2007; Pope et al., 1997 |
| | 514/520 nm | Fifth overtone of vibrational symmetric, and asymmetric stretches of O-H bands | Yakovenko et al., 2002; Sogandares and Fry 1997; Braun and Smirnov, 1993; Stomp et al., 2007 |
| | 605 nm | Fourth overtone of vibrational symmetric, and asymmetric stretches of O-H bands | |
| | 660 nm | Combined overtone of vibrational symmetric, asymmetric, and bending stretches of O-H bands | Tsubomura et al., 1980; Braun and Smirnov, 1993 |
| | 698 nm | Fourth overtone of vibrational symmetric, and asymmetric stretches of O-H bands | Braun and Smirnov, 1993 |
| IR | 750/760 nm | Small absorption peak due to third overtone of vibrational symmetric, and asymmetric stretches of O-H bands | Tsubomura et al., 1980; Braun and Smirnov, 1993 |
| | 836/850 nm | Small absorption shoulder due to Combined overtone of vibrational symmetric, asymmetric, and bending stretches of O-H bands | |
| | 970/975 nm | Second overtone of vibrational symmetric, and asymmetric stretches of O-H bands | Tsubomura et al., Pfaue, 2003; Stomp et al., 2007 |

### 2.6.2 Leaf nitrogen content

Plants can uptake soil nitrogen as nitrate and ammonia and utilise it for plant growth (Ohyama, 2010). Thus for agriculture purposes, fertiliser in the form of ammonia (NH3) or ammonium nitrate (NH4NO3) is supplied to the farm to provide sufficient nitrogen to the soil (Mason, 1977; Craig and Wollum, 1982; Gezgin and Bayrakll, 1995; van Grinsven et al., 2015). Moreover, nitrogen is a mobile macronutrient in plants that changes its content temporally (Kutman et al., 2011; Masclaux et al., 2010), tending to move from old leaves to new/fresh leaves in order to increase their biomass (Masclaux et al., 2010). Nitrogen is also a critical nutrient for biomass creation in grain-producing plants, with plant nitrogen concentration decreasing as dry biomass of the canopy increases (Chen et al., 2010). Interestingly, this trend is similar to the change in leaf water content over progressive crop growth stages (as seen in this study).

Approximately 30-50% of the nitrogen in green leaves is in the form of D-ribulose 1-5-diphosphate carboxylase (RuBisCO) (Kokaly, 2001), being the key photosynthetic enzyme/protein in green leaves (Gutteridge and Gatenby, 1995; Andersson and Backlund, 2008). Other functional involvement of nitrogen in plants is in the form of different proteins (Schrader, 1984; Howitt and Udvardi, 2000). Maintaining the nitrogen level in plants above a critical value is very important because nitrogen is used to form biomass with the progress in growth stages (Leghari et al., 2016). This critical value represents the minimum nitrogen concentration to be maintained in the plant so as to maximize crop growth (Blumenthal et al., 2008). However, using a high amount of nitrogen in the farm is not only expensive but leads to water pollution, as the irrigated water is wasted through runoff and leaching (Knox et al., 2012; Elrashidi et al., 2005), meaning that optimal use of fertilisers should be applied on the farm.

Interestingly, water is also a major contributor to the protein's three-dimensional structure (Franks, 1988), and protein controls the structure of its surrounding water, known as the hydration of protein (Franks, 1988). This protein hydration is critical, as its biological activity reduces in the absence of hydrating water (Chaplin, 2006). Consequently, the association of water and protein makes it difficult to estimate the precise amount of nitrogen in a crop and more so remotely.

The remote estimation of canopy/leaf nitrogen content essentially depends on the vibrational properties of the amide bonds of the plant proteins (Kokaly, 2001; Damodaran, 2008). Nitrogen shows higher light absorption characteristics in ultraviolet bands (Ogawa et al., 1964) and short-wave infrared bands (Widlowski et al., 2015). The various stretching, bending, and torsion in the different amide bonds present in proteins have shown absorption characteristics at wavelengths longer than 3000 nm (Haris and Chapman, 1994). Table 2.6 shows the light absorption wavelengths for amide bonds in proteins (Haris and Chapman, 1994). Moreover, researchers have also found a few wavelengths in the 400-2500 nm region (515, 520, 525, 550, 575, 743, 1116, 2173, and 2359 nm) of the electromagnetic spectrum correlated to nitrogen content (Thenkabail et al., 2016). However, apart from 2173 and 2359 nm wavelengths (Kokaly, 2001), none of the other bands has known causation (small absorption features) for this correlation.

There is no known nitrogen/protein absorption wavelength available between the 400-1000 nm region of the electromagnetic spectrum, which has a light absorption sensitivity to the nitrogen content in the leaves. Thus, the only logical way that the 400-1000 nm reflectance data can be used for nitrogen estimation is through empirical proxy relationships with parameters such as greenness (Hansen and Schjoerring, 2003) and chlorophyll of the crop (Curran et al., 1992; Haboudane et al., 2002), or some empirical relations between vegetation indices and vegetation nitrogen content (Reyniers et al., 2006; Hansen and Schjoerring, 2003; Chen et al. 2010).

Some studies have shown a correlation between red-edge-based indices and the nitrogen content of the crop. The double peak canopy nitrogen index (DCNI) is an example of a red-edge-based index where 720, 700, and 670 nm wavelengths were used (Chen et al. 2010). The DCNI formula, along with other indices, is shown in Table 2.7. Similarly, Yao et al. (2010) used a spectroradiometer with 400-2500 nm range to collect canopy level reflectance from a wheat crop. Yao et al. (2010) studied various indices, and the involvement of 720, 725, and 736 nm wavelengths showed the usefulness of the red-edge region for nitrogen estimation. In another study, Feng et al. (2008) also used red-edge region wavelengths to estimate wheat crop leaf nitrogen. Feng et al. (2008) recommended spectroradiometer-based reflectance signatures to create a red-edge position index (Cho and Skidmore, 2006) and mND705 (normalised difference index at 705 nm) (Sims and Gamon, 2002) indices for leaf nitrogen content estimation.

Table 2.6: Infrared wavelength absorption of amide bonds in protein (adapted from Harris and Chapman, 1994).

| Wavelength (nm) | Chemical bond origin |
|---|---|
| 3030 | N-H stretching |
| 3225 | N-H stretching |
| 5917-6250 | C=O stretching, C-N stretching, N-H bending |
| 6349-6757 | C-N stretching, N-H bending |
| 7686-8137 | C-N stretching, C=O stretching, N-H bending, O=C-N bending |
| 13030-16000 | O=C-N bending |
| 12500-15630 | N-H bending |
| 16500-18620 | C=O bending |
| 50000 | C-N torsion |

Table 2.7: Indices found to be used for leaf nitrogen content estimation in literature.

| Index Formula | short form | Full form | Reference |
|---|---|---|---|
| $\frac{(1+0.45)(R_{800}^2+1)}{R_{670}+0.45}$ | $Vi_{opt}$ | Optimal vegetation index | Reyniers et al., 2006 |
| $\frac{R_{573}-R_{440}}{R_{573}+R_{440}}$ | $NDVI_{g-b}$ | Green-blue normalised difference vegetation index | Hansen and Schjoerring , 2003 |
| $\frac{\frac{R_{720}-R_{700}}{R_{700}-R_{670}}}{R_{720}-R_{670}+0.03}$ | $DCNI$ | Double peak canopy nitrogen index | Chen et al. 2010 |
| $\frac{R_{450}}{R_{550}}$ | $BGI2$ | Blue Green Index 2 | Zarco-Tejada et al., 2005 |
| $\frac{MCARI}{MTVI2}$ | Combined Index | $MCARI = [(R_{700}-R_{670}-0.2)(R_{700}-R_{550})]\left(\frac{R_{700}}{R_{670}}\right)$<br>$\mathrm{MTVI2} = 1.5 * \frac{(1.2*(R_{800}-R_{550})-2.5*(R_{670}-R_{550}))}{\sqrt{(2*R_{880}+1)^2-\left(6*R_{800}-5*R_{670}^{\frac{1}{2}}\right)-0.5}}$ | Eitel et al., 2007<br>Daughtry et al., 2000<br>Haboudane et al., 2004 |
| $3*\left[(R_{700}-R_{670}-0.2)*(R_{700}-R_{550})\right]\left(\frac{R_{700}}{R_{670}}\right)$ | TCARI | Transformed chlorophyll absorption in reflectance index | Haboudane et al., 2002 |

Stroppiana et al. (2009) experimented with data from a paddy field. They observed blue-green reflectance region based index, called the optimal normalized difference index (NDIopt), to be more sensitive than the traditional normalized difference vegetation index (NDVI) to changes in the plant nitrogen concentration while also being less affected by crop biophysical properties. Du et al. (2016) estimated nitrogen content in rice leaves using 32-band active hyperspectral sensing. The central wavelength of these bands was between 500 to 910 nm, with four wavelengths in the red-edge region. The authors used a total of 32 bands for making a machine learning model, with a maximum $R^2$ of 0.75 obtained. In another study, Fan et al. (2019) used canopy level spectroradiometer-based spectral signatures from a maize crop to estimate leaf nitrogen content. Partial least square regression analysis was carried out on the collected data resulting in $R^2$ of 0.77. Similarly, Tan et al. (2018) collected temporal spectroradiometer-based hyperspectral reflectance spectra from an experimental wheat crop canopy. The study was focused on a statistical analysis of available methods of leaf nitrogen estimation, with an index named NREAI found to give the highest $R^2$ of 0.97, with chlorophyll used as a proxy indicator for estimating leaf nitrogen. Tial et al. (2014) also used spectroradiometer-based canopy (including background) reflectance spectra of a rice crop and found the simple ratio of 553 and 537 nm bands more reliable for leaf nitrogen content estimation under various cultivation conditions.

In a drone-based study, Liu et al. (2017) used spectral signatures (450-950 nm) of a wheat crop at different growth stages. Field-based spectroradiometer readings were also collected simultaneously. A few bands, including from the red-edge region, were selected using correlation analysis. The Back Propagation (BP) neural network and multifactor statistical regression method were implemented on the selected bands for the leaf nitrogen content model training and evaluation. The model gave an $R^2$ between 0.85 – 0.96 for different growth stages of the crop. Similarly, Liang et al. (2018) used ground-based spectroradiometer and aircraft-based hyperspectral data from an experimental winter wheat farm. However, this was mixed-pixel data as the spatial resolution of the aircraft data was 3m. First-derivative indices at 520 nm and 715 nm were found to produce an $R^2$ of 0.75. The authors recommended to use less than 30 nm bandwidth for leaf nitrogen content estimation. Tian et al. (2011) created two-band and three-band hyperspectral indices for estimating paddy canopy-level leaf nitrogen concentration. The data was collected from the ground, airborne (AVIRIS), and spaceborne (Hyperion satellite) platforms. The newly identified two-band index - R533/R565, and three-band index R705/(R717 + R491) resulted in an $R^2$ less than 0.76. The use of the green-colour wavelength region shows that the higher correlation was due to the difference in green colour among different nitrogen treatment plots.

In very few studies, leaf water and nitrogen contents were studied together using hyperspectral data. Strachan et al. (2002) used canopy-level 350-1000 nm hyperspectral data to demonstrate the maize development under nitrogen and water stress conditions. Canonical discriminate analysis was used to classify different nitrogen rate canopies. The authors suggested to carry out more research to understand the dynamics of nitrogen estimation under various water stress conditions. In another study, Feng et al. (2016) developed a water resistance nitrogen index (WRNI) and tested it on a winter wheat crop. Canopy level reflectance spectra were collected (~400-1000 nm), and plants were destructively sampled for estimating leaf water content and leaf nitrogen content. WRNI was calculated using the ratio of normalised difference red-edge (Fitzgerald et al., 2006) and a floating-position water band index (Strachan et al., 2002). The WRNI gave $R^2$ between 0.79-0.85. Corti et al. (2017) conducted a pot experiment under different water and nitrogen treatments. Spectroradiometer-based 400-1000 nm spectral signatures were collected and used to estimate crop biophysical and biochemical properties, including leaf water and nitrogen content. All of the crop parameters were estimated using various indices. However, no analysis was presented to understand the effect of water and nitrogen variables on their estimation.

## 2.7 Radiative transfer model

The basis of any canopy model (geometric, turbid, hybrid, computer simulation) is either 1. Geometric optics theory, 2. Radiative transfer theory, or 3. Average transmittance theory. The popular PROSAIL model is based on radiative transfer theory. Geometric optics theory uses optical principles and parallel-ray geometry to model a defined shape (cone, sphere, cylinder, ellipsoid, etc.) canopy (Li and Alan, 1985). The link between the movement of incident radiation and optical properties of vegetation elements and their distribution within the canopy is given by transmittance theory. However, radiative transfer theory works on the solution of the integro-differential equation for a specific radiance. The solution of this equation leads to canopy reflectance (Goel et al., 1988). The inversion of these models results in the estimation of crop biophysical and biochemical properties.

The radiative transfer equation is based on the fact that when the beam of radiation travels, it loses energy to absorption, gains energy by emission, and redistributes energy by scattering. The radiative transfer (RT) approach is one of the popular methods to derive the vegetation reflectance spectra. The engine of the radiative transfer theory is integrodifferential equations. The RT equation for unpolarised light is

$$\frac{\partial\, I(\tau;\, \hat{s})}{\partial\, \tau} = -I(\tau;\, \hat{s}) + \left(\frac{1}{4\pi}\right) \int p(\,\hat{s}, \hat{s}')I(\tau;\, \hat{s})dw' + \varepsilon(\hat{r}, \hat{s})/\sigma p \quad , \qquad (2.8)$$

Where parameters of the equation are as follows:

| | |
|---|---|
| $I$ | Specific intensity (Radiance or Brightness). average power flux density within a unit frequency band centred at a given frequency, within a unit solid angle (unit: watt/meter/Steradian/Hz at position vector **r** in the direction ŝ in a 3D space). |
| $\sigma$ | Sum of scattering and absorption cross-sections of medium particle. This means the power absorbed/scattered by the particle is $\sigma I$. |
| $dw'$ | The element of a solid angle. Integration over $w'$ is taken to include the contributions from all directions $\hat{s}'$. |
| $\tau$ | Optical distance defined by $\int \sigma\rho\, ds$ where $\rho$ is the number of particles per unit volume with which the incident radiation interact. |
| $p(\hat{s}, \hat{s}')$ | Phase function represents the probability that the radiance in the direction $\hat{s}'$ will be scattered into a solid angle about direction ŝ. |
| $\varepsilon(\hat{r}, \hat{s})$ | emission from within the canopy in the VIS and NIR regions is negligible and hence $\varepsilon(\hat{r}, \hat{s}) = 0$. |

The use of specific intensity in this equation is quite useful because it is intrinsic to the source and conserved along the ray path. Thus the same value should be measured every time. The solution of these equations involve:

i. Finding the phase functions (specification) of the scattering properties of various canopy elements (not related to the phase of a wave). Its origin is from astronomy - 'lunar phases'. Here, the absorption coefficient of the canopy is required, which is higher than that for atmospheric particles. In PAR, the absorption coefficient is 0.85, while in NIR, it is 0.5-0.15 (Goel et al., 1988).

ii. The solution of the radiative transfer equation for a given boundary condition is an iterative process of updating specific intensity (*I*). The steps are as follows:

   a. Put initial guess of $I$ in the RHS of *equation (2.8)* and integrate with boundary conditions to get a new *I*. However, deciding the boundary condition is challenging, as the top of the canopy is exposed to both direct (specular) radiation and diffuse flux of scattered radiation.

   b. Use new *I* again, in RHS of *equation (2.8)* and calculate new *I*.

   c. Continue this process until the value of *I* doesn't fall within the desired level of accuracy.

The reflectance spectra are affected by various parameters like solar radiation, canopy architecture, soil characteristics etc. Solar radiation reaching the canopy can be divided into two parts: direct radiation (without scattering) and diffused radiation (with scattering). Direct flux direction is decided by solar zenith angle, while diffuse flux radiation is characterized by angular distribution. When the atmosphere is cloudy, then the reflectance contains less information (Goel et al., 1988). Many canopy-reflectance (CR) models assume that diffused radiation is isotropic and that SKYL (fraction of incident radiation that is diffused) is a given parameter (less than 15% in NIR). However, SKYL depends on atmospheric conditions (dust and water vapours). It is also wavelength-dependent in a way that it is more sensitive for visible wavelengths and less sensitive in the NIR region of the electromagnetic spectrum. Reflectance can be roughly approximated as a function of the angle of incidence such that $R = a\alpha^2 + b\alpha + c$, where $R$ is reflectance, α is the angle of incidence, and $a, b, c$ are wavelength-dependent constants (Goel et al., 1988).

The movement of incident solar flux inside the canopy (towards the soil and then towards the sensor) depends on various factors like scattering and absorbing properties of the vegetation elements, the canopy's density, and the canopy's orientation. These factors result in various flux types received by the sensor. Flux received by the sensor can be three types – i) One-time scattered flux (scattered by vegetation); ii) Multiple time scattered fluxes by various vegetation elements (not by ground), and iii) Soil reflected flux (with or without interacting with the vegetation).

The vegetation density can be characterized by LAI, while LAD is characterized by distribution density function $f(\Phi_L + \Psi_L)$. Where $\Phi_L$ is leaf inclination and $\Psi_L$ is leaf azimuthal angle. Based on these, canopies can be described by six types of vegetation: planophile, erectophile, extremophile (forest canopies), uniform, and spherical. Maize can be categorized as planophile and erectophile canopy.

BRDF is closely related to LAD. Planophile canopy has the least variability in reflectance as a function of the solar and view zenith angle. However, for an erectophile type canopy, the reflectance in VIS decreases with an increase in solar zenith angle while it increases in NIR (Kimes et al., 1984). For example, BRDF of corn in NIR and VIS region changes differently. For corn, the reflectance distribution in VIS and NIR is like 'shallow bowl shape', whereas values of reflectance increase with view zenith angle for most azimuth angles. NIR region backscattering is seen more than VIS region, while BRDF for NIR and VIS in backscattering direction are different. For a source at the zenith, the BRDF can be approximated by Lambertian surface with mostly diffused radiation in all other directions. With the increase in solar zenith angle, it becomes a non-Lambertian surface (due to specular reflectance).

It is observed that BRDF of bare soil is highly Non-Lambertian (with respect to vegetation canopies) due to its higher roughness (Eaton et al., 1974). If LAI is greater than three, soil BRDF can be considered Lambertian as the canopy becomes dense and very little soil is visible. But, if LAI is less, then the effect of soil on reflectance increases (more absorption due to internal scattering) and affects more in hotspot direction (due to specular radiation). The research community well accepts the radiative transfer models and their inversion process. However, the study of these models is out of the scope of this PhD research. The details of different RT models have been discussed in Appendix 0.

## 2.8 Research gaps

The synthesis of the literature relevant to the remote estimation of crop biophysical and biochemical parameters have revealed the following research gaps:

i. The existing methods for remote estimation of LAI using optical data give foliage LAI and need local tuning to get near to true LAI values. Moreover, most of the models overestimate the LAI for initial crop growth stages and underestimate it as the crop reaches maturity (Yao et al., 2008). This is majorly due to the lack of crop-specific architectural information in the models (Welles and Norman, 1991).

ii. There are multiple knowledge gaps in the optical remote sensing area for the estimation of leaf water content. Most of the indices and models are made for satellite-based mixed pixel data, which may not work well for pure pixel data. Moreover, mixed pixel data do not perform well for the early growth stage of the crop due to minimum canopy coverage and coarse spatial resolution of data. The pure pixel data has not been explored intensively for estimating the leaf water content of the crop so that plant-level decisions can be made. (Jones and Sirault, 2014 ; Cheng et al., 2006, Chen et al., 2006; Kokaly and Clark, 1999)

iii. Very little work is available on remote measurement of leaf nitrogen content with respect to the change in leaf water content. Considering the association of water molecules with plant protein, the bands or indices for estimating leaf nitrogen content from visible to near-infrared region (400-

1000 nm) are expected to be affected by the water molecules around plant proteins.

iv. The radiative transfer crop model - PROSPECT/PROSAIL is one of the popular crop simulation models. However, these models are entirely based on independent leaf/canopy constituent absorption properties of electromagnetic spectra. This makes the model weak for field-based studies. Moreover, the unavailability of transmission spectra in the remote sensing technique adds uncertainty to the inversion process of these models. (Colombo et al., 2008; Baret and Fourty, 1997; Jacquemoud et al., 1996)

v. There is little research available where process-based crop models were fed near-real-time drone-based estimation as crop parameter products. This kind of research has the potential to produce precise information about crop health.

vi. In the field of remote sensing-based crop research, very few studies were found on the understanding of leaf-level water and nitrogen dynamics across different crop growth stages. Knowledge of these dynamics will be extremely helpful in distinguishing water and nitrogen stress in the plant.

## 2.9 Chapter summary

This chapter compiled state-of-the-art literature in optical sensing for drone-based precision agriculture. First, an overview of precision agriculture and the use of drones in precision agriculture has been discussed. The chapter also presented existing popular vegetation indices used to measure crop biophysical and biochemical properties and their limitations. An overview of various crop biophysical and biochemical properties estimation processes was presented. Towards the end of the chapter, radiative transfer models were explained. Ultimately research gaps were presented, and the first four were selected for framing objectives. These research objectives were presented in chapter one, with the gaps and objectives addressed in chapters three to six.

# Chapter 3

# Site description and data acquisition


*An image captured during the hyperspectral camera-mounted drone flight, over the research farm.*

# 3. Site description and data acquisition

Research gaps listed in chapters one and two were addressed by doing field experiments from June 2017 to Feb 2020. The data collected till Rabi 2017-18 seasons were used to understand the crop dynamics and data collection process. A semi-controlled pot experiment was also carried out, and learnings of this experiment were used for data collection from field-based experiments. The pot experiment details are given in Appendix 1. The field data collected from Rabi 2018-19 seasons were used for the modelling purpose in this research. This chapter discussed the details of the field experiment and the collected dataset. The collected data were used to create and validate biophysical, biochemical, and crop stress estimation models explained in chapters four, five, and six.

## 3.1 Field experiment: Research farm and data collection

The research farm used to do data collection for this PhD work was part of an Indo-Japan project named "Data sciences based farming support system for sustainable crop production under climate change". The project started in June 2017. The *Kharif* 2017 and *Rabi* 2017-18 cultivation was undertaken in the first stage of the project, while in the second stage, only the *Rabi* seasons of 2018-19 and 2019-20 were used for cultivation. The *Rabi* season was selected to precisely understand the water stress effect on the crop, which was not possible during the *Kharif* season as the frequent rainfall events in the *Kharif* season do not allow the crop to reach heavy water stress condition. For this research, the first stage was used to understand the crop behaviour, data collection process and set protocols for stage-two data collection. During stage two, field stay was done to collect farm data on a daily basis. Thus, only stage-two data was used for model creation and validation in this research. For data collection during *Rabi* 2018-19 and 2019-20 seasons, the field stay was 45 days from the 6-leaf stage of the crop to the silking stage, followed by multiple field visits until the maturity stage. The protocol for collecting data from various sensors is given in Appendix 2, and details of the field stay are given in Appendix 3.

### 3.1.1 Details of the research farm

The study was conducted for maize crop (Scientific name: Zea mays L.; Variety: Cargil 900M (gold)) in the Agro Climate Research Centre farm of Professor Jayashankar Telangana State Agricultural University, located at Hyderabad, Telangana, India. The study area is a semi-arid region that lies between 17°19'27.2"N – 17°19'28.3"N and 78°23'55.4"E – 78°23'56.2"E, as shown in Figure 3.1. The details of the research farm are given in Table 3.1. The second stage crop was sown during 2018-19 and 2019-20 Rabi seasons. The details of the sowing date and various management practices are given in Table 3.2. The ground truth and drone-based data collection were undertaken frequently during all the growth stages of the crop. The experiment was laid out in split-plot design with a combination of three irrigation schedules and three fertilisation levels based on a climatological approach (Halagalimath et al., 2017). The ratio of irrigation water (IW) and cumulative pan evaporation (CPE) was used to decide the day on which plots need to be irrigated. Irrigation at IW/CPE ratio of 0.6, 0.8, and 1 was selected for plots with three irrigation levels. During each irrigation, 50 mm water was supplied to the scheduled plots through pipes directed through a water meter. Accordingly, IW was kept constant (50 mm), and daily readings from pan evaporimeters (in mm) used to find the IW/CPE ratio and thus the timing of irrigation for the different plots. Three levels of nitrogen fertilisation (100, 200, and 300 kg nitrogen $ha^{-1}$) were given to each irrigation plot type. This combination of three irrigation and three fertilisation levels resulted in nine unique plots, and so with each replicated thrice, there was a total of 27 subplots (3 water x 3 nitrogen x 3 replications), as shown in Figure 3.1 (b). Each plot of size 4.2 m x 4.8 m was treated with one of the three different water and nitrogen levels to enable the subplots to be at low, medium and high water and fertiliser stress conditions. For each treatment, a plant to plant spacing of 20 cm and row to row spacing of 60 cm was adopted, resulting in a plant density of ~8.33 plants per $m^2$. Nitrogen was applied to all the plots at three different stages – sowing, six-leaf stage, and tasseling stage. Figure 3.2 shows the plots arrangement diagram in the research farm.

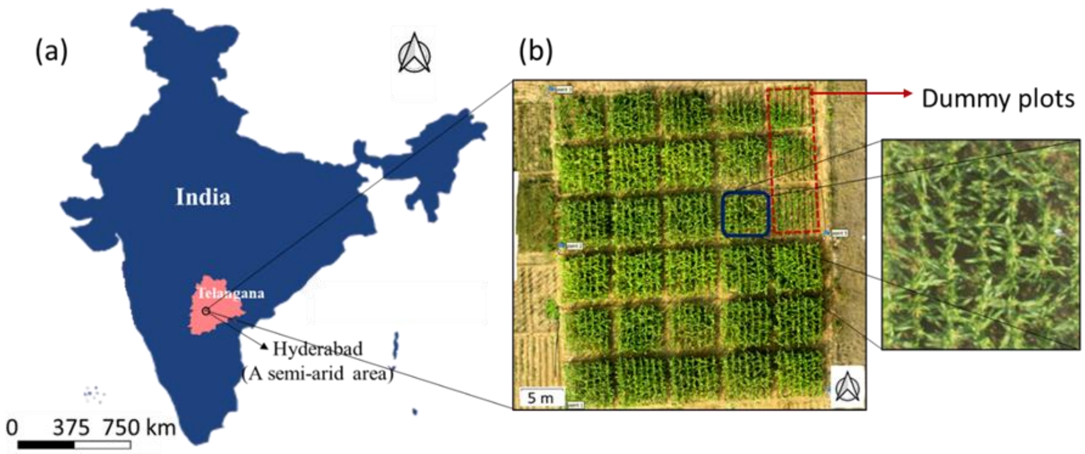


Figure 3.1: (a) Geographical location of the farm, located in a semi-arid zone in the southern part of India. (b) Layout of the research farm as seen from the drone, which can capture leaf-level high-resolution (around 1 $cm^2$ pixel resolution) images.

Table 3.1: Details of region and field

| | |
|---|---|
| Crop variety | Maize (Zea mays L.) – Cargil 900m gold (Monsanto) |
| Soil type | light red sandy-loam soil (soil profile data in Appendix 4) |
| Irrigation type | Furrow irrigation through bore well |
| Location | ARI, PJTSAU, Hyderabad, India (First site: 17°19'27.5"N and 78°23'53.0"E, Second site: 17°19'27.7"N and 78°23'55.6"E) |
| Annual rainfall | ~ 822 mm |
| Annual PET | 1700 to 1960 mm |

Table 3.2: Details of various field experiment treatments

| Treatment | Meaning | Rabi (Winter) 2018-2019 | Rabi (Winter) 2019-2020 |
|---|---|---|---|
| Crop duration | | 16/10/2018–20/02/2019 | 18/10/2019–16/02/2020 |
| N1 | Low nitrogen | 100 kg/ha | 90 kg/ha |
| N2 | Ideal nitrogen | 200 kg/ha | 180 kg/ha |
| N3 | Overdose nitrogen | 300 kg/ha | 240 kg/ha |
| I1 | High water stress | Irrigation when IW/CPE = 0.6 | Irrigation at 60% DASM |
| I2 | Moderate water stress | Irrigation when IW/CPE = 0.8 | Irrigation at 40% DASM |
| I3 | No water stress | Irrigation when IW/CPE = 1.2 | Irrigation at 20% DASM |

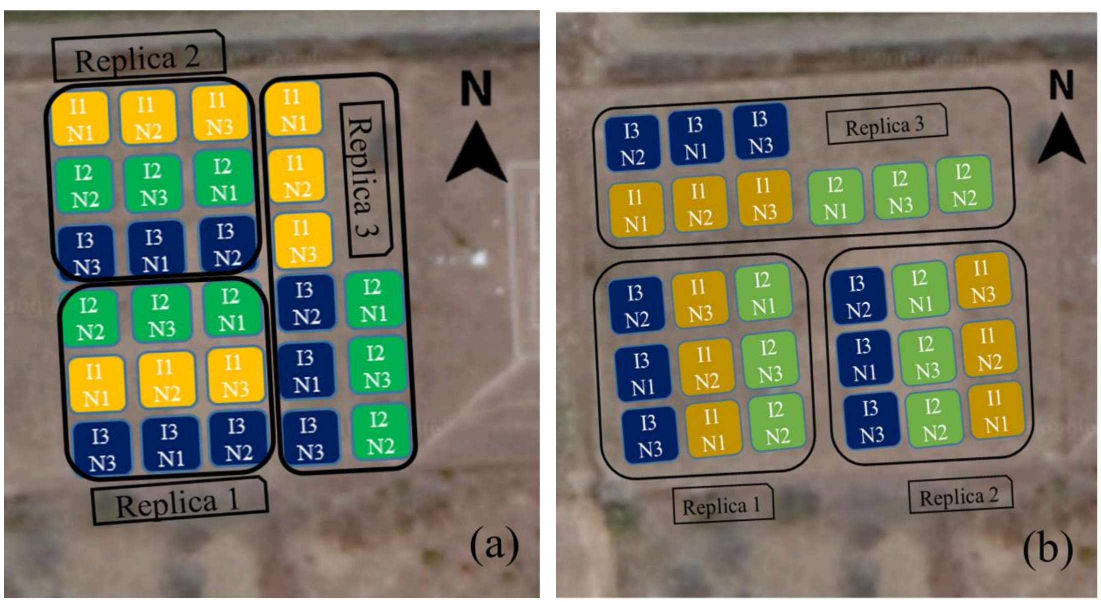


Figure 3.2: Treatment details given to the plots during (a) *Rabi* 2018-19, and (b) Rabi 2019-20 seasons. A total of three replications are used, and in each replication, a total of 9 treatments (subplots) with different water and fertiliser were applied.

### 3.1.2 Drone-based data collection

Drone-based RGB images were captured periodically from a height of 25 m during 2018-19 and from a height of 40 m during 2019-20 season (keeping pixel resolution around 2 cm). An overlap of 70–80 % at the front and 50–70 % at the side was maintained in consecutive RGB images captured by the drone-mounted camera, as shown in Figure 3.3. This overlap ensured the creation of a quality orthomosaic (Raj et al., 2019). In 2018–19 Rabi season, a 'Canon IXUS' camera (Canon IXUS 160, 20 megapixels, programmed to capture images continuously at three-second intervals, FoV of 55° × 50°) was used. In Rabi 2019–20 season, a 'Micasense Altum' camera (2064 x 1544 pixel, per band, Blue at 475 nm and 32 nm BW, Green at 560 nm and 27 nm BW, Red at 668 nm and 14 nm BW) was used because the Canon camera was damaged in the last flight of the 2018–19 season.

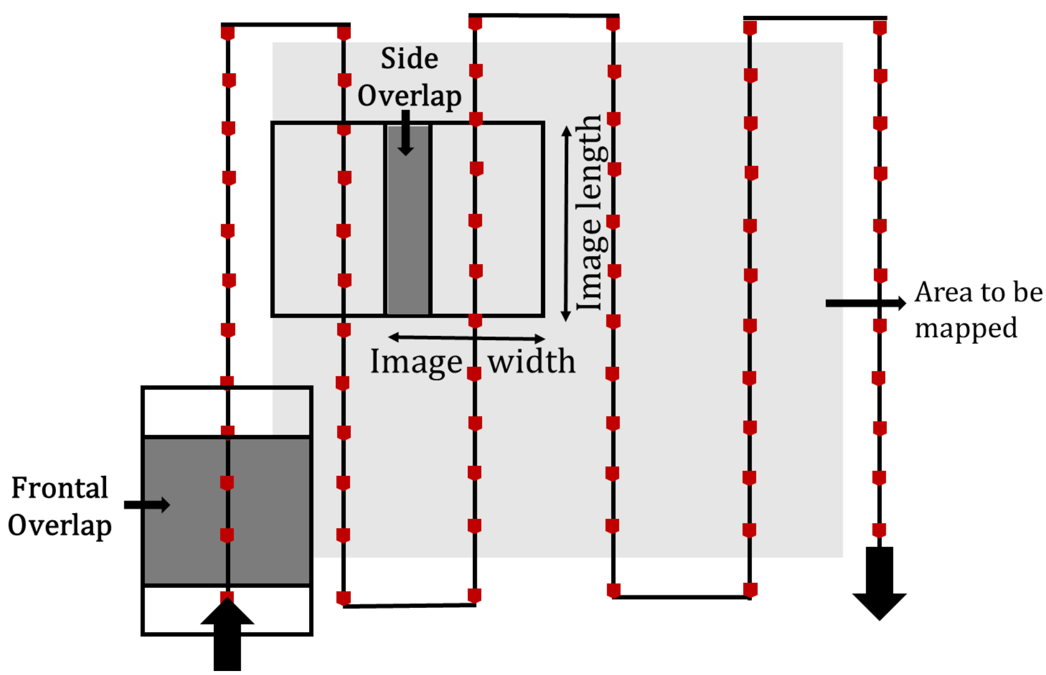


Figure 3.3: Frontal and side overlaps of images taken by the drone-mounted camera moving in a serpentine motion (image is not on scale). The image is adapted from Raj et al., 2019.

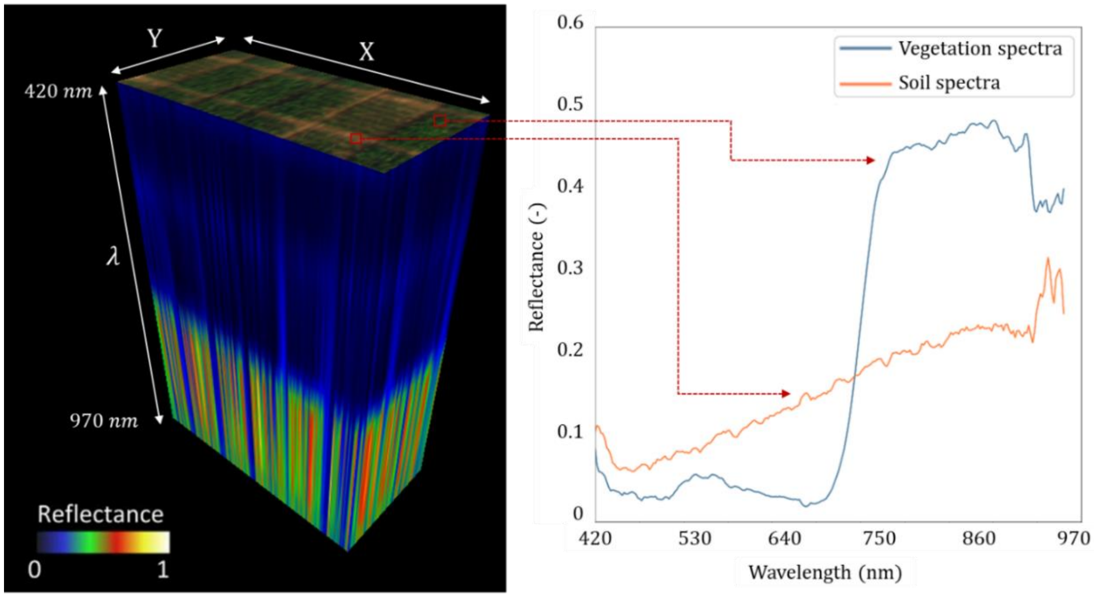


Figure 3.4: Hyperspectral data cube - a three-dimensional representation of a hyperspectral image. Here, X and Y represent the spatial dimension, while the Z dimension (denoted by $\lambda$) shows the spectral information according to wavelength for each pixel in the image. The top layer of the cube is showing an RGB map of a section of the farm. The spectral information of a vegetation and soil pixel is shown at the right of the plot.

A drone-based push-broom hyperspectral camera (Bayspec OCI-F-HR hyperspectral imager; frame rate 50 fps, FWHM 2.1nm, FOV 20 degree, total 240 bands) was used to collect top-of-canopy farm images in the 400-1000 nm spectral range. The data were captured temporally from a height of 50 metres above the ground having around 1 cm spatial resolution. The created hyperspectral cube of the farm map is shown in Figure 3.4. The detailed process of drone-based data collection is presented in Appendix 5.

### 3.1.3 On-ground data collection

The LAI of each plot was recorded using a Licor 2200-C canopy analyser with a 270° view angle cap and three 'below' canopy readings per plot on the same day of each flight. Three samples of LAI data were collected from a rectangular subplot of innermost three rows (pictorial representation of a subplot is given in Figure 3.5), and the values averaged and corrected based on atmospheric sky condition. Canopy height was measured by taking five samples from each sub-plot. The plants were randomly selected from the corners of the rectangular block and one from the centre of the block, as shown in Figure 3.5. Appendix 2 explains the basis on which the number of samples for LAI and height data was decided. Various canopy structural properties such as top leaf angle and leaf area were also recorded during different growth stages. Five plants (four plants from corners and one plant from the center) from each of the nine plots were chosen, and the area of every leaf calculated based on the lengths and widths of the leaves, as shown in Figure 3.6. No destructive sampling was done to record the lengths and widths of the leaves. The per-plant total leaf area of these five plants was averaged and multiplied with the number of plants in the respective plots. The total leaf area in a plot was then divided by the plot ground area, being 4.2 m × 4.8 m. The LAI calculated using this method was considered to be the closest possible to the true LAI and termed $LAI_{actual}$.


Figure 3.5: Picture of a subplot. Every subplot is of size 4.2 m x 4.8 m. Red colour box at the center of the subplot indicates a portion from which all the non-destructive data was collected.

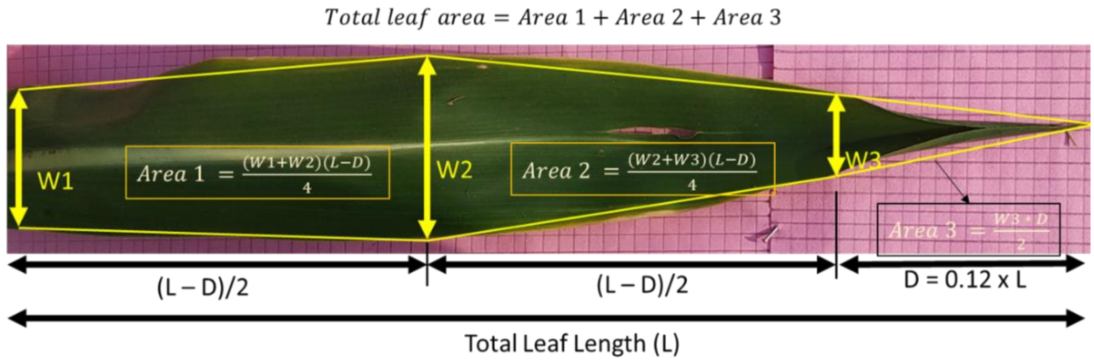


Figure 3.6: Calculation of the actual area of a leaf by using the length and width of the leaf, measured at different locations. The area is calculated based on the geometric formulae shown.

After the collection of drone-based hyperspectral images, a hand-held spectroradiometer of make Spectra Vista GER 1500 was used to collect leaf spectral signatures from one leaf of each of the 27 subplots. Three spectroradiometer readings were acquired from each leaf, and the leaf plucked and packed in an airtight pre-weighed zip bag for measuring the LWC. The destructive sampling was done only from side rows of the subplots, and the inner three rows remained intact throughout the season. One leaf from the destructive sampling zone of every sub-plot (preferably second last row) was selected, and three spectroradiometer reading were collected from that leaf. Then the leaf was plucked out and packed in a zip bag for further lab chemical analysis to find water and nitrogen content in the leaf. Most of the data were collected from 10:00 AM to 2:00 PM when the sun was near zenith, but canopy height was taken even at different times as the maize crop height had no relationship with the sun angle.

The destructive sampling was done at regular intervals throughout the lifecycle of the crop. The prime objective of the destructive sampling was to find out the precise nitrogen and water content in the leaves over different growth stages of the crop so that it can be used as ground-truth information and to tune models based on drone-based data. Protocols to collect on-ground data is presented in Appendix 2.

### 3.1.4 Processing of destructive leaf samples

After collecting the hyperspectral signatures from leaves, the leaves were plucked out and packed into respective pre-weighed airtight zip-bag. Later, individual leaf-filled zip-bags were again weighed and the subtraction of before and after weights of zip-bags were used as the fresh weight of the leaves. The leaves were then cut into small pieces, put into a pre-weighted aluminium foil vessel, and weighted again. The leaf-filled aluminium foil vessel was then put in an oven at 60 degrees Celsius for around 72 hours to get completely dry samples. The dried samples in the aluminium foil vessels were weighed again, and the dry weight of the leaves obtained. The fresh weight and dry weight of the leaf samples were used to obtain the leaf water content using

$$LWC = \frac{weight_{fresh} - weight_{dry}}{weight_{fresh}}. \tag{3.1}$$

To obtain the nitrogen content in the leaf samples, the dry leaves were crushed into small pieces and passed through a fine sieve to get the powdered sample. The powdered sample was then fed to a CHNS elemental analyser (details in Appendix 6), and from every sample, two replicates were analyzed. A total of 271 leaf samples were analyzed through an elemental analyzer. The CHNS analyzer must be fed with the homogenised powdered sample. The preprocessing of leaf samples are time-consuming and critical as the homogenisation of the leaf samples are very important to get reliable results with good repeatability. Figure 3.7 shows the step-by-step approach used, starting from leaf collection to making its fine powder. Table 3.3 compiles all the data collected from the field and their respective uses.

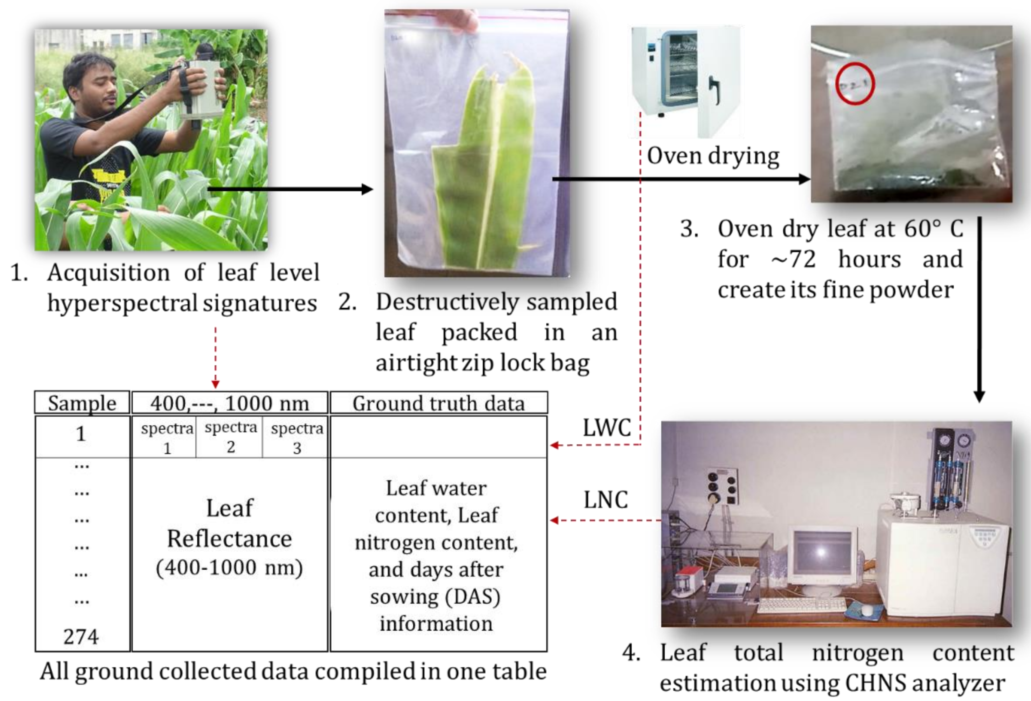


Figure 3.7: Steps to get ground truth leaf nitrogen and leaf water content data from destructively sampled leaf.

Table 3.3: Data collected from the field.

| Data | Instrument used | Pixel size/ Number of samples per plot | Use of the data |
|---|---|---|---|
| High spatial and temporal resolution top-of-canopy RGB images | Hexacopter-mounted Canon IXUS (Rabi 2018-19 season), and Micasense Altum (Rabi 2019-20 season) | Pixel size < 2 cm | Input for remote estimation of the crop height and the green-canopy cover fraction |
| High spatial and temporal resolution top-of-the-canopy hyperspectral images | Hexacopter-mounted Bayspec Hyperspectral imager (400-1000 nm) | Spatial resolution ~ 2 cm<br><br>Spectral resolution = 2.4 nm | Model training and testing |
| Foilage LAI | Licor Canopy analyser Model: 2200-C | Three 'below' canopy readings per plot, and frequent readings for atmospheric correction | Training of the LAI Model |
| True LAI | The lengths and widths of leaves were measured using a scale (Figure 3.6) | Five plants per plot for nine plots are recorded (one time) | To calculate the actual LAI of the plot for validation of all of the LAI models |
| Top leaf angle | Clinometer mobile application | Leaf angles of top 5–6 leaves from five plants per plot | Used to create the *VLADF* model |
| Canopy height | Metre scale | An average height of five plants per plot is used to represent the height of the canopy of one plot | Validation for height estimation model |
| Hyperspectral signatures | Spectroradiometer (SVC GER1500) (400 - 1000 nm) | Three signatures per leaf sample | Indices creation |
| Leaf water content | 60-72 hours in an oven at 60°C | One leaf per plot | Ground-truthing the estimated leaf water |
| Leaf nitrogen content | CHNS elemental analyser | 3-4 mg of samples replicated twice | Ground-truthing the estimated leaf nitrogen |
| Tassel count | Manual counting | Each plant in every plot | For validation of tassel counting model |
| Yield | Weighing Method | Middle three rows of the plot | Connecting crop stress and fertilisation effect |

## 3.2 Ground truth data description

Manually collected crop physical and chemical properties data were used as ground truth in this research. To check the impact of different irrigation and fertilisation treatments on the crop measured variable (yield, LAI, height, leaf water and nitrogen content), one-way analysis of variance (ANOVA) test was performed on the data set. The results concluded a statistically significant impact of treatments on leaf water content, grain yield, LAI, and crop height as shown below.

Leaf water content: $F(2,24) = 9.402$, $p = 0.001$

Grain yield: $F(8, 18) = 21.449$, $p = 1.05e\text{-}7$

LAI: $F(8, 18) = 4.555$, $p = 0.003$

Crop height: $F(8,18) = 10.248$, $p = 2.57e\text{-}5$

To check whether the treatments were significantly different, the Tukey HSD test was performed. Interestingly, the effect of various treatments on the leaf nitrogen content was not statistically significant. However, the trend of leaf nitrogen was found such that low fertilisation treatment plants showed lesser leaf nitrogen than plants treated with sufficient or high doses of fertilisation.

Results of variables that showed significant differences with the One-way ANOVA test followed by post-hoc Tukey HSD Test had been explored. Table 3.4 shows a statistically significant difference between LWC of I1, I2 and I1, I3 irrigation treatment plants. Table 3.5 shows the effect of different treatments on grain yield, LAI, and crop height.

Table 3.4: Tukey HSD test results for irrigation treatment effect on LWC

| Irrigation treatments (9 samples) | Tukey HSD p-value | |
|---|---|---|
| I1 and I2 | 0.009 | p<0.01 |
| I1 and I3 | 0.001 | p<0.01 |
| I2 and I3 | 0.664 | insignificant |

Table 3.5: Post-hoc Tukey HSD test results showing statistically sigificant difference between biophysical properties of crop due to differnet irrigation and fertilisation treatments.

| **Tukey HSD p-value** | | | |
|---|---|---|---|
| **Treatments (3 samples)** | **Grain yield** | **LAI** | **Height** |
| I1N1 and I1N2 | insignificant | insignificant | insignificant |
| I1N1 and I1N3 | insignificant | insignificant | insignificant |
| I1N1 and I2N1 | insignificant | insignificant | $p<0.05$ |
| I1N1 and I2N2 | insignificant | insignificant | $p<0.01$ |
| I1N1 and I2N3 | $p<0.05$ | $p<0.05$ | insignificant |
| I1N1 and I3N1 | $p<0.01$ | $p<0.01$ | $p<0.01$ |
| I1N1 and I3N2 | $p<0.01$ | $p<0.05$ | $p<0.01$ |
| I1N1 and I3N3 | $p<0.01$ | insignificant | $p<0.01$ |
| I1N2 and I1N3 | insignificant | insignificant | insignificant |
| I1N2 and I2N1 | insignificant | insignificant | insignificant |
| I1N2 and I2N2 | insignificant | insignificant | $p<0.05$ |
| I1N2 and I2N3 | insignificant | insignificant | insignificant |
| I1N2 and I3N1 | $p<0.05$ | $p<0.05$ | $p<0.01$ |
| I1N2 and I3N2 | $p<0.01$ | insignificant | $p<0.01$ |
| I1N2 and I3N3 | $p<0.01$ | insignificant | $p<0.01$ |
| I1N3 and I2N1 | insignificant | insignificant | insignificant |
| I1N3 and I2N2 | insignificant | insignificant | insignificant |
| I1N3 and I3N1 | insignificant | insignificant | $p<0.05$ |
| I1N3 and I3N2 | $p<0.01$ | insignificant | $p<0.05$ |

Table 3.5: Post-hoc Tukey HSD test results showing statistically significant difference between biophysical properties of crop due to different irrigation and fertilisation treatments. (Continued)

| Treatments (3 samples) | Grain yield | LAI | Height |
|---|---|---|---|
| I1N3 and I3N3 | $p<0.01$ | insignificant | $p<0.05$ |
| I2N1 and I2N2 | insignificant | insignificant | insignificant |
| I2N1 and I2N3 | insignificant | insignificant | insignificant |
| I2N1 and I3N1 | $p<0.01$ | insignificant | insignificant |
| I2N1 and I3N2 | $p<0.01$ | insignificant | insignificant |
| I2N1 and I3N3 | $p<0.01$ | insignificant | insignificant |
| I2N2 and I2N3 | insignificant | insignificant | insignificant |
| I2N2 and I3N1 | $p<0.05$ | insignificant | insignificant |
| I2N2 and I3N2 | $p<0.01$ | insignificant | insignificant |
| I2N2 and I3N3 | $p<0.01$ | insignificant | insignificant |
| I2N3 and I3N1 | insignificant | insignificant | insignificant |
| I2N3 and I3N2 | insignificant | insignificant | insignificant |
| I2N3 and I3N3 | $p<0.01$ | insignificant | insignificant |
| I3N1 and I3N2 | insignificant | insignificant | insignificant |
| I3N1 and I3N3 | $p<0.05$ | insignificant | insignificant |
| I3N2 and I3N3 | insignificant | insignificant | insignificant |

### 3.2.1 Leaf water content

One leaf from the top-of-the canopy (which can be seen from the drone) of every plot was destructively sampled over a period of time, and its leaf water content (LWC), and leaf nitrogen content (LNC) were obtained. It was found that LWC depends on water stress present in the plant (due to soil moisture stress) and also on the growth stage of the crop. As the growth stage increases, the water holding capacity of the leaves decreases. Figure 3.8 shows temporal LWC distribution in I1, I2, and I3 plants treatments. The growth stage timing and irrigation & rainfall events are also indicated in the plot. Until 26 days after sowing (DAS), all the plots were treated with the same amount of water; thus, there was no observable difference in LWC of any treatment until 26 DAS. The growth stages also started early in I3 plots, and this difference is visible from the tasseling stage where for I3, and I2 plots, 50% tasseling event was recorded around 65 DAS while for I1 plots, 50% tasseling event was recorded around 72 DAS.

The late tasseling was majorly due to significant water stress present in the plots. One of the interesting observations about the LWC percentage in different plots is, for I3 plots, the LWC percentage remains higher than I2 until the tasseling-silking stage and then dropped below the percentage of I1 plots after the tasseling-silking stage. This trend was even maintained for I2 plots. It seems that, after the tasseling/silking stage, the water requirement in the stem for the formation of cobs was more than in the leaves, thus for all water-sufficient plots, the LWC percentage decreased to support the maximum cob formation. However, water-stressed plants could not support the cob formation process at the right time. The effect of the water stress was evident on the height and LAI of the plots. Section 3.2.3 and section 3.2.4 has discussed the effect of water and nitrogen stress on canopy LAI and height.

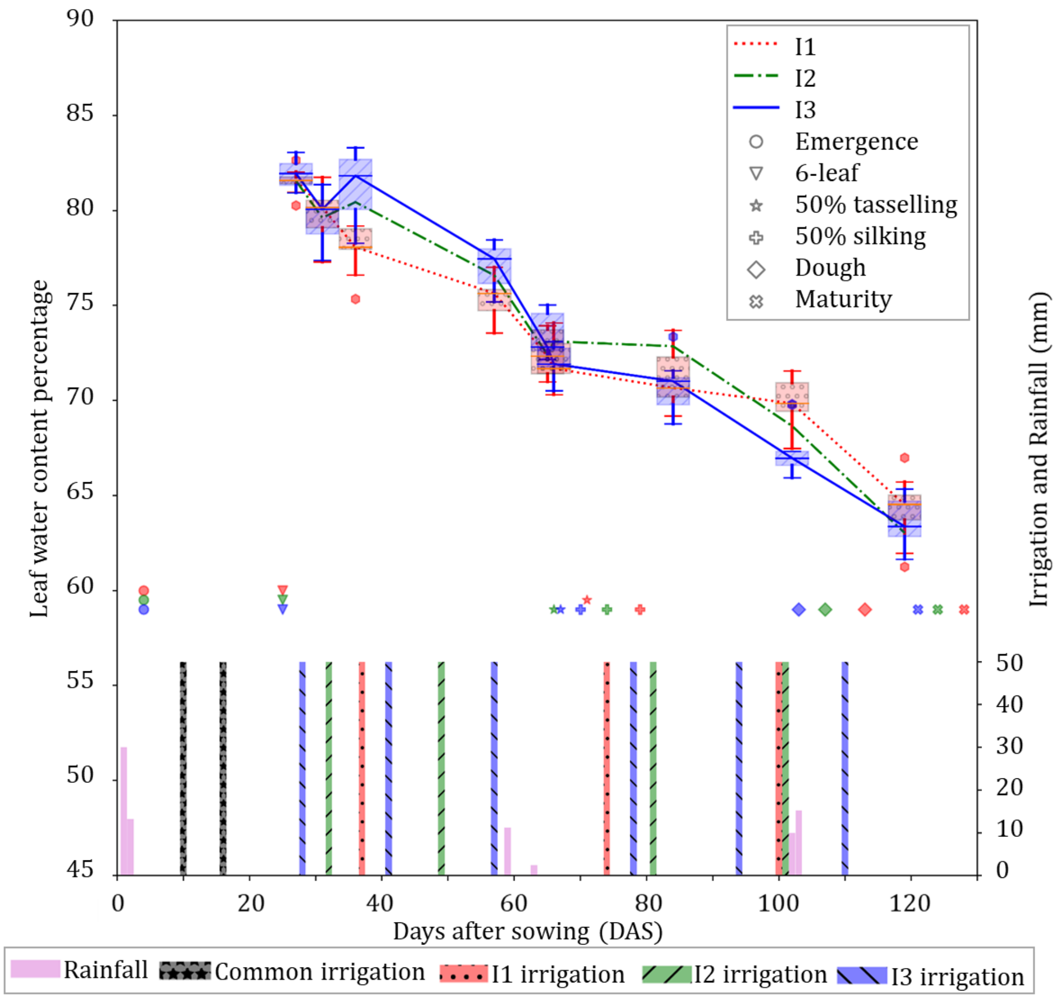


Figure 3.8: Temporal LWC of different irrigation treatment plants and their growth stages. The primary y-axis shows LWC percentage, and the secondary y-axis shows irrigation and rainfall values in mm.

### 3.2.2 Leaf nitrogen content

The same leaf which was used to determine the LWC was analysed in the CHNS analyzer and the total LNC of the leaves were obtained. Figure 3.9 shows the temporal LNC in the different treatment plots. The maximum value of leaf-nitrogen can be observed at the early stage of the crop, and it keeps reducing as the plant grows. The change in leaf nitrogen can be correlated with the fertiliser management done on the farm. Maintaining the optimal amount of nitrogen in the leaves/plant is critical as nitrogen is the second major yield deciding factor after water (along with pest management). If the availability of nitrogen in the plant is low, then the kernel formation will be reduced, and less number of doughs will be formed, resulting in a low yield. The availability of nitrogen in the plant depends not only on fertilizer provided in the soil but also on soil moisture. Even if there is enough soil nitrogen available, the plant might not uptake the soil nitrogen due to low water availability to transfer the nitrogen from the soil to stem and then leaves. Figure 3.9 shows how leaf-nitrogen changes with various growth stages of the crop. It can also be observed that if nitrogen treatment was kept the same, then water application does make a difference in LNC. It can also be seen that for all plots treated with sufficient water (I2 and I3), the LNC before the tasseling stage was around 32 mg/g, but for limited nitrogen treatment plots, it was around 28 mg/g. This difference in LNC even for sufficiently water-treated plots makes a huge yield-gap between I1 and I3 plots.

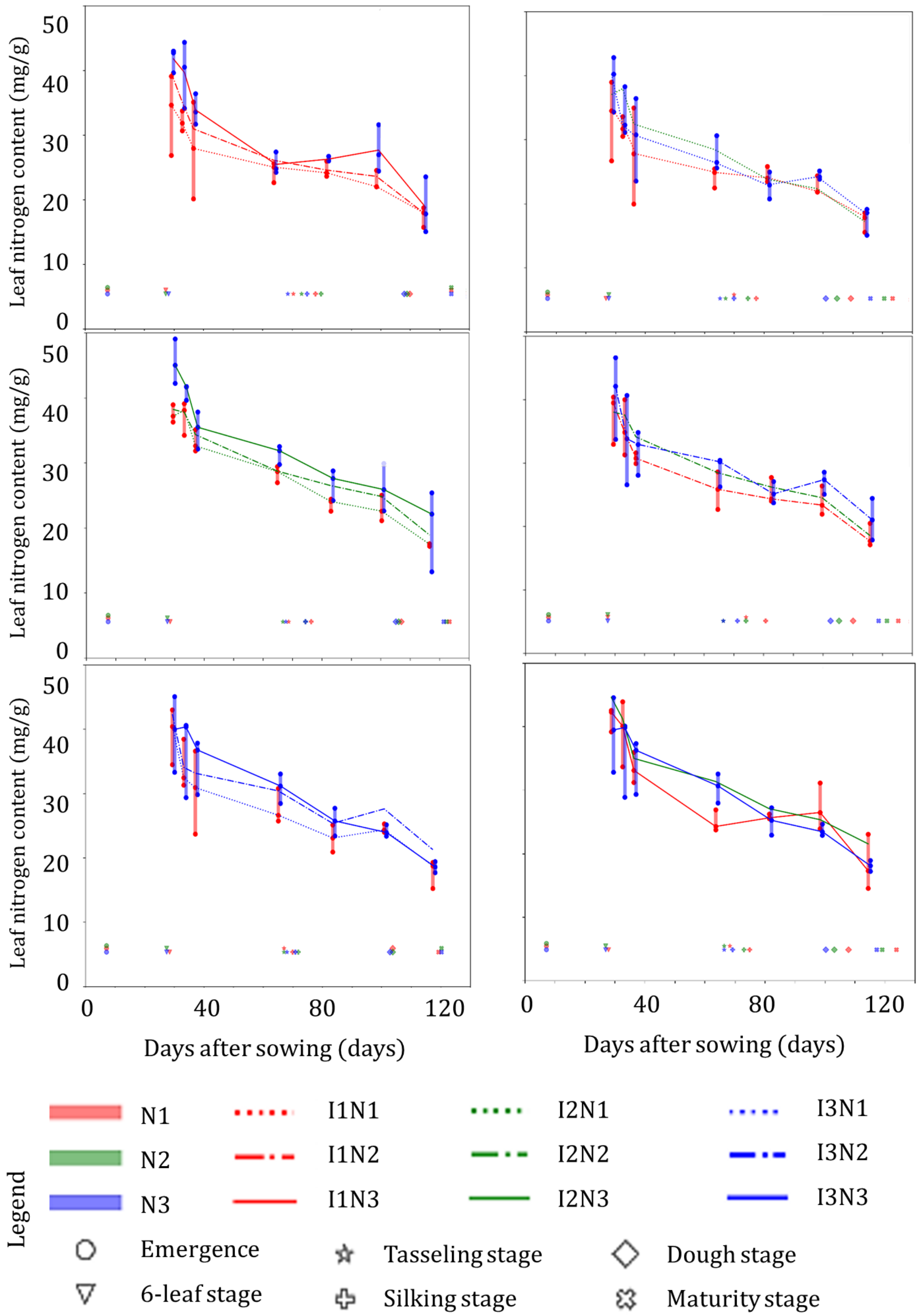


Figure 3.9: Temporal LNC of different irrigation and nitrogen treatment plants and their growth stages.

### 3.2.3 Leaf area index and canopy height

The analysis of various treatments on LAI and height is discussed in this section. In figure 3.10 and 3.11, LAI and height values of different treatment canopies are shown, respectively. Plots treated with low nitrogen but different water levels show the highest variability in LAI/height, with the highest LAI/height in the I3N1 and lowest LAI/height in the I1N1 case. However, this variability reduces when nitrogen is provided in a sufficient amount (LAI/height of all the treatments significantly increases when compared to I1N1 plots). All water stress plots have low LAI values than I3 plots. However, plots treated with sufficient water does not show any visible change in LAI when nitrogen treatment changes. When low N plots were treated with different water treatments (Figure 3.10 / Figure 3.11), then it was observed that LAI/height was higher than when there was no water stress, and thus it can be concluded that in the case of low N availability, water plays an important role in deciding LAI. I.e. more water higher the LAI/height. In the condition where water-stressed plots are treated with different N levels, data has shown higher LAI/height when high N is given. In the case of no water-stressed plots, changing levels of N seems not to affect the LAI /height values.

### 3.2.4 Crop yield

Analysis of yield data showed a general trend that the yield increases with an increase in input resources with a significantly high yield in the case of the I3N3 treatment and the lowest yield in the I1N1 treatment. However, for water stress condition, I1N3 seem to perform better than I2N1 and comparable to I2N2 treatments. Treatment-wise yield and harvesting index is shown in Figure 3.12. From the analysis, it is evident that optimal use of nitrogen does make a change in grain yield in the case of limited water availability.

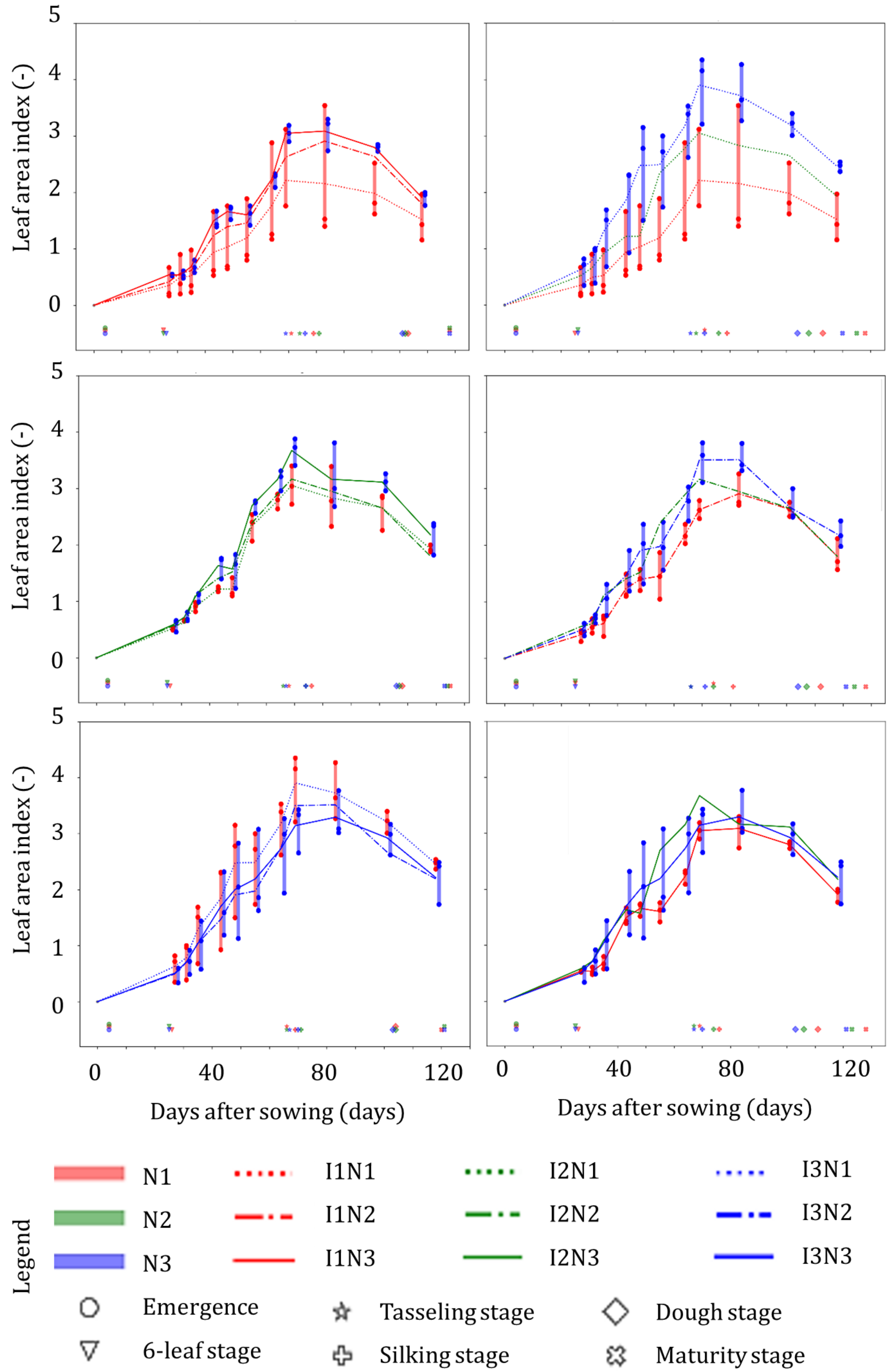


Figure 3.10: Temporal LAI of different treatment plants and their growth stages.

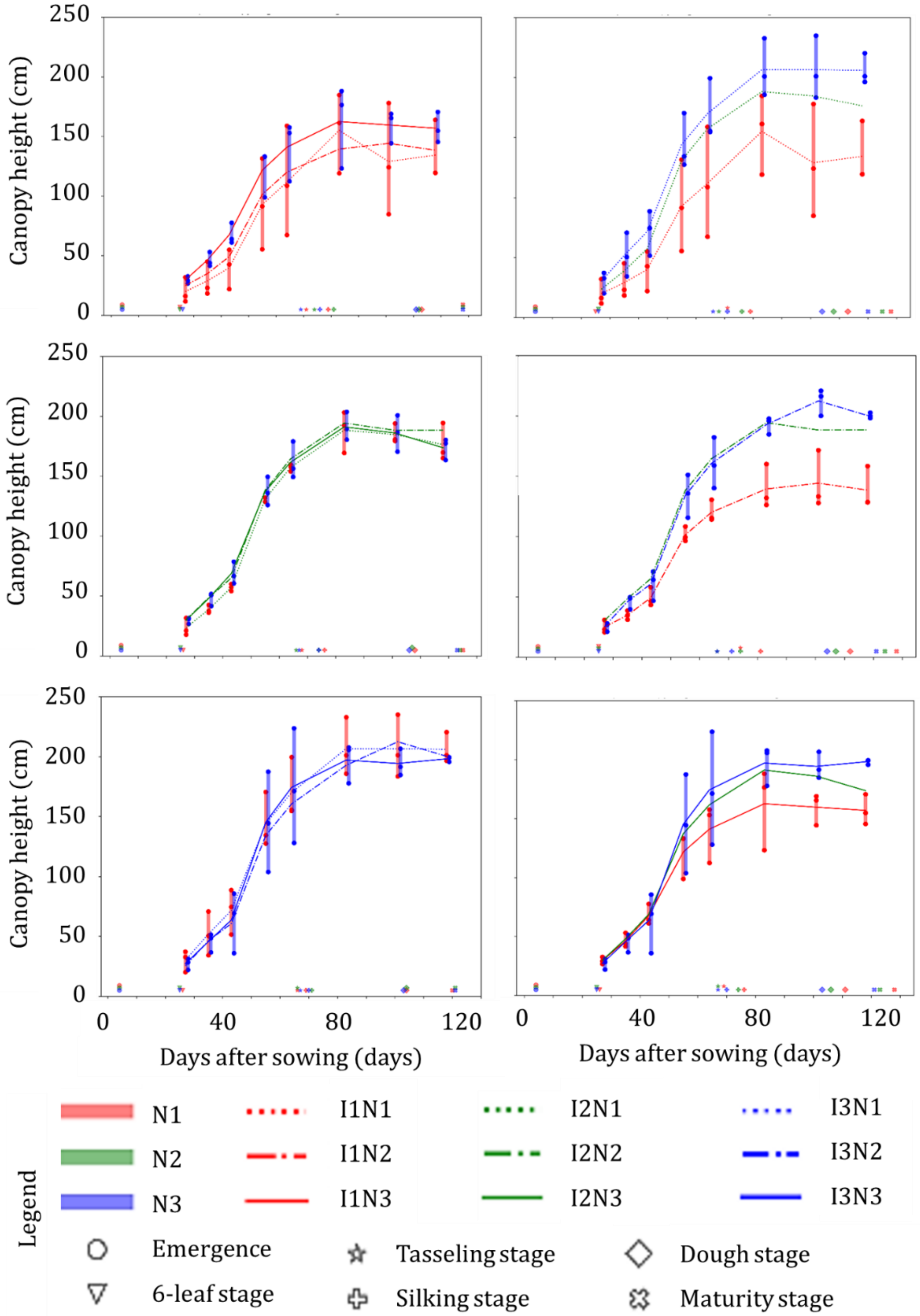


Figure 3.11: Temporal height of different treatment plants and their growth stages.

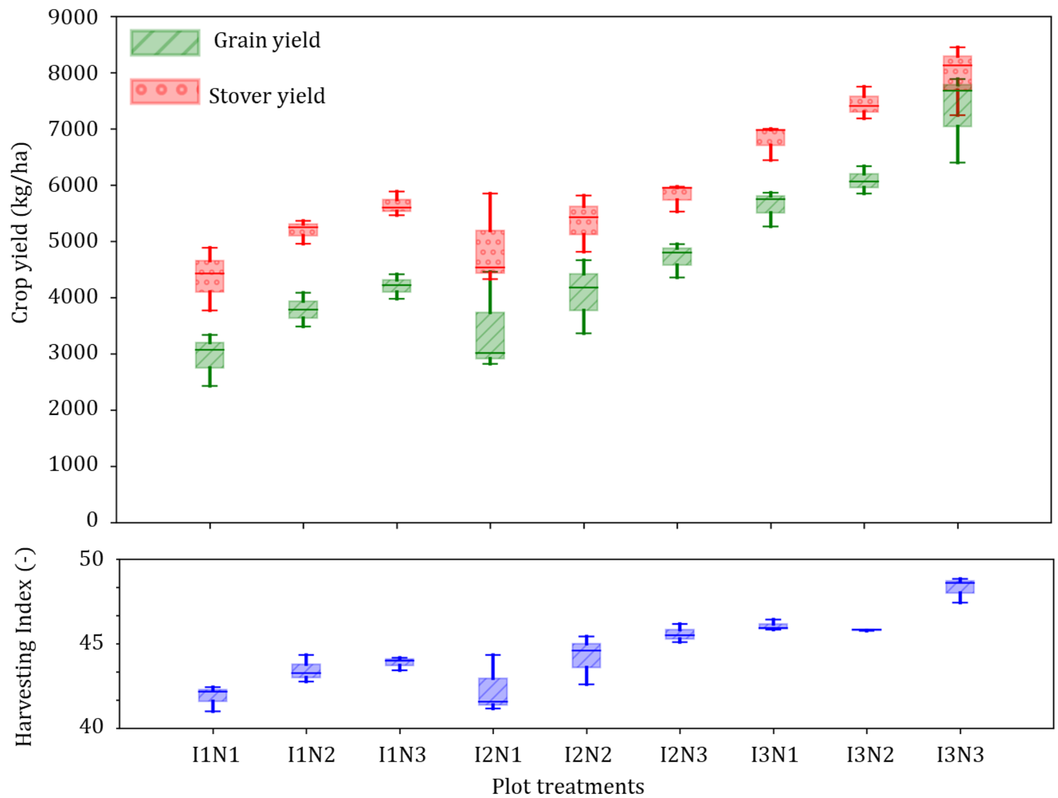


Figure 3.12: Stover and grain yield of different treatment plots. The solid line within the box shows the median value, and the whiskers represent the top and bottom 25 percentile values.

### 3.2.5 Tassel counting

From ground truth data, it was found that the tasseling stage in I1 plots was delayed by 2-8 days when compared to I2 and I3 plots. The delay was minimum for I1N3 plots and maximum for I1N1 plots. Here, it should be noted that the tasseling stage was considered as the time when 50% of the plants in a plot get completely open tassels. However, the appearance of tassels (which might not be completely open) in all the plots seems to occur around the same time (60 days after sowing for the Rabi 2018 season). The analysis showed that the increase in the number of tassels per day was different for water-stressed and water-sufficient plots. For I3 and I2, after seven days of the appearance of

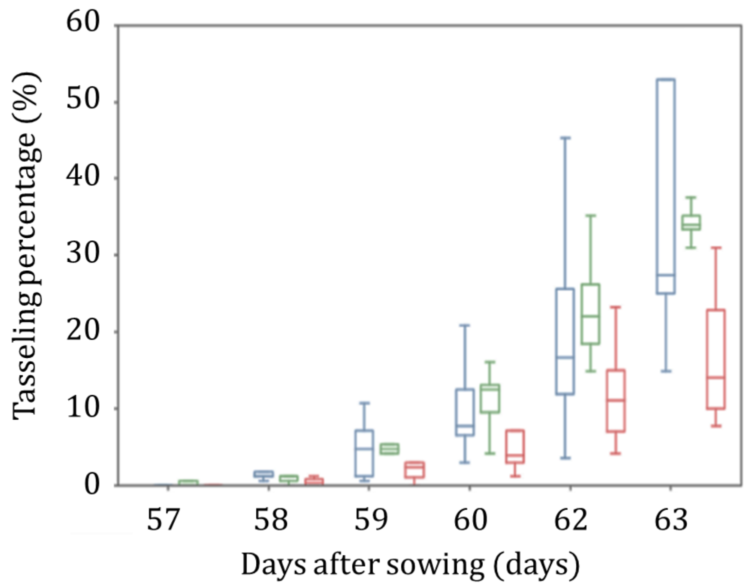


Figure 3.13: Box-whisker plot of tasseling percentage in different water treatment plots. The solid line within the box shows the median value, and the whiskers represent the top and bottom 25 percentile values.

the first tassel, the total percentage of tassels changed to 30-45%. However, for I1 plots, the total percentage of tassels changed to 10-20%. This different rate of change of tassels can play a crucial role in identifying water-stressed plots better during the tasseling stage. This rate may also be affected by pests present in the farm (e.g. even if the soil moisture is sufficient, but there is a pest in the plot, the tassel appearance rate can be less than expected). Figure 3.13 shows the box-whisker plot of temporal tassel-percentage change in the I1, I2, and I3 plots.

## 3.3 Preprocessing of hyperspectral data

Hyperspectral data from two different instruments were collected from the farm. One is based on a hand-held spectroradiometer that gives point data, and the second is a drone-based hyperspectral push-broom (line scanner) imager that gives a hyperspectral data cube for the whole farm. The wavelength range of both hyperspectral sensors was 400-1000 nm.

### 3.3.1 Spectroradiometer data

The collected spectroradiometer data (SVC GER1500, FOV 1 degree, 381 bands) had a high-frequency noise associated with it. A Savitsky-Golay filter was used to smooth the data by removing high-frequency noise. Figure 3.14 shows the raw and smooth spectra of a bright sunlit leaf, while Figure 3.15 shows a snapshot of the spectroradiometer data collection and the raw data file, which needs to be converted into reflectance values by dividing target radiance with a reference radiance. After removing high-frequency noise from the data, the spectrum was coupled with ground truth information (water content, nitrogen content and other crop information), as shown in Figure 3.7. A total of 272 leaves were analysed and stored in the dataframe, which was used for further analysis.

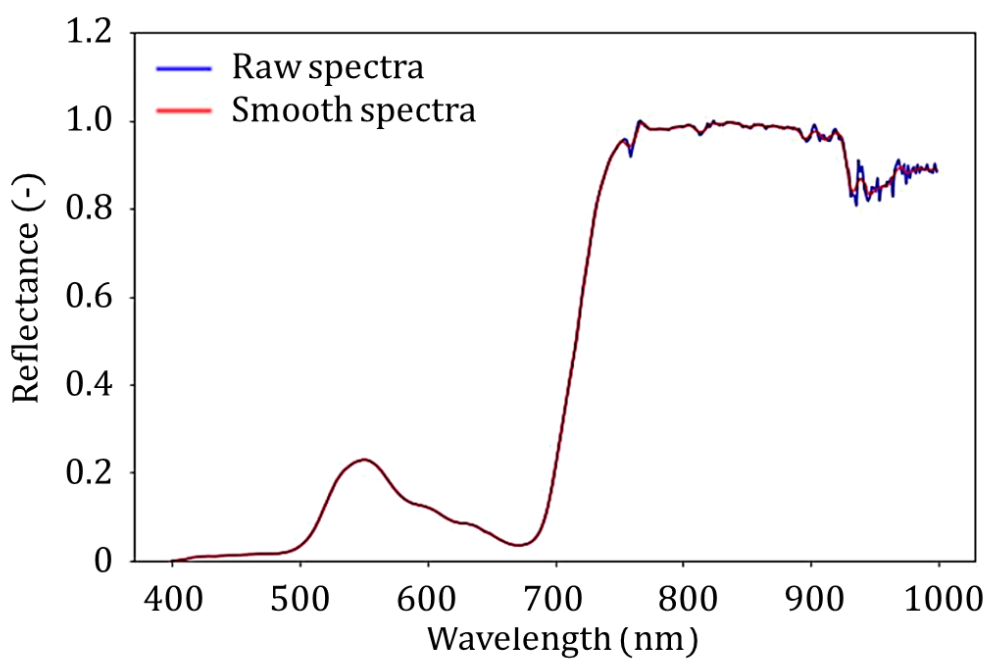


Figure 3.14: Raw spectra having high-frequency noise (majorly after 900 nm), and its smooth version after applying a Savitsky-Golay filter.

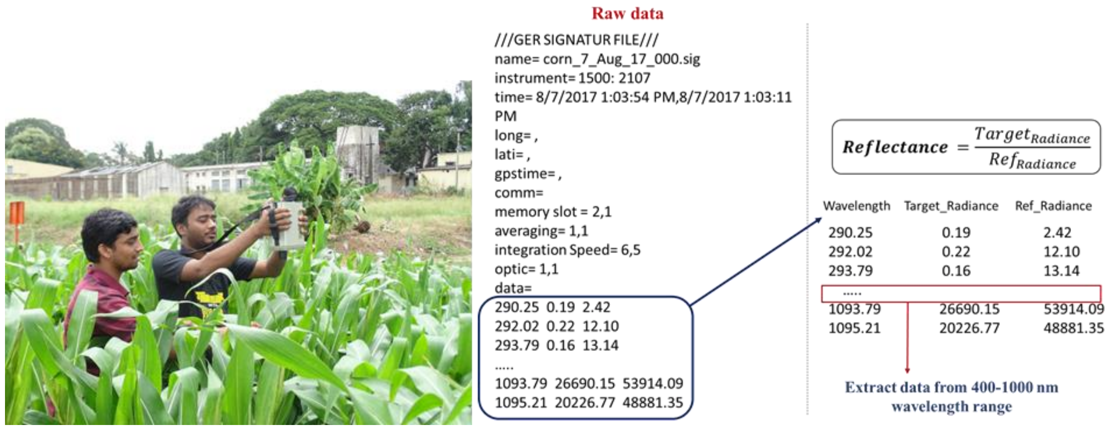


Figure 3.15: Left image is a spectroradiometer data collection snapshot, and the right-hand side text-image is raw spectroradiometer data and the reflectance formula.

### 3.3.2 Hyperspectral imager data

The hyperspectral sensor was a line scanner type from Bayspec, requiring the raw data to be preprocessed in their cube creator software. The software does orthorectification and gives a reflectance hyperspectral cube. However, the pixel radiometric values contain high-frequency noise, which needs to be corrected using the Savitsky-Golay filter. The hyperspectral data may also show some missing lines in some of the stitched tiles. These missing lines have been corrected by replacing the missing value with band-wise average values of adjacent pixels. One tile with missing lines before and after correction is shown in Figure 3.16. The Hyperspectral images were collected from a 50 m height. The flight height was determined based on the required 1.0 cm spatial resolution to ensure pure pixels are obtained in the image. Consequently, the perpendicular distance between the drone and the ground to achieve this was calculated based on the instantaneous FOV of the sensor. Figure 3.17 shows the false colour composite image of the farm and a few spectra of the selected area. As the spatial resolution of the image is in sub-cm, thus individual leaf level spectra can be extracted.

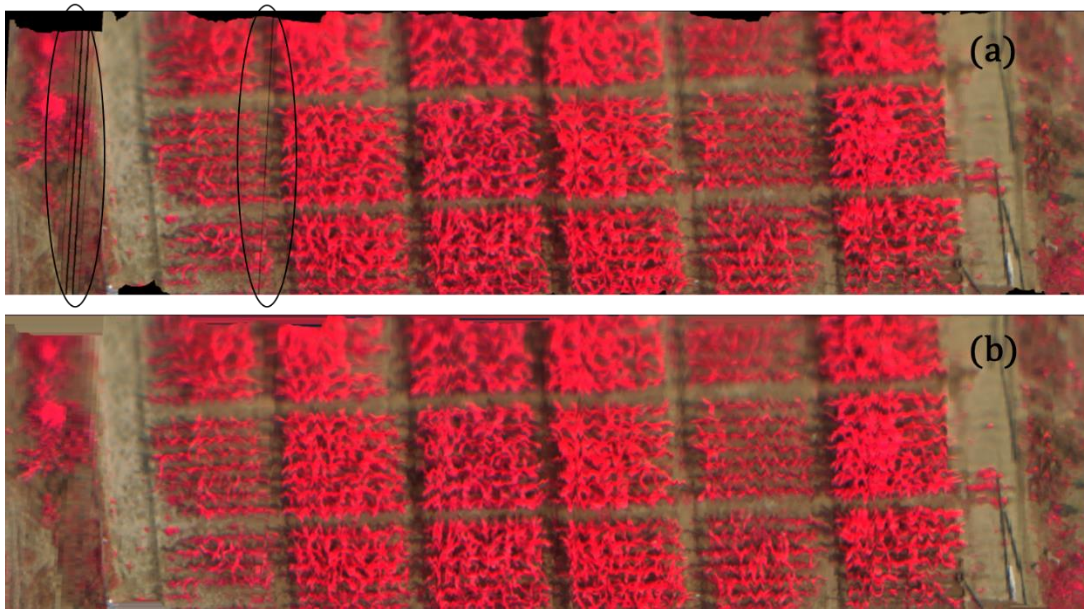


Figure 3.16: The false color composite image tile (a) showing some missing lines in the data and (b) the corrected image where all the missing lines are filled with the band-wise neighbor pixel values.

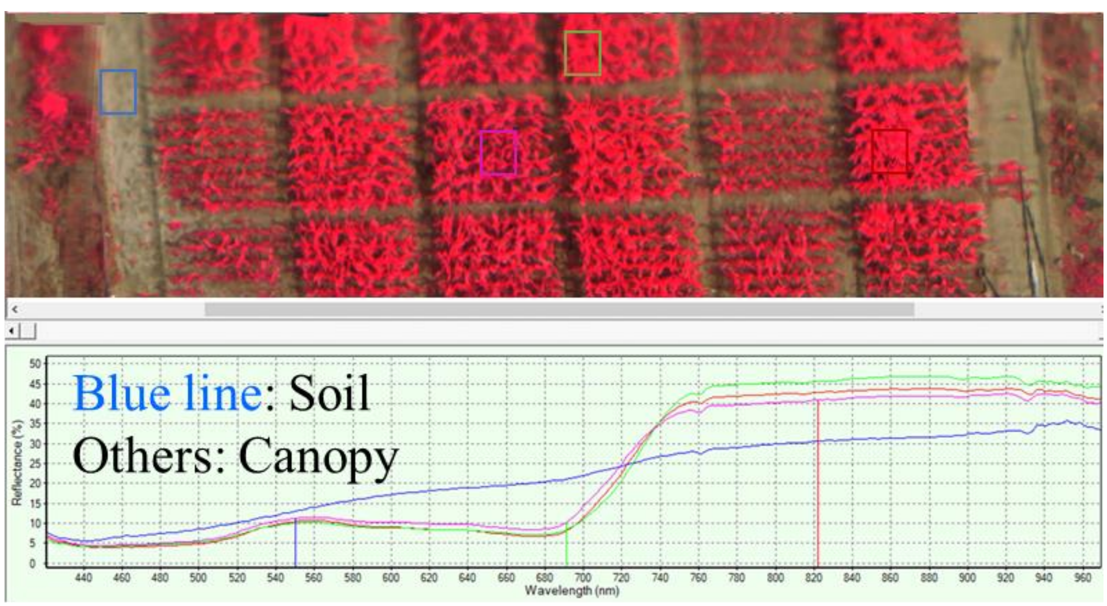


Figure 3.17: False-color composite image of the farm and reflectance spectra of some selected locations. Image is taken from 50 m height.

## 3.4 Chapter summary

This chapter presented the details of the field experiment setup and dataset used for this research, including the research farm location, ground truth and drone-based data collection, and destructive sampling steps. A graphical and statistical representation of the field details and the collected data were provided throughout the chapter. This dataset will be used to create models for estimating crop biophysical and biochemical properties as discussed in chapters four, five, and six.

# Chapter 4
# Estimation of maize biophysical parameters


*A 3-dimensional point-cloud mesh of the research farm (07th Jan 2019) created using top-of-canopy, drone-based RGB images. The mesh maps are used to develop the digital surface model of the farm.*

# 4. Estimation of maize biophysical parameters

Crop biophysical parameters like green canopy cover (GCC), crop height, LAI, and tasseling/flowering percentage are good indicators of crop growth. Deviation of these crop biophysical parameters from optimal values at any given growth stage can be used as an indication of stress present in the canopy. The top-of-canopy RGB and hyperspectral images were used to estimate various biophysical properties of the maize crop. The dataset was explained in chapter three. The airborne RGB images were processed to create an orthomosaic and DSM to obtain the GCC and the canopy height, respectively. Moreover, a vertical leaf area distribution factor *(VLADF)* was developed from ground measurements of crop architectural properties and fed as input to a new LAI estimation model to obtain effective LAI and true LAI separately. Finally, tasseling percentage of maize was calculated using one hyperspectral band images. The development of these models is discussed herein.

**Note:** Part of this chapter has been published as - Raj, R., Walker, J.P., Pingale, R., Nandan, R., Naik, B. and Jagarlapudi, A., 2021. Leaf area index estimation using top-of-canopy airborne RGB images. International Journal of Applied Earth Observation and Geoinformation, 96, p.102282.

## 4.1 Green canopy cover

The orthomosaics created by Metashape® were imported into the QGIS® software, and every subplot extracted from the respective orthomosaic using a subplot shapefile. To estimate the GCC of subplots, the subplot RGB image was first converted into an HSV (hue/saturation/value) colour space. This colour space image was used for classification based on the colour of the object. In this image type, the hue channel was used to decide the colour type; the saturation channel represented shades of that colour; the value channel represented the brightness of the colour. Using HSV images, the green pixels that represent the green-canopy were classified from each subplot as shown in Figure 4.1(a), and


Figure 4.1: (a) Image thresholding using the hue, saturation and value (HSV) method to calculate the green-canopy cover fraction, as seen from top-of-the-canopy image; and (b) digital surface model (DSM) of the plot made from 7 Jan 2019 RGB images.

the GCC fraction calculated using

$$Green\ canopy\ cover\ fraction = \frac{number\ of\ green\ pixels\ in\ a\ subplot}{Total\ number\ of\ pixels\ in\ a\ subplot}. \qquad (4.1)$$

## 4.2 Canopy height

The DSM shown in Figure 4.1(b) was used as an input to the height estimation model. This DSM was exported from Metashape as a TIFF file and imported into the QGIS® software. All the plots were cut out and analysed individually in QGIS®. The Otsu method (Otsu, 1979) was then used to separate all the pixels that represent the canopy area in individual plots. Figure 4.2 represents the process of estimating the canopy height from the cropped DSM of the individual plot. Figure 4.2a is the DSM of one of the plots (plot number 27) for 19 Dec 2018. The average of the lowest five percentile elevation in Fig 4.2a was assumed to portray the ground elevation in that plot (Fig 4.2f) using a histogram of the DSM (Fig 4.2b). Since two classes were present (canopy and ground) in the DSM, two Gaussian curves were present in the histogram. The histogram was smoothed using the probability density function (Fig 4.2c) with the elevation value at the peak of the canopy gaussian curve assumed as the threshold to classify the canopy pixels from ground pixels. An example of the classified DSM is shown in Fig 4.2d, with the average canopy elevation found by averaging all the pixel values above the T° threshold height (Fig 4.2e), and the estimated height of the canopy calculated by subtracting ground elevation from canopy elevation (Fig 4.2g). The method was applied to all the plots for all orthomosaic over the study period. This method yielded an RMSE of 10 cm for the initial growth stages and an RMSE of around 20 cm for the maturity stage. The error in estimated canopy height is considered acceptable because the ground truth height against which it was compared had a standard deviation of ~15 cm for the crop at the silking stage. The analysis result of the canopy height estimation model is shown in Figure 4.3, and estimated temporal plot height maps are shown in Figure 4.4.

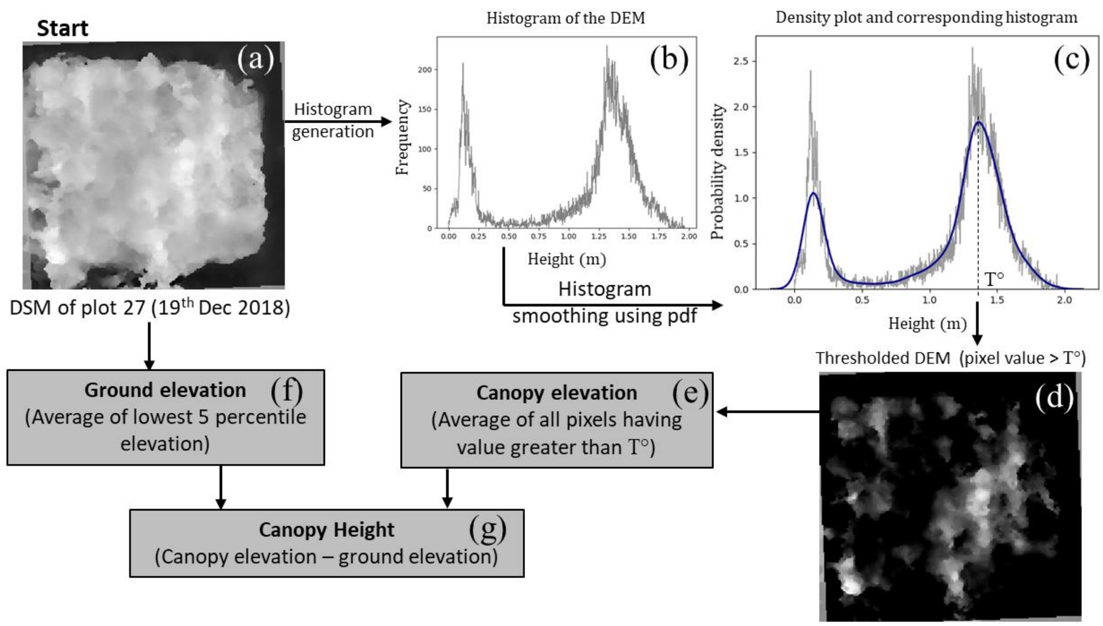


Figure 4.2: Framework for estimating canopy height from plot-level digital surface model (DSM). Histogram of the plot-level DSM is used to classify the canopy and background pixels. The height at which the peak of the canopy class is observed is selected as the threshold to separate high canopy pixels. The average of these high elevation pixels (considered as top of canopy pixels) is then subtracted from the lowest five percentile elevation pixels (considered as ground elevation) to obtain the canopy height of the plot.

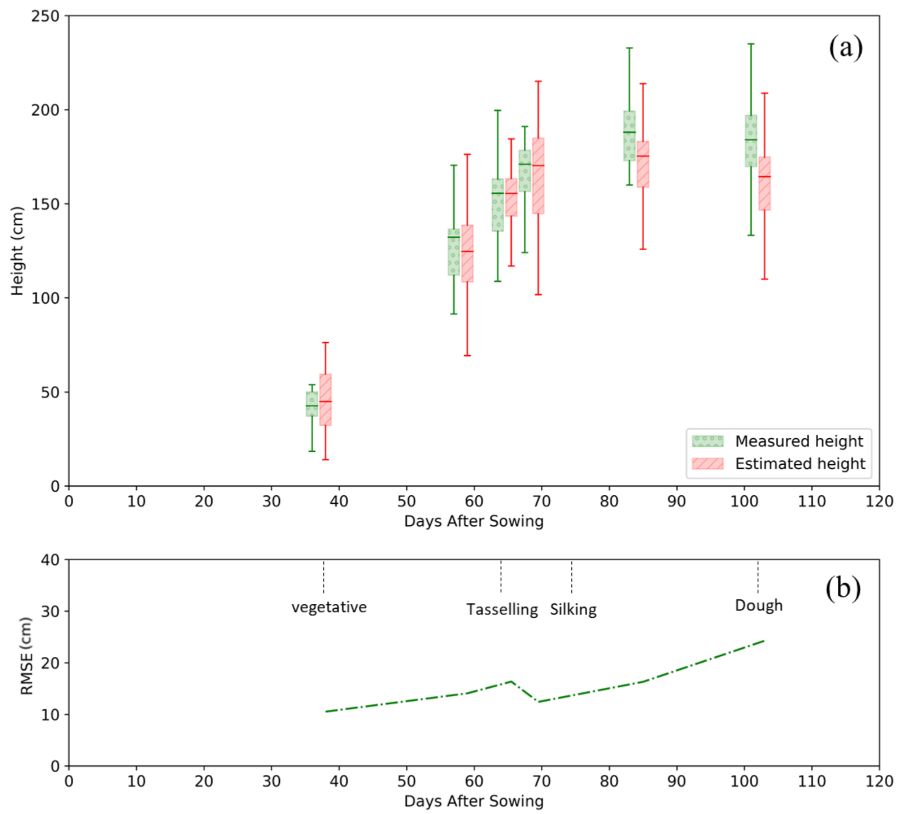


Figure 4.3: (a) Box-whisker plot of measured and estimated canopy heights where centre part (box) represents middle 50 percentile of the data set (horizontal line in the box represents median value) and whisker represents lower and upper quartile of the data and (b) RMSE of the estimated canopy height.

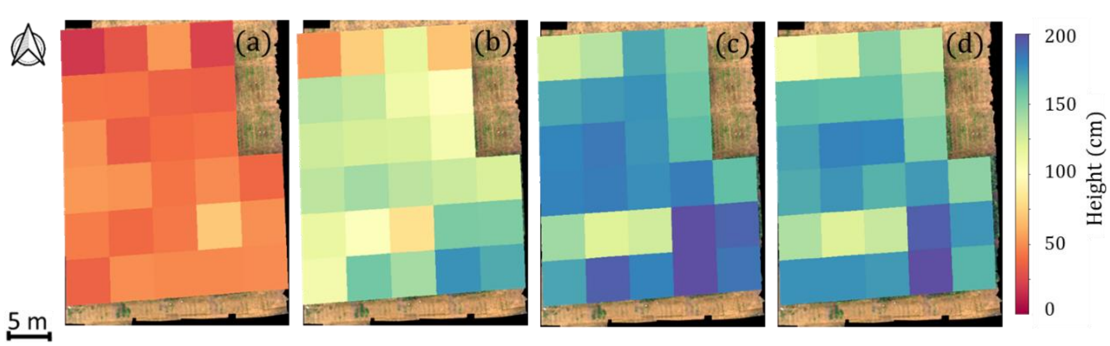


Figure 4.4: Average canopy height of plots at (a) early vegetative stage, (b) pre-tasseling stage, (c) silking stage, and (d) dough stage.

## 4.3 Leaf Area Index (LAI)

In this research, two alternate methods of LAI estimation have been developed and compared for estimating the LAI of a maize crop using top-of-canopy RGB images collected throughout the growing season using a hexacopter. Both an empirical and conceptual model are developed, with inputs of 1) height of the canopy; 2) green-canopy cover (GCC), and 3) the *VLADF*, which connects the top leaf area to the bottom part of the canopy leaf area. The empirical model was trained on the Licor 2200C canopy analyser data using a linear combination of the inputs described above. The conceptual model was developed using only *VLADF* and products derived from drone-based images, without using any training data. The framework of the research is shown in Figure 4.5. Following section will discuss *VLADF* and LAI estimation models.

### 4.3.1 The *VLADF* concept

The VLADF model developed here uses the crop sowing date and canopy height to provide a factor that relates canopy total leaf area to the top-of-canopy leaf area visible from the drone-based image. The camera that is mounted on the drone can only see the ground-projected leaf area of the top-of-canopy leaves, as illustrated in Figure 4.6. The average top leaf angle value can be used to convert this projected area into the actual top leaf area using

$$Top\ of\ the\ canopy\ leaf\ area = \frac{Projected\ leaf\ area\ (A)}{Sin\theta}. \qquad (4.2)$$

The average leaf angle value can be noted from the farm at the time of flying the drone (using a clinometer), or taken from the graph in Figure 4.7 (a), created in this research from the farm data collected during the Rabi 2018-19 and 2019-20 seasons. It should be noted that the standard deviation of the average top leaf angle at different growth stages was between 7° (for the initial growth stages) and 12° (for the later growth stages). The lengths and the widths of the leaves along with the leaf angles were calculated to determine the actual leaf area in a plant. This information was used to develop the *VLADF* and compare the estimated LAI with the actual LAI. In developing the VLADF, information about the leaf area (collected from the data of the Rabi 2018-19 season) was used to relate the top-of-canopy leaf area with the full canopy leaf area. The following steps were used to determine the VLADF:

(i) Divide the vertical profile of the plant into two sections based on the height and the age of the plant (Days after Sowing - DAS). The top section depth is decided based on the depth that is captured by the drone-based camera. The top part of the plant is denoted by T, and the bottom part is denoted by B (Figure 4.6).

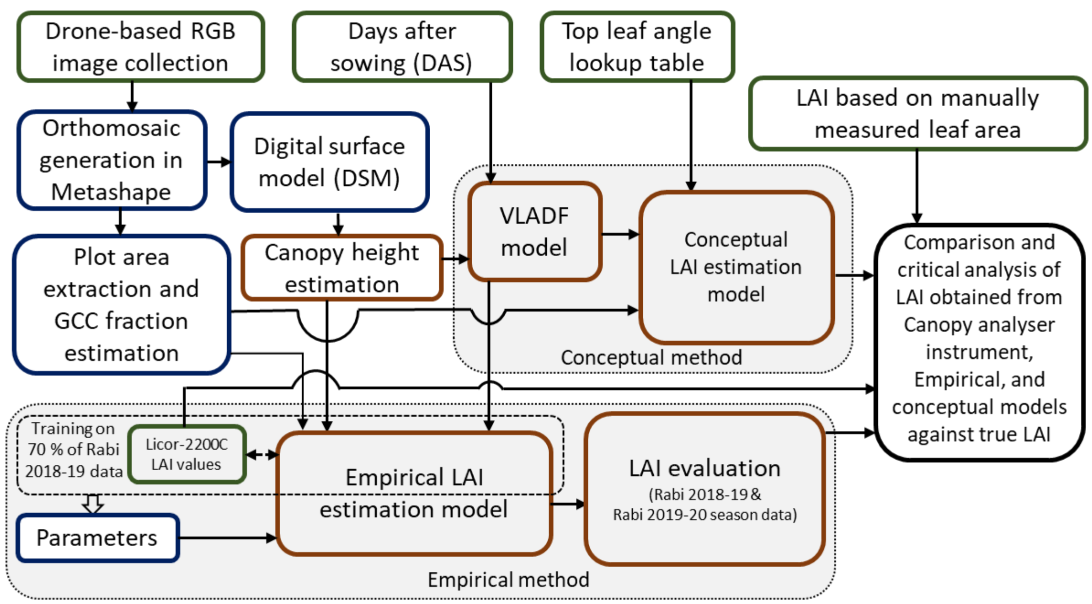


Figure 4.5: Features derived from drone-based red-green-blue (RGB) data including canopy height and green-canopy cover (GCC) together with vertical leaf area distribution factor (*VLADF*) values (a lookup-table derived from 2 years of canopy architectural properties data), are used as input to the LAI estimation models. The empirical LAI estimation model was trained with canopy analyser data, and results compared with the conceptual LAI estimation results, and with manually measured LAI from calculating the area of all the leaves.

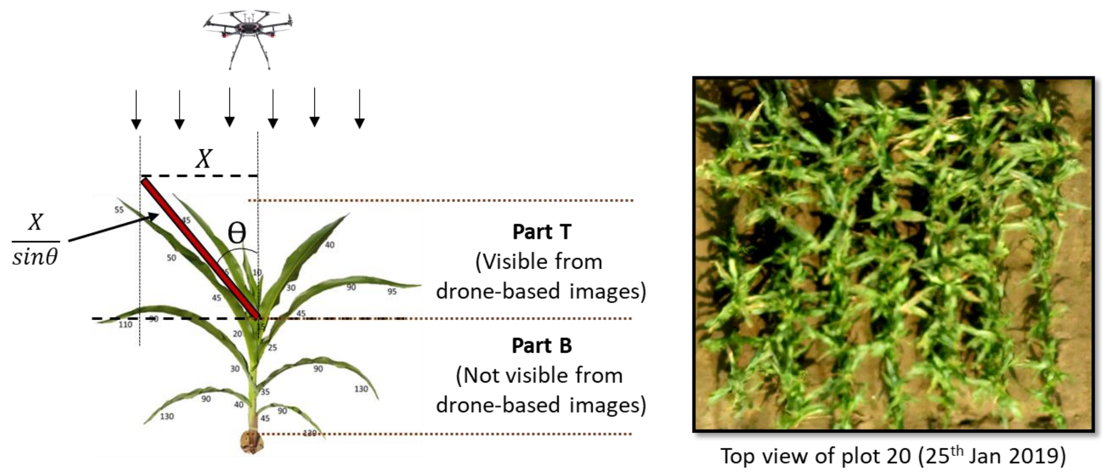


Figure 4.6: Image representing the relationship between the projected top leaf area (X) - as approximated by average of top leaves - to the actual top leaf area (X/Sinθ). The top part (T) of the canopy is visible from drone-based images, however the bottom part (B) of the canopy is not visible in the images. The complete leaf area that is based on the top section leaf area is therefore calculated by a factor which is obtained from the *VLADF*. As an example, the image to the right is a view of a plot in which the visible leaf area is the projected area.

(ii) Find the total leaf area of part T ($area_T$) and part B ($area_B$). Scale the leaf area of part T to 'one' and, accordingly, find the factor for the leaf area of part B separately for height and DAS-based analysis. The separate calculation of VLADF for height, and DAS is vital, because the same DAS plants can have different heights.

(iii) The final value of *VLADF* is obtained after averaging height and DAS based *VLADF* by using

$$VLADF_{height} = 1 + \frac{area_B}{area_T} \qquad (4.3)$$

$$VLADF_{DAS} = 1 + \frac{area_B}{area_T} \qquad (4.4)$$

$$VLADF = \frac{VLADF_{height} + VLADF_{DAS}}{2}. \qquad (4.5)$$

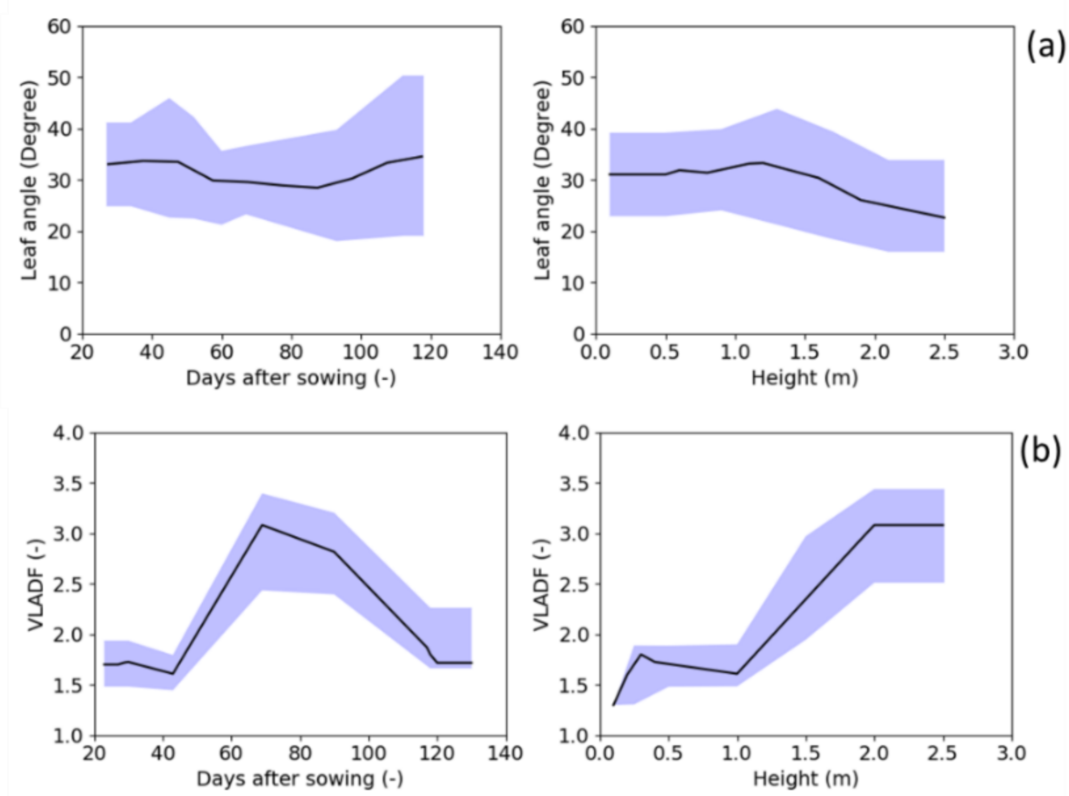


Figure 4.7: (a) Top-of-canopy average leaf angle based on the days after sowing (DAS) and the canopy height; (b) A *VLADF* graph based on the DAS and the canopy height. The graphs are used as lookup table to find the average *VLADF* factor for a canopy which is based on height and age of the crops. The shaded area represents variability of the values within 75% confidence limits as approximated by $\pm 1.15 * SD$ of the dataset.

The *VLADF* values used were from a lookup table based on the graph shown in Figure 4.7 (b) (created from the data of 2018-19 Rabi season). If the DAS is known, it can be directly used in the model; otherwise, techniques such as those explained in Sadeh et al. (2019) can be used to estimate the DAS information.

The input of DAS to the *VLADF* model acts as a proxy indicator of the growth stage of the crop. The *VLADF* model also incorporates the fact that canopies in the same growth stage can be of different heights with different vertical leaf area distributions. Therefore, the average of the height and the DAS-based factors is taken as the *VLADF* value to be used. The *VLADF* model can be used for all maize cultivars having similar growing degree day (GDD) characteristics. To further improve the model, DAS could be replaced with GDD. However, in that case, the farm-level diurnal atmospheric temperature is required to calculate the GDD.

### 4.3.2 Empirical model

The empirical LAI estimation model developed in this research used the estimated canopy height, GCC, and the VLADF as input. These three inputs capture all of the physical parameters that can impact the LAI of the canopy. However, the contribution of GCC to the model is insignificant when the top-of-canopy leaf area is saturated due to canopy closure. The contribution of the canopy height is also minimal when the canopy reaches its maximum height for similar reasons. Accordingly, most of the existing models cannot perform well when these two parameters achieve their maximum limit and values do not change much with further crop growth. The addition of the VLADF input to LAI estimation was hypothesized to improve the performance as VLADF incorporates the changes that occur inside the canopy, which cannot be captured from the airborne imagery of the top of the canopy. The framework of the LAI estimation model has already been shown in Figure 4.5.

The model was trained to the Licor 2200-C LAI using a linear regression on 70 % of the Rabi 2018-19 data (randomly sampled from every growth stage), tested on the remaining 30 % of the Rabi 2018-19 data, and validated on the data from the Rabi 2019-20 season. The resulting model was

$$LAI_{empirical} = 1.15 * GCC + 0.74 * Canopy_{height} + 0.78 * VLADF - 1.29, \quad (4.6)$$

where $LAI_{estimated}$ is the model output, $GCC$ is the fraction of the green-canopy cover, $Canopy_{height}$ is the estimated canopy height from the DSMs of the farm and $VLADF$ is vertical leaf area distribution factor.

### 4.3.3 Conceptual model

In contrast to the empirical model, the VLADF values were also used to independently calculate the LAI using the following conceptual construct

$$LAI_{conceptual} = VLADF * (Top\ of\ the\ canopy\ leaf\ area) = \frac{VLADF * GCC}{sin(\Theta)}, \quad (4.7)$$

where Θ is the average top leaf angle of the crop, which can be taken from Figure 4.7 (a) or measurements at the time of flying the drone. Here, *VLADF* is a multiplication factor which relates the top-of-canopy leaf area to total leaf area, dependent on DAS and canopy height. The top-of-canopy leaf area in this conceptual model is derived from GCC, being the horizontal projection of the leaf area as seen from the drone camera (Figure 4.6). The actual top-of-canopy leaf area is obtained from the plant geometry by dividing GCC with the sine of the average leaf angle. Once the actual leaf area of the top-of-canopy is estimated, it is multiplied by the *VLADF* to obtain the full canopy leaf area. This method was tested against the one-time true leaf area index measurements of the nine plots (combination of three different levels of irrigation and fertiliser treatments).

### 4.3.4 Results and discussion

The VLADF relationships developed from the Rabi 2018-19 crop structural parameters data were evaluated for the Rabi 2019-20 season data, using the detailed plant structural parameters recorded from the nine sub-plots at 93 DAS of the Rabi 2019-20 season crop. The height of the nine sub-plot canopies ranged between 138 cm and 219 cm. Based on the estimated height and the DAS of these nine plots, VLADF was calculated using the relationships in Figure 4.6. The region between higher and lower limit lines (Figure 4.8) show the '(model VLADF)$\pm$(1.15*SD)' region for 93 DAS. The multiplier value of '1.15' was used to represent a confidence interval of 75 %. Only one value was substantially outside the expected range with all other plots within an acceptable range.

The empirical LAI estimation correlated with the LAI values of the canopy analyser with a coefficient of determination ($R^2$) that equals 0.84 and 0.77, and an RMSE of 0.36 and 0.45 on the test (30 % of Rabi 2018-19 data) and the validation (Rabi 2019-20 data) data, respectively. These RMSE values can be considered low because the canopy analyser instrument itself has a standard deviation of 0.2 for the same location data (calculated by taking repeated canopy analyser readings from the same location). A slight overestimation of the LAI for the early growth stage of the crop and an underestimation for the late growth stage of the plants was also found (Figure 4.9).

This deviation from the true values is better than the results of other published models, including Delegido et al. (2013), which used the spaceborne red-edge index to estimate LAI of multiple crops, including maize, with an $R^2$ of 0.82 and RMSE of 0.6 when compared with Licor LAI-2000 values. While Haboudane et al. (2004) achieved a similar level of accuracy, they used the more costly drone-based hyperspectral data to estimate LAI with a modified triangular

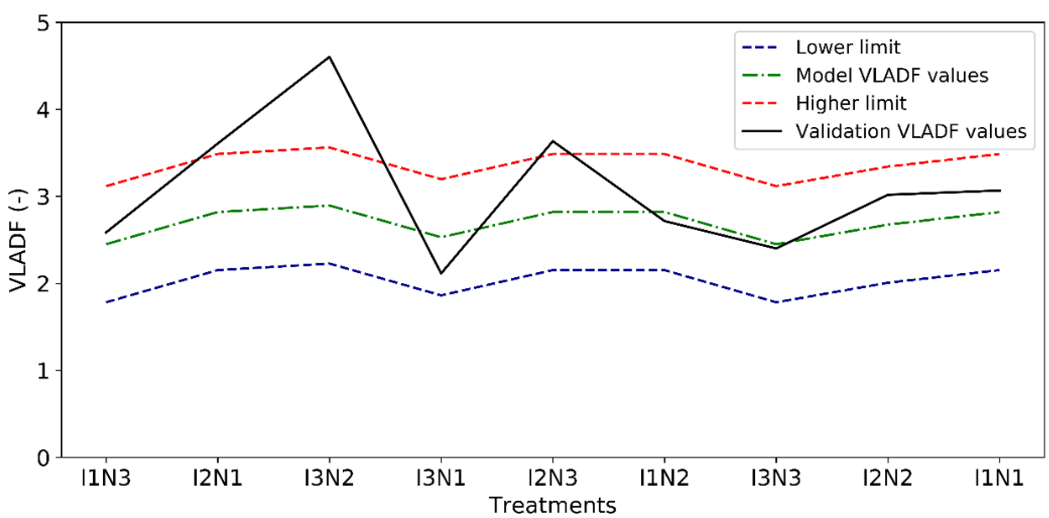


Figure 4.8: Evaluation result of the *VLADF* model for canopies at 93 days after sowing with different canopy heights. The model performance was found to be within the tolerable limit.

vegetation index (MTVI2) and modified chlorophyll absorption ratio index (MCARI2) developed from empirical analysis of the PROSPECT and SAILH models; an $R^2$ of 0.89 and RMSE of 0.46 was achieved for maize crop for the same season data. Moreover, Jay et al. (2017) achieved an $R^2$ of 0.89 and RMSE 0.23 for sugar beet crop for LAI estimation till the vegetative stage, using an index based approach with UAV-based multispectral data, when considering the same growth stage the research presented in this paper for maize crop achieved an $R^2$ of 0.91 and RMSE 0.29. When using the more complex PROSAIL inversion model for LAI estimation, Jay et al. (2017) only achieved an $R^2$ between 0.68 - 0.81 and RMSE of 0.39 - 0.72. While the empirical model presented here has shown comparatively good results relative to other studies when evaluated with Licor canopy analyser data, comparison with the true LAI values showed a coefficient of determination of only 0.56 and an RMSE of 1.34 (Figure 4.10(b)).

In contrast, the conceptual LAI estimation correlated with the true LAI from measurements yielded an improved coefficient of determination of 0.59 with an RMSE of 0.73. These results can be contrasted with the allometric model of Colaizzi et al. (2017), which used a calibrated log-normal function by considering cumulative growing degree days, canopy height, and plant population as model inputs. The inputs were collected through field sensors and manual field observations. Using destructive sampling to calculate the true LAI of the canopy, an $R^2$ of 0.54 and RMSE 1.14 was achieved for maize crop LAI.

As shown in Figure 4.10(c) Licor-based LAI values seem reliable only until the vegetative stage of the crop, being when the LAI of the canopy is low. Once the LAI of the canopy increases above 4, the Licor-based measurements of LAI start saturating. Similar observations were noted by Smith et al. (1993) and Cutini et al. (1998) where the LAI 2000 canopy analyser consistently underestimated canopy LAI. This problem of under-prediction is majorly due to the assumption that leaves of the canopy are randomly distributed, which is not valid in many cases (Breda, 2003; Gower et al., 1999). However, it should also be noted that LAI estimated from Licor-2200C measurements represent the foliage area index, which gets affected by stem and other non-green plant elements. In contrast, the conceptual LAI model proposed here considers only leaf area, thus more correctly representing the true leaf area index. The temporal LAI map is shown in Figure 4.11.

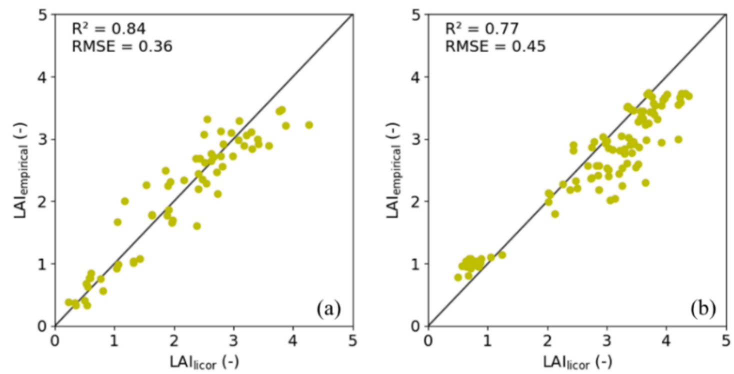


Figure 4.9: Scatterplots representing the results of the empirical LAI model on (a) test (30 % of Rabi 2018-19) and (b) validation (100 % of Rabi 2019-20) data.

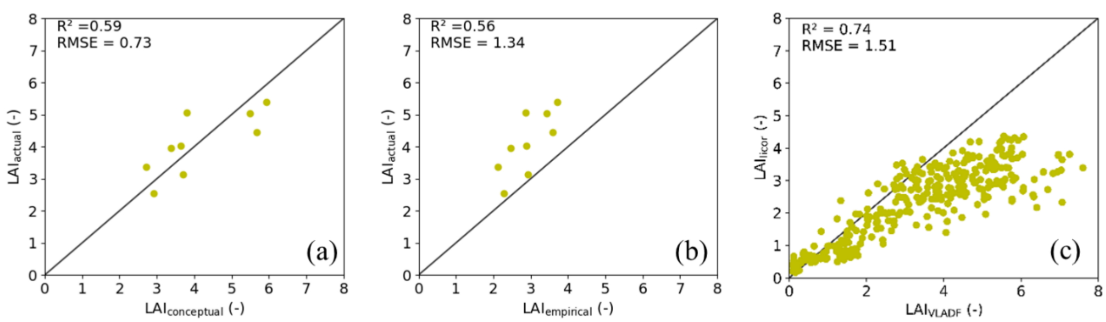


Figure 4.10: Comparison of the LAI estimates from the (a) conceptual $LAI_{conceptual}$ against manual measurements $LAI_{actual}$; (b) Empirical $LAI_{empirical}$ against the manual measurements $LAI_{actual}$ and; (c) Empirical $LAI_{empirical}$ against the conceptual $LAI_{VLADF}$.

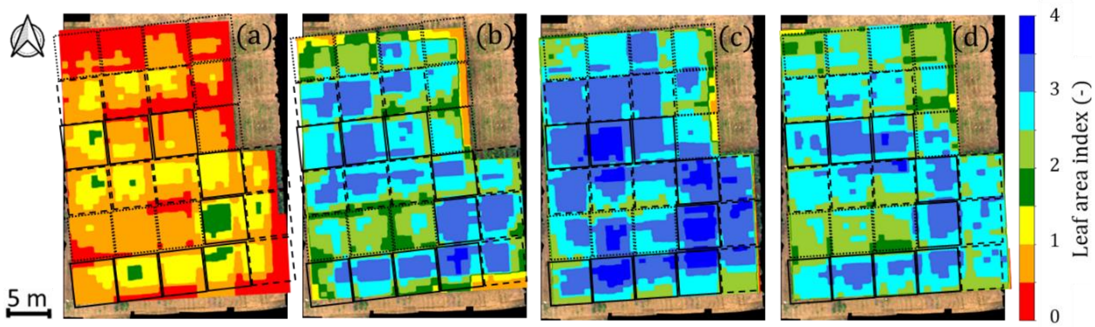


Figure 4.11: Estimated canopy LAI at (a) early vegetative stage, (b) pre-tasseling stage, (c) silking stage, and (d) dough stage. Solid line boxes represent sufficiently irrigated plots, dashed line boxes for moderately irrigated, and less irrigated plots are shown with dotted line boxes.

## 4.4 Maize tassel counting

Tasseling stage is one of the critical growth stages of maize, with the number of tassels having a positive relationship to the grain yield (Guei and Wassom, 1996). Moreover, water stress in the crop affects the appearance of tassels in the plant (NeSmith and Ritchie, 1992). It has been observed that water stress in the crop also delays the tasseling stage in maize (Cakir, 2004). The information of tasseling percentage at the early tasseling stage can be used to identify water stress areas in the farm. Thus, tassel counting is one of the topic of intersest in precision agriculture. Kurtulmus et al. (2014) acquired 46 ground-based hand-held RGB images of corn tassels and used computer vision and support vector machines to detect maize tassels, with an achieved 86.8% accuracy. Zadjali et al. (2020) acquired high-resolution UAV-based RGB images to locate maize tassels using the Faster-R-CNN based deep learning model, where they achieved a mean average precision of 91.78% and F1 score of 97.98%, with a recall of 98.32%. Liu et al. (2020) also implemented a Faster R-CNN model on high-resolution UAV-based RGB images collected from a 15-meter height, with different feature extraction techniques in the model and results similar to Zadjali et al. (2020).

Considering the importance of this biophysical parameter, tassel identification and counting were done in this research. The objective was to use a simple model which can reach the accuracy to data intensive deep learning techniques. Accordingly, a single-band of drone-based hyperspectral data was identified, and tassel counting was done using image processing techniques. However, various techniques are available in which deep learning techniques like YOLO, Resnet, etc. are implemented to count the number of tassels from drone-based RGB images (Kumar et al., 2019; Liu et al., 2020). The ground-truth data for the actual number of tassels in different treatment plots were recorded on a daily basis after the appearance of the first tassel in the plot, as explained in chapter 3.

Data exploration of the hyperspectral band images was done, and it is found that a narrow wavelength region around 701 nm gives the highest contrast between tassel pixels and canopy pixels. In the 701 nm band image, the tassels appear bright, and the rest of the canopy appears dark. The maize leaves at the tasseling stage have high chlorophyll content, which increases the photosynthetic activities resulting in higher absorption around 701 nm wavelength (Gitelson et al., 2001; Cinque et al., 2000). However, the maize tassels have a higher amount of anthocyanin present in them (Duangpapeng et al., 2018). The anthocyanin shows extremely low absorption around the 701 nm wavelength resulting in higher reflectance (Gitelson et al., 2001; Gallik, 2012; Merzlyak et al., 2012; Duangpapeng et al., 2018). This difference in reflectance creates a high contrast between tassel pixels (bright) and all other pixels (dark).

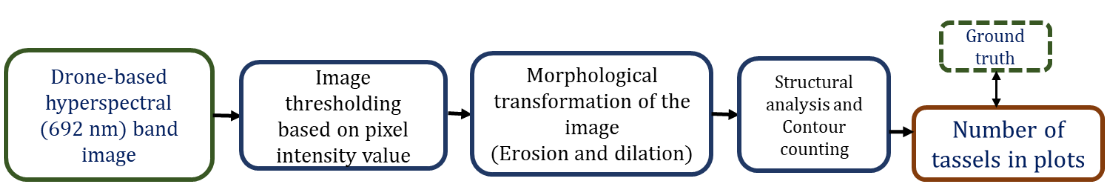


Figure 4.12: Tassel counting estimation model using drone-based hyperspectral single band image.

This property was used to classify all the bright pixel in the image using the blob detection method.

Figure 4.12 shows the framework of the model used to count the number of tassels. The 692 nm band image is divided into 27 parts as per the treatments given on the farm. This was done to compare the ground truth information with the model output. Every plot image was thresholded based on intensity value, and then morphological operations like erosion and dilation of the image pixels were done to nullify the effect of small parts of the same tassels and to combine all the close proximity bright spots in one big spot (when a tassel opens then it makes 5-6 bright spots in the image at in very close proximity. All these bright spots transforms into one with erosion and dilation). Contour mapping and counting of contours on the dilated image resulted in the counting of the number of tassels present in every plot. A sample band image (701 nm) and tassel counted image is shown in Figure 4.13.

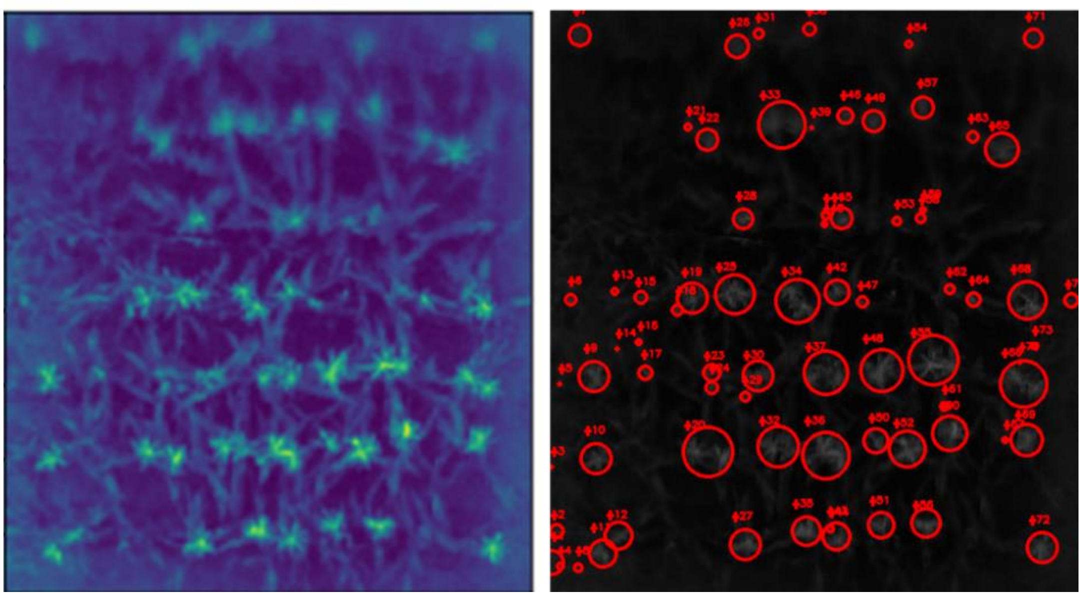

Figure 4.13: Single-band (701 nm) image of the maize canopy (Left) and tassels detected by counting contour method (Right).

Table 4.1: Performance measure statistics of tassel counting algorithm.

| Measure | Value (percentage) |
|---|---|
| Precision | 97.7 |
| Recall (Sensetivity) | 89.2 |
| False Positive Rate (FPR) | 00.7 |
| False Negative Rate (FNR) | 10.7 |
| Accuracy | 96.4 |
| F1 | 93.2 |

The results were analysed and compared with ground truth data with the actual count of tassels at 71 and the detected number of tassels at 73 (Figure 4.13). There were a total of eight incidents where two nearby tassels were counted as one, eight incorrect tassels detected, and two tassels missed by the algorithm. Similar results were obtained for all the plots. Precision, recall, false-positive rate (FPR), false-negative rate (FNR), accuracy and F1 score were calculated and shown in Table 4.1. Higher accuracy confirmed the good classification accuracy of the algorithm.

## 4.5 Chapter summary

This chapter discussed the methods to obtain maize crop biophysical properties like green canopy cover (GCC), crop height, leaf area index (effective and true), and tasseling percentage. The GCC, canopy height, and LAI was obtained using drone-based RGB images, and the results of canopy height and LAI validated against ground-based measurements. A new method called the vertical leaf area distribution factor (VLADF) was introduced in this chapter and used to estimate near-to-true LAI values. The LAI model has shown better performance than other existing models in literature, especially for early growth stage crop where other models fail to perform. Tassel counting was also undertaken in this chapter using one band of drone-based hyperspectral image bands. An image processing technique was applied to count the tassels from the image and showed high accuracy. These crop biophysical parameters were used for crop stress area identification, as explained in chapter five.

*This page has intentionally been left blank.*

# Chapter 5

# Crop stress estimation using biophysical parameters

*Field data collection is always labour intensive and time-consuming. A model which can remotely estimate the required crop parameters and inform about the crop health is need of the hour. This chapter suggests such a technique which will allow users to do so. The image shows the author collecting crop LAI using a canopy analyser instrument.*

# 5. Crop stress estimation using biophysical parameters

The biophysical properties of a crop are a good indicator of potential crop stress conditions. However, these visible properties cannot indicate the non-visible stress areas e.g. early water or nutrient stress. In this chapter, the biophysical properties estimated in chapter four have been used to predict crop stress level. Accordingly, canopy height, LAI, and tasselling percentage were used to identify areas that are not growing as expected for a healthy crop. First, the APSIM model was used to simulate temporal LAI and canopy height under optimal management conditions, and thus used as a reference for estimating healthy crop parameters. The temporal LAI and canopy height estimated in chapter four were then compared with the simulated reference values using a linear and random forest model. While these methods can identify stress and non-stressed areas, they cannot indicate the reason behind the stress. These stress areas were further investigated for water and/or nitrogen stress using the models build in chapter six.

## 5.1 Selection of APSIM model

"All models are wrong, but some are useful" is a popular quote by British statistician George E. P. Box. Various models are available for simulation of crop behaviour and agricultural production, including APSIM, DSSAT, MLCan, and WOFOST. These are process-based crop simulation models with some pros and cons. For example, the DSSAT height estimation module is insensitive to change in weather and management practices and thus needs field-based calibration data (Jones et al., 1998). Moreover, the MLCan model does not give crop height as an output. Therefore, the APSIM (Agricultural Production Systems sIMulator) model was used here to simulate crop growth under actual farm weather and different irrigation and fertilisation conditions with similar soil properties. Temporal values of crop LAI, canopy height, and soil moisture of all the plots were simulated and used as a reference to compare with actual farm data. Figure 5.1 shows the application of APSIM to this research. The main objective behind the use of the

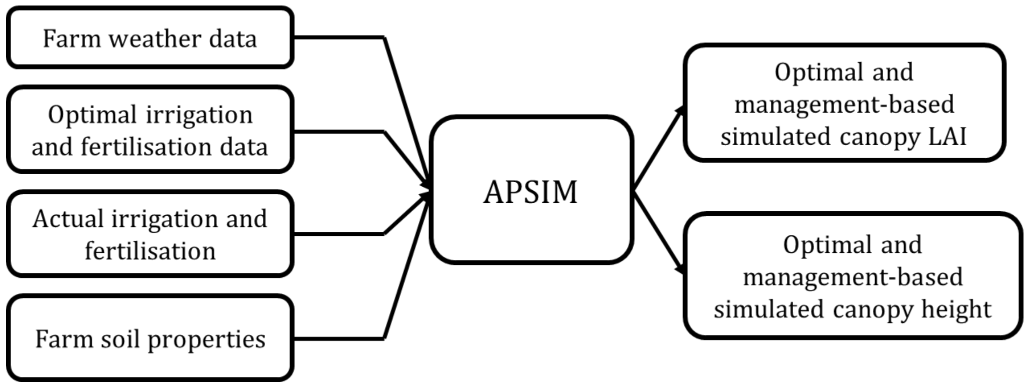


Figure 5.1: APSIM model input and output data.

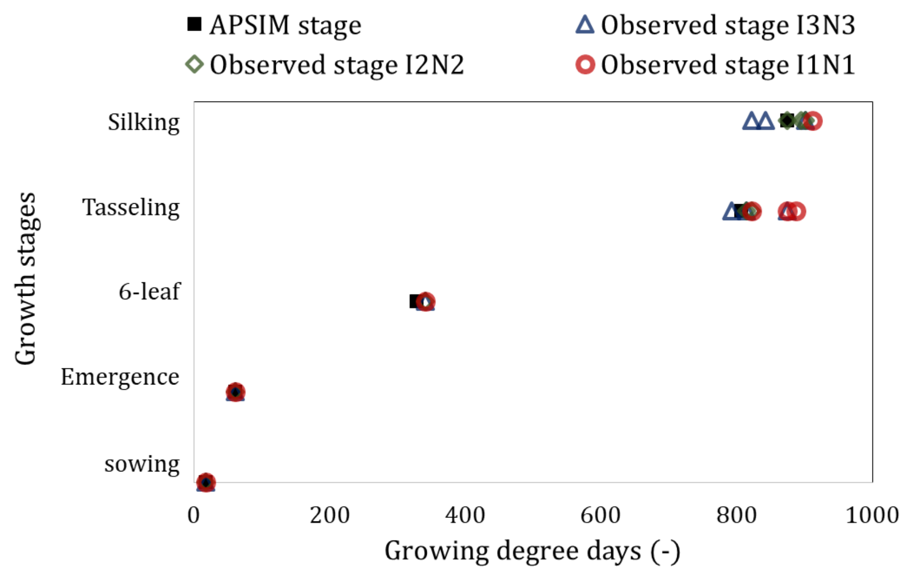


Figure 5.2: Growing degree days (GDD) based growth stage occurrence from APSIM simulations and observed farm data (triplicate) for the 'mh12' seed variety. The soil and weather properties were taken as per recorded farm conditions.

APSIM model was to get reference/optimal values for crop biophysical parameters. The reference values were used to compare the observed parameters for further analysis.

## 5.2 Selection of seed variety

The maize seed variety used for farming was 'Cargil 900m gold'. However, the same maize seed variety was not available in APSIM. To select a seed variety from available options, a comparative analysis of growing degree days (GDD), and LAI of various varieties with respect to farm observed responses were made. The 'mh12' seed variety was found to give the closest response to the field observed data and thus selected for further analysis. Figure 5.2 shows the growth stage occurrence with respect to change in GDD for APSIM simulation at the 'mh12' maize variety. The GDD difference between simulated and observed growth stages were less than 100 for tasseling and silking stages. The differences were negligible for the emergence and 6-leaf stage. Other data used for APSIM simulation is presented in Appendix 7.

## 5.3 LAI and canopy height simulation

The LAI and canopy height of maize were simulated in APSIM for various management conditions (as shown in table 3.2 of chapter three), with output compared against the observed LAI and height values of respective treatment plots. It was found that the APSIM model was insensitive to changes in LAI and height during the initial growth stage but gave better results as it moved towards the maturity stage. Figure 5.3 shows the simulated and observed canopy LAI values, with the simulated initial growth stage LAI being always remained equal to optimal condition simulated LAI. However, the simulated height was found to be underestimated compared to the observed farm values for all scenarios. Figure 5.3 and 5.4(a) show the comparison of simulated and observed crop LAI and height, respectively. The problem of canopy height underestimation was resolved by updating the height values proportional to the rate of change of LAI until the canopy closure stage. This was done because there was a high correlation between canopy height and LAI. Thus, the rate of change of canopy height was expected to follow a similar trend as canopy LAI. The updated canopy height graph is shown in Figure 5.4 (b).

The simulation of optimal values was obtained by maintaining the simulated soil moisture above 70% of the field capacity. The APSIM simulated temporal LAI and updated canopy height for optimal irrigation and fertilisation conditions have shown the capacity to be used as reference LAI and height values.

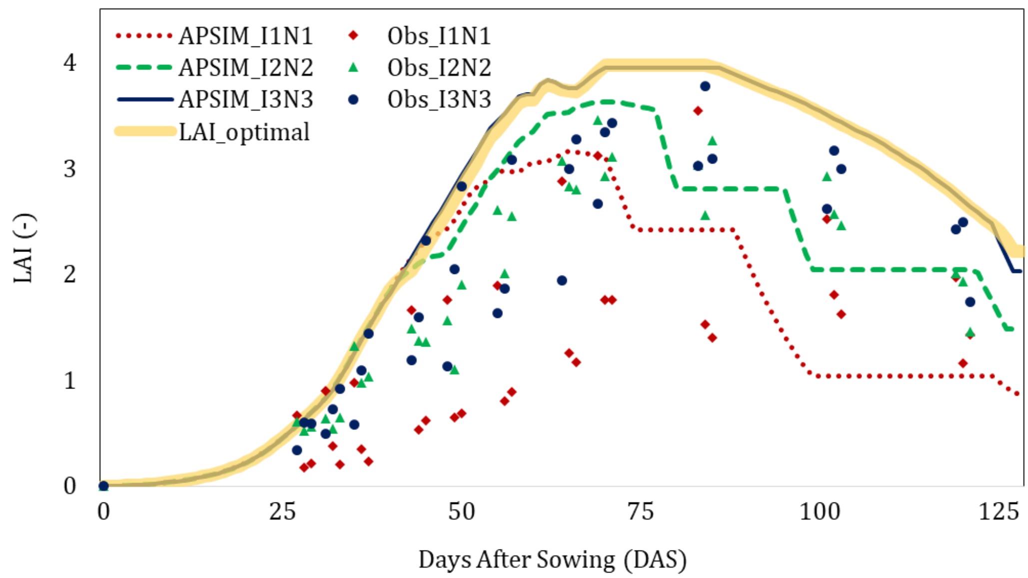


Figure 5.3: Simulated and observed temporal LAI of different treatment plots. The model seems to be insensitive during the initial growth stage and remains at optimal values even for low irrigation and low fertilization treatment plots.

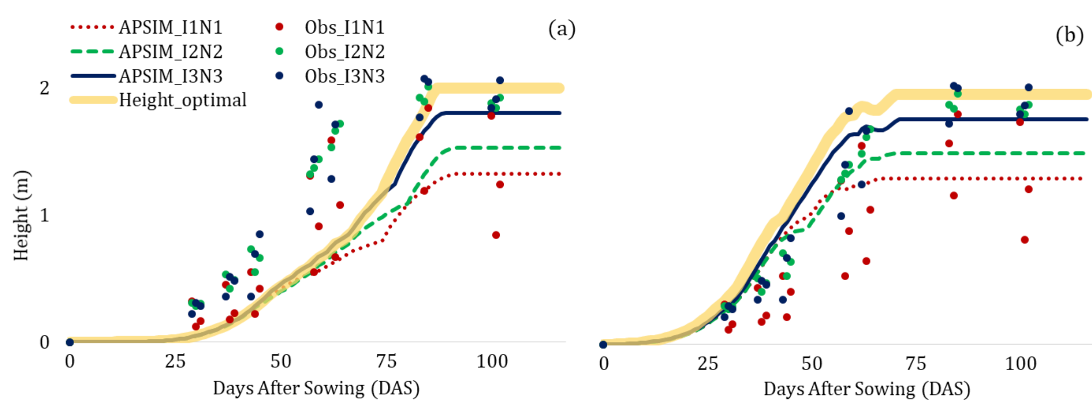


Figure 5.4: (a) Simulated and observed temporal canopy height for different treatment plots, with the model highly underestimating the canopy height until the tasseling/silking (canopy closure) stage. (b) Canopy height output after updating the height values proportional to the rate of change of LAI until the canopy closure stage.

## 5.4 Crop stress detection

Crop water and/or nutrient stress results in crop yield reduction. To minimise this reduction, identification of stressed areas are important, as crop stress directly affects plant growth. Crop biophysical parameters like LAI and height are reduced depending on the severity of the stress. This reduction becomes more visible when the crop passes the vegetative stage. For crops that are provided three times less irrigation than required, the yield was reduced by around three times, and observed crop LAI and height were reduced to around 55% and 70% of optimal values, respectively. A similar reduction in LAI and height values were also seen in the APSIM simulated results for late growth stages, as shown in Figure 5.3 and Figure 5.4. It is evident that the APSIM simulation result for early crop growth stages is not sensitive to management practices. However, the optimal condition simulated values can be used as reference. Moreover, the simulated results for late growth stages are close to the field observed values, making the model results useful. The framework of this study is shown in Figure 5.5. The

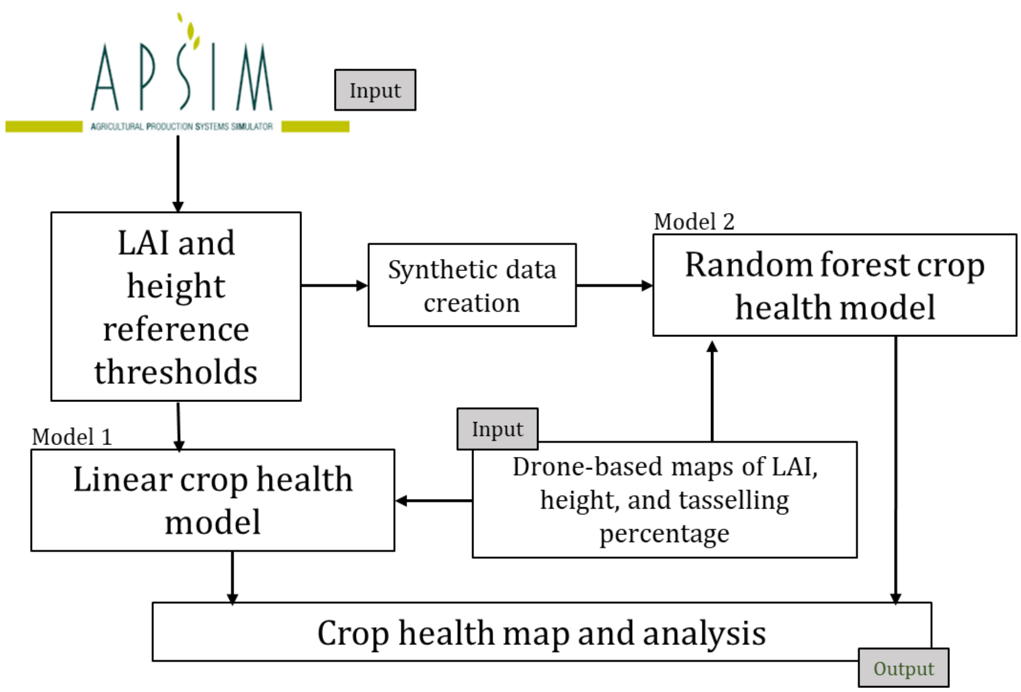


Figure 5.5: Framework of crop stress detection model using drone-based crop biophysical properties and APSIM-based simulations.

APSIM simulated LAI and height results have been used in two different models to predict the stress levels of the plot. The first method used a linear approach, while the second method used the Random Forest algorithm.

### 5.4.1 Linear model

In the linear approach, three inputs - LAI, height, and tassel percentage information, were used to predict the crop stress level using $Healthiness\ Index$. $Healthiness\ Index$ should be taken as an indicator to classify the crops based on their biophysical parameters (LAI, height, and tasselling percentage). This index will be used to highlight the areas having low Healthiness Index indicating high chances of the crop being stressed. For any growth stage before tasseling, only LAI and height information were used, and for any growth stage after tasselling, tasselling percentage information was also added in the model along with LAI and height. Two thresholds have been created to decide the stress levels in the crop. If the observed (drone-based) LAI and height values are around APSIM simulated optimal values, it is considered a healthy crop. However, the plots were considered severely stressed if the observed values were equal or less than 0.55 and 0.65 times of simulated optimal LAI and height, respectively. For tassel percentage-based predication, 45% tasseling within one week of onset of tassel was considered as an optimal condition (healthy crop), with and tasselling percentage less than 10%, regarded as severe stress condition. All observations in between optimal and stressed levels were linearly scaled. The thresholds are given in Table

Table 5.1: Stress and healthy plots thresholding criteria for $Healthiness\ Index$ creation.

<table>
<tr><th>Parameter</th><th>Healthy condition</th><th>Severe stress condition</th></tr>
<tr><td>LAI</td><td rowspan="2">APSIM simulation value at optimal management condition ($APSIM_{optimal}$)</td><td>$0.55 * APSIM_{optimal}$</td></tr>
<tr><td>Canopy height</td><td>$0.65 * APSIM_{optimal}$</td></tr>
<tr><td>Tasseling percentage</td><td>45% of the total number of plants</td><td>10% of the total number of plants</td></tr>
</table>

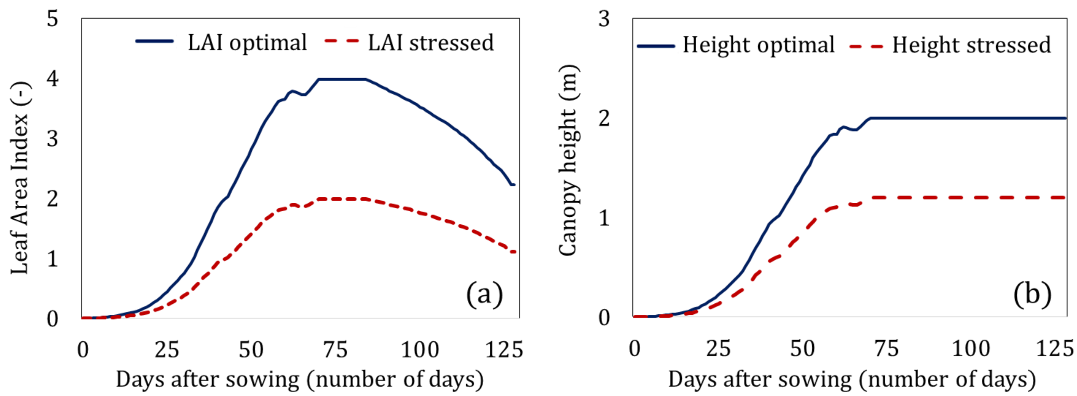


Figure 5.6: (a) Simulated optimal canopy LAI and 0.55 times optimal values indicating stressed canopy LAI. (b) Simulated optimal values of temporal height and 0.65 times of optimal values are indicating stressed canopy height values.

5.1. Figure 5.6 shows the optimal and stressed levels of the temporal height and LAI. The formulae used to predict the healthiness/ stress level using $Healthiness\ Index$ of the plots for the pre-tasseling stage

$$Healthiness\ Index_{pre-tasseling} = \frac{LAI_{pred} + Height_{pred}}{2}, \qquad (5.1)$$

and for the post-tasseling stage

$$Healthiness\ Index_{post-tasseling} = \frac{LAI_{pred} + Height_{pred} + Tassel_{pred}}{3} \qquad (5.2)$$

Where,

$$LAI_{pred} = 2 * \frac{LAI_{observed}}{LAI_{optimal}} - 1, \qquad (5.3)$$

$$Height_{pred} = 2.5 * \frac{Height_{observed}}{Height_{optimal}} - 1.5, \qquad (5.4)$$

$$Tassel_{pred} = \frac{Tassel_{observed} - 10}{35}. \qquad (5.5)$$

Here, $LAI_{observed}$, $Height_{observed}$, and $Tassel_{observed}$ are the remotely sensed values of LAI, height, and tassel percentage of the crop, respectively. $LAI_{optimal}$ and $Height_{optimal}$ are the optimal values for LAI and height, respectively, for the corresponding DAS crop.

The *Healthiness Index* is a value between 0 to 1, where stressed plants are indicated by 0, and healthy plants are indicated by 1. The linear model was implemented on the drone-based LAI, height, and tasselling percentage farm maps. If the observed value was greater than the optimal value or less than the severe stress threshold value, then the observed value is made equal to the nearest threshold value.

### 5.4.2 Random Forest model

Selection of the random forest (RF) model was made considering its proven ability to be less sensitive towards the quality of training samples and overfitting (Belgiu et al., 2016). Moreover, the ensemble of decision trees of RF makes this a reliable model (Breiman, 2001). Accordingly, in this research, the RF approach, two inputs - LAI and crop height - were used to predict the crop stress level. Despite using an optimal and threshold approach as the maximum and minimum threshold, as for the linear model, the training data of the RF approach used these lines as the mean and generated random Gaussian data (5% SD from the mean) around each line as shown in Figure 5.7. A moderate stress level was also defined in this model by simulating the ASPIM model for I2N2 based treatment details.

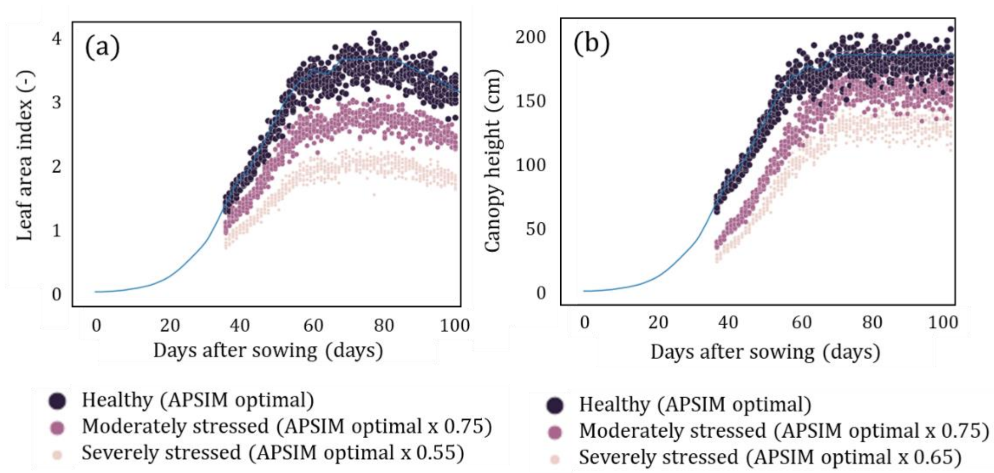


Figure 5.7: Synthetic data plot for (a) LAI, and (b) canopy height, showing three levels of crop healthiness. The reference for these thresholds were taken from APSIM simulated results for the I1N1, I2N2 and optimal condition plots.

The RF model was trained on the synthetic data, with the hyperparameter values tuned to obtain the best-suited values. The created RF model was having n_estimators = 1400, random_state = 42, criterion = entropy, and min_samples_split=10. The model output ranged from 0 to 1, indicating 0 for stressed plots and 1 for healthy plots. These values were named $Healthiness\ Index$. This model was then implemented on the drone-based LAI, and crop height maps and $Healthiness\ Index$ farm maps were obtained.

### 5.4.3 Crop healthiness map

Crop healthiness maps for different growth stages were made using the RF and linear model. Figure 5.8 shows the results of the linear and RF models on temporal drone data. The random forest result were found to be more accurate, being able to differentiate between I3, I2, and I1 plots more efficiently. As the crop moves towards the maturity stage, the model's performance also improves. The Dough stage healthiness map makes all I3, I2, and I1 plots distinguishable from other stage crops. Quantitative analysis of the models was undertaken by correlating the plot-wise average values of the predicted healthiness level (between 0-1) with the yield values. Figure 5.9 shows the scatter plot correlation values for 6-leaf, tasseling, silking stage, and dough stage. It was found that the RF model performed relatively better than the linear model for all growth stages. For the early vegetative stage (6-leaf stage), the obtained $R^2$ were 0.42, and 0.45 for the linear and RF model, respectively. For the tasseling stage, $R^2$ for the linear model was 0.56, and for the RF model was 0.61. The silking stage performed similar to the tasseling stage, with $R^2$ of 0.56, and 0.58 for the linear and RF models, respectively. The dough stage gave the best performance with $R^2$ of 0.63, and 0.67 for the linear and RF models, respectively. As the healthiness and crop yield are positively correlated, the better $R^2$ for the RF model shows its comparatively better performance than the linear model.

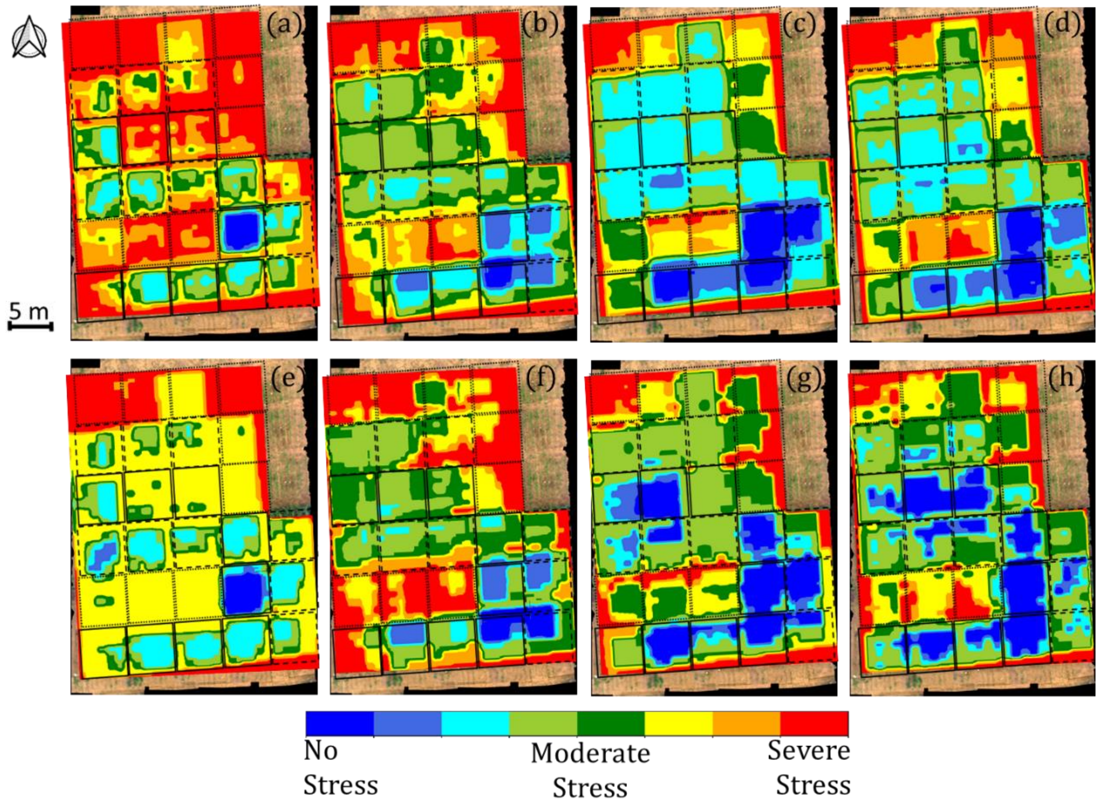


Figure 5.8: Temporal crop stress map of maize farm using random forest model (a-d) and linear model (e-h). The maps are in sequence starting from early vegetative stage, tasseling stage, silking stage, and dough stage. Solid line boxes represent I3 irrigated plots, dashed line boxes represent I2 irrigated plots, and dotted line boxes represent I1 irrigated plots.

## 5.5 Summary

In this chapter, the APSIM crop model was simulated to obtain crop LAI and crop height for various management conditions, including optimal conditions. The simulated LAI and height values were used as a reference to create two models; one linear and the second a machine learning model. The drone-based LAI, height, and tasselling percentage maps were then fed into the models to create the healthiness index maps of the farm. The machine learning model (random forest) gave slightly better performance than the linear model. These healthiness maps

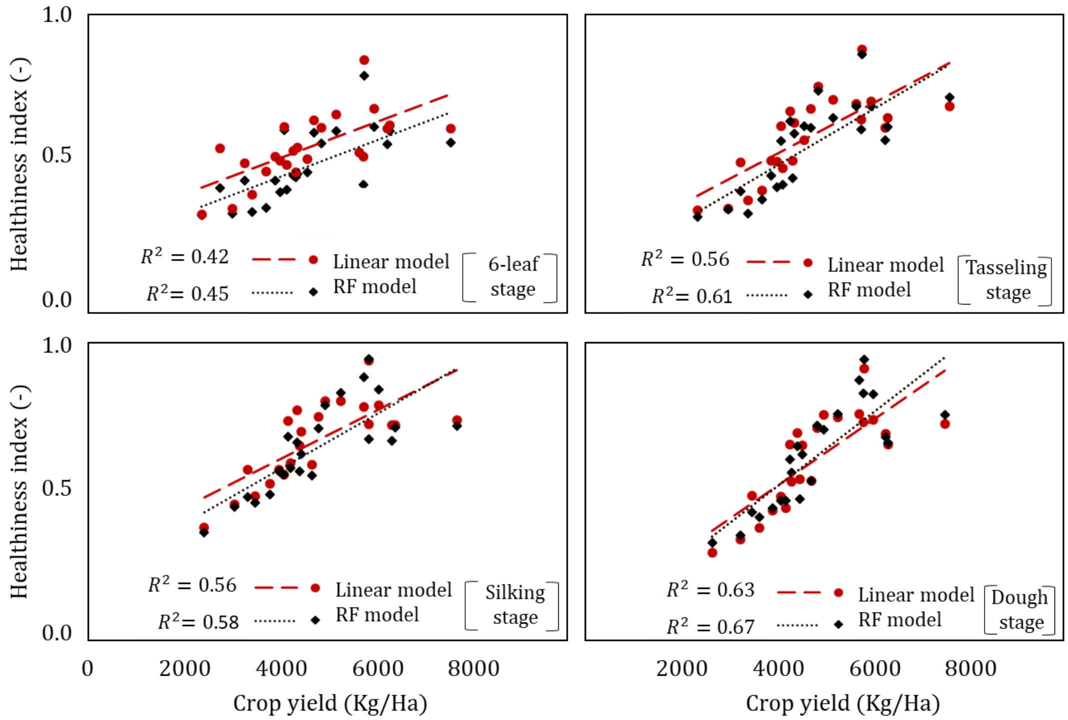


Figure 5.9: Scatterplot between plot-wise average healthiness index and crop yield for (a) early vegetative, (b) tasseling, (c) silking stage and (d) dough stage.

indicate the plots with different stress levels but do not give the reason for the stress. Accordingly, these maps were further classified as water and nitrogen stress areas using the methods developed in chapter six.

# Chapter 6
# Estimation of maize biochemical properties

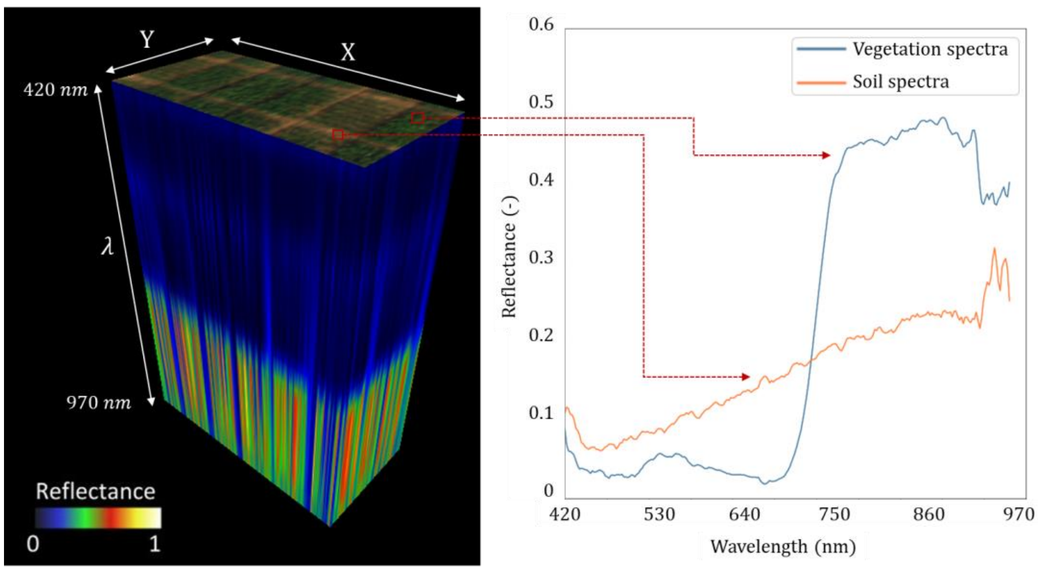


*Hyperspectral data cube - a three-dimensional representation of a hyperspectral image. Here, X and Y represent the spatial dimension while the Z dimension (denoted by λ) shows the spectral information according to wavelength for each pixel in the image. The top layer of the cube is showing an RGB map of a section of the farm. The spectral information of a vegetation and soil pixel is shown at the right of the plot. The absorption at different bands contains information about various chemical properties of the scanned material.*

# 6 Estimation of maize biochemical parameters

Note: Most of the contents of this chapter have been published as

- Raj, R., Walker, J.P., Vinod, V., Pingale, R., Naik, B. and Jagarlapudi, A., 2021. Leaf water content estimation using top-of-canopy airborne hyperspectral data. International Journal of Applied Earth Observation and Geoinformation, 102, p.102393.
- Raj, R., Walker, J.P., Pingale, R., Banoth, B.N. and Jagarlapudi, A., 2021. Leaf nitrogen content estimation using top-of-canopy airborne hyperspectral data. International Journal of Applied Earth Observation and Geoinformation, 104, p.102584.

## 6.1 Leaf water content

A drone-based push-broom hyperspectral (400-1000 nm) imager was used to collect temporal data from a research farm. Hand-held spectroradiometer data was collected coincident with the flights to provide leaf-level spectral signatures (400-1000 nm) from plants grown in plots treated with different water and fertiliser doses. These leaves were subsequently plucked, and the LWC estimated using the oven drying method. The hand-held spectroradiometer and associated LWC data were then used to identify the pure-pixel narrowband normalised indices sensitive to LWC. The bands involved in the LWC indices were chosen based on their response to different water vibrational absorption regions of the electromagnetic spectrum. These indices were then calculated using the farm-scale hyperspectral images collected using the drone, and the minimum/maximum values of these indices and respective LWC used to generate synthetic data for training a gradient boosting machine (GBM) model. The GBM model was then evaluated on the actual farm data. The framework of this research is shown in Figure 6.1.

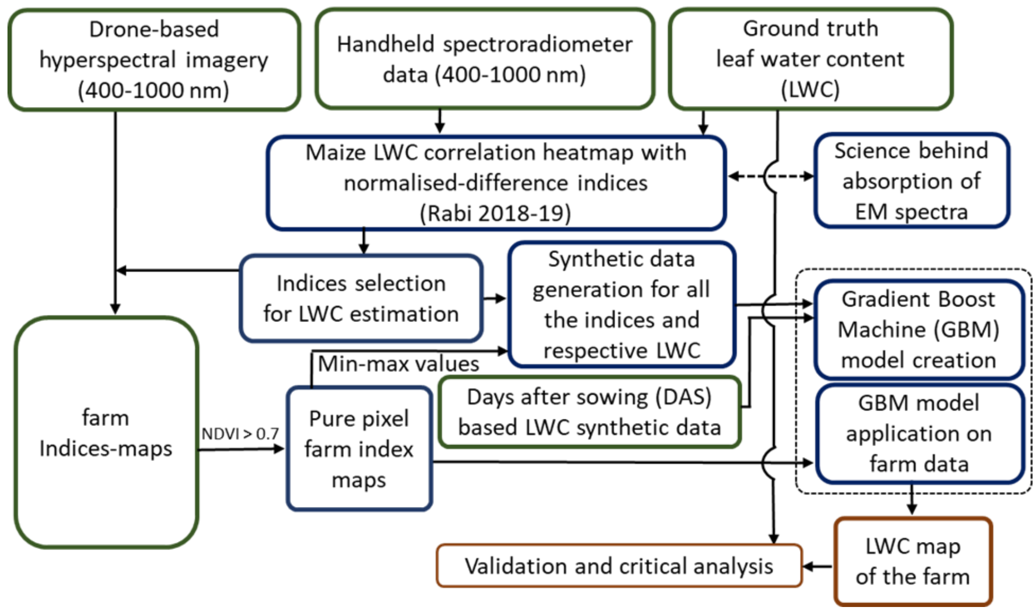


Figure 6.1: The framework of the leaf water content (LWC) model development and evaluation.

### 6.1.1 Index selection

The number of bands in the spectroradiometer and hyperspectral imager data was 381 and 242, respectively. However, most of the bands in narrowband hyperspectral data show a high correlation to each other and thus contain similar information (Thenkabail and Lyon, 2016). The bands having redundant information or not having any relation with LWC should therefore be removed from the analysis as they create unnecessary complexity (Thenkabail and Lyon, 2016). Thus, it is crucial to select only those bands which contain information about the LWC. One such approach of dimensionality reduction can be to choose only one band from the highly correlated set of bands. However, this band correlation method may discard the highly correlated bands having critical information about the crop parameter being measured (Kumar et al., 2001). Accordingly, Partial Least Square Regression has been used as a popular algorithm in chemometrics to reduce dimensionality, but this approach may not distinguish bands having little effect on the LWC (Hanrahan and Patil, 2005). Moreover, these models remain completely empirical in nature. It, therefore, becomes imperative to identify important bands for estimation of a specific crop property based on the science behind the electromagnetic spectrum's reflectance properties.

In this research, spectroradiometer data was used for identification of bands/indices for estimation of leaf water content. From 381 bands of spectroradiometer data ranging from 400-1000 nm, a total of 72390 possible unique normalised difference indices were created according to

$$Normalised\ difference\ index\ (NDI) = \frac{Reflectance\ at\ band\ i - Reflectance\ at\ band\ j}{Reflectance\ at\ band\ i + Reflectance\ at\ band\ j}, \quad (6.1)$$

where i and j are bands ranging from 400 to 1000 nm. Each of the indices was correlated with the actual leaf water content (measured after oven drying the leaves). The correlation heatmap is shown in the results section. The highly correlated zones of the indices-LWC correlation heatmap were analysed with respect to the water-sensitive bands present in the 400-1000 nm wavelength region, as discussed in the literature review chapter in Table 2.5.

Table 6.1 lists all the indices created in this research used for further analysis. Based on analysis of the seven newly identified indices, it was found that the FOSBNDI-1, FOSBNDI-2, and COSBNDI indices also showed a high sensitivity for LWC with drone-based data. However, FSOSBNDI, SAPBNDI, SOSBNDI, and WASCOSBNDI did not show any visible sensitivity towards LWC with drone-based hyperspectral data and only worked well with spectroradiometer data, limiting the use of the later four indices in drone-based sensing applications.

Table 6.1: Vegetation pure pixel, narrowband indices for estimation of leaf water content.

| Index Formula | short from | Full form | Index Range | Usability |
|---|---|---|---|---|
| $\frac{R660-R420}{R660+R420}$ | COSBNDI | Combined overtone of stretching bands - normalised difference index | -0.50 to 0.30 (Negative correlation) | Spectroradiometer and drone data |
| $\frac{R529-R698}{R529+R698}$ | FOSBNDI-1 | Forth overtone of stretching bands - normalised difference index 1 | -0.35 to 0.45 (Postive correlation) | |
| $\frac{R529-R605}{R529+R605}$ | FOSBNDI-2 | Forth overtone of stretching bands - normalised difference index 2 | -0.20 to 0.45 (Positive correlation) | |
| $\frac{R475-R449}{R475+R449}$ | FSOSBNDI | Fifth and sixth overtone of stretching bands - normalised difference index | -0.20 to 0.45 (Negative correlation) | Spectroradiometer data only |
| $\frac{R750-R970}{R750+R970}$ | SAPSBNDI | Small absorption peak of stretching bands - normalised difference index | -0.27 to 0.68 (Positive correlation) | |
| $\frac{R791-R970}{R791+R970}$ | SOSBNDI | Second overtone of stretching bands - normalised difference index | ~-0.15 to 0.65 (Positive correlation) | |
| $\frac{R800-R847}{R800+R847}$ | WASCOSBNDI | Water absorption shoulder due to combined overtone of stretching bands - normalised difference index | ~0 to 0.2 (Positive correlation) | |

### 6.1.2 Model creation

Based on the three newly identified indices (FOSBNDI-1, FOSBNDI-2 and COSBNDI), and the second version of Enhanced Vegetation Index (EVI2), farm index-maps were created using the drone-based hyperspectral data. EVI2 was selected due to its proven capability of being sensitive to equivalent water thickness of the canopy (Cheng et al., 2006; Cheng et al., 2008), and calculated according to (Jiang et al., 2008)

$$EVI2 = 2.5\left(\frac{NIR-R}{NIR+(6*R)-(7.5*B)+1}\right). \quad (6.2)$$

As the images' spatial resolution was 1 cm, most of the vegetation pixels were scanned as pure pixels. However, to remove the background pixels (non-vegetation pixels) from the farm index maps, narrowband NDVI values of all the pixels were thresholded at a value of 0.7 and assigned a null value. These pixels included mostly non-vegetation pixels and some mixed pixels at the edges of the field.

The maximum and minimum value of each index-map of pure pixels was then used to generate synthetic data for model training as follows. Depending on the index and LWC relation (whether positively or negatively correlated), extreme index values were assigned to the highest and lowest LWC values, respectively. Assuming a linear relationship, a straight line was interpolated between the extreme values of the indices and LWC, as shown by the dashed line in Figure 6.2. The linear relation was chosen as it has no spectral saturation (Tian et al., 2011), and Pasqualotto et al. (2018) and Sun et al. (2019) have found that a linear relation with LWC gives a better estimation than exponential or polynomial relations. Considering the interpolated values as being the mean of an observational distribution for LWC, 1,000 Gaussian distributed points were generated within 10% of the interpolated LWC value. The generated points are shown by the black dots in Figure 6.2. Along with this index-LWC synthetic data, crop growth-stage based LWC synthetic data was also created. Here a second-order polynomial fit line was selected as it gave a better representation of the temporal LWC, with a Gaussian noise generated within 5% of the interpolated LWC values.

A total of 20,000 sets of points were used from the synthetic data to train the GBM model developed to estimate LWC. The GBM was selected as it combines the predictions from multiple decision trees to generate a final prediction. The GBM performs the sequential improvement of decision trees to convert weak learners into strong learners and produce the best metrics for the algorithm to fit the data by tuning the hyperparameters (Friedman, 2001). The hyperparameters of the GBM regression were tuned, and the optimal values selected for the model's weights. The hyperparameter tuning result is shown in

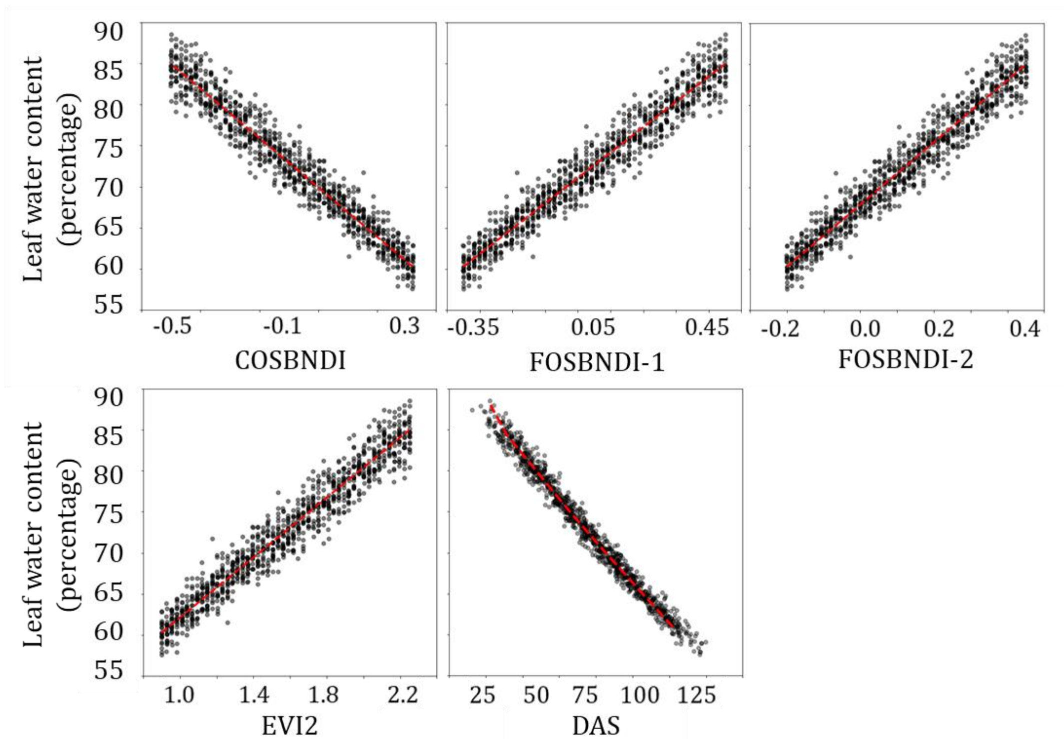


Figure 6.2: Synthetic Leaf water content (LWC) data for the newly created indices and 'days after sowing' (DAS) information. The dashed red lines represent the interpolated values between the minimum and maximum of the index and LWC. The black dots represent Gaussian distributed points. The dashed line in the DAS-LWC plot represents a second-order polynomial fit line.

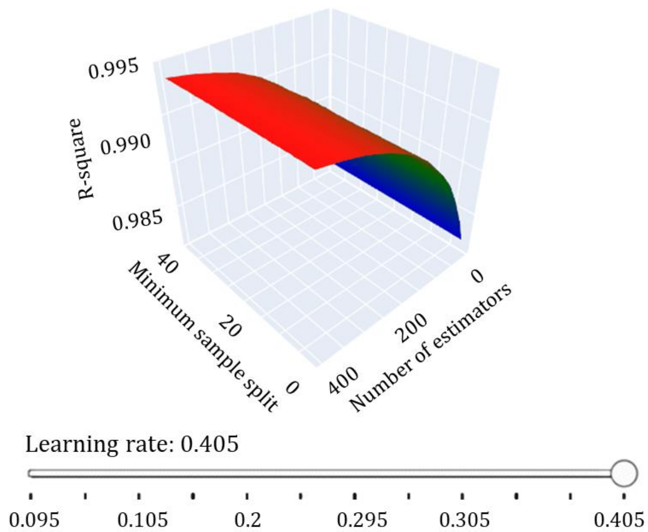


Figure 6.3: Hyperparameter tuning graph for the Gradient Boosting Machine (GBM) algorithm. The best set of parameters was obtained at learning rate – 0.405, minimum sample split – 7, and the number of estimators – 400.

Figure 6.3. The model trained on synthetic data was then implemented on the index maps obtained from the drone-based hyperspectral data.

### 6.1.3 Results and discussion

The LWC correlation heatmap created using 72390 unique indices as explained in equation 6.1 is shown in Figure 6.4. Analysis of the correlation heatmap clearly showed that the wavelengths associated with water absorption bands created the highest correlation regions. Thus, index selection was made based on those indices that gave the highest correlation when coupled with the water absorption bands. Figure 6.4 shows the heatmap with marked water absorption wavelengths. The indices created using brown/red zone wavelengths showed maximum correlation, while the indices created using the violet zone showed the least correlation with maize LWC. The identified indices are shown in Table 6.1.

The GBM model created in this research was evaluated on spectroradiometer based index data with an $R^2$ of 0.93 and RMSE of 1.6 % (g/g), as shown in Figure 6.5. The GBM model was also evaluated for the 6-leaf stage (35 DAS) and late-vegetative stage (56 DAS) farm maps. Figure 6.6 shows the colour-coded farm maps for better visualisation of the spatial distribution of LWC in the farm. The map visualisation methods explained in Crameri et al.

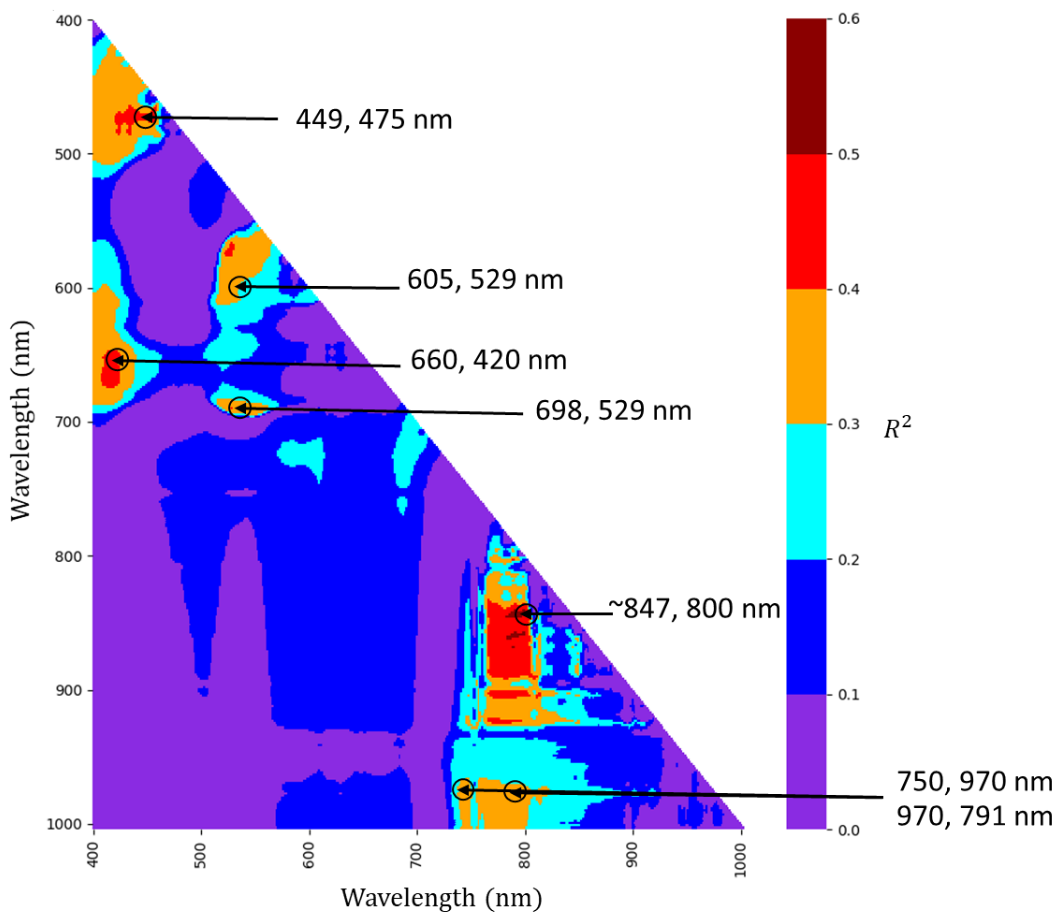


Figure 6.4: Heatmap of the coefficient of determination between narrowband (two nm bandwidth) normalised difference vegetation indices and leaf-water content. The highly correlated indices are shown in red colour, and least correlation indices are shown in violet colour. The indices created used the wavelengths shown on the x and y-axis as per equation 6.1.

(2020) have been used to create the color coded LWC maps of the farm. Accordingly, the farm-map has been smoothed with a Gaussian filter and overlayed with different line-type boxes to indicate the I1, I2, and I3 irrigation plots. For the 6-leaf and late-vegetative stage maps, water-stressed plots (I1) could easily be identified as having lower LWC. This can be verified from the box-whisker plot shown in Figure 6.7, where the 35 and 56 DAS plant's LWC of I1 plot were less than that for the I3 plot plants. However, the visual difference between I2 and I3 plots cannot be seen. The box-whisker plots of different irrigation treatment plots and ground truth data are shown in Figure 6.7.

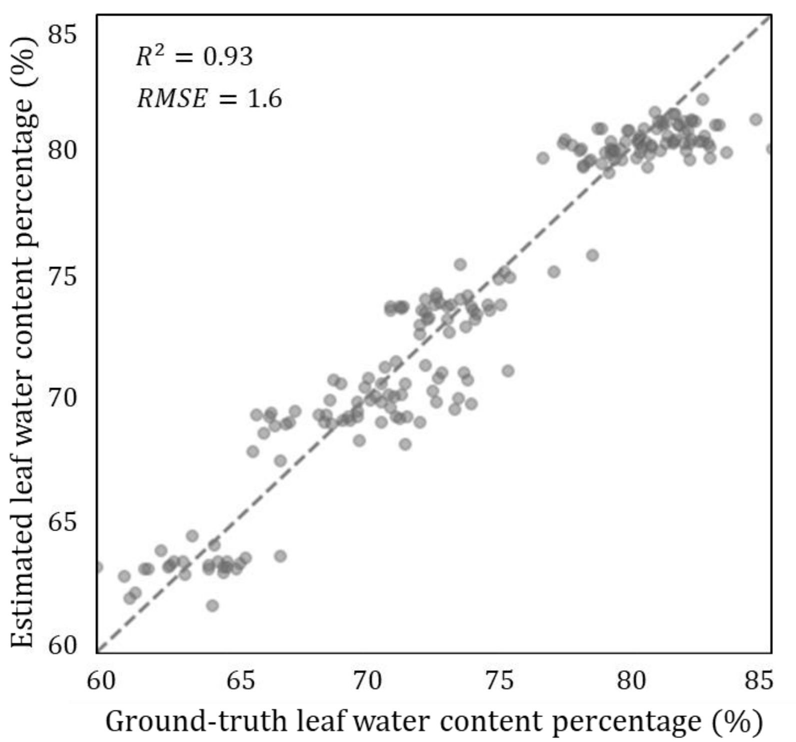


Figure 6.5: Evaluation of the GBM model trained on the synthetic data against spectroradiometer data. The dots of the scatterplot are semi-transparent. Relatively darker areas of the scatterplot show overlapping of points in those regions.

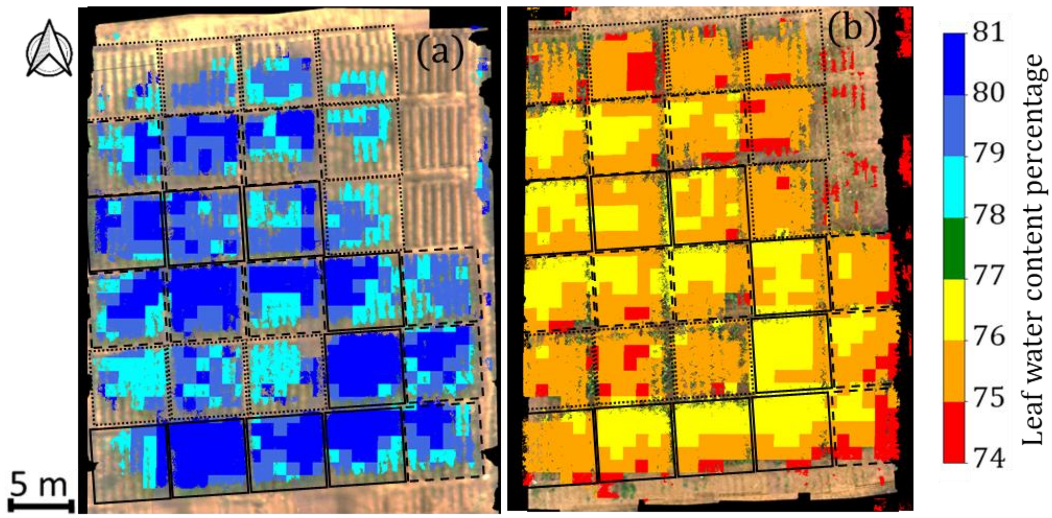


Figure 6.6: Colour coded leaf water content (LWC) maps of a maize farm. (a) The LWC farm map at the 6-leaf stage (35 days after sowing); (b) The LWC farm map at late-vegetative stage (56 days after sowing). The LWC difference of sufficiently irrigated (solid line boxes with I3 irrigation), moderately irrigated (dashed line boxes), and less irrigated (dotted line boxes) plots can be easily seen in the farm maps.

The water absorption indices and LWC model developed in this research can be used for early growth stage (from 6-leaf stage to tasselling stage) leaf water content estimation of a crop using narrowband pure pixel airborne optical data. Indices were developed using hand-held spectroradiometer data taken from approximately 10 cm distance from leaves and applied to drone-based data obtained from about 50 m distance from the leaves, with three of the seven indices found to show the sensitivity needed for LWC estimation of crops treated with different irrigation amounts. This highlights the utility of the three indices (FOSBNDI-1, FOSBNDI-2, and COSBNDI) in the field of drone-based sensing. However, as these indices have been derived from pure vegetation pixel data, implementation of these indices on mixed pixel data may drastically reduce the sensitivity to LWC. Importantly, with the distance between the leaves and the drone-based sensor being only 50 m, the atmospheric effect on the hyperspectral data is minimal compared to that on satellite or airborne data.

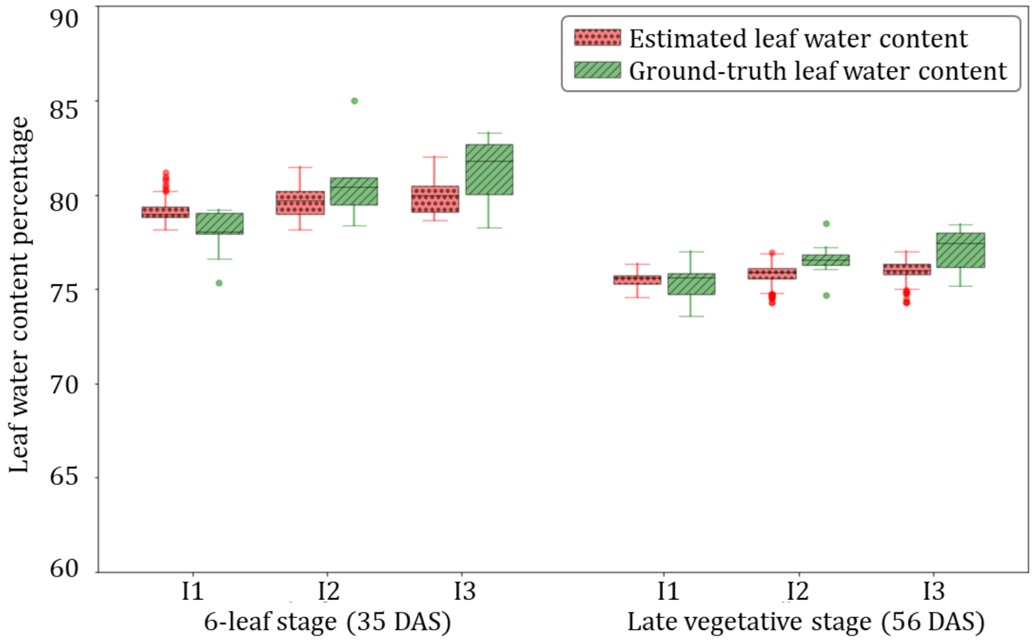


Figure 6.7: Box-whisker plots of estimated and ground-truth leaf water content for the 6-leaf stage and late vegetative stage plants. The 6-leaf stage data were collected at 35 days after sowing (DAS) and the late vegetative stage data were collected at 56 DAS. I1, I2, and I3 represent the three irrigation levels applied in the different plots of the research farm, with I3 representing sufficient irrigation, I2 moderate, and I1 water-stressed plots.

However, the other four LWC indices identified from the spectroradiometer (FSOSBNDI, SAPBNDI, SOSBNDI, and WASCOSBNDI) may still have lost their sensitivity when applied to UAV data due to the increased distance between the leaf and sensor. Importantly, by training the model to synthetic data, the model will have reduced dependence on the collected data, meaning that it should be applicable to other fields and seasons with the same maize variety.

Another interesting observation is that these indices lose sensitivity as the bandwidth is increased. The analysis was done on different bandwidth data (2 nm to 30 nm) by creating multiple index-LWC correlation heatmap. The correlation heatmap comparison is given in Figure 6.8. A correlation similar to the 2 nm bandwidth indices is observed until 11 nm bandwidth, after which

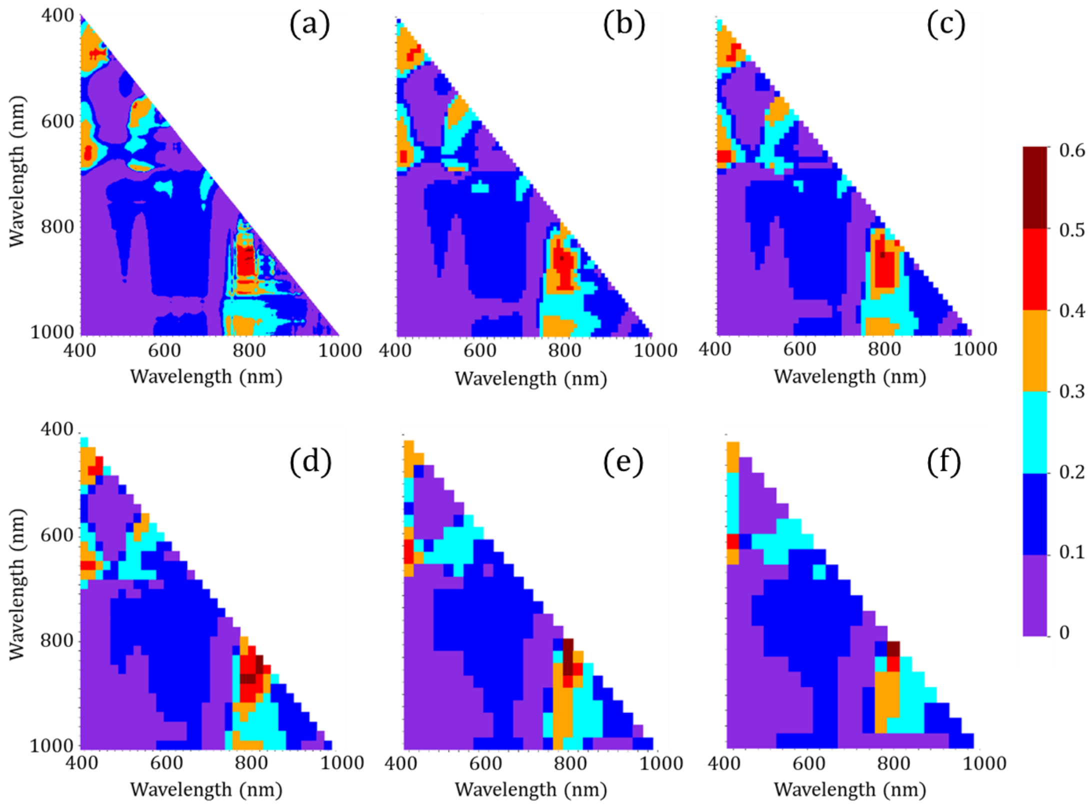


Figure 6.8 The LWC correlation heatmap of (a) 2 nm , (b) 8 nm, (C) 11 nm, (d) 18 nm, (e) 22 nm, and (f) 30 nm bandwidth data.

there is substantially less sensitivity towards LWC. Thus, this research suggests that for LWC estimation, sensors should be made by considering the wavelengths given in Table 6.1 as central wavelength with less than 11 nm bandwidth for each band. Moreover, researchers from different parts of the world should use and test these indices/wavelengths on various crops to estimate LWC.

There are multiple studies that have used hyperspectral data to estimate the leaf/vegetation water content. However, most of them have acquired data from the entire 400-2500 nm range to utilise the primary water absorption bands. Moreover, process-based models like PROSPECT/ PROSAIL do not produce any change in the 400-900 nm spectra when LWC changes in the crop. Pasqualotto et al. (2018) have used airborne 400-2500 nm data to get the canopy water content for multiple crop types (lucerne, corn, potato, sugar beet and onion). The authors have used primary water absorption bands to get water absorption area and depth water index. Using these indices with an exponential fit, the authors achieved an $R^2$ of around 0.75, but the model could not perform well for areas having less than 30% of vegetation cover. Herrmann et al. (2020) used an 11 band drone-based hyperspectral imager to collect temporal data from a maize crop. The study identified 570 nm and 620 nm wavelengths as being more sensitive to different irrigation crop treatments. The study also estimated relative crop water content using a partial least square regression on all 11 bands (420, 440, 490, 550, 640, 670, 700, 740, 780, 860 and 910 nm) with an $R^2$ of 0.55.

In another study, Sun et al., (2019) used spectroradiometer data in the range 400-2500 nm to estimate LWC of a winter wheat crop. Various indices were tested and an $R^2$ of 0.77 achieved. Cheng et al. (2011) used 350-2500 nm spectroscopic data to estimate the LWC of 47 species present in the tropical forests of Panama using continuous wavelet analysis. The model had an $R^2$ in the range of 0.71-0.75. In contrast, Corti et al., (2017) used 400-1000 nm hyperspectral imager data to estimate spinach canopy water content using a partial least square regression model and achieved an $R^2$ of 0.87. By comparison, the research presented in this paper achieved an $R^2$ of 0.93 and RMSE of 1.6 % (g/g) even when applied exclusively to early vegetative stages of the maize crop. This shows that the 400-1000 nm sensors' cost-effectiveness and usefulness of identified optimal bands make this range equally powerful for pure-pixel data as compared to 400-2500 nm data. Moreover, the sensors that capture data in the range of 400-2500 nm are costly and give enormous data volumes, which also creates storage and analysis issues.

## 6.2 Leaf nitrogen content

After collection of drone-based and hand-held hyperspectral data, the leaves plucked (saem leaf which were used for LWC) and the leaf total nitrogen content were obtained using the Dumas method based CHNS instrumental analyser (Dhaliwal et al., 2014). The collected data were then used to identify the bands and indices more sensitive to change in leaf nitrogen content (LNC) than leaf water content (LWC). The maximum and minimum values of indices, growth stage information, were then used to create synthetic linear data to train a gradient boosting machine learning algorithm (GBM). Drone-based hyperspectral data were used to evaluate the model, and the results critically analysed with respect to LWC information. The framework of this research is shown in Figure 6.9.

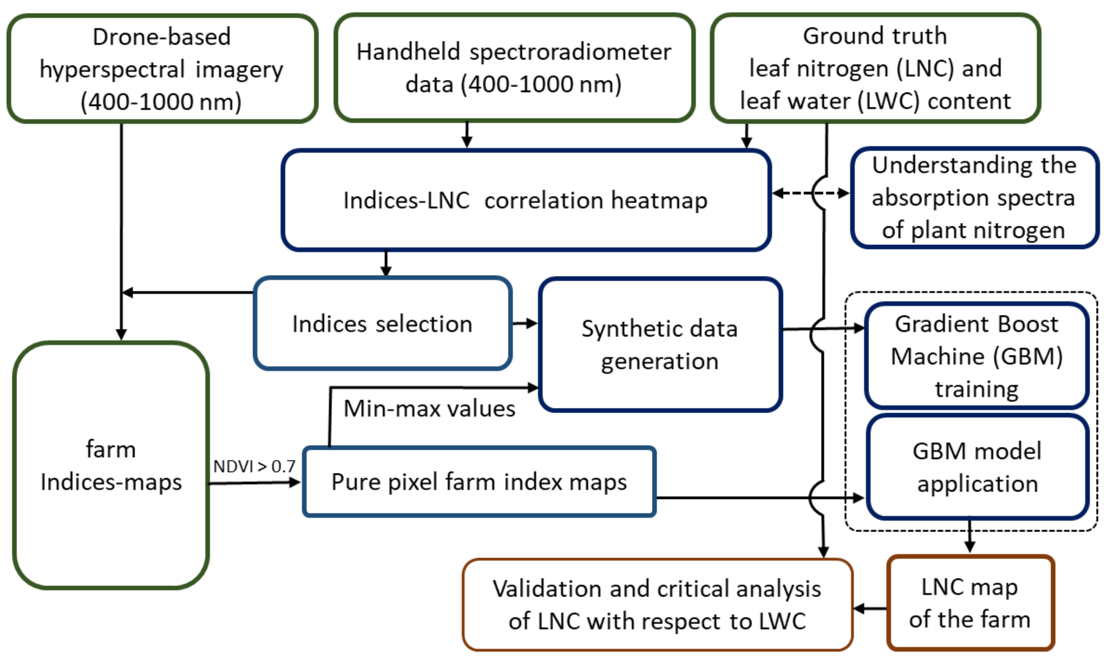


Figure 6.9: The structure of the leaf nitrogen content estimation model used in this research.

### 6.2.1 Index selection

The indices identified in this research were created using the narrow-band, pure pixel leaf-level hyperspectral signatures obtained from the spectroradiometer data. The 381 bands of the spectroradiometer were used to create 72,390 ($^{381}C_2$) unique two-band normalised difference indices as per equation 6.1. The correlation coefficient between each of the 72,390 indices and LNC was obtained and presented as a heatmap in Figure 6.10(a). Interestingly, highly correlated areas in the index-LNC correlation heatmap were found to be the similar as highly correlated areas in the index-LWC correlation heatmap created for LWC. This restricted use of the index-LNC correlation heatmap for finding nitrogen-sensitive indices independently from information on water content as the same indices were also highly sensitive to LWC. To find the indices more correlated with LNC than LWC, a correlation difference heatmap between the LNC and LWC heatmap was created. The difference heatmap is shown in Figure 6.10(b). After comparing the correlation heatmaps and the difference heatmap, four indices were selected for further analysis. The identified wavelengths for these indices are indicated in Figure 6.10 and listed in Table 6.2. Out of these four indices, only the RedEdge1 index showed spatial variability on the drone-based image. Thus, the RedEdge1 index along with the DCNI index from literature was selected for further analysis.

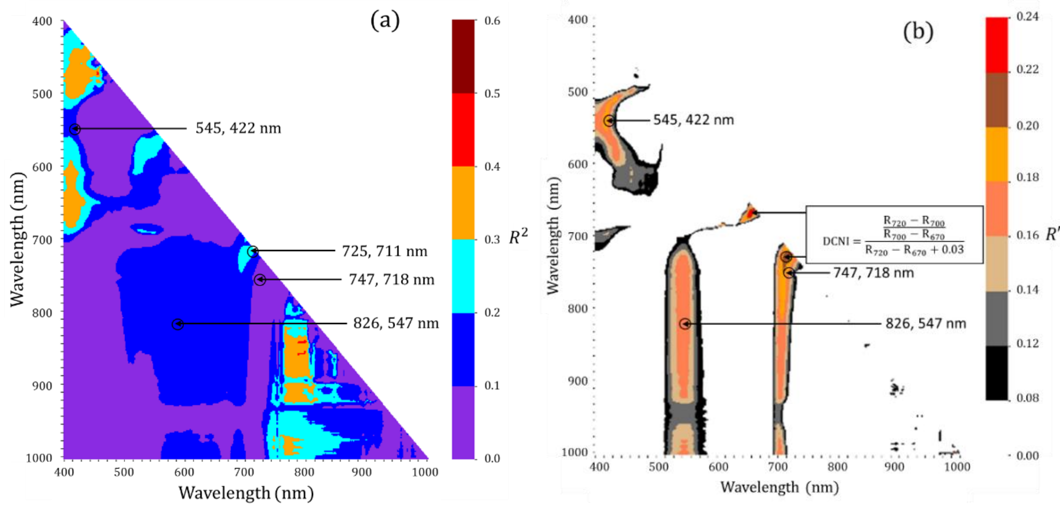


Figure 6.10: (a) Heatmap of $R^2$ between narrow-band normalized difference indices and leaf nitrogen content. (b) The heat map of LNC-LWC correlation coefficient difference $R'$ showing only those indices having a superior correlation with LNC compared to LWC. Indices in the white part of heatmap are correlated more with LWC than LNC.

Table 6.2: Pure pixel, narrow-band indices identified in this research for LNC estimation.

| Index Formula | Short from | Range | Usability |
|---|---|---|---|
| $\frac{R_{545}-R_{422}}{R_{545}+R_{422}}$ | $GBslope_{Index}$ | 0-0.35 | Spectroradiometer data only |
| $\frac{R_{826}-R_{547}}{R_{826}+R_{547}}$ | $GreenNIR_{Index}$ | 0.2-0.8 | |
| $\frac{R_{747}-R_{718}}{R_{747}+R_{718}}$ | $RedEdge2_{Index}$ | 0.1-0.5 | |
| $\frac{R_{725}-R_{711}}{R_{725}+R_{711}}$ | $RedEdge1_{Index}$ | 0.2-0.4 | Spectroradiometer and drone data |

### 6.2.2 Model creation

Drone-based hyperspectral band images were used to create farm-index maps for the newly identified index - RedEdge1 (Table 6.2) and the DCNI index (Chen et al., 2010). The spatial resolution of the farm map was around 1 cm resulting in most canopy pixels being a pure pixel. The purity of the vegetation pixels resulted in higher narrow-band NDVI values of each vegetation pixel when compared to NDVI values of background pixels. Pixels having an NDVI value less than 0.7 were either non-vegetative or mixed pixel at the leaf edges. These lower NDVI pixels were therefore assigned a null value in the map. A similar background removal approach was used in making LWC maps.

Synthetic data was created for model training, using the maximum and minimum values of individual pure pixel vegetation index maps. As RedEdge1 and DCNI were both positively correlated with LNC, the minimum and maximum values were assigned to the minimum and maximum ground-truth LNC, respectively. A straight line was interpolated between the extreme values and 1000 random Gaussian distributed points generated within 10% of the interpolated value as shown in Figure 6.11. Along with the synthetic index data, a decreasing trend of LNC with progressive growth stages was modeled using days after sowing (DAS) information. The DAS-LNC data was created using Gaussian noise around a third-order polynomial fit to the median values of ground truth data. Use of synthetic data for model training will reduce the model dependence on collected data resulting in improved model repeatability.

A GBM model for LNC estimation was trained on 20,000 sampled points from the synthetic data. The GBM model was chosen for its promising performance as in LWC model. Moreover, the property of the GBM model to convert weak learners to strong learners by performing sequential improvement of decision trees (Friedman, 2001) made it a suitable choice

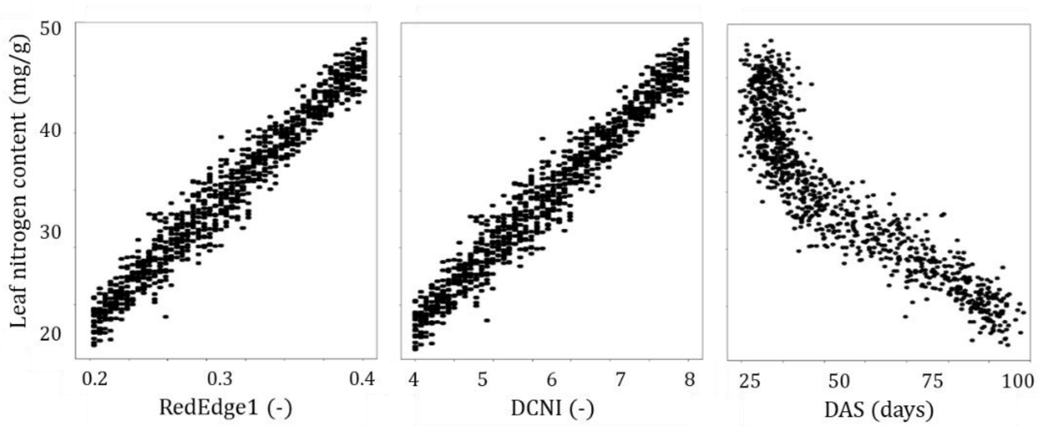


Figure 6.11: The synthetic data for RedEdge1, DCNI, and DAS relation with LNC.

for LNC estimation. Optimal hyperparameters of the model were obtained using a GridSearchCV algorithm (Zhao et al., 2020). The best parameters were obtained with a learning rate of 0.395, minimum sample split of 12, and number of estimators of 1,900. The LNC obtained from the GBM model was termed as estimated LNC.

### 6.2.3 Results and discussion

Various indices identified from the literature have been tested to estimate LNC. These indices were created to estimate canopy nitrogen content and, to date, mainly tested on canopy-level low spatial resolution data. The performance of these indices on pure-pixel narrow-band data was poor. Apart from DCNI, no other index available in literature could give an $R^2$ greater than 0.05. The RedEdge1 index (identified in this research) and DCNI (identified from literature) farm index maps were created. Average index values for each treatment were used to create scatter plots with respective CHNS-based LNC values. As shown in Figure 6.12, it was found that the RedEdge1 index and DCNI were correlated to LNC with an $R^2$ of 0.27 and 0.20, respectively.

The GBM model estimated temporal and spatial distribution of crop LNC is shown in Figure 6.13. Comparison of these maps with LWC showed that, in general, LNC was high in the areas where LWC was also high. Although this is true, as LNC and LWC have a high correlation ($R^2$ of 0.7) as shown in Figure 6.14, the efficiency of the LNC model could be checked by analysing the LNC distribution in the same LWC area. The analysis of water-stressed and non-water stressed plots was undertaken separately to see the effect of different LWC on the LNC model. Moreover, the correlation between estimated LNC and CHNS-based LNC was made. The maps were analysed for the 6-leaf and pre-tasseling stages, where the water-stressed plots gave an $R^2$ of 0.63 and RMSE of 2.74 mg/g, but the plots with higher LWC gave an $R^2$ of 0.26 and RMSE of 4.54 mg/g. This shows that the LNC model can identify nitrogen stress areas from the water-stressed plots, but the model could not perform well for regions where no water stress was present. This is a limitation of the model, suggesting that the LNC model should only be applied once the LWC model has been used to classify low and high LWC areas, as suggested in Raj et al. (2021). The scatter plots between estimated LNC and CHNS-based LNC for different conditions are shown in Figure 6.15, with the model giving an $R^2$ of 0.33 and RMSE of 5.35 mg/g when tested on 6-leaf and pre-tasseling stage data with no discrimination of water-stressed regions. However, the model accuracy increased to an $R^2$ of 0.63 and RMSE of 2.74 mg/g when applied to only the water-stressed regions.

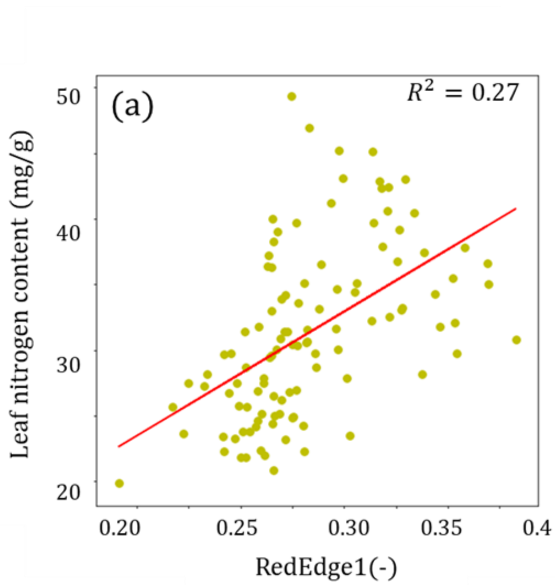


Figure 6.12: Scatter plot between ground truth LNC and plot-wise averaged index value of (a) RedEdge1 and (b) DCNI index.

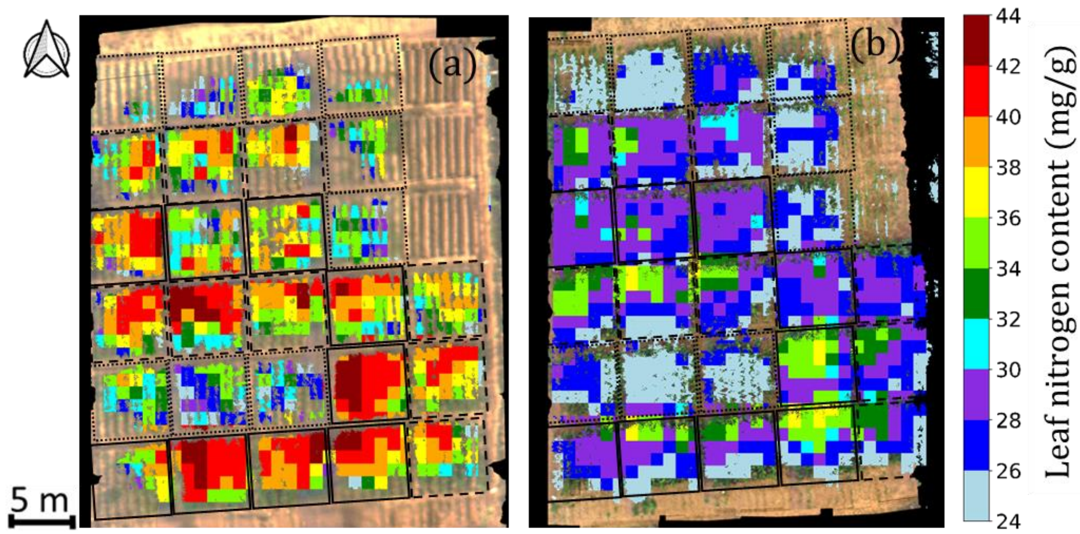


Figure 6.13: Colour-coded farm leaf nitrogen map obtained from the trained GBM showing nitrogen content in plant leaves on (a) 6-leaf stage and (b) pre-tasseling stage.

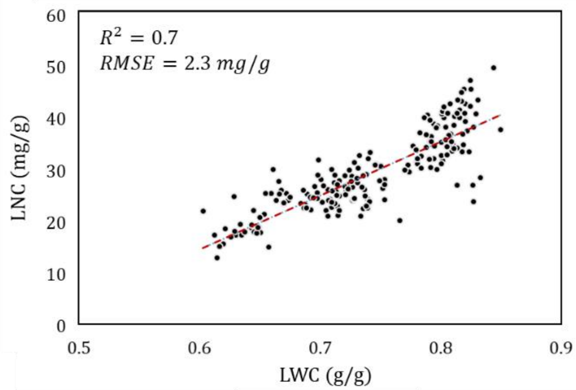


Figure 6.14: Scatter plot between LWC and LNC indicating a strong dependence of LNC on LWC.

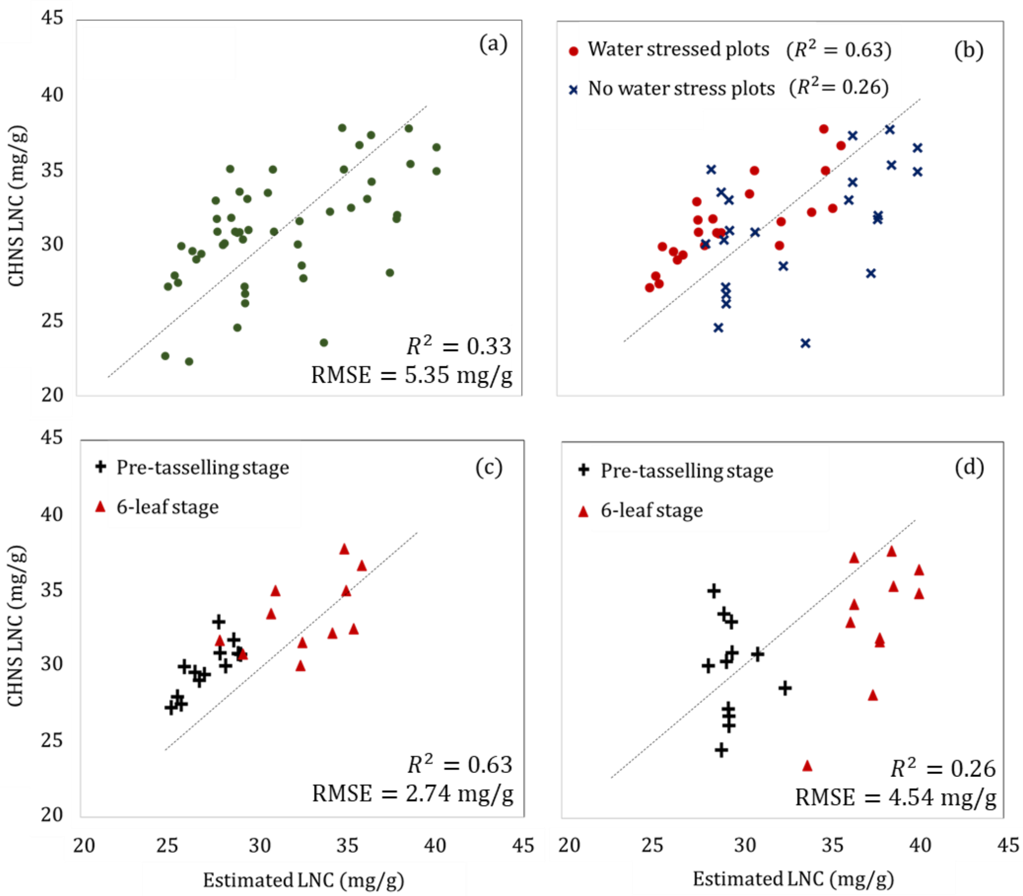


Figure 6.15: (a) Scatter plot between estimated and CHNS-derived LNC values for all plots; (b) Water stress classification-based scatter plot for all plots; (c) Growth-stage based scatter plot for water-stressed plots only; (d) Growth-stage based scatter plot for non-water stressed plots only.

The indices used in this research – DCNI and RedEdge1 – were created using bands from the red edge region of the electromagnetic spectrum. Chen et al. (2010), who introduced the DCNI index, presented a detailed analysis of the sensitivity of nitrogen concentration to the relative height changes in the peaks of derivative spectra of the leaf spectral signature. In this research, those peaks were found in the red-edge zone of the spectra around 700 nm and 720 nm, as depicted in Figure 6.16. Importantly, Chen et al. (2010) found that the nitrogen concentration in the leaves was highly correlated with the relative height changes of those peaks, which can be estimated using the ratio of the average heights of the two peaks. However, Chen et al. (2010) did not give any scientific reasoning for this high correlation. Chen et al. (2010) also added the 670 nm wavelength in the DCNI index to reduce the effects of LAI on the index, which may be helpful for mixed pixel data, but not for pure-pixel data. The LNC model presented in this research was for pure vegetation pixels, which enabled the RedEdge1 index to give better results than DCNI without adding other factors in the index to remove the effects of crop biophysical properties.

The literature-based indices did not show high correlation with leaf nitrogen content. This may be because literature-based indices, until now, have been mostly validated for canopy level nitrogen content which are influenced by the biomass and other biophysical properties of the crop available in each pixel area. However, in this research, the indices were tested for pure-pixel leaf level total nitrogen content which is independent of any crop biophysical properties.

One crucial observation made in this research is that the identified indices tended to lose sensitivity to LNC estimation as the bandwidth broadened. Figure 6.17 shows the comparative correlation difference heatmap between LNC and LWC created with different bandwidth data. The analysis was undertaken on bandwidth correlation difference heatmaps created using a 2 nm to 11 nm bandwidth dataset. The indices performed similarly until 5 nm bandwidth data, with the correlation reducing drastically as the bandwidth further broadened.

Thus, this research suggests that for distinguishing LNC and LWC, data should be collected with sensors having the central wavelengths given in Table 6.2 with a less than 5 nm bandwidth.

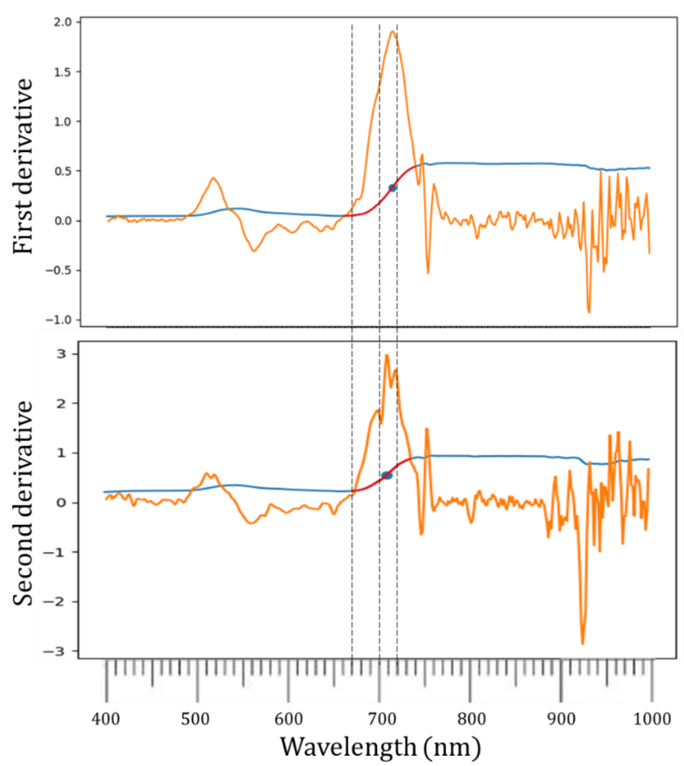


Figure 6.16: Orange lines show derivatives of typical leaf reflectance spectra. The two peaks can be observed in the second derivative spectra around 700 nm and 720 nm. The blue line spectra is the leaf reflectance spectra.

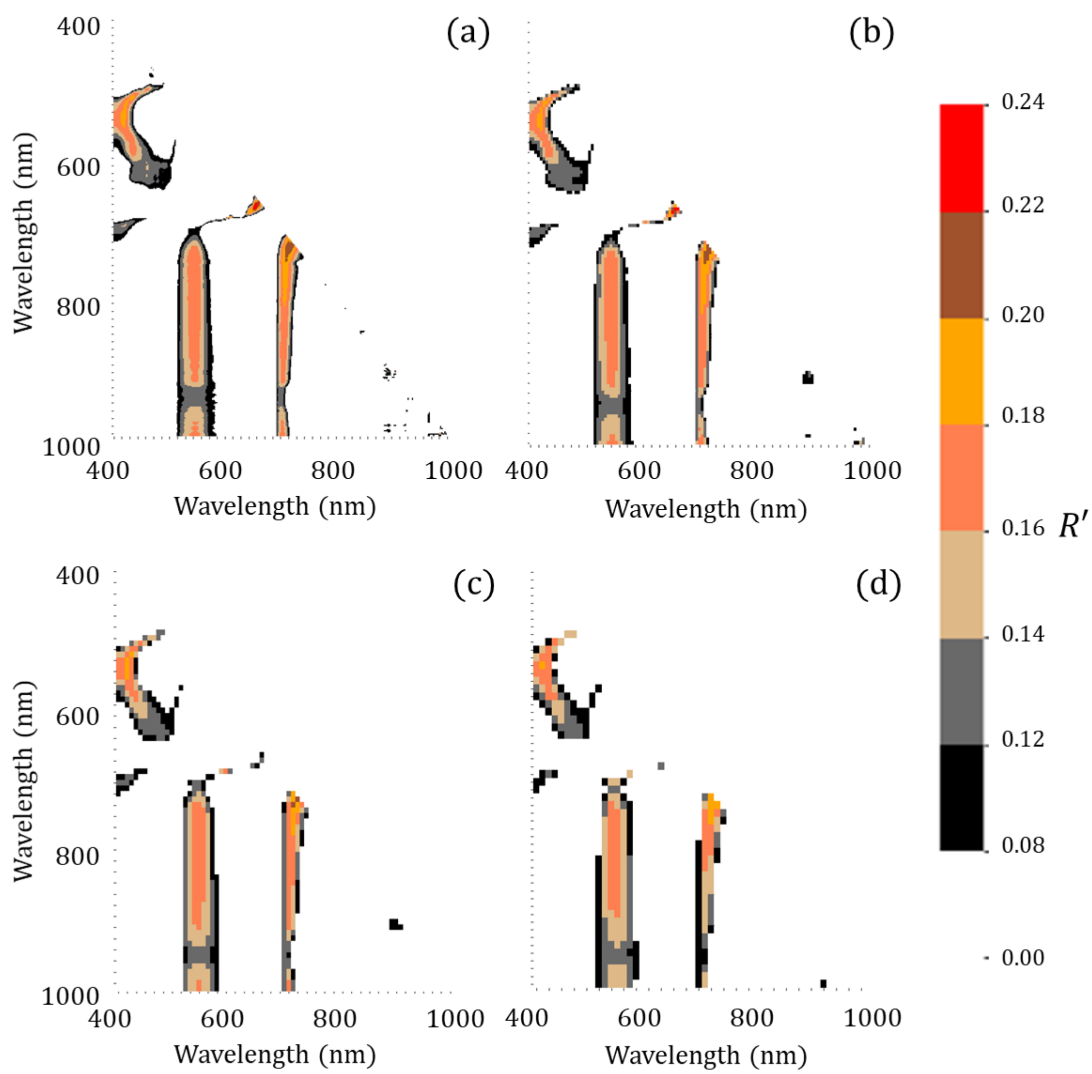


Figure 6.17: Comparison of correlation coefficient difference heat map showing only those indices which show superior correlation with LNC compared to LWC. The bandwidths used to create these leaf nitrogen content heatmaps are as follows: (a) 2 nm, (b) 5 nm, (c) 8 nm, (d) 11 nm.

The 6-leaf stage and tasselling stage maps were classified based on estimated water and nitrogen values. Figure 6.18 shows the plot-level stress classification map. The red and blue color plots represent the stress classification using biophysical parameters, as explained in chapter five.

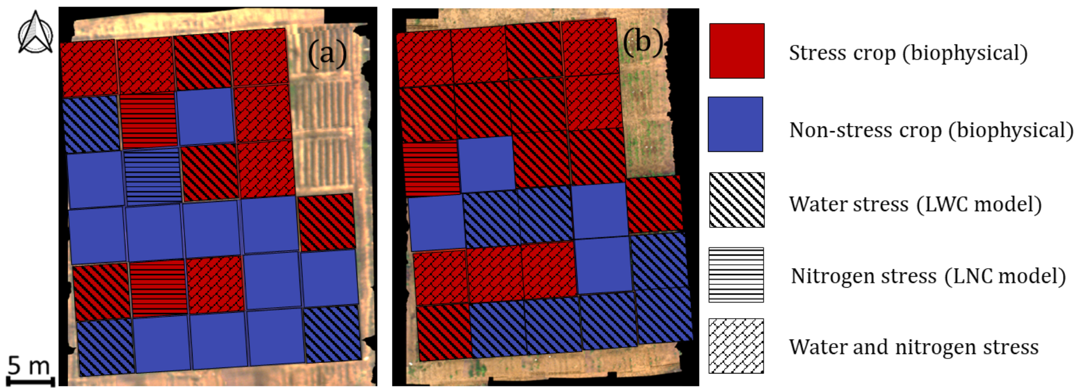


Figure 6.18: The combined water and nitrogen stress map for (a) 6-leaf stage and (b) pre-tasseling stage of 2018-19 *Rabi* season.

Different fillers are given based on the LWC and LNC model output. There are no cases where biophysical property based estimation suggests no stress condition, but the biochemical models classify it as a stress condition. However, if the biophysical property-based model classifies plots as a healthy condition but biochemical suggests water, nitrogen, or both type of stress, the plot was classified based on the biochemical content model.

## 6.3 Chapter summary

This chapter discussed the methods of LWC and LNC estimation from hyperspectral data and developed a LWC model using a new hyperspectral (400-1000 nm) approach for estimation of LWC at an early crop growth stage. Seven indices were created using spectroradiometer data based on the overtone frequencies of O-H bonds of water molecules. Three of the seven indices were shown to have sensitivity for LWC estimation from drone-based hyperspectral data. The model created from these indices estimated LWC at the 6-leaf stage and before tasseling stage of the crop growth with an $R^2$ of 0.93 and RMSE of 1.6 % (g/g). This early growth stage LWC estimation can be used to identify water-stressed plots, and thus potential yield loss can be avoided. Accordingly, this model can be used for estimating spatial and temporal LWC changes across farms in near-real-time to take scientific-based decision making on irrigation management. In the second part of the chapter, some indices were identified for estimating LNC and implemented on the farm hyperspectral data. Due to the high dependency of LNC on LWC, a critical analysis of the distribution of LNC in the LWC areas was undertaken, demonstrating that the LNC model was capable of distinguishing nutrient stress areas where water stress was present. A stress classification map was prepared by combining biophysical and biochemical estimation model results.

*This page has intentionally been left blank.*

# Chapter 7
# Conclusions and future scope

*There are many ideas about future farming, and in all of them, researchers have identified that farming will become autonomous and on-farm plant level decisions will be made. This research is a little step towards this concept of future farming. This image is adapted from Ham Farms website.*

# 7. Conclusions and future scope

The research presented in this thesis developed a method to make plant-level farm management decisions using remotely sensed, high-resolution data. The research showed how crop biophysical properties could be used to identify stress areas in the farm, and using crop water and nitrogen models; the stressed areas can be further classified into water and/or nitrogen stress zones. Most of the currently available farm data analysis methods estimate the crop stress at canopy level with a large pixel size as one point. However, considering the futuristic approach to farming, plant level decision making will be needed.

## 7.1 Salient features and research outcomes

The models developed in this research can be used for instantaneous and early-stage water and nitrogen stress detection in the crop. Moreover, using the biophysical properties of the crop in association with APSIM simulation, long term crop stress areas can also be identified. Some of the salient features of this research are:

- The LAI model has introduced the concept of vertical leaf area distribution factor (VLADF), using which near-to-true LAI values can be calculated using drone-based RGB images.
- Height estimation model has shown that for flat and sparse canopy, crop height can be calculated with use of only DSM data.
- The build leaf water and nitrogen content estimation models have performed with high accuracy even for early growth stages of the crop.
- The bandwidth of the hyperspectral data for accurate estimation of LWC and LNC have been found to be less than 11 nm, and 5nm, respctively. But it has been seen that narrower the bandwidth, better the result.
- The fusion of leaf water and nitrogen content models were able to distinguish between the water and nitrogen stress areas precisely in the water stress regions.

## 7.2 Conclusions

The analysis of ground truth data about crop biophysical parameters has revealed that these parameters get affected by water stress. Differences in canopy height or LAI in water stress and optimally irrigated plots are high. However, different nitrogen treatments for the same irrigation levels plots could not distinguish between LAI or height values for high and low fertilisation treatment plots. The analysis of ground truth data about crop biochemical parameters has revealed that the leaf water and leaf nitrogen content both reduces as the crop moves towards the maturity stage. Thus, a single value of leaf water or leaf nitrogen content cannot represent the stress level for all the growth stages, and therefore a growth stage based estimation parameter models are required.

Using drone-based RGB data, two models for estimation of leaf area index from top-of-canopy images were developed and evaluated in this research. The first, an empirical model trained and tested on Licor canopy analyser data, was found to have higher $R^2$ and lower RMSE values than existing farm-level remote sensing-based LAI estimation techniques. But as this model was trained on Licor canopy analyser data, it was more representative of foliage area index and thus had a poor estimation of the leaf area index derived from manual measurements. The second model was based on the conceptual use of a VLADF (vertical leaf area distribution factor), estimated through allometric properties of the canopy, to relate top-of-canopy leaf area to full canopy leaf area for different growth stages and heights of the crop. This enabled the changes within the canopy to be captured even during canopy closure (i.e. post tasselling stage). This new model can therefore be used for analysing spatial and temporal LAI changes across farms in near real-time with an $R^2$ of ~0.6 and RMSE of 0.73 when compared to independent manual measurements.

The APSIM model was simulated to obtain temporal LAI and crop height for optimal management conditions. The simulated canopy height was underestimated until the crop's tasselling stage but performed fine for the productive stage of the crop. The simulated height till the tasselling stage was corrected using the rate of change of simulated LAI values. Two models were created using the simulated reference data to estimate the healthiness/stress levels in the crop. First, a linear model logic was made and tested on the drone-based data. As the healthiness of the crop is directly proportional to the yield, thus to validate the linear model, the healthiness factor was correlated to crop yield and $R^2$ of 0.42, 0.56, and 0.63 were obtained for the early vegetative, tasselling, and dough stage, respectively. Second, a random forest model was trained on the synthetic data generated using simulated LAI and height values. The model is validated similar to the linear model, and $R^2$ of 0.45, 0.61, and 0.67 were obtained for the early vegetative, tasselling, and dough stage, respectively. The random forest model seemed to perform better than the linear model. This model can be used for long term stress (water or pest) detection on the farm.

The 701 nm band of hyperspectral data was used to detect the maize tassels using image processing techniques. The model has shown high precision - 97.7, and a low false-negative rate - 10.7. The tasselling percentage after one week of onset of tassels have also found to be correlated with the water stress in the plots. Lower the tasselling percentage from 45% percentage level, higher the water stress.

The hyperspectral data has been used to develop a new approach for leaf water content (LWC) and leaf nitrogen content (LNC) estimation at an early crop growth stage. For estimation of LWC, Seven indices were created using spectroradiometer data based on the overtone frequencies of O-H bonds of water molecules. Three of the seven indices were shown to have a sensitivity for LWC estimation from drone-based hyperspectral data. The model created from these indices has shown precise estimation of LWC at the 6-leaf stage and before tasseling stage of the crop growth with an $R^2$ of 0.93 and RMSE of 1.6 % g/g. This early growth stage LWC estimation can be used to identify water-stressed plots, and thus potential yield loss can be avoided. Accordingly, this model can be used for estimating spatial and temporal LWC changes across farms in near-real-time to undertake decision making on irrigation management.

For estimation of LNC, four indices were created using spectroradiometer data. The selection was made from those areas of indices-LNC correlation heatmap, where the correlation for nitrogen was greater than the correlation for water. One of the seven indices has shown to have a sensitivity for LNC estimation from drone-based hyperspectral data. Two wavelengths in the red-edge zone has found to be sensitive towards LNC. The model created using this index has shown a maximum $R^2$ of 0.64 and 0.43 on water stress areas for pre-tasseling and 6-leaf stage crop, respectively. The model has shown a lower $R^2$ of 0.12 and 0.25 on high LWC plants for pre-tasseling and 6-leaf stage crop, respectively. This suggests that LNC model accuracy will be higher in the water-stressed areas. Thus, before applying the LNC model, the farm needs to be classified in water stress and no water stress areas using the LWC model to decide the water and nitrogen stress of the crop. The LNC model can distinguish nitrogen stress areas within the water-stressed locations. However, the LNC model has weakly performed on those areas where LWC was higher.

## 7.3 Limitations

This research has the following limitations:

1. The VLADF-based true-LAI estimation model created in this research is only applicable to maize crops with similar architectural properties. For any crop with different architectural properties, only field data need to be collected to create another VLADF table.

2. The APSIM simulation model used in this research was not calibrated for local field conditions. Instead, the best-fitting parameters with known field data were used to simulate the optimal condition biophysical properties. This model would benefit from being calibrated for local field conditions in scenarios where reference field values are unknown.

3. The LWC/LNC indices and models created in this research do not

incorporate stress conditions due to pests and diseases. Accordingly, the model prediction will not represent such external factors, resulting in potential inaccuracies in the estimation of LNC and LWC.

4. The practical implementation of techniques suggested in this research for marginal farmers is a challenge due to its high cost. Moreover, the operation of these technologies needs technical expertise. Thus, disruptive policy intervention may be required in order to achieve widespread implementation.

## 7.4 Future scope

This research opens up multiple dimensions for many other researchers to improve the model by introducing/improving the following:

1. This research has focussed on analysing irrigation and fertilisation management. However, there can be other biotic stresses due to pests or diseases which may affect crop growth. There is a need to add the pest/ disease estimation model to precisely comment on the reason for crop stress.

2. A new concept of vertical leaf area distribution factor (VLADF) has been introduced in this research. However, this model is created using two years of ground-truth data about crop structural parameters at a single site, thus limited to the maize crop. The architectural information input to the VLADF model can be made dynamic by taking input from the point cloud created using the overlapping top-of-canopy RGB images. This will allow the model to work for various crop species without using a lot of ground samples. The VLADF model needs to be tested at different sites and for different crop types.

3. One of the major research gaps (in remote sensing) found during this research is that very few studies are available on the dynamics of temporal leaf nitrogen content with respect to change in leaf water

content. As LWC and LNC are closely related, and this research found that the LNC is not easily distinguished for higher LWC areas, the reason for these limitations needs to be identified using more controlled experiments.

4. The detection of water absorption bands identified in this research indices should be checked for different crops. The study of atmospheric effects in different humid conditions on the sensitivity of these indices can be a good research question for future studies.
5. This research focused on the 'leaf-level analysis'. This can be scaled to the canopy level, and the results are compared against models like PROSAIL. This kind of analysis may help in connecting process-based RT models with field-based data analysis.
6. The height module of the APSIM model gives highly attenuated results. This is also the problem with models like DSSAT. The height module of these models can be made more sensitive to the implemented management practices.
7. The tassel counting model developed in this research is validated on a small farm. This model needs to be tested on a big size farm, preferably a farmer’s field.
8. The models developed in this research can be put together as a decision support system and need to be tested on the actual farm condition. The biophysical properties like LAI, crop height, and tasseling percentage and biochemical properties like leaf water and nitrogen content can be used in a spatial decision support system where on a computer/mobile screen, farmers/users can see the locations and severity of crop stress and suggestions related to management actions can be provided. This will enable farmers to make near-real-time farm management decisions. A small step has already been taken in this direction and a farm-health

visualization platform is under preparation. The initial version of the platform can be seen at https://agroinformaticslab.github.io/.

9. This research is limited to the identification of stressed areas. However, to make farm-level management decisions, it has to be estimated that how much water or fertiliser needs to be supplied at a particular location in the farm. More research needs to be done on creating models for the estimation of these farm management actions.

# References:

Abutalipov, R.N., Bolgov, Y.V. and Senov, H.M., 2016, October. Flowering plants pollination robotic system for greenhouses by means of nano copter (drone aircraft). In 2016 IEEE Conference on Quality Management, Transport and Information Security, Information Technologies (IT&MQ&IS) (pp. 7-9). IEEE.

Acevo-Herrera, R., Aguasca, A., Bosch-Lluis, X., Camps, A., Martínez-Fernández, J., Sánchez-Martín, N. and Pérez-Gutiérrez, C., 2010. Design and first results of an UAV-borne L-band radiometer for multiple monitoring purposes. Remote Sensing, 2(7), pp.1662-1679.

Ajayi, O.G., Salubi, A.A., Angbas, A.F. and Odigure, M.G., 2017. Generation of accurate digital elevation models from UAV acquired low percentage overlapping images. International journal of remote sensing, 38(8-10), pp.3113-3134.

Allen, W.A., Gausman, H.W., Richardson, A.J. and Thomas, J.R., 1969. Interaction of isotropic light with a compact plant leaf. Josa, 59(10), pp.1376-1379.

Al-Zadjali, A., Shi, Y., Scott, S., Deogun, J.S. and Schnable, J., 2020, April. Faster R-CNN-based deep learning for locating corn tassels in UAV imagery. In Autonomous Air and Ground Sensing Systems for Agricultural Optimization and Phenotyping V (Vol. 11414, p. 1141406). International Society for Optics and Photonics.

Andersson, I. and Backlund, A., 2008. Structure and function of Rubisco. Plant Physiology and Biochemistry, 46(3), pp.275-291.

Aroca, R., 2012. Plant responses to drought stress. *From morphological to molecular features*. Springer-Verlag Berlin Heidelberg. ISBN 978-3-642-32653-0. pp.1-5.

Anon. 2018a. 'Landinfo'. Retrieved (http://www.landinfo.com/satellite-imagery-pricing.html).

Anon. 2018b. 'Satellite Imaging Corp'. Retrieved on 01 April 2021, from http://www.satimagingcorp.com/satellite-sensors/geoeye-2/.

Arvin R. Mosier, J. Keith Syers, and John R. Freney. 2013. Agriculture and the Nitrogen Cycle : Assessing the Impacts of Fertilizer Use on Food Production and the Environment. edited by A. Mosier. Island Press.

Atafar, Zah Wu ra, Alireza Mesdaghinia, Jafar Nouri, Mehdi Homaee, Masoud Yunesian, Mehdi Ahmadimoghaddam, and Amir Hossein Mahvi. 2010. 'Effect of Fertiliser Application on Soil Heavy Metal Concentration'. *Environmental Monitoring and Assessment* 160(1–4):83–89.

Baret, F. and Fourty, T., 1997. Estimation of leaf water content and specific leaf weight from reflectance and transmittance measurements. Agronomie, 17(9-10), pp.455-464.

Behera, Soumit K., Pankaj Srivastava, Uday V. Pathre, and Rakesh Tuli. 2010. 'An Indirect Method of Estimating Leaf Area Index in Jatropha Curcas L. Using LAI-2000 Plant Canopy Analyzer'. *Agricultural and Forest Meteorology* 150(2):307–11.

Bell, Lindsay W., Felicity Byrne (nee Flugge), Mike A. Ewing, and Len J. Wade. 2008. 'A Preliminary Whole-Farm Economic Analysis of Perennial Wheat in an Australian Dryland Farming System'. *Agricultural Systems* 96(1–3):166–74.

Bellvert, J., et al. "Mapping crop water stress index in a 'Pinot-noir'vineyard: comparing ground measurements with thermal remote sensing imagery from an unmanned aerial vehicle." Precision agriculture 15.4 (2014): 361-376.

Belgiu, M. and Drăguţ, L., 2016. Random forest in remote sensing: A review of applications and future directions. ISPRS journal of photogrammetry and remote sensing, 114, pp.24-31.

Bendig, Juliane, Kang Yu, Helge Aasen, Andreas Bolten, Simon Bennertz, Janis Broscheit, Martin L. Gnyp, and Georg Bareth. 2015. 'Combining UAV-Based Plant Height from Crop Surface Models, Visible, and near Infrared Vegetation Indices for Biomass Monitoring in Barley'. *International Journal of Applied Earth Observation and Geoinformation* 39:79–87.

Berni, Jose AJ, et al. "Thermal and narrowband multispectral remote sensing for vegetation monitoring from an unmanned aerial vehicle." IEEE Transactions on Geoscience and Remote Sensing 47.3 (2009): 722-738.

Blum, A., 2011. Plant water relations, plant stress and plant production. In *Plant breeding for water-limited environments* (pp. 11-52). Springer, New York, NY.

Blumenthal, J.M., Baltensperger, D.D., Cassman, K.G., Mason, S.C. and Pavlista, A.D., 2008. Importance and effect of nitrogen on crop quality and health. In Nitrogen in the Environment (pp. 51-70). Academic Press.

Bonan, Gordon B. 1993. 'Importance of Leaf Area Index and Forest Type When Estimating Photosynthesis in Boreal Forests'. *Remote Sensing of Environment* 43(3):303–14.

Bousquet, L., Lachérade, S., Jacquemoud, S. and Moya, I., 2005. Leaf BRDF measurements and model for specular and diffuse components differentiation. Remote Sensing of Environment, 98(2-3), pp.201-211.

Braun, C.L. and Smirnov, S.N., 1993. Why is water blue?. Journal of Chemical Education, 70(8), p.612.

Breda, N.J., 2003. Ground-based measurements of leaf area index: a review of methods, instruments and current controversies. Journal of experimental botany, 54(392), pp.2403-2417.

Breiman, L., 2001. Random forests. Machine learning, 45(1), pp.5-32.

Broadbent, F. and Rauschkolb, R., 1977. Nitrogen fertilization and water pollution. California Agriculture, 31(5), pp.24-25.

Bryson, R. J., N. D. Paveley, W. S. Clark, R. Slylvester-Bradley, and R. K. Scott. 1997. 'Use of In-Field Measurements of Green Leaf Area and Incident Radiation to Estimate the Effects of Yellow Rust Epidemics on the Yield of Winter Wheat'. *Developments in Crop Science* 25(C):77–86.

Bullock, David S. and Donald G. Bullock. 2000. 'From Agronomic Research to Farm Management Guidelines: A Primer on the Economics of Information and Precision Technology'. *Precision Agriculture* 2(1):71–101.

Büning-Pfaue, H., 2003. Analysis of water in food by near infrared spectroscopy. Food Chemistry, 82(1), pp.107-115.

Cakir, R., 2004. Effect of water stress at different development stages on vegetative and reproductive growth of corn. Field Crops Research, 89(1), pp.1-16.

Calderón, R., Navas-Cortés, J.A., Lucena, C. and Zarco-Tejada, P.J., 2013. High-resolution airborne hyperspectral and thermal imagery for early detection of Verticillium wilt of olive using fluorescence, temperature and narrow-band spectral indices. Remote Sensing of Environment, 139, pp.231-245.

Campbell, C.A., Selles, F., Zentner, R.P. and McConkey, B.G., 1993. Available water and nitrogen effects on yield components and grain nitrogen of zero-till spring wheat. Agronomy Journal, 85(1), pp.114-120.

Carter, G.A., 1991. Primary and secondary effects of water content on the spectral reflectance of leaves. *American journal of botany*, *78*(7), pp.916-924.

Casas, A., Riaño, D., Ustin, S.L., Dennison, P. and Salas, J., 2014. Estimation of water-related biochemical and biophysical vegetation properties using multitemporal airborne hyperspectral data and its comparison to MODIS spectral response. Remote Sensing of Environment, 148, pp.28-41.

Ceccato, P., Flasse, S., Tarantola, S., Jacquemoud, S. and Grégoire, J.M., 2001. Detecting vegetation leaf water content using reflectance in the optical domain. *Remote sensing of environment*, *77*(1), pp.22-33.

Cetinsoy, E., 2015, June. Design and control of a gas-electric hybrid quad tilt-rotor UAV with morphing wing. In 2015 International Conference on Unmanned Aircraft Systems (ICUAS) (pp. 82-91). Ieee.

Cinque, G., Croce, R. and Bassi, R., 2000. Absorption spectra of chlorophyll a and b in Lhcb protein environment. Photosynthesis research, 64(2-3), pp.233-242.

Chaplin, M., 2006. Do we underestimate the importance of water in cell biology?. Nature Reviews Molecular Cell Biology, 7(11), pp.861-866.

Chaplin, M., 2008. Water absorption spectrum. *Water Structure and Science*.

Chaudhary, P., Godara, S., Cheeran, A.N. and Chaudhari, A.K., 2012. Fast and accurate method for leaf area measurement. International journal of computer applications, 49(9), pp.22-25.

Chen, J. M. and T. A. Black. 1991. 'Measuring Leaf Area Index on Plant Canopies with Brach Arquitecture'. *Agricultural and Forest Meteorology* 57(1953):1–12.

Chen, J. M. and T. A. Black. 1992. 'Defining Leaf Area Index for Non-flat Leaves'. *Plant, Cell & Environment* 15(4):421–29.

Chen, J.M., Rich, P.M., Gower, S.T., Norman, J.M. and Plummer, S., 1997. Leaf area index of boreal forests: Theory, techniques, and measurements. Journal of Geophysical Research: Atmospheres, 102(D24), pp.29429-29443.

Chen, P., Haboudane, D., Tremblay, N., Wang, J., Vigneault, P. and Li, B., 2010. New spectral indicator assessing the efficiency of crop nitrogen treatment in corn and wheat. Remote Sensing of Environment, 114(9), pp.1987-1997.

Cheng, T., Rivard, B. and Sanchez-Azofeifa, A., 2011. Spectroscopic determination of leaf water content using continuous wavelet analysis. *Remote Sensing of Environment*, *115*(2), pp.659-670.

Cheng, Y.B., Zarco-Tejada, P.J., Riaño, D., Rueda, C.A. and Ustin, S.L., 2006. Estimating vegetation water content with hyperspectral data for different canopy scenarios: Relationships between AVIRIS and MODIS indexes. *Remote Sensing of Environment*, *105*(4), pp.354-366.

Cheng, Y.B., Ustin, S.L., Riaño, D. and Vanderbilt, V.C., 2008. Water content estimation from hyperspectral images and MODIS indexes in Southeastern Arizona. *Remote Sensing of Environment*, *112*(2), pp.363-374.

Christiansen, M.P., Laursen, M.S., Jørgensen, R.N., Skovsen, S. and Gislum, R., 2017. Designing and testing a UAV mapping system for agricultural field surveying. Sensors, 17(12), p.2703.

Cho, M.A. and Skidmore, A.K., 2006. A new technique for extracting the red edge position from hyperspectral data: The linear extrapolation method. Remote sensing of environment, 101(2), pp.181-193.

Clevers, J.G., Kooistra, L. and Schaepman, M.E., 2010. Estimating canopy water content using hyperspectral remote sensing data. *International Journal of Applied Earth Observation and Geoinformation*, *12*(2), pp.119-125.

Colaizzi, P.D., Evett, S.R., Brauer, D.K., Howell, T.A., Tolk, J.A. and Copeland, K.S., 2017. Allometric method to estimate leaf area index for row crops. Agronomy Journal, 109(3), pp.883-894.

Colombo, R., Meroni, M., Marchesi, A., Busetto, L., Rossini, M., Giardino, C. and Panigada, C., 2008. Estimation of leaf and canopy water content in poplar plantations by means of hyperspectral indices and inverse modeling. Remote Sensing of Environment, 112(4), pp.1820-1834.

Corti, M., Gallina, P.M., Cavalli, D. and Cabassi, G., 2017. Hyperspectral imaging of spinach canopy under combined water and nitrogen stress to estimate biomass, water, and nitrogen content. Biosystems Engineering, 158, pp.38-50.

Craig, J.R. and Wollum, A.G., 1982. Ammonia volatilization and soil nitrogen changes after urea and ammonium nitrate fertilization of Pinus taeda L. Soil Science Society of America Journal, 46(2), pp.409-414.

Crameri, F., Shephard, G.E. and Heron, P.J., 2020. The misuse of colour in science communication. Nature communications, 11(1), pp.1-10.

Cristóbal, J., Graham, P., Prakash, A., Buchhorn, M., Gens, R., Guldager, N. and Bertram, M., 2021. Airborne Hyperspectral Data Acquisition and Processing in the Arctic: A Pilot Study Using the Hyspex Imaging Spectrometer for Wetland Mapping. Remote Sensing, 13(6), p.1178.

Curran, P.J., Dungan, J.L., Macler, B.A., Plummer, S.E. and Peterson, D.L., 1992. Reflectance spectroscopy of fresh whole leaves for the estimation of chemical concentration. Remote Sensing of Environment, 39(2), pp.153-166.

Cutini, A., Matteucci, G. and Mugnozza, G.S., 1998. Estimation of leaf area index with the Li-Cor LAI 2000 in deciduous forests. Forest Ecology and Management, 105(1-3), pp.55-65.

Damodaran, S., 2008. Amino acids, peptides and proteins. Fennema's food chemistry, 4, pp.425-439.

Daughtry, C.S.T., Walthall, C.L., Kim, M.S., De Colstoun, E.B. and McMurtrey Iii, J.E., 2000. Estimating corn leaf chlorophyll concentration from leaf and canopy reflectance. Remote sensing of Environment, 74(2), pp.229-239.

Delegido, J., Verrelst, J., Meza, C.M., Rivera, J.P., Alonso, L. and Moreno, J., 2013. A red-edge spectral index for remote sensing estimation of green LAI over agroecosystems. European Journal of Agronomy, 46, pp.42-52.

Deng, L., Mao, Z., Li, X., Hu, Z., Duan, F. and Yan, Y., 2018. UAV-based multispectral remote sensing for precision agriculture: A comparison between different cameras. ISPRS journal of photogrammetry and remote sensing, 146, pp.124-136.

Dhaliwal, G.S., Gupta, N., Kukal, S.S. and Kaur, M., 2011. Standardization of automated Vario EL III CHNS analyzer for total carbon and nitrogen determination in soils. Communications in soil science and plant analysis, 42(8), pp.971-979.

Drewry, D. T., P. Kumar, S. Long, C. Bernacchi, X. Z. Liang, and M. Sivapalan. 2010. 'Ecohydrological Responses of Dense Canopies to Environmental Variability: 1. Interplay between Vertical Structure and Photosynthetic Pathway'. *Journal of Geophysical Research: Biogeosciences* 115(4):1–25.

Du, L., Gong, W., Shi, S., Yang, J., Sun, J., Zhu, B. and Song, S., 2016. Estimation of rice leaf nitrogen contents based on hyperspectral LIDAR. International Journal of Applied Earth Observation and Geoinformation, 44, pp.136-143.

Duan, S.B., Li, Z.L., Wu, H., Tang, B.H., Ma, L., Zhao, E. and Li, C., 2014. Inversion of the PROSAIL model to estimate leaf area index of maize, potato, and sunflower fields from unmanned aerial vehicle hyperspectral data. International Journal of Applied Earth Observation and Geoinformation, 26, pp.12-20.

Duangpapeng, P., Ketthaisong, D., Lomthaisong, K., Lertrat, K., Scott, M.P. and Suriharn, B., 2018. Corn tassel: A new source of phytochemicals and antioxidant potential for value-added product development in the agro-industry. Agronomy, 8(11), p.242.

Dufrêne, Eric and Nathalie Bréda. 2010. 'International Association for Ecology Estimation of Deciduous Forest Leaf Area Index Using Direct and Indirect Methods Published by : Springer in Cooperation with International Association for Ecology Stable URL : Http://Www.Jstor.Org/Stable/4221092'. *Ecology* 104(2):156–62.

Eaton, Frank D., and Inge Dirmhirn. "Reflected irradiance indicatrices of natural surfaces and their effect on albedo." Applied Optics 18.7 (1979): 994-1008.

Eitel, J.U.H., Long, D.S., Gessler, P.E. and Smith, A.M.S., 2007. Using in-situ measurements to evaluate the new RapidEye™ satellite series for prediction of wheat nitrogen status. International Journal of Remote Sensing, 28(18), pp.4183-4190.

Eitel, J.U., Gessler, P.E., Smith, A.M. and Robberecht, R., 2006. Suitability of existing and novel spectral indices to remotely detect water stress in Populus spp. Forest Ecology and Management, 229(1-3), pp.170-182.

Elrashidi, M.A., Mays, M.D., Peaslee, S.D. and Hooper, D.G., 2005. A technique to estimate nitrate–nitrogen loss by runoff and leaching for agricultural land, Lancaster County, Nebraska. Communications in soil science and plant analysis, 35(17-18), pp.2593-2615.

Etminan, A., Tabatabaeenejad, A. and Moghaddam, M., 2020. Retrieving Root-Zone Soil Moisture Profile From P-Band Radar via Hybrid Global and Local Optimization. *IEEE Transactions on Geoscience and Remote Sensing*, *58*(8), pp.5400-5408.

Fan, W., Hu, B., Miller, J. and Li, M., 2009. Comparative study between a new nonlinear model and common linear model for analysing laboratory simulated-forest hyperspectral data. International Journal of Remote Sensing, 30(11), pp.2951-2962.

Fang, Meihong, et al. "A new spectral similarity water index for the estimation of leaf water content from hyperspectral data of leaves." Remote Sensing of Environment 196 (2017): 13-27.

Fassnacht, Karin S., Stith T. Gower, John M. Norman, and Ross E. McMurtric. 1994. 'A Comparison of Optical and Direct Methods for Estimating Foliage Surface Area Index in Forests'. *Agricultural and Forest Meteorology* 71(1–2):183–207.

Feilhauer, H., Asner, G.P. and Martin, R.E., 2015. Multi-method ensemble selection of spectral bands related to leaf biochemistry. Remote Sensing of Environment, 164, pp.57-65.

Feng, W., Yao, X., Zhu, Y., Tian, Y.C. and Cao, W.X., 2008. Monitoring leaf nitrogen status with hyperspectral reflectance in wheat. European Journal of Agronomy, 28(3), pp.394-404.

Feng, W., Zhang, H.Y., Zhang, Y.S., Qi, S.L., Heng, Y.R., Guo, B.B., Ma, D.Y. and Guo, T.C., 2016. Remote detection of canopy leaf nitrogen concentration in winter wheat by using water resistance vegetation indices from in-situ hyperspectral data. Field Crops Research, 198, pp.238-246.

Feret, J.B., François, C., Asner, G.P., Gitelson, A.A., Martin, R.E., Bidel, L.P., Ustin, S.L., Le Maire, G. and Jacquemoud, S., 2008. PROSPECT-4 and 5: Advances in the leaf optical properties model separating photosynthetic pigments. Remote sensing of environment, 112(6), pp.3030-3043.

Féret, J.B., Gitelson, A.A., Noble, S.D. and Jacquemoud, S., 2017. PROSPECT-D: Towards modeling leaf optical properties through a complete lifecycle. Remote Sensing of Environment, 193, pp.204-215.

Finn, M.P., Lewis, M., Bosch, D.D., Giraldo, M., Yamamoto, K., Sullivan, D.G., Kincaid, R., Luna, R., Allam, G.K., Kvien, C. and Williams, M.S., 2011. Remote sensing of soil moisture using airborne hyperspectral data. *GIScience & Remote Sensing*, *48*(4), pp.522-540.

Fitzgerald, G.J., Rodriguez, D., Christensen, L.K., Belford, R., Sadras, V.O. and Clarke, T.R., 2006. Spectral and thermal sensing for nitrogen and water status in rainfed and irrigated wheat environments. Precision Agriculture, 7(4), pp.233-248.

Friedman, J.H., 2001. Greedy function approximation: a gradient boosting machine. Annals of statistics, pp.1189-1232.

Franks F. (1988) Protein Hydration. In: Franks F. (eds) Characterization of Proteins. Biological Methods. Humana Press. https://doi.org/10.1007/978-1-59259-437-5_5

Freitas, S.R., Mello, M.C. and Cruz, C.B., 2005. Relationships between forest structure and vegetation indices in Atlantic Rainforest. Forest ecology and management, 218(1-3), pp.353-362.

Gabriel, Jose L., Pablo J. Zarco-Tejada, P. Juan López-Herrera, Enrique Pérez-Martín, Maria Alonso-Ayuso, and Miguel Quemada. 2017. 'Airborne and Ground Level Sensors for Monitoring Nitrogen Status in a Maize Crop'. *Biosystems Engineering* 160:124–33.

Gago, J., Douthe, C., Coopman, R.E., Gallego, P.P., Ribas-Carbo, M., Flexas, J., Escalona, J. and Medrano, H., 2015. UAVs challenge to assess water stress for sustainable agriculture. Agricultural water management, 153, pp.9-19.

Gallik, S., 2012. Determination of the anthocyanin concentration in table wines and fruit juices using visible light spectrophotometry. Cell Biology, 2(1), pp.1-12.

Gamon, J.A., Field, C.B., Goulden, M.L., Griffin, K.L., Hartley, A.E., Joel, G., Penuelas, J. and Valentini, R., 1995. Relationships between NDVI, canopy structure, and photosynthesis in three Californian vegetation types. Ecological Applications, 5(1), pp.28-41.

Gao, B.C., 1996. NDWI—A normalized difference water index for remote sensing of vegetation liquid water from space. Remote sensing of environment, 58(3), pp.257-266.

Gao, B.C., Montes, M.J., Davis, C.O. and Goetz, A.F., 2009. Atmospheric correction algorithms for hyperspectral remote sensing data of land and ocean. *Remote sensing of environment*, *113*, pp.S17-S24.

Gao, Y., Walker, J.P., Allahmoradi, M., Monerris, A., Ryu, D. and Jackson, T.J., 2015. Optical sensing of vegetation water content: a synthesis study. *IEEE Journal of Selected Topics in Applied Earth Observations and Remote Sensing*, *8*(4), pp.1456-1464.

Garrigues, S., N. V. Shabanov, K. Swanson, J. T. Morisette, F. Baret, and R. B. Myneni. 2008. 'Intercomparison and Sensitivity Analysis of Leaf Area Index Retrievals from LAI-2000, AccuPAR, and Digital Hemispherical Photography over Croplands'. *Agricultural and Forest Meteorology* 148(8–9):1193–1209.

Ge, X., Wang, J., Ding, J., Cao, X., Zhang, Z., Liu, J. and Li, X., 2019. Combining UAV-based hyperspectral imagery and machine learning algorithms for soil moisture content monitoring. PeerJ, 7, p.e6926.

Gezgin, S. and Bayrakll, F., 1995. Ammonia volatilization from ammonium sulphate, ammonium nitrate, and urea surface applied to winter wheat on a calcareous soil. Journal of plant nutrition, 18(11), pp.2483-2494.

Gitelson, Anatoly A. 2004. 'Wide Dynamic Range Vegetation Index for Remote Quantification of Biophysical Characteristics of Vegetation'. *Journal of Plant Physiology* 161(2):165–73.

Gitelson, A.A., Merzlyak, M.N. and Chivkunova, O.B., 2001. Optical properties and nondestructive estimation of anthocyanin content in plant leaves. Photochemistry and photobiology, 74(1), pp.38-45.

Goel, Narendra S. "Models of vegetation canopy reflectance and their use in estimation of biophysical parameters from reflectance data." Remote Sensing Reviews 4.1 (1988): 1-212.

Gonzalez-Dugo, V., Durand, J.L. and Gastal, F., 2010. Water deficit and nitrogen nutrition of crops. A review. Agronomy for sustainable development, 30(3), pp.529-544.

Goswami, S., Gamon, J., Vargas, S. and Tweedie, C., 2015. Relationships of NDVI, Biomass, and Leaf Area Index (LAI) for six key plant species in Barrow, Alaska (No. e1127). PeerJ PrePrints.

Govaerts, Y.M., Jacquemoud, S., Verstraete, M.M. and Ustin, S.L., 1996. Three-dimensional radiation transfer modeling in a dicotyledon leaf. Applied Optics, 35(33), pp.6585-6598.

Gower, S.T., Kucharik, C.J. and Norman, J.M., 1999. Direct and indirect estimation of leaf area index, fAPAR, and net primary production of terrestrial ecosystems. Remote sensing of environment, 70(1), pp.29-51.

Guei, R.G. and Wassom, C.E., 1996. Genetic analysis of tassel size and leaf senescence and their relationships with yield in two tropical lowland maize populations. African Crop Science Journal, 4(3), pp.275-281.

Gupta, K.J. ed., 2020. Nitrogen Metabolism in Plants: Methods and Protocols. Springer New York.

Gutteridge, S. and Gatenby, A.A., 1995. Rubisco synthesis, assembly, mechanism, and regulation. The Plant Cell, 7(7), p.809.

Haboudane, D., Miller, J.R., Pattey, E., Zarco-Tejada, P.J. and Strachan, I.B., 2004. Hyperspectral vegetation indices and novel algorithms for predicting green LAI of crop canopies: Modeling and validation in the context of precision agriculture. Remote sensing of environment, 90(3), pp.337-352.

Haboudane, D., Miller, J.R., Tremblay, N., Zarco-Tejada, P.J. and Dextraze, L., 2002. Integrated narrow-band vegetation indices for prediction of crop chlorophyll content for application to precision agriculture. Remote sensing of environment, 81(2-3), pp.416-426.

Hadjimitsis, D.G., Clayton, C.R.I. and Hope, V.S., 2004. An assessment of the effectiveness of atmospheric correction algorithms through the remote sensing of some reservoirs. *International Journal of Remote Sensing*, *25*(18), pp.3651-3674.

Halagalimath, S.P., 2017. Effect of scheduling irrigation and mulching on growth and yield of maize (Zea mays L.). Journal of Farm Sciences, 30(1), pp.45-48.

Han, M., Zhang, H., DeJonge, K.C., Comas, L.H. and Trout, T.J., 2016. Estimating maize water stress by standard deviation of canopy temperature in thermal imagery. *Agricultural Water Management*, *177*, pp.400-409.

Hanrahan, G., Udeh, F. and Patil, D.G., 2005. Chemometrics and Statistics| Multivariate Calibration Techniques.

Hansen, P.M. and Schjoerring, J.K., 2003. Reflectance measurement of canopy biomass and nitrogen status in wheat crops using normalized difference vegetation indices and partial least squares regression. Remote sensing of environment, 86(4), pp.542-553.

Hardisky, M. A., and V. Klemas. "M. Smart.(1983). The influence of soil salinity, growth form, and leaf moisture on spectral radiance of spartina alterniflora canopies." Photogrammetric Engineering & Remote Sensing 16.9: 1581-1598.

Haris, P.I. and Chapman, D., 1994. Analysis of polypeptide and protein structures using Fourier transform infrared spectroscopy. In Microscopy, Optical Spectroscopy, and Macroscopic Techniques (pp. 183-202). Humana Press.

Henry, G. M., M. A. DeLorenzo, D. K. Beede, H. H. Van Horn, C. B. Moss, and W. G. Boggess. 1995. 'Determining Optimal Nutrient Management Strategies for Dairy Farms'. *Journal of Dairy Science* 78(3):693–703.

Hernández-Clemente, R., Navarro-Cerrillo, R.M. and Zarco-Tejada, P.J., 2012. Carotenoid content estimation in a heterogeneous conifer forest using narrow-band indices and PROSPECT+ DART simulations. Remote Sensing of Environment, 127, pp.298-315.

Herrmann, I., Bdolach, E., Montekyo, Y., Rachmilevitch, S., Townsend, P.A. and Karnieli, A., 2020. Assessment of maize yield and phenology by drone-mounted superspectral camera. Precision Agriculture, 21(1), pp.51-76.

Hossain, M. and V. P. Singh. 2000. 'Fertiliser Use in Asian Agriculture : Implications for Sustaining Food Security and the Environment'. 155–69.

Howitt, S.M. and Udvardi, M.K., 2000. Structure, function and regulation of ammonium transporters in plants. Biochimica et Biophysica Acta (BBA)-Biomembranes, 1465(1-2), pp.152-170.

Hsiao, T.C., 1973. Plant responses to water stress. *Annual review of plant physiology*, *24*(1), pp.519-570.

Hsiao, T.C., Fereres, E., Acevedo, E. and Henderson, D.W., 1976. Water stress and dynamics of growth and yield of crop plants. In *water and plant life* (pp. 281-305). Springer, Berlin, Heidelberg.

Huete, A., Didan, K., Miura, T., Rodriguez, E.P., Gao, X. and Ferreira, L.G., 2002. Overview of the radiometric and biophysical performance of the MODIS vegetation indices. Remote sensing of environment, 83(1-2), pp.195-213.

Huang, Y., Walker, J.P., Gao, Y., Wu, X. and Monerris, A., 2015. Estimation of vegetation water content from the radar vegetation index at L-band. *IEEE Transactions on Geoscience and Remote Sensing*, *54*(2), pp.981-989.

Hunter, K.M., Shakib, F.A. and Paesani, F., 2018. Disentangling coupling effects in the infrared spectra of liquid water. The Journal of Physical Chemistry B, 122(47), pp.10754-10761.

Hunt Jr, E. Raymond, and Barrett N. Rock. "Detection of changes in leaf water content using near-and middle-infrared reflectances." Remote sensing of environment 30.1 (1989): 43-54.

Hunt, E. Raymond, et al. "Evaluation of digital photography from model aircraft for remote sensing of crop biomass and nitrogen status." Precision Agriculture 6.4 (2005): 359-378.

Hunt Jr, E.R., Li, L., Yilmaz, M.T. and Jackson, T.J., 2011. Comparison of vegetation water contents derived from shortwave-infrared and passive-microwave sensors over central Iowa. *Remote Sensing of Environment*, *115*(9), pp.2376-2383.

Idso, S.B., Jackson, R.D., Pinter Jr, P.J., Reginato, R.J. and Hatfield, J.L., 1981. Normalizing the stress-degree-day parameter for environmental variability. Agricultural meteorology, 24, pp.45-55.

Ihuoma, Samuel O., and Chandra A. Madramootoo. "Sensitivity of spectral vegetation indices for monitoring water stress in tomato plants." Computers and Electronics in Agriculture 163 (2019): 104860.

Ishida, T., Kurihara, J., Viray, F.A., Namuco, S.B., Paringit, E.C., Perez, G.J., Takahashi, Y. and Marciano Jr, J.J., 2018. A novel approach for vegetation classification using UAV-based hyperspectral imaging. Computers and electronics in agriculture, 144, pp.80-85.

Jacquemoud, Stéphane, and L. S. Ustin. "Modeling leaf optical properties." Photobiological Sciences Online (2008).

Jacquemoud, Stéphane, et al. "PROSPECT+ SAIL models: A review of use for vegetation characterization." Remote sensing of environment 113 (2009): S56-S66.

Jacquemoud, S., Ustin, S.L., Verdebout, J., Schmuck, G., Andreoli, G. and Hosgood, B., 1996. Estimating leaf biochemistry using the PROSPECT leaf optical properties model. Remote sensing of environment, 56(3), pp.194-202.

Jay, S., Maupas, F., Bendoula, R. and Gorretta, N., 2017. Retrieving LAI, chlorophyll and nitrogen contents in sugar beet crops from multi-angular optical remote sensing: Comparison of vegetation indices and PROSAIL inversion for field phenotyping. Field Crops Research, 210, pp.33-46.

Jia, B., Wang, W., Ni, X., Lawrence, K.C., Zhuang, H., Yoon, S.C. and Gao, Z., 2020. Essential processing methods of hyperspectral images of agricultural and food products. Chemometrics and Intelligent Laboratory Systems, 198, p.103936.

Jiang, Z., Huete, A.R., Didan, K. and Miura, T., 2008. Development of a two-band enhanced vegetation index without a blue band. Remote sensing of Environment, 112(10), pp.3833-3845.

Jin, S., Su, Y., Gao, S., Wu, F., Hu, T., Liu, J., Li, W., Wang, D., Chen, S., Jiang, Y. and Pang, S., 2018. Deep learning: individual maize segmentation from terrestrial lidar data using faster R-CNN and regional growth algorithms. Frontiers in plant science, 9, p.866.

Jonckheere, I., Fleck, S., Nackaerts, K., Muys, B., Coppin, P., M. and Weiss, and F. Baret. 2004. 'Methods for Leaf Area Index Determination Part I : Theories , Techniques and Instruments'. Agric. For. Meteorol. 19–35.

Jones, Davey L., Paul Cross, Paul J. A. Withers, Thomas H. Deluca, David A. Robinson, Richard S. Quilliam, Ian M. Harris, David R. Chadwick, and Gareth Edwards-jones. 2013. 'Nutrient Stripping : The Global Disparity between Food Security and Soil Nutrient Stocks'. 851–62.

Jones, H.G. and Sirault, X.R., 2014. Scaling of thermal images at different spatial resolution: the mixed pixel problem. Agronomy, 4(3), pp.380-396.

Jones, J.W., Tsuji, G.Y., Hoogenboom, G., Hunt, L.A., Thornton, P.K., Wilkens, P.W., Imamura, D.T., Bowen, W.T. and Singh, U., 1998. Decision support system for agrotechnology transfer: DSSAT v3. In Understanding options for agricultural production (pp. 157-177). Springer, Dordrecht.

Justice, C.O., Vermote, E., Townshend, J.R., Defries, R., Roy, D.P., Hall, D.K., Salomonson, V.V., Privette, J.L., Riggs, G., Strahler, A. and Lucht, W., 1998. The Moderate Resolution Imaging Spectroradiometer (MODIS): Land remote sensing for global change research. IEEE transactions on geoscience and remote sensing, 36(4), pp.1228-1249.

Keller, M., 2005. Deficit irrigation and vine mineral nutrition. American Journal of Enology and Viticulture, 56(3), pp.267-283.

Kim, W.S., Lee, D.H., Kim, Y.J., Kim, T., Lee, W.S. and Choi, C.H., 2021. Stereo-vision-based crop height estimation for agricultural robots. Computers and Electronics in Agriculture, 181, p.105937.

Kim, Y., Glenn, D.M., Park, J., Ngugi, H.K. and Lehman, B.L., 2010. Hyperspectral image analysis for plant stress detection. In *2010 Pittsburgh, Pennsylvania, June 20-June 23, 2010* (p. 1). American Society of Agricultural and Biological Engineers.

Kim, Y., Still, C.J., Hanson, C.V., Kwon, H., Greer, B.T. and Law, B.E., 2016. Canopy skin temperature variations in relation to climate, soil temperature, and carbon flux at a ponderosa pine forest in central Oregon. *Agricultural and Forest Meteorology*, *226*, pp.161-173.

Kimes, D. S. "Modeling the directional reflectance from complete homogeneous vegetation canopies with various leaf-orientation distributions." JOSA A 1.7 (1984): 725-737.

Kingwell, Ross and Amy Fuchsbichler. 2011. 'The Whole-Farm Benefits of Controlled Traffic Farming: An Australian Appraisal'. *Agricultural Systems* 104(7):513–21.

Knox, J.W., Kay, M.G. and Weatherhead, E.K., 2012. Water regulation, crop production, and agricultural water management—Understanding farmer perspectives on irrigation efficiency. Agricultural water management, 108, pp.3-8.

Kokaly, Raymond F. "Investigating a physical basis for spectroscopic estimates of leaf nitrogen concentration." Remote Sensing of Environment 75, no. 2 (2001): 153-161

Kokaly, R.F. and Clark, R.N., 1999. Spectroscopic determination of leaf biochemistry using band-depth analysis of absorption features and stepwise multiple linear regression. *Remote sensing of environment*, *67*(3), pp.267-287.

Konings, A.G., Piles, M., Das, N. and Entekhabi, D., 2017. L-band vegetation optical depth and effective scattering albedo estimation from SMAP. Remote Sensing of Environment, 198, pp.460-470.

Kumar, A., Taparia, M., Rajalakshmi, P., Desai, U.B., Naik, B. and Guo, W., 2019. Uav based remote sensing for tassel detection and growth stage estimation of maize crop using f-rcnn. Computer Vision Problems in Plant Phenotyping.

Kurtulmuş, F. and Kavdir, I., 2014. Detecting corn tassels using computer vision and support vector machines. Expert Systems with Applications, 41(16), pp.7390-7397.

Kutman, U.B., Yildiz, B. and Cakmak, I., 2011. Effect of nitrogen on uptake, remobilization and partitioning of zinc and iron throughout the development of durum wheat. Plant and Soil, 342(1), pp.149-164.

Leghari, S.J., Wahocho, N.A., Laghari, G.M., HafeezLaghari, A., MustafaBhabhan, G., HussainTalpur, K., Bhutto, T.A., Wahocho, S.A. and Lashari, A.A., 2016. Role of nitrogen for plant growth and development: A review. Advances in Environmental Biology, 10(9), pp.209-219.

Lemaire, G. and Gastal, F., 2018. Crop responses to nitrogen. Encyclopedia of sustainability science and technology. New York, NY: Springer, 1, pp.159-184.

Li, Xiaowen, and Alan H. Strahler. "Geometric-optical modeling of a conifer forest canopy." IEEE Transactions on Geoscience and Remote Sensing 5 (1985): 705-721.

Liaghat, S. and S. K. Balasundram. 2010. 'A Review: The Role of Remote Sensing in Precision Agriculture'. *American Journal of Agricultural and Biological Science* 5(1):50–55.

Liang, L., Di, L., Huang, T., Wang, J., Lin, L., Wang, L. and Yang, M., 2018. Estimation of leaf nitrogen content in wheat using new hyperspectral indices and a random forest regression algorithm. Remote Sensing, 10(12), p.1940.

Liu, Jiangui and Elizabeth Pattey. 2010. 'Retrieval of Leaf Area Index from Top-of-Canopy Digital Photography over Agricultural Crops'. *Agricultural and Forest Meteorology* 150(11):1485–90.

Liu, Y., Cen, C., Che, Y., Ke, R., Ma, Y. and Ma, Y., 2020. Detection of maize tassels from UAV RGB imagery with faster R-CNN. Remote Sensing, 12(2), p.338.

Liu, H., Zhu, H. and Wang, P., 2017. Quantitative modelling for leaf nitrogen content of winter wheat using UAV-based hyperspectral data. International Journal of Remote Sensing, 38(8-10), pp.2117-2134.

Li, Z., Jin, X., Yang, G., Drummond, J., Yang, H., Clark, B., Li, Z. and Zhao, C., 2018. Remote sensing of leaf and canopy nitrogen status in winter wheat (Triticum aestivum L.) based on N-PROSAIL model. Remote Sensing, 10(9), p.1463.

Liu, Y., Cen, C., Che, Y., Ke, R., Ma, Y. and Ma, Y., 2020. Detection of maize tassels from UAV RGB imagery with faster R-CNN. Remote Sensing, 12(2), p.338.

Luo, W., Xu, X., Liu, W., Liu, M., Li, Z., Peng, T., Xu, C., Zhang, Y. and Zhang, R., 2019. UAV based soil moisture remote sensing in a karst mountainous catchment. Catena, 174, pp.478-489.

Masclaux-Daubresse, C., Daniel-Vedele, F., Dechorgnat, J., Chardon, F., Gaufichon, L. and Suzuki, A., 2010. Nitrogen uptake, assimilation and remobilization in plants: challenges for sustainable and productive agriculture. Annals of botany, 105(7), pp.1141-1157.

Mason, M.G., 1977. Sources of nitrogen for cereals: urea, ammonium nitrate or sulphate of ammonia?. Journal of the Department of Agriculture, Western Australia, Series 4, 18(1), pp.15-19.

Matese, Alessandro, et al. "Intercomparison of UAV, aircraft and satellite remote sensing platforms for precision viticulture." Remote Sensing 7.3 (2015): 2971-2990.

Ma, X., He, Q. and Zhou, G., 2018. Sequence of Changes in Maize Responding to Soil Water Deficit and Related Critical Thresholds. Frontiers in plant science, 9, p.511.

Meisinger, J. J. and G. W. Randall. 1991. Chapter 5 Estimating Nitrogen Budgets for Soil-Crop Systems.

Merlin, O., Al Bitar, A., Walker, J.P. and Kerr, Y., 2010. An improved algorithm for disaggregating microwave-derived soil moisture based on red, near-infrared and thermal-infrared data. *Remote Sensing of Environment*, *114*(10), pp.2305-2316.

Merzlyak, M.N., Chivkunova, O.B., Solovchenko, A.E. and Naqvi, K.R., 2008. Light absorption by anthocyanins in juvenile, stressed, and senescing leaves. Journal of Experimental Botany, 59(14), pp.3903-3911.

Mielcarek, M., Stereńczak, K. and Khosravipour, A., 2018. Testing and evaluating different LiDAR-derived canopy height model generation methods for tree height estimation. International journal of applied earth observation and geoinformation, 71, pp.132-143.

Migliaccio, M. and Gambardella, A., 2005. Microwave radiometer spatial resolution enhancement. IEEE Transactions on Geoscience and Remote Sensing, 43(5), pp.1159-1169.

Mohorič, T. and Bren, U., 2020. How does microwave irradiation affect the mechanism of water reorientation?. Journal of Molecular Liquids, 302, p.112522.

Moore, Graham A. and J. Paul Tyndale-Biscoe. 1999. 'Estimation of the Importance of Spatially Variable Nitrogen Application and Soil Moisture Holding Capacity to Wheat Production'. *Precision Agriculture* 1(1):27–38.

Moya, I., Camenen, L., Evain, S., Goulas, Y., Cerovic, Z.G., Latouche, G., Flexas, J. and Ounis, A., 2004. A new instrument for passive remote sensing: 1. Measurements of sunlight-induced chlorophyll fluorescence. Remote Sensing of Environment, 91(2), pp.186-197.

Mueller, Nathaniel D., James S. Gerber, Matt Johnston, Deepak K. Ray, Navin Ramankutty, and Jonathan A. Foley. 2012. 'Closing Yield Gaps through Nutrient and Water Management'. *Nature* 490(7419):254–57.

Muñoz-Huerta, Rafael F., Ramon G. Guevara-Gonzalez, Luis M. Contreras-Medina, Irineo Torres-Pacheco, Juan Prado-Olivarez, and Rosalia V. Ocampo-Velazquez. 2013. 'A Review of Methods for Sensing the Nitrogen Status in Plants: Advantages, Disadvantages and Recent Advances'. *Sensors (Switzerland)* 13(8):10823–43.

Navia, J., Mondragon, I., Patino, D. and Colorado, J., 2016, June. Multispectral mapping in agriculture: Terrain mosaic using an autonomous quadcopter UAV. In 2016 International Conference on Unmanned Aircraft Systems (ICUAS) (pp. 1351-1358). IEEE.

Neinavaz, E., Skidmore, A.K., Darvishzadeh, R. and Groen, T.A., 2017. Retrieving vegetation canopy water content from hyperspectral thermal measurements. *Agricultural and forest meteorology*, *247*, pp.365-375.

NeSmith, D.S. and Ritchie, J.T., 1992. Effects of soil water-deficits during tassel emergence on development and yield component of maize (Zea mays). Field Crops Research, 28(3), pp.251-256.

Nguy-Robertson, Anthony, Anatoly Gitelson, Yi Peng, Andrés Viña, Timothy Arkebauer, and Donald Rundquist. 2012. 'Green Leaf Area Index Estimation in Maize and Soybean: Combining Vegetation Indices to Achieve Maximal Sensitivity'. *Agronomy Journal* 104(5):1336–47.

Oehlschläger, J., Schmidhalter, U. and Noack, P.O., 2018, September. UAV-based hyperspectral sensing for yield prediction in winter barley. In 2018 9th Workshop on Hyperspectral Image and Signal Processing: Evolution in Remote Sensing (WHISPERS) (pp. 1-4). IEEE.

Ogawa, M., Y. Tanaka, and A. S. Jursa. "Isotope shift of the nitrogen absorption bands in the vacuum ultraviolet region." Canadian Journal of Physics 42.9 (1964): 1716-1729.

Ohyama, T., 2010. Nitrogen as a major essential element of plants. Nitrogen assimilation in plants, 37(2), pp.2-17.

Olson, R.A., Dreier, A.F., Thompson, C., Frank, K. and Grabouski, P.H., 1964. Using fertilizer nitrogen effectively on grain crops.

Osborne, S. L., J. S. Schepers, D. D. Francis, and M. R. Schlemmer. 2002. 'Use of Spectral Radiance to Estimate In-Season Biomass and Grain Yield in Nitrogen- and Water-Stressed Corn'. *Crop Science* 42(1):165–71.

Otsu, N., 1979. A threshold selection method from gray-level histograms. IEEE transactions on systems, man, and cybernetics, 9(1), pp.62-66.

Pasqualotto, N., Delegido, J., Van Wittenberghe, S., Verrelst, J., Rivera, J.P. and Moreno, J., 2018. Retrieval of canopy water content of different crop types with two new hyperspectral indices: Water Absorption Area Index and Depth Water Index. International journal of applied earth observation and geoinformation, 67, pp.69-78.

Patanè, C. 2011. 'Leaf Area Index, Leaf Transpiration and Stomatal Conductance as Affected by Soil Water Deficit and VPD in Processing Tomato in Semi Arid Mediterranean Climate'. *Journal of Agronomy and Crop Science* 197(3):165–76.

Peguero-Pina, José Javier, et al. "Photochemistry, remotely sensed physiological reflectance index and de-epoxidation state of the xanthophyll cycle in Quercus coccifera under intense drought." Oecologia 156.1 (2008)

Peñuelas, J., Gamon, J.A., Fredeen, A.L., Merino, J. and Field, C.B., 1994. Reflectance indices associated with physiological changes in nitrogen-and water-limited sunflower leaves. Remote sensing of Environment, 48(2), pp.135-146.

Peters-Lidard, C. D., M. S. Zion, and E. F. Wood. "A soil-vegetation-atmosphere transfer scheme for modeling spatially variable water and energy balance processes." Journal of Geophysical Research: Atmospheres 102.D4 (1997): 4303-4324.

Petrou, M., 1999. Mixed pixel classification: an overview. Information Processing for Remote Sensing, pp.69-83.

Pinheiro, C. and Chaves, M.M., 2011. Photosynthesis and drought: can we make metabolic connections from available data?. *Journal of experimental botany*, *62*(3), pp.869-882.

Pope RM, Fry ES . (1997). Absorption spectrum (380–700 nm) of pure water. II. Integrating cavity measurements. Appl Opt 36: 8710–8723.

Qu, Yonghua, Jihua Meng, Huawei Wan, and Yetao Li. 2016. 'Preliminary Study on Integrated Wireless Smart Terminals for Leaf Area Index Measurement'. *Computers and Electronics in Agriculture* 129:56–65.

Rahman, K. M. Atiku. and Dunfu Zhang. 2018. 'Effects of Fertilizer Broadcasting on the Excessive Use of Inorganic Fertilizers and Environmental Sustainability'. *Sustainability (Switzerland)* 10(3).

Raj, R., Kar, S., Nandan, R. and Jagarlapudi, A., 2020. Precision agriculture and unmanned aerial Vehicles (UAVs). In Unmanned Aerial Vehicle: Applications in Agriculture and Environment (pp. 7-23). Springer, Cham.

Raj, R., Suradhaniwar, S., Nandan, R., Jagarlapudi, A. and Walker, J., 2019, April. Drone-based sensing for leaf area index estimation of citrus canopy. In International Conference on Unmanned Aerial System in Geomatics (pp. 79-89). Springer, Cham.

RAMI: Radiative Transfer Model Intercomparison (RAMI). Link: http://rami-benchmark.jrc.ec.europa.eu/html/rami3/models/4sail2/4sail2.php, accessed on 06th Jan 2018

Reddy, T.Y., Reddy, V.R. and Anbumozhi, V., 2003. Physiological responses of groundnut (Arachis hypogea L.) to drought stress and its amelioration: a critical review. *Plant growth regulation*, *41*(1), pp.75-88.

Reyniers, M., Walvoort, D.J. and De Baardemaaker, J., 2006. A linear model to predict with a multi-spectral radiometer the amount of nitrogen in winter wheat. International Journal of Remote Sensing, 27(19), pp.4159-4179.

Rondeaux, Geneviève, Michael Steven, and Frédéric Baret. "Optimization of soil-adjusted vegetation indices." Remote sensing of environment 55.2 (1996): 95-107.

Roujean, Jean-Louis, and Francois-Marie Breon. "Estimating PAR absorbed by vegetation from bidirectional reflectance measurements." Remote sensing of Environment 51.3 (1995): 375-384.

Rouse, J. W., Haas, R. H., Schell, J. A., and Deering, D. W., 1973, Third ERTS Symposium, NASA SP-372 I, pp. 309-17.

Rueda-Ayala, V.P., Peña, J.M., Höglind, M., Bengochea-Guevara, J.M. and Andújar, D., 2019. Comparing UAV-based technologies and RGB-D reconstruction methods for plant height and biomass monitoring on grass ley. Sensors, 19(3), p.535.

Running, Steven W. and Joseph C. Coughlan. 1988. 'A General Model of Forest Ecosystem Processes for Regional Applications I. Hydrologic Balance, Canopy Gas Exchange and Primary Production Processes'. *Ecological Modelling* 42(2):125–54.

Sadeh, Y., Zhu, X., Chenu, K. and Dunkerley, D., 2019. Sowing date detection at the field scale using CubeSats remote sensing. Computers and Electronics in Agriculture, 157, pp.568-580.

Samoy, K.C., Cantre, M.A., Corpuz, A.C., De Dios, J.L., Sibayan, E.D. and Cruz, R.T., 2008. Controlled irrigation in leaf color chart-based and growth stage-based nitrogen management. Philippine Journal of Crop Science (Philippines).

Savci, Serpil. 2012. 'An Agricultural Pollutant: Chemical Fertilizer'. *International Journal of Environmental Science and Development* 3(1):73–80.

Schläpfer, D., Popp, C. and Richter, R., 2020. Drone data atmospheric correction concept for multi-and hyperspectral imagery–the droacor model. The International Archives of Photogrammetry, Remote Sensing and Spatial Information Sciences, 43, pp.473-478.

Schmale Iii, David G., Benjamin R. Dingus, and Charles Reinholtz. "Development and application of an autonomous unmanned aerial vehicle for precise aerobiological sampling above agricultural fields." Journal of Field Robotics 25.3 (2008): 133-147.

Schrader, L.E., 1984. Function and Transformations of Nitrogen in Higher Plants. Nitrogen in crop production, pp.55-65.

Schulze, E.D. and Hall, A.E., 1982. Stomatal responses, water loss and $CO_2$ assimilation rates of plants in contrasting environments. In *Physiological plant ecology II* (pp. 181-230). Springer, Berlin, Heidelberg.

Sea, William B., Philippe Choler, Jason Beringer, Richard A. Weinmann, Lindsay B. Hutley, and Ray Leuning. 2011. 'Documenting Improvement in Leaf Area Index Estimates from MODIS Using Hemispherical Photos for Australian Savannas'. *Agricultural and Forest Meteorology* 151(11):1453–61.

Seo, Y. and Umeda, S., 2021. Evaluating Farm Management Performance by the Choice of Pest-Control Sprayers in Rice Farming in Japan. Sustainability, 13(5), p.2618.

Sharma, Nayana and Ritu Singhvi. 2017. 'Effects of Chemical Fertilizers and Pesticides on Human Health and Environment : A Review'. 10(December):675–79.

Shen, X., Walker, J.P., Ye, N., Wu, X., Boopathi, N., Yeo, I.Y., Zhang, L. and Zhu, L., 2020. Soil Moisture Retrieval Depth of P-and L-Band Radiometry: Predictions and Observations. *IEEE Transactions on Geoscience and Remote Sensing*.

Sims, D.A. and Gamon, J.A., 2002. Relationships between leaf pigment content and spectral reflectance across a wide range of species, leaf structures and developmental stages. Remote sensing of environment, 81(2-3), pp.337-354.

Sinclair, T.R., 1986. Water and nitrogen limitations in soybean grain production I. Model development. Field Crops Research, 15(2), pp.125-141.

Smith, N.J., Chen, J.M. and Black, T.A., 1993. Effects of clumping on estimates of stand leaf area index using the LI-COR LAI-2000. Canadian Journal of Forest Research, 23(9), pp.1940-1943.

Spoorthi, S., Shadaksharappa, B., Suraj, S. and Manasa, V.K., 2017, February. Freyr drone: Pesticide/fertilizers spraying drone-an agricultural approach. In 2017 2nd International Conference on Computing and Communications Technologies (ICCCT) (pp. 252-255). IEEE.

Spratt, E.D. and Gasser, J.K.R., 1970. Effects of fertilizer-nitrogen and water supply on distribution of dry matter and nitrogen between the different parts of wheat. Canadian Journal of Plant Science, 50(6), pp.613-625.

Sogandares FM, Fry ES . (1997). Absorption spectrum (340–640 nm) of pure water. I. Photothermal measurements. Appl Opt 33: 8699–8709.

Sritarapipat, T., Rakwatin, P. and Kasetkasem, T., 2014. Automatic rice crop height measurement using a field server and digital image processing. Sensors, 14(1), pp.900-926.

Stomp, M., Huisman, J., Stal, L.J. and Matthijs, H.C., 2007. Colorful niches of phototrophic microorganisms shaped by vibrations of the water molecule. The ISME journal, 1(4), pp.271-282.

St-Onge, B., Treitz, P. and Wulder, M.A., 2003. Tree and canopy height estimation with scanning lidar. In Remote Sensing of Forest Environments (pp. 489-509). Springer, Boston, MA.

Strachan, I.B., Pattey, E. and Boisvert, J.B., 2002. Impact of nitrogen and environmental conditions on corn as detected by hyperspectral reflectance. Remote Sensing of environment, 80(2), pp.213-224.

Stroppiana, Daniela, Mirco Boschetti, Roberto Confalonieri, Stefano Bocchi, and Pietro Alessandro Brivio. 2006. 'Evaluation of LAI-2000 for Leaf Area Index Monitoring in Paddy Rice'. *Field Crops Research* 99(2–3):167–70.

Sun, H., Feng, M., Xiao, L., Yang, W., Wang, C., Jia, X., Zhao, Y., Zhao, C., Muhammad, S.K. and Li, D., 2019. Assessment of plant water status in winter wheat (Triticum aestivum L.) based on canopy spectral indices. Plos one, 14(6), p.e0216890.

Tan, C., Du, Y., Zhou, J., Wang, D., Luo, M., Zhang, Y. and Guo, W., 2018. Analysis of different hyperspectral variables for diagnosing leaf nitrogen accumulation in wheat. Frontiers in Plant Science, 9, p.674.

Terman, G.L., Ramig, R.E., Dreier, A.F. and Olson, R.A., 1969. Yield-Protein Relationships in Wheat Grain, as Affected by Nitrogen and Water 1. Agronomy Journal, 61(5), pp.755-759.

Tian, Y.C., Yao, X., Yang, J., Cao, W.X., Hannaway, D.B. and Zhu, Y., 2011. Assessing newly developed and published vegetation indices for estimating rice leaf nitrogen concentration with ground-and space-based hyperspectral reflectance. Field Crops Research, 120(2), pp.299-310.

Thenot, F., Méthy, M. and Winkel, T., 2002. The Photochemical Reflectance Index (PRI) as a water-stress index. International Journal of Remote Sensing, 23(23), pp.5135-5139.

Thenkabail, P.S. and Lyon, J.G. eds., 2016. Hyperspectral remote sensing of vegetation. CRC press.

Thenkabail, P.S., Smith, R.B. and De Pauw, E., 2002. Evaluation of narrowband and broadband vegetation indices for determining optimal hyperspectral wavebands for agricultural crop characterization. Photogrammetric engineering and remote sensing, 68(6), pp.607-622.

Thorpe, M.J., Moll, K.D., Jones, R.J., Safdi, B. and Ye, J., 2006. Broadband cavity ringdown spectroscopy for sensitive and rapid molecular detection. Science, 311(5767), pp.1595-1599.

Tian, Y.C., Gu, K.J., Chu, X., Yao, X., Cao, W.X. and Zhu, Y., 2014. Comparison of different hyperspectral vegetation indices for canopy leaf nitrogen concentration estimation in rice. Plant and Soil, 376(1), pp.193-209.

Tokekar, Pratap, Joshua Vander Hook, David Mulla, and Volkan Isler. 2013. 'Sensor Planning for a Symbiotic UAV and UGV System for Precision Agriculture'. *IEEE International Conference on Intelligent Robots and Systems* 32(6):5321–26.

Tsouros, D.C., Bibi, S. and Sarigiannidis, P.G., 2019. A review on UAV-based applications for precision agriculture. Information, 10(11), p.349.

Tsubomura, H., Yamamoto, N., Matsuo, N. and Okada, Y., 1980. The visible absorption spectrum of water. Proceedings of the Japan Academy, Series B, 56(7), pp.403-407.

Underwood, J. and Wittig, C., 2004. Two-photon photodissociation of H2O via the B state. Chemical physics letters, 386(1-3), pp.190-195.

van Grinsven, H.J., Bouwman, L., Cassman, K.G., van Es, H.M., McCrackin, M.L. and Beusen, A.H., 2015. Losses of ammonia and nitrate from agriculture and their effect on nitrogen recovery in the European Union and the United States between 1900 and 2050. Journal of environmental quality, 44(2), pp.356-367.

Verhoef, Wouter. "Light scattering by leaf layers with application to canopy reflectance modeling: the SAIL model." Remote sensing of environment 16.2 (1984): 125-141.

Viets, Frank G. 1971. 'Water Quality in Relation to Farm Use of Fertilizer'. *BioScience* 21(10):460–67.

Vose, James M., James M. Vose, Phillip M. Dougherty, Phillip M. Dougherty, James N. Long, James N. Long, Frederick W. Smith, Frederick W. Smith, Henry L. Gholz, Henry L. Gholz, Paul J. Curran, and Paul J. Curran. 1994. ‘Factors Influencing the Amount and Distribution of Leaf Area of Pine Stands’. *Ecological Bulletins* 43(43):102–14.

Walker, J.P., Houser, P.R. and Willgoose, G.R., 2004. Active microwave remote sensing for soil moisture measurement: a field evaluation using ERS-2. *Hydrological processes*, *18*(11), pp.1975-1997.

Wall, L., Larocque, D. and Léger, P.M., 2008. The early explanatory power of NDVI in crop yield modelling. International Journal of Remote Sensing, 29(8), pp.2211-2225.

Wang, M., 2007. Remote sensing of the ocean contributions from ultraviolet to near-infrared using the shortwave infrared bands: simulations. Applied optics, 46(9), pp.1535-1547.

Wang, X. and Xing, Y., 2016. Effects of irrigation and nitrogen fertilizer input levels on soil-n content and vertical distribution in greenhouse tomato (Lycopersicum esculentum Mill.). *Scientifica*, *2016*.

Weisenburger, Dennis D. 1993. 'Human Health Effects of Agrichemical Use'. *Human Pathology* 24(6):571–76.

Welch, L.F., 1979. *Nitrogen use and behavior in crop production* (Vol. 761). Agricultural Experiment Station, College of Agriculture, University of Illinois at Urbana-Champaign.

Welles, J.M. and Norman, J.M., 1991. Instrument for indirect measurement of canopy architecture. Agronomy journal, 83(5), pp.818-825.

Widlowski, J.L., Mio, C., Disney, M., Adams, J., Andredakis, I., Atzberger, C., Brennan, J., Busetto, L., Chelle, M., Ceccherini, G. and Colombo, R., 2015. The fourth phase of the radiative transfer model intercomparison (RAMI) exercise: Actual canopy scenarios and conformity testing. Remote Sensing of Environment, 169, pp.418-437.

Wu, C., Niu, Z., Tang, Q. and Huang, W., 2008. Estimating chlorophyll content from hyperspectral vegetation indices: Modeling and validation. Agricultural and forest meteorology, 148(8-9), pp.1230-1241.

Wu, K., Rodriguez, G.A., Zajc, M., Jacquemin, E., Clément, M., De Coster, A. and Lambot, S., 2019. A new drone-borne GPR for soil moisture mapping. Remote Sensing of Environment, 235, p.111456.

Xu, C., Zeng, W., Huang, J., Wu, J. and Van Leeuwen, W.J., 2016. Prediction of soil moisture content and soil salt concentration from hyperspectral laboratory and field data. *Remote Sensing*, *8*(1), p.42.

Xu, J.X., Ma, J., Tang, Y.N., Wu, W.X., Shao, J.H., Wu, W.B., Wei, S.Y., Liu, Y.F., Wang, Y.C. and Guo, H.Q., 2020. Estimation of Sugarcane Yield Using a Machine Learning Approach Based on UAV-LiDAR Data. Remote Sensing, 12(17), p.2823.

Yakovenko, A.A., Yashin, V.A., Kovalev, A.E. and Fesenko, E.E., 2002. Structure of the vibrational absorption spectra of water in the visible region. BIOPHYSICS-PERGAMON-C/C OF BIOFIZIKA, 47(6), pp.891-895.

Yang, X. and Miyako, E., 2020. Soap Bubble Pollination. Iscience, 23(6), p.101188.

Yao, Y., Liu, Q., Liu, Q. and Li, X., 2008. LAI retrieval and uncertainty evaluations for typical row-planted crops at different growth stages. Remote Sensing of Environment, 112(1), pp.94-106.

Yao, X., Zhu, Y., Tian, Y., Feng, W. and Cao, W., 2010. Exploring hyperspectral bands and estimation indices for leaf nitrogen accumulation in wheat. International Journal of Applied Earth Observation and Geoinformation, 12(2), pp.89-100.

Yilmaz, M.T., Hunt Jr, E.R. and Jackson, T.J., 2008. Remote sensing of vegetation water content from equivalent water thickness using satellite imagery. *Remote Sensing of Environment*, *112*(5), pp.2514-2522.

Yuan, W., Li, J., Bhatta, M., Shi, Y., Baenziger, P.S. and Ge, Y., 2018. Wheat height estimation using LiDAR in comparison to ultrasonic sensor and UAS. Sensors, 18(11), p.3731.

Zarco-Tejada, P.J., Miller, J.R., Noland, T.L., Mohammed, G.H. and Sampson, P.H., 2001. Scaling-up and model inversion methods with narrowband optical indices for chlorophyll content estimation in closed forest canopies with hyperspectral data. IEEE Transactions on Geoscience and Remote Sensing, 39(7), pp.1491-1507.

Zarco-Tejada, P.J., Berjón, A., López-Lozano, R., Miller, J.R., Martín, P., Cachorro, V., González, M.R. and De Frutos, A., 2005. Assessing vineyard condition with hyperspectral indices: Leaf and canopy reflectance simulation in a row-structured discontinuous canopy. Remote Sensing of Environment, 99(3), pp.271-287.

Zarco-Tejada, P.J., González-Dugo, V. and Berni, J.A., 2012. Fluorescence, temperature and narrow-band indices acquired from a UAV platform for water stress detection using a micro-hyperspectral imager and a thermal camera. *Remote sensing of environment*, *117*, pp.322-337.

Zheng, W. and ZENG, Z.Y., 2004. A review on methods of atmospheric correction for remote sensing images. *Remote Sensing Information*, *4*, pp.66-67.

Zhang, Chunhua and John M. Kovacs. 2012. 'The Application of Small Unmanned Aerial Systems for Precision Agriculture: A Review'. *Precision Agriculture* 13(6):693–712.

Zhao, S., Mao, X., Lin, H., Yin, H. and Xu, P., 2020. Machine Learning Prediction for 50 Anti-Cancer Food Molecules from 968 Anti-Cancer Drugs. International Journal of Intelligence Science, 10(1), pp.1-8.

Zygielbaum, A.I., Gitelson, A.A., Arkebauer, T.J. and Rundquist, D.C., 2009. Non-destructive detection of water stress and estimation of relative water content in maize. *Geophysical research letters*, *36*(12).

*This page has intentionally been left blank.*

# Appendices

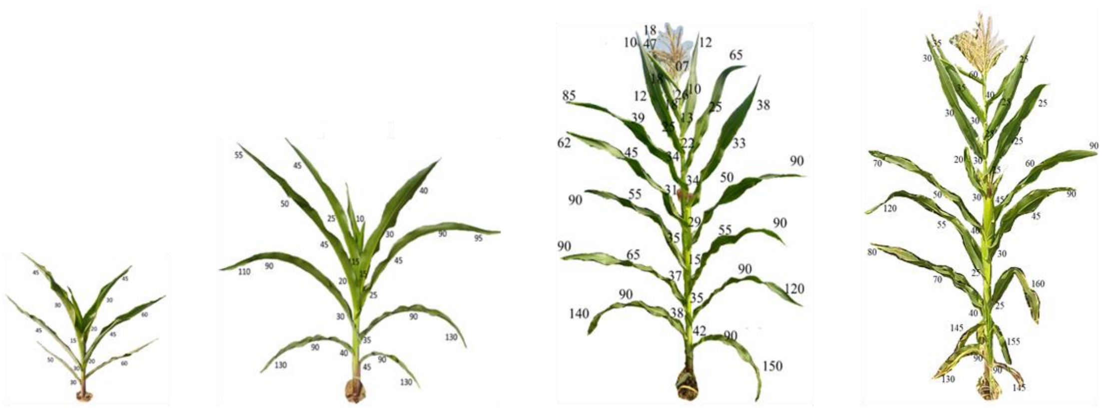

6-leaf stage | Vegetative stage | Tasseling/Silking stage | Grain filling stage

*The crop goes through different growth stages throughout its life cycle. During every growth stage, the requirements of plants vary depending on the dynamics of that growth stage. Thus, plant level analysis needs to consider the crop properties at that growth stage.*

# Appendix 0: Vegetation reflectance models

Solar radiation incident on a canopy is reflected, transmitted and scattered in a very complex manner. To study the vegetation properties from remote sensing requires measuring this reflected and altered radiation. Moreover, various available canopy reflectance models incorporate the physics of light interaction with the canopy. The models can be categorized into four categories (Goel et al., 1988).

- Geometrical models: A geometrical shape is prescribed for the canopy under the assumption that the canopy is an array of opaque or translucent sub-canopies. This is good for sparse canopies where multiple scattering can be neglected, and the mutual shadow effect is minimal at low zenith angles.
- Turbid medium models: This model is used for homogenous canopies where the canopy is assumed to be a turbid medium with absorbing and scattering particles. It is better for denser canopies where vegetation elements like leaves, shoots, and branches etc. are smaller in comparison to the height of the canopy.
- Hybrid (mix of geometrical and turbid medium) model: The model is used for heterogeneous canopies, where the canopy is divided into sub-canopies with each sub-canopy treated with a different geometrical model (depending on the geometrical shape of sub-canopy) where each geometrical model is assumed to be turbid.
- Computer simulation models: Here, the radiation inside the canopy is obtained through computer simulations, and the canopy is assumed to be a stochastic collection of vegetation elements. The Monte Carlo procedure is used to identify specific areas of various vegetation elements almost on a photon-to-photon basis. It allows realistic simulation of radiation in the canopy rather than making an assumption about it.

Before analyzing the canopy reflectance model, it is important to understand the leaf reflectance characteristics, as a major part of the canopy is made up of leaves. The study of light interaction with plants and their leaves is very important for understanding energy transfer processes between vegetation and its atmosphere (Peters et al. 1997). In order to generate a physical leaf model, it is important to study the optical properties of leaf-constituents like chlorophyll, carotenoid, anthocyanin, water, lignin, cellulose, nitrogen etc. In 1969, a paper considered leaves as a transparent plate with a rough plane-parallel surface named "plate model" of a leaf (Allen et al., 1969). The experiment was carried out on maize leaves but later became an effective model for huge subsets of the leaf types. PROSPECT is considered to be an improved version of the generalised "plate model". There are many other models of a leaf, e.g. Compact Spherical Particle Models (used for needle-shaped leaves), N-Flux model etc. Basically, the reflectance and transmission spectrum of a leaf is a function of light-absorbing compounds (chlorophylls, carotenoids, anthocyanin, water, cellulose, lignin, starch, proteins, etc.) concentration and the internal scattering of light. Thus, there are two important factors to model a physically realistic leaf. One is the refractive index, and the second is the specific absorption coefficients of leaf constituents. There are various leaf models that have been used since the 1960s. The plate model is one of the oldest leaf models and is still used for most of the flat leaves. The compact Spherical Particle Model of the leaf is useful for needle-shaped leaves. Apart from this, there are models based on the N-Flux model, Radiative transfer equations, Stochastic approach, and the ray-tracing model (RAMI, 2018).

## 1.1 PROSPECT

The model PROperties SPECTra (PROSPECT) is an example of a leaf plate model and is the classical approach for deriving leaf optical properties spectra (reflectance and transmittance) from 400 nm to 2500 nm. The physics behind the model assumes that the specific absorption coefficient k of each leaf constituent (like water, chlorophyll, dry matter) is wavelength-dependent but independent of vegetation species (Jacquemoud et al., 2008). The first paper on PROSPECT was published almost three decades ago (Jacquemoud et al., 1990). In the original version of PROSPECT, a total of three inputs were required to run the model: mesophyll structure ($N$), pigment concentration ($C_{a+b}$), and water content ($C_w$). Slowly, more leaf biochemical constituents were added, like 'leaf dry matter'. In 2008, a more advanced version of this model, called PROSPECT-5, included a total of six inputs (Jacquemoud et al., 2009), being $N$ (Number of compact layers specifying the average number of air/cell walls interfaces within the mesophyll), chlorophyll ($C_{a+b}$), carotenoid ($Car$), brown pigment ($Cbrown$), equivalent water thickness ($C_w$) and leaf mass per unit area or dry matter ($C_m$).

The input of dry matter ($C_m$), consists of cellulose, lignin, and protein (Nitrogen). It was a deliberate attempt to put all three variables together to get a better estimation of input biochemical constituents after inversion of the model (retrieving leaf biochemical constituents from leaf spectra 400-2500 nm). This was undertaken because the protein content can't be retrieved after inversion of the model due to the strong water absorption feature in fresh leaves and because cellulose and lignin were poorly identified and quantified in dry leaves as separate constituents in that wavelength range (Jacquemoud et al., 2008). However, in the shortwave-infrared range, there are specific absorption bands present for chemical bonds in cellulose, lignin and proteins, which can be measured from remote sensing. Thus protein, cellulose, and lignin were introduced as the input variables of PROSPECT, but retrieval of these elements from the inversion method could not be achieved (Fourty et al., 1996; Govaerts et al., 1996; Fourty and Baret, 1998).

PROSPECT-5 has improved the performance of PROSPECT by updating parameters like angle of incidence of incoming radiation and refractive index. In PROSPECT, the angle of incidence of incoming radiation was empirically set to 60°, which has been found to be an overestimated angle. In the Bidirectional Reflectance Distribution Function (BRDF) modelling of leaves (Bousquet et al., 2005), a physical link has been established between the probability density function of facet orientations (D), surface roughness parameter ($\sigma$), and angle ($\alpha$). In this experiment $\sigma = 0.5$ was found to be realistic for most of the leaves, and accordingly, maximum angle of incident incoming radiation was reduced to 40°. Consequently, PROSPECT accuracy was improved at high absorption wavelengths (Feret et al., 2008). The refractive index of a leaf was calibrated through empirical methods by using open source data from LOPEX and ANGERS (Feret et al., 2008).

Further advances with PROSPECT have included the addition of anthocyanin as one of the input parameters, known as PROSPECT-D (D stands for Dynamic). Anthocyanin is one of the major leaf pigments after chlorophyll and carotenoid. The percentage of anthocyanin increases in the leaf as it shifts from juvenile to senescent stage. Inversion of PROSPECT-D has shown better retrieval of leaf constituents, especially for carotenoid (Feret et al., 2017).

From a remote sensing perspective, PROSPECT is an important model, as inversion allows retrieval of leaf biochemical constituents by using leaf reflectance collected through a hyperspectral sensor. However, remote sensing can only give reflectance, not transmittance (one of the requirements for inversion); thus, poor estimation ($R^2$=0.65) is achieved (Fang et al., 2017). In the PROSPECT model, it is assumed that the leaf surface roughness parameter ($\sigma$), the refractive index of leaf material ($n(k)$), and the specific absorption coefficient of leaf absorbers ($k_{spe(k)}$) remains the same for all the leaf species. However, apart from $k_{spe(k)}$, σ and $n(k)$ will vary from one leaf species to another depending on the nature of the leaf surface and the wax type on its surface. Thus, there is a need to perform experiments to find leaf surface roughness and refractive index parameters of leaf material to calibrate the model for various species (Feret et al., 2008).

There are other models like 'LEAFMOD' and 'LIBERTY' which are also used for generating leaf spectra. The Leaf Experimental Absorptivity Feasibility model (LEAFMOD) uses a one-dimensional radiative transfer equation in a slab of leaf material with homogeneous optical properties. However, the carotenoid leaf pigment is not considered in this model. Moreover, the 'Leaf Incorporating Biochemistry Exhibiting Reflectance and Transmittance Yields' (LIBERTY) is a compact spherical particle model which is widely used for needle-shaped leaves (Jacquemoud et al., 2008).

## 1.2 SAIL

SAIL stands for 'Scattering by Arbitrary Inclined Leaves'. Unlike PROSPECT, the canopy model SAIL is used to generate canopy reflectance by considering various canopy factors like canopy background, crown clumping, leaf area index, leaf angle distribution, sun angle, etc. The first version of SAIL was developed in 1981, and the first paper was published in 1984, even before PROSPECT. The SAIL model is very important from a remote sensing point of view as, from a distance sensor (satellite or airborne), only canopy reflectance is measurable, which has many effects associated with it. SAIL provides a four-stream optical property of the canopy layer at the output. As shown in Figure A0.1, the SAIL model segments all the radiation, interacting with the canopy into four parts.

1. Direct solar incident flux,
2. Direct observed radiance,
3. Total diffused downward flux, and
4. Total diffused upward flux.

The first version of SAIL had a very simplistic assumption about the canopy layer, which was assumed to be horizontal and infinitely extended, having only small, and flat leaves which are homogenous in nature (Verhoef et al., 1984). SAIL has experienced a total of 6 versions, with the latest version named 4ASIL2. Developed in 2003, it also has better realistic assumptions than SAIL. The hot-spot effect was added in SAIL as a function of the ratio of leaf size to canopy height and named SAILH. GeoSAIL or 2M-SAIL was developed to consider vertical heterogeneity in canopies. In 2007, 4SAIL2 was developed as a numerically robust and speed-optimized version of SAIL, while 4SAIL2 added the crown clumping effect. All models are presented in table A0.1.

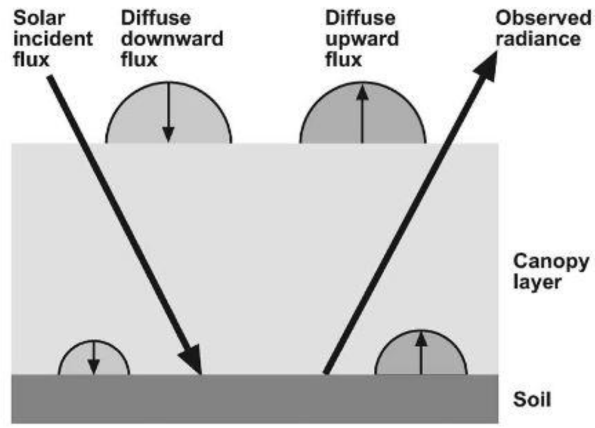


Figure A0.1: Four-stream radiative transfer modelling concept (adapted from Verhoef et al., 1984).

Table A0.1: Various models of SAIL (apated from RAMI, 2018).

| Property / Model | SAIL | SAILH | GeoSAIL | SAIL++ | 4SAIL | 4SAIL2 |
|---|---|---|---|---|---|---|
| Year of Development | 1981 | 1989 | 1999 | 2000 | 2003 | 2003 |
| Type | Turbid medium | Hybrid | Hybrid | Hybrid | Hybrid | Hybrid |
| Hotspot effect | No | Yes | Yes | Yes | Yes | Yes |
| Number of canopy layer | 1 | 1 | 2 | 1 | 1 | 2 |
| Singularity removal | No | No | No | Yes | Yes | Yes |
| Numerical precision | Single | Single | Single | Double | Double | Single |
| Speed optimization | No | No | No | Yes | yes | Yes |
| Number of diffuse streams | 2 | 2 | 2 | 72 | 2 | 2 |
| Internal flux profile supported | No | No | No | No | Yes | No |
| Thermal application supported | No | No | No | No | Yes | No |
| Non-Lambertian Soil BRDF | No | No | No | No | No | Yes |
| Clumping effect | No | No | No | No | No | Yes |

4SAIL2 is different from the previous versions of SAIL because it incorporates the effect of non-Lambertian soil BRDF and clumping effect while modelling canopy reflectance. No other SAIL model has these two parameters. In order to accommodate the vertical heterogeneity of the canopy, 4SAIL2 segments the canopy into two layers, similar to GeoSAIL. However, unlike the 4SAIL model, the thermal application is not supported in 4SAIL2, which needs to be provided with three types of inputs – structural, spectral, and observational parameters. Below are details of these parameters:

i. Structural parameters: LAI, average leaf slope (a), LIDF bimodality parameter (b), hotspot parameter (q), fractional brown leaf area (fB), layer dissociation factor (D), soil BRDF parameter (b, c, B0, h), soil moisture, and crown coverage.

ii. Spectral parameters: Output from PROSPECT, fractional diffused sky irradiance, and dry soil reflectance.

iii. Observational parameters: Solar zenith angle, viewing zenith angle, and relative azimuth angle.

The practical application of all models (SAIL or PROSPECT) is observed in their inversion, where leaf biophysical and biochemical parameters can be estimated from reflectance data.

In Figure A0.2, $R_m = R + \Delta R$, where $\Delta R$ is the difference between measured and calculated reflectance of canopy/leaf spectra. Here, C --> R can be seen as a direct problem and R --> C will be an inverse problem. The process of using actual leaf/canopy reflectance to determine leaf/canopy biochemical or biophysical parameters (i.e. Rm --> C) should be considered as a separate problem because the simple inverse problem will not consider issues in actually measured reflectance. One can use ΔR --> ΔC to do a sensitivity analysis of any intervention made in the system.

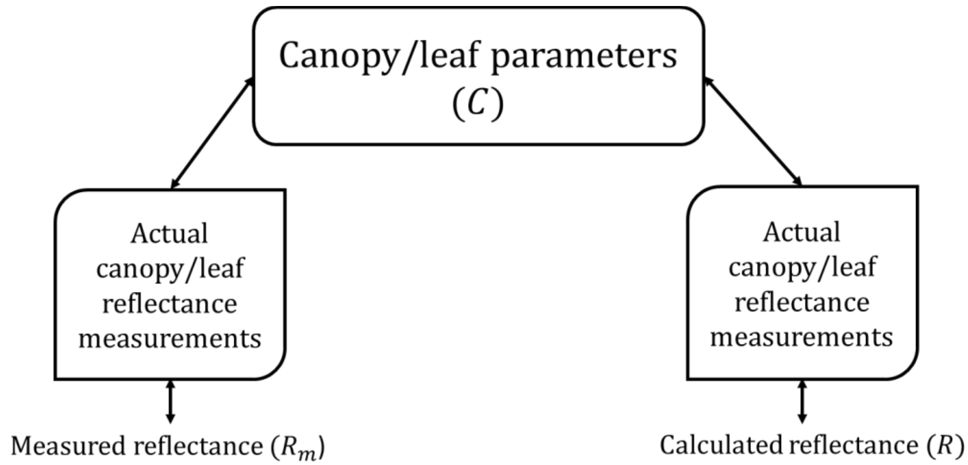


Figure A0.2: Estimation of canopy parameters from reflectance data and direct and inverse problem schematic representation (adapted from RAMI, 2018).

*This page has intentionally been left blank.*

# Appendix 1: Semi-controlled pot Experiment

A pot experiment was carried out on tomato plants to study the effect of water stress on plants and the corresponding hyperspectral signatures. The experiment was done in a semi-controlled environment at IITB-Monash Research Academy (IITB-Campus, Mumbai, India) during the Kharif season of 2017. The plants were exposed to two different water treatment levels, and three replicas were performed to confirm the results. The experimental setup was made in such a way as to allow wind and sunlight on the plants but to restrict the natural precipitation. This was done majorly to control the soil moisture of the pots. Figure A1.1(a) shows the formal setup for the pot experiment. Figure A1.1(b) shows the pots' spatial layout, where the red color circles signify the pots with high water stress, while the green color circles represent pots with no water stress. To monitor and manage the water stress, each pot's actual soil moisture was measured on a diurnal basis from around 5 PM to 6 PM. A pre-calibrated TDR (IMKO HD2 with a dual-probe setting) based soil moisture probe was used to record the soil moisture measurements during the day. The field capacity of the soil was calculated using experimentation and found to be at 30%. The experimental pots were irrigated based on an inherent assumption that soil density was consistent amongst the pots, and crop water requirement was calculated accordingly. For example, if the measured soil moisture (MSM) in a red pot was 13%, then the pot's soil moisture should reach 18% with additional irrigation. Similarly, If MSM in a green pot is 22%, then irrigations should increase the soil moisture content by at least eight units, i.e., 30%. If the soil moisture is found to be more than the intended limit, no irrigation was made on that day. In addition, hyperspectral data from a spectroradiometer (Spectra Vista GER1500) (400 nm – 1000 nm) were collected bi-weekly to monitor the effect of water stress on the plant leaves. It was evident that stressed plants had smaller leaves, smaller height, and less leaf area index with respect to healthy leaves.

A total of 180 reflectance spectra samples from low soil moisture plants and

178 reflectance spectra samples from optimally-irrigated plants were collected over two months of plant growth. Figure A1.2 shows the mean reflectance of healthy and stressed plants collected over a two-month duration. Results showed that the mean reflectance of healthy plants was higher than that of stressed plants. However, around red and blue wavelength regions, the mean reflectance values were found to be almost equal. It should also be noted that the standard deviation (SD) of stressed plant reflectance was found to be higher than the SD of reflectance from healthy plants. Moreover, the SD value for both the cases was more than the difference of reflectance between healthy and stressed plants, which suggests that the absolute value of reflectance spectra should not be used to separate healthy and stressed plants.

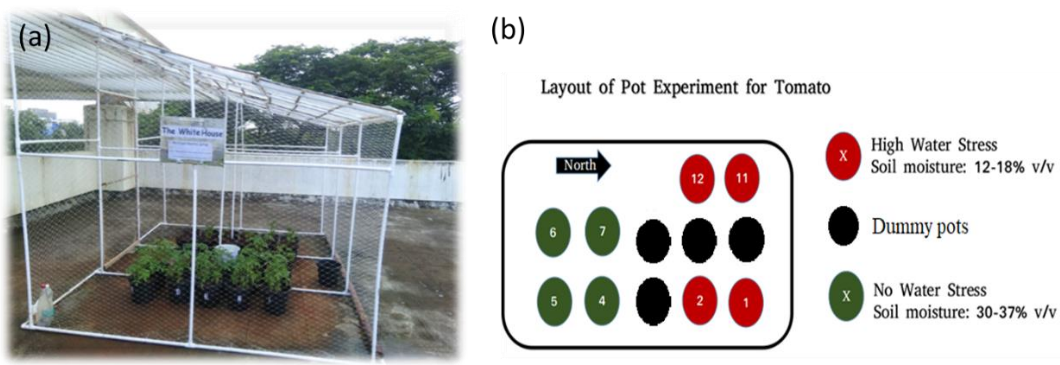


Figure A1.1: (a). Mesh-house covered with transparent plastic sheet on the roof. The plastic sheet is used to stop rainwater from getting inside the pots, and (b) layout of the pots in the mesh-house where red color circles represent low soil moisture pots and the green color circle represents optimally irrigated location pots.

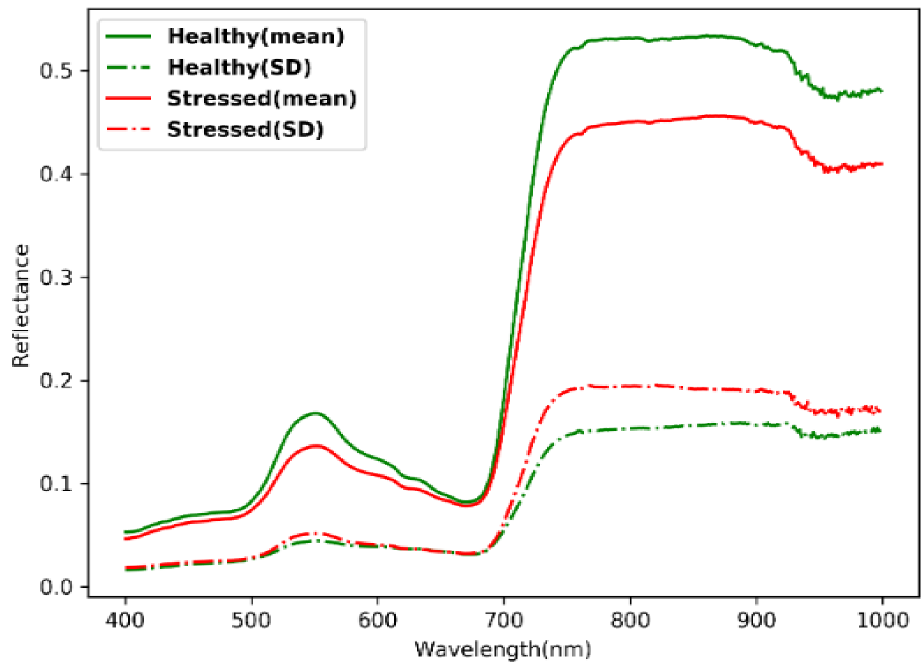


Figure A1.2: Mean reflectance signature and standard deviation of healthy and stressed tomato plants

*This page has intentionally been left blank.*

# Appendix 2: Protocol for collecting data from various instruments

## 1.1 Spectroradiometer

- Spectral signatures should be collected between 10:00 AM to 2:00 PM only if the atmospheric condition is sunny and the sky is clear. If the sky is cloudy then there is high chances of data being noisy.
- Specular radiation from the leaf should not be measured using the spectroradiometer as it contains information only from the top surface of the leaf and not from within the leaf. During data collection, the sensor of the spectroradiometer should be placed in such a way that it should avoid collecting specular radiation. This can be achieved by placing the sensor at 90° plane from the sun's specular radiation direction.
- For each subplot, a separate reference spectra should be taken before the collection of leaf reflectance. This will help in reducing the effect of atmospheric variability
- The sampled maize-leaf should be kept parallel to the ground, and the spectroradiometer should focus on it from a near perpendicular direction such that there should be no shadow on the leaf
- One well sunlit leaves should be selected from each subplot, and three spectral signatures should be collected from that leaf.
- It should be taken care that the lens of the spectroradiometer is clean all the time. No water droplet or dust particle stick to it. Put the sensor-cap on the sensor if the spectroradiometer is not in use.
- The reference reflectance panel should be kept clean and should be protected from dust particles in the field.
- How to decide the number of spectral signatures from one leaf:
  A flat plane leaf was taken, and 15 reflectance signatures from it were obtained using spectroradiometer from different parts of the leaf. The experiment was done at 1:00 PM under direct sunlight in clear sky

condition. There was negligible variation in visible region reflectance (actually no deviation from 400 – 750 nm) but in NIR region, a significant variation is observed with maximum SD of 0.0219. After statistical analysis, it is found that if no of samples is increased, then the SD from mean will decrease. In this research three samples were selected as this gives SD = 0.011 which means the researcher can be 95% and 99.7% confident that average reflectance values are +-7% and +-10% of achievable mean respectively. 7% is approximately 0.044 in absolute values.

The spectral signatures have been taken in clear sky condition as shadows cause high variability in reflectance values even if data is collected from same leaf samples.

## 1.2 LAI meter

- LAI data should be collected between 10:00 AM to 2:00 PM only if the atmospheric condition is either sunny or uniform overcast. Cloudy sky condition should be avoided but not overruled.
- If the sky condition is cloudy then, for each subplot, a separate k-file should be generated before collecting LAI data. If the sky is clear sunny or overcast then, one k-file would be sufficient for one replica of nine subplots.
- Data should be collected from three points inside the canopy (from the red colour box in figure 3.4), ~15 cm above the ground and it should be taken care that the lens is not directly blocked by any leaf.
- It should be taken care that, while collecting the data, collector's own shadow should not fall on the fisheye lens of the LAI meter
- How to decide the number of below readings per plot for LAI data:

  Intensive LAI data collection was done form 9 plots (all the water and nitrogen treatments). From each plot, 1, 3, 5, 8, and 10 below reading were collected. Before the acquisition of below readings, the separate

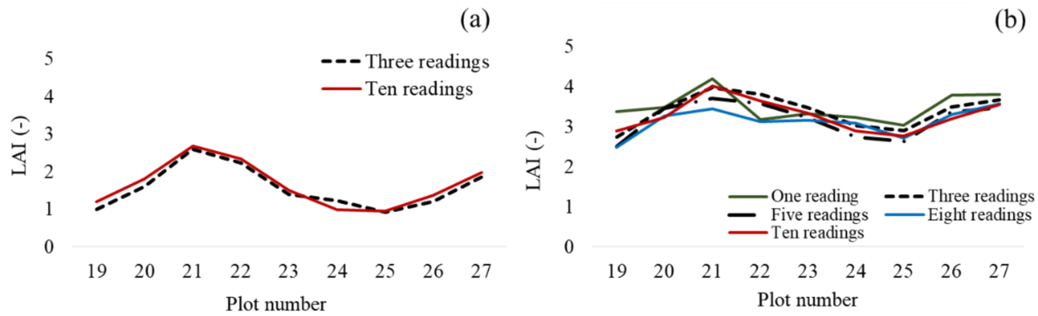


Figure A2.1: (a) Comparison of LAI values with three samples and ten samples for 38 days old crop and (b) comparison of LAI values with one, three, five, eight, and ten samples for 70 days old crop. In both cases, it can be seen that three samples per plot are sufficient enough to give LAI representation of plots.

above-canopy readings were also collected. After scattering correction, all the data is plotted, as shown in figure A2.1. It is observed that the LAI value with 10 number of readings closely follows the LAI values with 3 number of readings. It is also observed that the variability of the LAI values is more for the highly uneven (unevenly distributed sparse canopy) plots. Still, LAI values obtained from 3 number of below readings seems to be a good representation of the canopy LAI (as taken by 10 number of readings).

- It needs to be taken care that the leaf should fit completely inside the sensor of the nutrition analyzer, and no part of the sensor is left uncovered
- The leaf should be dry and clean

## 1.3 Plant height and leaf angle

- Five random plants were considered for measuring plants height. The plants were sampled from the four corners and one from the center of the rectangular area shown in figure 3.7.

- The heights were measured from ground to just below the uppermost leaf in the vertically upward direction, perpendicular to the ground (no slanting).
- Leaf angle were measured using the mobile application (application: Clinometer) from three different vertical heights (bottom, middle and top of the canopy)
- How to decide the number of plant height samples

  To decide how many samples need to be collected from a plot, the following steps were done:
  - First, one should see which variable need to be recorded. Here, we will take the example of measuring plant height from a plot. Now, one should decide the accepted error in height measurement, which can be tolerated in the research. E.g. whether 20 cm height difference from mean will not affect the research or 40 cm will not affect. This is important as many statistical approaches need this logical input from the researcher. Here 20 cm is kept as an acceptable deviation.
  - Collect as many samples as possible from a plot. Here total, 20 plant heights are taken from one plot, and this is done for all the unique treatments.
  - Now start numerical analysis:
    - Make all possible groups of 5 samples, 7 samples, 10 samples, 13 samples, 15 samples, 18 samples etc. From the 20 heights measured. In the case of 5 samples, the total group will be $^{20}C_5$ , i.e. 15504.
    - Take the average of each group and put it into a list. 'Average of average' of these group will be equal to the average of 20 measured samples. Just average each group so that its deviation from sample mean can be calculated.
    - Now find SD of this list.

- Similarly SD for all the samples like 7, 10, 13 etc. can be found out.
- Now apply Gaussian curve rule, i.e. 95 % of the data lies in +- 1.96*SD range.
- Now find the confidence Interval:

$$CI = \left[Sample_{mean} + -1.96 * SD,\ Sample_{mean}\right]$$

- Check at what no. of samples (5, 7, 8, 10, 13...) the decided variation (acceptable error in height from mean) is satisfying with the confidence interval. Means, if the value of 2*1.96*SD is greater than the tolerance level, then one needs to increase the no of samples. (2*1.96*SD because the value can go either left or right to the mean). Here the 20 cm deviation comes when the number of samples kept at 5 plants per plot.

## 1.4 Nutrition analyzer (used from June 2017 to March 2018)

- Nutrition analyzer data should be collected from the same leaf from which hyperspectral signatures are collected
- Before collecting the data from the leaf, calibrate the instrument by pressing the sensor until 'beep' sound is heard. Perform the calibration at regular interval
- While collecting data, the instrument should be kept in shadow. If strong sun radiation is there, then the researcher should use his/her own shadow to shade the instrument

*This page has intentionally been left blank.*

# Appendix 3: Details of Field Stay

Crop Cycle Date: 16th Oct 2018 (Sowing) to 14th Feb 2019 (Harvesting)

Field Stay Date: 11th Nov 2018 to 25th Dec 2018

Other field visits: 28-30 Oct 2018, 06-08 Jan 2019, 24-25 Jan 2019, 10-12 Feb 2019

Six-Leaf Stage Date: 12th Nov 2018

Tasseling starts: 12th Dec 2018 (50% tasseling: 20th Dec 2018)

Silking stage: 22 Dec 2018 – 01 Jan 2019

Dough Stage: 25 Jan 2019

Maturity: 14 Feb 2019

……………………………………………………………………………………………………………

The objective of Field stay:

1. To record spectral signatures from a broad range of leaf-N and leaf-water content in the plants over its crop cycle and also destructively sample and preprocess leaves for CHNS analysis.
2. To record each variable mentioned in table A3.1 at a high temporal and spatial resolution

(These destructively sampled leaves have been used for CHNS analysis)

Please refer the tables as per details given below:s

- A3.1: List of all crop and soil parameters collected from the farm
- A3.2: Details of instruments used for data collection
- A3.3: Detailed list of the type of data collected and their codes
- A3.4: Growth stage-based data collection

- A3.5: Detailed data collection schedule

Table A3.1: List of collected crop and soil parameters.

| Sr. No | Variable | Instrument/method |
|---|---|---|
| 1 | Leaf Hyperspectral Signature | Spectroradiometer (GER1500) |
| 2 | Drone-based high resolution canopy hyperspectral image | Hyperspectral imager (BaySpec OCI-F-HR) |
| 3 | Leaf C, H and N content | CHNS Analyzer (Lab) |
| 5 | Plot-wise soil moisture | Soil moisture sensor (SensProut, UoT) |
| 6 | Soil nitrogen content | CHNS Analyzer |
| 7 | Leaf Temperature | IR temperature sensor (FieldPiece) |
| 8 | Leaf angle | Manually (clinometer) /image processing |
| 9 | Plant height | Measuring tape |

Table A3.2: Details of instruments.

| Instrument name | Company | description |
|---|---|---|
| Spectroradiometer | Spectra Vista | Spectral range: 400-1000 nm. It's a handheld instrument (captures one pixel at a time with 4-degree FOV) |
| Hyperspectral imager | Bayspec | Spectral range: 400-1000 nm, Spatial resolution: less than 1 cm (at 40 m flight height), and Bandwidth: 2.1 nm |
| CHNS Analyzer | Thermo Finnigan | It is based on the principle of "Dumas method" which involves the complete and instantaneous oxidation of the sample by "flash combustion". The combustion products are separated by a chromatographic column and detected by the thermal conductivity detector (T.C.D.), which gives an output signal proportional to the concentration of the individual components of the mixture. |
| LAI meter | Licor | Uses canopy gap fraction and beers law to calculate LAI |
| Handheld IR temp. sensor** | Fieldpiece | Accuracy: ±1.5°F and a resolution of 0.5°F |
| Clinometer | Android app | Measures leaf angle (Accuracy +-5°) |
| Soil Moist. sensor | Sensprout | Installed by University of Tokyo |

Table A3.3: List of data collected and their code.

| Level | Type | code | Data |
|---|---|---|---|
| Soil | Destructive | SN | Soil sample for nitrogen content of each treatment |
| Soil | Fixed Sensor based | SM | Hourly soil moisture of each treatment (total 9) |
| Leaf | Destructive | LF | Leaf samples for leaf-water, N and C content (9*3 = 27 samples) |
| Leaf | Remotely sensed | HyS | Hyperspectral signature (Spectroradiometer) |
| Leaf | Remotely sensed | LT | Leaf temperature using IR temperature sensor |
| Leaf | Non-destructive | LA | Plant top leaves angles (Clinometer) and Leaf angle distribution in the vertical profile of the plant (image processing) |
| Leaf/canopy | Remotely sensed | HyI | Hyperspectral imaging using drone |
| Canopy | Non-destructive | LAI | LAI meter data with 3 samples from each plot |
| Canopy | Non-destructive | PH | Plant height (each plot 5 samples) |

Table A3.4: Maize growth stages and data collection.

| **Growth Stage** | **Days after sowing** | **Data collection** (see table 1.5) |
|---|---|---|
| Sowing | 0 | SN (before fertilizer application), SM |
| Germination | 6-8 | SM |
| 6-leaf stage | 25-30 | SN (before fertilizer application), SM, LF, HyS, LA, HyI, LAI, PH |
| -------------------- | 50-64 | SM, LF, HyS, LA, HyI, LAI, PH |
| Tasseling and Silking | 64-85 | SN (before fertilizer application), SM, LF, LFC, HyS, LT, LA, HyI, LAI, PH |
| Milk Stage | 85-95 | SM, LF, LFC, HyS, LT, LA, HyI, LAI, PH |
| Dough Stage | 95-105 | SM, LF, LFC, HyS, LT, LA, HyI, LAI, PH |
| Dent stage | 105-115 | SM, LF, LFC, HyS, LT, LA, HyI, LAI, PH |
| Physiological maturity | 115-120 | SN (after Harvesting), SM, LF, LFC, HyS, LT, LA, HyI, LAI, PH |

Table A3.5 is showing a detailed schedule of data collection. High temporal resolution data is collected throughout its crop's life cycle, but the main focus is given until the tasseling stage of the crop as higher the number of tassels, greater the yield. In table A3.5, Column name in red colour (SN and LF) shows a schedule of destructive sampling. All the destructive sampling are done from 27 plots with one leaf per plot, and soil will be sampled at a depth of 0-15 and 15-30 cm depth. HyS (3 signatures from each leaf), LT (three readings each leaf) and LA (using clinometer) are collected from the same leaf which is sampled destructively. To record LAI, 3 points are taken from each plot. PH is measured for five plants from each sub-plot. LA is taken using a clinometer. 5pp or 1pp means sampling from 5 plants per plot or one plant per plot, respectively. Soil moisture sensors (SM) are installed in 9 plots (I3 x N3) since the date of sowing. HyI data are collected in such a way to get leaf-level pixel resolution.

Total 271 leaves samples (from 27 plots) are collected destructively during the crop life cycle.

Table A3.5: Detailed data collection schedule and farm events.

| **Date** | **Event** | **Day** | **SN** (Destructive) | **LF** (Destructive) | **HyS** | **LT** | **LA** | **HyI** | **LAI** | **PH** |
|---|---|---|---|---|---|---|---|---|---|---|
| 16th Oct | Sowing | 0 | Y (before sowing) | | | | | | | |
| | | 1 - 26 | | | | | | | | |
| 12th Nov | Six Leaf Stage | 28 | Y | Y | Y | | Y | Y | Y | |
| 13th Nov | Irrigation to I3 plots | 29 | | Y | Y | | | | | |
| 14th Nov | Urea to I3 plots | 30 | | | | | | | | Y |
| 16th Nov | | 32 | | Y | Y | | | | Y | |
| 17th Nov | Irrigation to I2 plots, Leaf dry powder samples made and stored | 33 | | Y | Y | | | | | |
| 18th Nov | Urea to I2 plots | 34 | | | | | | | | |
| 20th Nov | | 36 | | | | | | Y | Y | |
| 21st Nov | | 37 | | Y | Y | | | Y | | Y |

Table A3.5: Detailed data collection schedule and farm events (Continued ...)

| Date | Event | Day | SN (Destructive) | LF (Destructive) | HyS | LT | LA | HyI | LAI | PH |
|---|---|---|---|---|---|---|---|---|---|---|
| 22nd Nov | | 38 | | Y | Y | | Y | | | Y |
| 23rd Nov | Irrigation to I1 plots | 39 | | | | | | | | |
| 24th Nov | Urea to I1 plots | 40 | | | | | | | | |
| 26th Nov | Leaf dry powder samples made and stored | 42 | | | | | | | | |
| 27th Nov | I3 plots are irrigated | 43 | | | | | Y | | | |
| 28th Nov | | 44 | | | | | | Y | Y | Y |
| 03rd Dec | | 48 | | | | | | | Y | |
| 10th Dec | | 55 | | | | | | | Y | IITH |
| 11th Dec | Tassels start coming | 56 | | | | | | | | |
| 12th Dec | Irrigation to I3 | 57 | | Y | Y | | | Y | | |
| 13th Dec | Tassels are seen in many plots. Slow but continuous rain occurred at 13th night to 14th morning. Stress from I1 and I2 has minimised. | 58 | | Tassel count has done | | | | Y | | |
| 14th Dec | Very Cloudy sky, no direct sunlight. Stress from I1 and I2 has minimised. | 59 | | Tassel count has done | | | | | | |
| 15th Dec | Sunny day. Stress in I1 and I2 seen. | 60 | | Tassel count has done | | | | | | |
| 17th Dec | Slow but continuous rain occurred at 17th night to 18th morning. Stress from I1 and I2 has minimised. | 62 | | Tassel count has done | | | | | | Y |

Table A3.5: Deatiled data collection schedule and farm events (Continued …)

| Date | Event | Day | SN (Destructive) | LF (Destructive) | HyS | LT | LA | HyI | LAI | PH |
|---|---|---|---|---|---|---|---|---|---|---|
| 18th Dec | Very Cloudy condition and little precipitation type scene | 63 | | | | | | | | |
| 19th Dec | | 64 | | | | | | Y | Y | |
| 20th Dec | 50% tasseling | 65 | | Y | Y | Y | | | | |
| 21th Dec | | 66 | | Y | Y | | | | | |
| 22nd Dec | | 67 | | Y | Y | Y | | Y | | |
| 24th Dec | | 69 | | | | | Y | | Y | |
| 31st Dec | Irrigation to I1 | 76 | | | | | | | | |
| 01st Jan | Irrigation to I3 | 77 | | | | | | | | |
| 02nd Jan | Soil Sample collection from I2 and I3 plots (total 8 plots) | 78 | Y | | | | | | | |
| 04th Jan | Irrigation to I2 | 80 | | | | | | | | |
| 7th Jan | | 83 | | Y | Y | Y | | Y | Y | Y |
| 8th Jan | | 84 | | Y | Y | | | | | |
| 24th Jan | | 100 | | | | | | | | Y |
| 25th Jan | | 101 | | Y | Y | Y | | Y | Y | |

# Appendix 4: Soil profile

| Soil profile layers depth (cm) | soil type | Clay (%) | Sand (%) | Silt (%) | Organic carbon (%) | Electrical conductivity (Ds/m) | Gravel (%) | Bulk density (g/cc) | Wilting point (% Vol) | Field capacity (% Vol) | Saturation (%Vol) | Available Water (cm/cm) | Saturated hydraulic conductivity (mm/h) |
|---|---|---|---|---|---|---|---|---|---|---|---|---|---|
| 20 | sandy loam | 18 | 79 | 3.28 | 0.6 | 0.5 | 33 | 1.52 | 11.1 | 17.6 | 42.5 | 0.05 | 24.86 |
| 30 | sandy loam | 16 | 73 | 11.424 | 0.1 | 0.2 | 37 | 1.62 | 9.5 | 16.3 | 38.8 | 0.05 | 17.59 |
| 40 | sandy loam | 18 | 69 | 13.424 | 0.1 | 0.4 | 60 | 1.62 | 10.7 | 18.3 | 38.7 | 0.04 | 8.66 |
| 50 | sandy loam | 18 | 67 | 15.28 | 0.1 | 0.3 | 37 | 1.67 | 10.8 | 18.4 | 36.9 | 0.06 | 10.12 |
| 60 | sandy loam | 18 | 69 | 13.28 | 0.1 | 0.2 | 36 | 1.57 | 10.7 | 18.7 | 40.6 | 0.06 | 16.87 |
| 70 | sandy loam | 17 | 69 | 13.424 | 0.2 | 0.3 | 33 | 1.52 | 10.2 | 18.6 | 42.6 | 0.07 | 23.64 |
| 80 | sandy loam | 18 | 65 | 16.992 | 0.2 | 0.4 | 35 | 1.46 | 10.9 | 20.4 | 45 | 0.07 | 24.93 |
| 90 | sandy loam | 20 | 69 | 11.424 | 0.1 | 0.4 | 27 | 1.60 | 12 | 19.7 | 39.8 | 0.06 | 14.41 |
| 100 | sandy loam | 18 | 69 | 13.28 | 0.1 | 0.4 | 48 | 1.51 | 10.8 | 19.1 | 42.9 | 0.05 | 17.91 |

*This page has intentionally been left blank.*

# Appendix 5: Drone-based hyperspectral and RGB data collection

A Hyperspectral Imager of make BaySpec having 240 spectral channel was installed on DJI Matrice 600 Hexacopter. The imager was fitted inside a gimbal, as shown in figure A5.1(a), and the gimbal is attached to the DJI Matrice 600 hexacopter drone, as shown in figure A5.1(b). Gimbal is one of the important parts of the system as it keeps the imager stable while the drone is flying and nullify the vibrations. Images taken without turning on the gimbal are full of ortho-distortions, artifacts, missing spatial line and sometimes out of focus. Figure A5.2 shows the difference between without gimbal and with gimbal stitched images in RGB bands. A5.2(a) and A5.2(b) images show the effect of the gimbal on data collection. A5.2(a) orthomosaic is created with images taken without a gimbal, and A5.2(b) orthomosaic is created with images taken with the help of a gimbal. Geometric distortions are easily seen in the A5.2(a) orthomosaic.

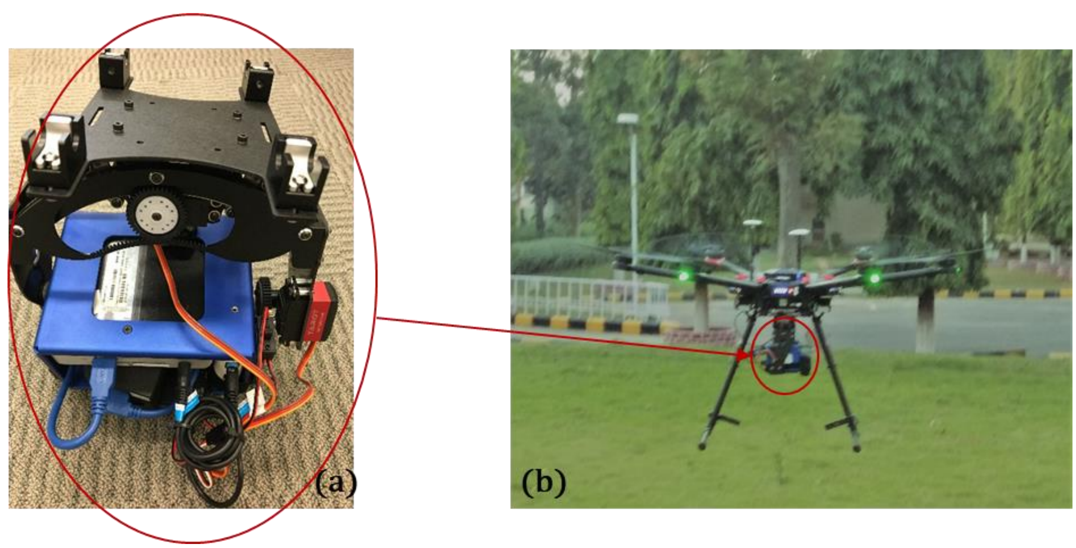


Figure A5.1: (a) Hyperspectral Imager installed inside a gimbal and (b) the complete gimble setup installed on a DJI Matrice 600 hexacopter drone.

(a) (b)

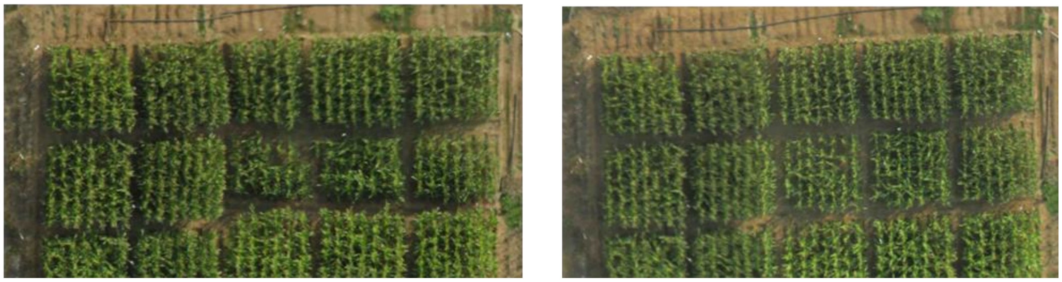

Figure A5.2: (a) Orthomosaic of images taken without gimble. (b) Orthomosaic of same area taken with gimble. The geometric distortion in the images can be seen when the images were captured without gimble.

For stating the hyperspectral camera for data collection, the onboard computer of the hyperspectral imager is first connected with mobile/computer through VNC viewer and below steps are taken:

- Open SpecGrabber and make sure that the focus of the imager is at infinity as the object and camera will be more than 16-meter distance
- 50 frames of white reference are saved by optimizing gain and limiting exposure time within 3.5 ms in the SpecGrabber software of the imager in such a way that the maximum intensity observed from white reference should be around 235.
- 50 frames of Dark background is also saved. The maximum intensity, in this case, should be around 10
- Raw images can be collected with some delay (e.g. 40 seconds) as the drone may take some time to reach the height and orient itself for data collection
- Before flying the drone just make sure that the imager is connected with GPS, imager sensor is not covered by its cap or anything, and the gimbal is on.

➢ The Drone controller is programmed for autopilot mode with UgCS ground station software to map the area of interest. The drone is programmed three times to collect data from three different heights. In this research, data is collected from 25m, 50m, and 75-meter height. Figure A5.3 shows a screenshot of the UgCS software when the drone is flying at 25-meter height. At 25 m, drone speed is kept at 1 m/s, at 50 m, drone speed is kept at 2 m/s and at 75 m the drone speed is kept at 3 m/s. The frame rate of the imager is fixed at 50 fps.


Figure A5.3: UgCS software user interface screenshot when the drone was collecting data from 25-meter height.

*This page has intentionally been left blank.*

# Appendix 6: CHNS Elemental Analyzer (Thermo Finnigan, Italy)

(Source: http://www.rsic.iitb.ac.in/chn.html)

This instrument is used to measure C, H and N. It is based on the principle of the Dumas method , which involves the complete and instantaneous oxidation of the sample by "flash combustion". The combustion products are separated by a chromatographic column and detected by the thermal conductivity detector (T.C.D.), which gives an output signal proportional to the concentration of the individual components of the mixture.

The instrument is calibrated with the analysis of std compounds using the K-factors calculations. Thus the instrument ensures maximum reliability of the results because the combustion gases are not split or diluted but directly carried to build in GC system simultaneous determination of CHNS can be done in less than 10 minutes. This method finds the greatest utility in finding out percentages of C, H, N, S, (O) in organic compounds which are generally combustible at 1800o C.

Reference material used:

- 2.5-Bis(5-tert-butyl-benzoxazol-2-yl)thiophene (BBOT) is used as Standard reference material for the leaf and soil samples as leaves contain a high amount of carbon.
- 3-4 mg of leaf powder samples were used for the analysis with a total of two replications

*This page has intentionally been left blank.*

# Appendix 7: APSIM model related data and simulation results

The APSIM model was simulated for various conditions and various maize variety types. After a comparative study 'mh12' was selected for the reference pupose as explained in capter five.

Figure A7.1 shows the weather data used for the simulation of the APSIM model. The weather data was recorded by an automatic weather station situated near the research farm and managed by the India Meteorological Department (IMD). Solar radiation in MJ per sq meter (radn), daily maximum temperature in degree Celcius (maxt), daily minimum temperature in degree Celcius (mint), rainfall in mm (rain), and evaporation in mm (evap) data were obtained from Oct 2018 to Feb 2019.

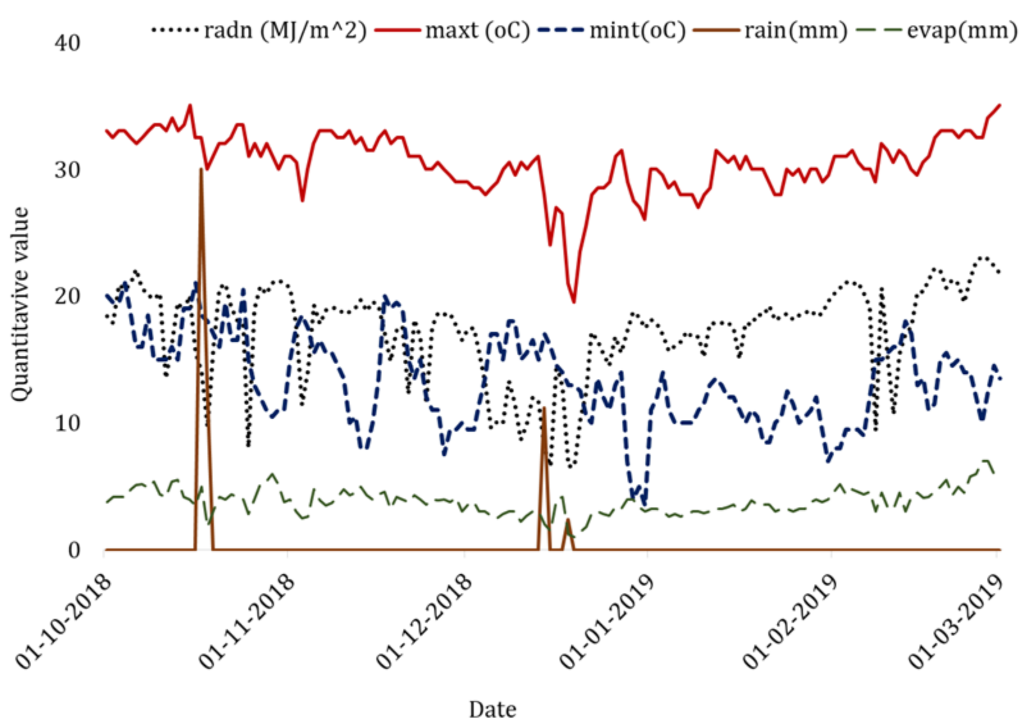


Figure A7.1: The weather data used for simulation of the APSIM model.

Figure A7.2 shows the APSIM simulated soil moisture (upto 30 cm of soil depth) variations based on soil properties, irrigation application, and precipitation events throughout the growing season. Three horizontal lines from top to bottom represent the saturation, field capacity, and permanent wilting point, respectively. The thick yellow color line between field capacity and permanent wilting point shows the level of minimum soil moisture value which was required to minimise the effect of soil moisture stress on the crop. Thus, the soil moisture was supposed to be in the region between field capacity and thick yellow line represented by management allowable deficit (MAD). If the soil moisture goes above the field capacity line, then the plot was considered over irrigated, and if the soil moisture goes below the thick yellow line, then the crop faces soil moisture stress. Soil moisture below permanent wilting point is a highly avoidable scenario where crop may dry down before reaching physiological maturity. The solid blue line is of I3 irrigated plots, dashed green

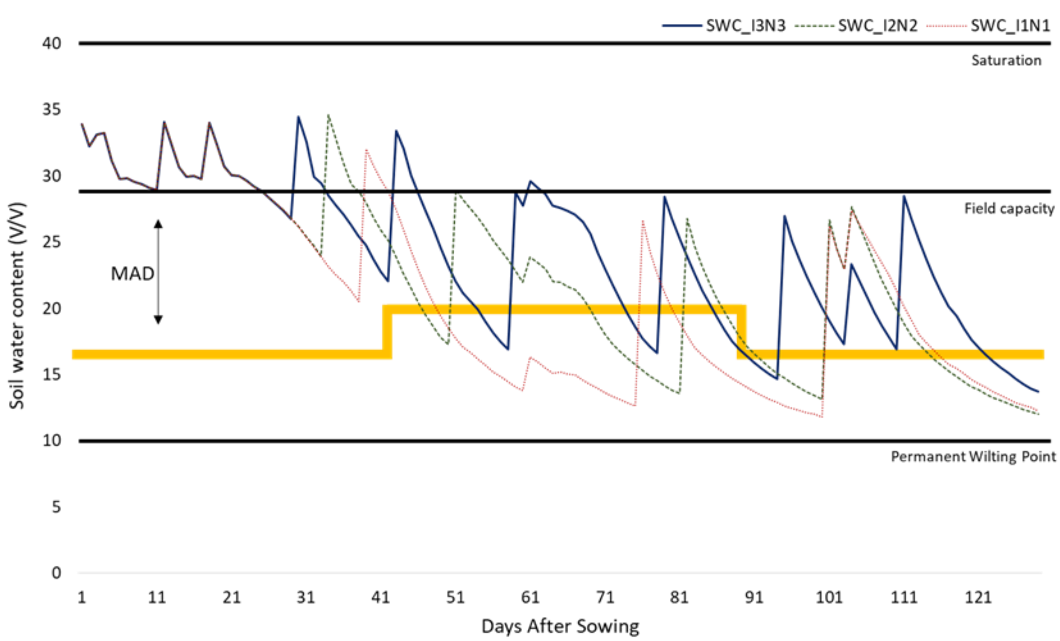


Figure A7.2: Temporal variation of soil moisture in I3, I2, and I1 irrigated plots. The region between the yellow line and field capacity shows the management allowable deficit (MAD). The soil moisture needs to be maintained in the region to make sure plants do not face water stress.

line is for I2 irrigated plots, and dotted red line is for I1 irrigated plots. It can be seen that the I3 irrigated plots mostly maintain the soil moisture values within the management allowable deficit (MAD) region. However, the I1 plots face water stress most of the time as its soil moisture goes below the MAD region very frequently. For optimal condition simulation of the APSIM model, soil moisture was maintained above 70% of the field capacity.

Figure A7.3 shows the comparison of APSIM and DSSAT simulation results for ‘Pionneer3394’ maize variety. The ‘mh12’ verity was not available in DSSAT,

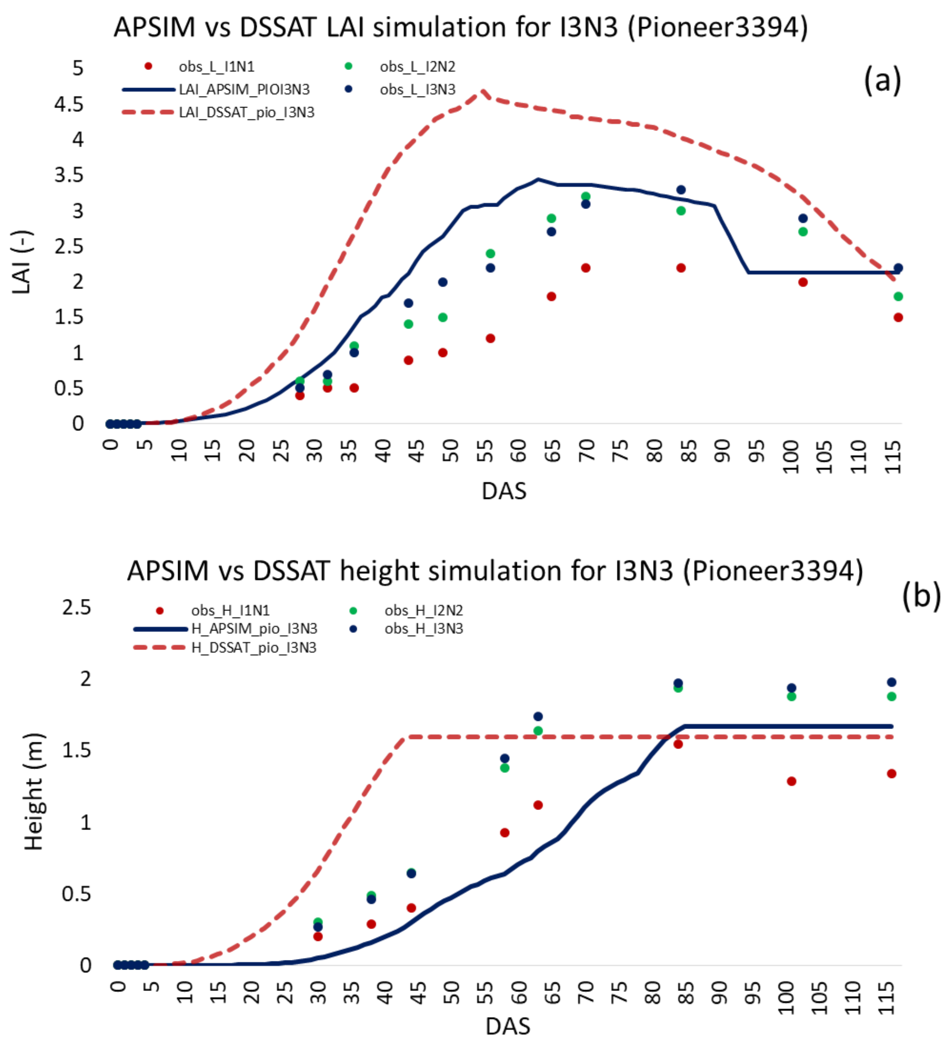


Figure A7.3: Comparison of APSIM and DSSAT simulation results for (a) LAI and (b) crop height. Same input data was used to simulate both models. The APSIM has found to be giving results closer to observed values.

so Pioneer3394 was chosen for comparison. The APSIM simulated results gave near to observed results.

Figure A7.4 shows the APSIM simulation canopy height and LAI values for 'Hycorn53' maize verity. This variety has performed similar to mh12, but mh12 gave slightly better results than Hycorn53, when compared to the field observed values.

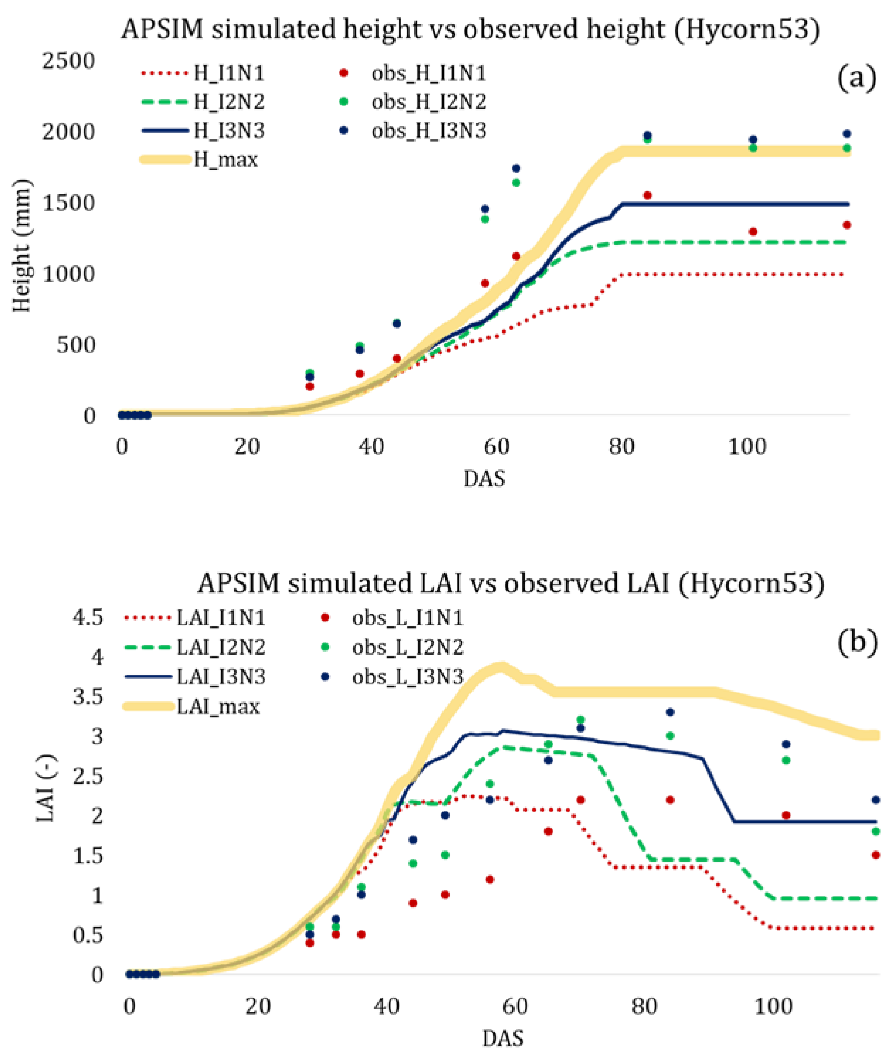


Figure A7.4: APSIM simulated results of (a) canopy height and (b) LAI for 'Hycorn53' maize verity.